University of Tennessee, Knoxville
Trace: Tennessee Research and Creative Exchange

Doctoral Dissertations | Graduate School

8-2012

Magnetic Excitations in the Iron Based Superconductors

Leland Weldon Harriger
lharrige@utk.edu

Recommended Citation
Harriger, Leland Weldon, "Magnetic Excitations in the Iron Based Superconductors. " PhD diss., University of Tennessee, 2012.
http://trace.tennessee.edu/utk_graddiss/1401

This Dissertation is brought to you for free and open access by the Graduate School at Trace: Tennessee Research and Creative Exchange. It has been accepted for inclusion in Doctoral Dissertations by an authorized administrator of Trace: Tennessee Research and Creative Exchange. For more information, please contact trace@utk.edu.

To the Graduate Council:

I am submitting herewith a dissertation written by Leland Weldon Harriger entitled "Magnetic Excitations in the Iron Based Superconductors." I have examined the final electronic copy of this dissertation for form and content and recommend that it be accepted in partial fulfillment of the requirements for the degree of Doctor of Philosophy, with a major in Physics.

Pengcheng, Dai, Major Professor

We have read this dissertation and recommend its acceptance:

Pengcheng Dai, Hanno Weitering, Adriana Moreo, Takeshi Egami

Accepted for the Council:
Carolyn R. Hodges

Vice Provost and Dean of the Graduate School

(Original signatures are on file with official student records.)

Magnetic Excitations in the Iron Based Superconductors

A Dissertation

Presented for the

Doctor of Philosophy

Degree

The University of Tennessee, Knoxville

Leland Weldon Harriger

August 2012

© by Leland Weldon Harriger, 2012
All Rights Reserved.

To my wife Anna, whose constant support and personal sacrifice of her own ambitions to make room for the demands of my own has made what otherwise would have been impossible possible.

Acknowledgments

I would like to begin by thanking my advisor Pengcheng Dai whose passion for science and dedication to his students provided me with the necessary environment to not only succeed in my research but also leave with a fond and lasting memory of the five years I spent in his group. I am grateful to have learned under someone whose drive for research was also well balanced in regards to the needs of his students.

I would also like to thank the numerous crystal growers whose efforts and long hours in the lab provided me with the crystals I used in my work: a special thanks goes to Huiquian Luo at IOP in Beijing for growing the 25g of $BaFe_2As_2$ single crystals that made integratable time of flight data possible. Another special thanks goes to Chenglin Zhang whose organization, hard work and perseverance resulted in the construction of one of the most successful pnictide crystal growth labs in operation, as well as his growth of $FeTe_{0.6}Se_{0.4}$ crystals I used in my work. I thank, as well, Meng Wang's contribution to the $FeTe_{0.6}Se_{0.4}$ growth, Zhengcai Li and Fang Zhou in growing $BaFe_{1.96}Ni_{0.04}As_2$ single crystals, and G.F. Chen for growth of $Fe_{1.05}Te$ single crystals.

I would like to acknowledge the help of all the local contacts who have assisted me in the course of my work: Astrid Schneidewing at FRM-II, Mark Lumsden and Karol Marty at HFIR, Jeff Lynn and Songxue Chi at NIST, Paul Freeman at ILL, and Chris Frost at ISIS.

I am also very grateful to all of my group members: Shiliang Li, Clarina de la Cruz, and Jun Zhao who were present early on in my work and who helped me start

on my path. A special thanks goes to the groups post doctorate Oliver Lipscombe who was around for the central part of my work, taught me the neutron scattering techniques in detail, and endured several years of questions on a daily basis. I am grateful to Mengshu Liu who collected additional data for me at MAPS when I could not be present and also shared in the frustration of the drawn out saga to properly integrating TOF data. Finally, I would like to acknowledge the remaining group members: Miaoyin Wang, Song Yu, and Scott Carr all of whom have provided engaging discussions on the physics of our field.

To end, I wish to thank the funding agencies that supported this work: U.S. NSF-DMR-1063866 and U.S. DOE BES No. DE-FG02-05ER46202.. As well, I am very grateful to the UT/ORNL collaboration, The Joint Institute of Neutron Science (JINS) for sponsoring my work through a Neutron Scattering Fellowship.

The men of experiment are like the ant, they only collect and use; the reasoners resemble spiders, who make cobwebs out of their own substance. But the bee takes the middle course: it gathers its material from the flowers of the garden and field, but transforms and digests it by a power of its own. Not unlike this is the true business of philosophy (science); for it neither relies solely or chiefly on the powers of the mind, nor does it take the matter which it gathers from natural history and mechanical experiments and lay up in the memory whole, as it finds it, but lays it up in the understanding altered and disgested. Therefore, from a closer and purer league between these two faculties, the experimental and the rational (such as has never been made), much may be hoped.

Francis Bacon, Novum Organum, Liberal Arts Press, Inc., New York, p 93.

Abstract

Presented within are neutron scattering studies detailing the spin dynamics of $BaNi_xFe_{2-x}As_2$ for x = 0 (parent), 0.04 (underdoped), and 0.1 (optimal) dopings, and $FeSe_xTe_{1-x}$ for x = 0 (parent), 0.3 (underdoped), and 0.4 (optimal) dopings. These recently discovered Fe-based superconducting compounds are strikingly similar, in many respects, to the cuprate class of unconventional superconductors and share qualitatively similar phase diagrams consisting of a long range ordered magnetic ground state in the parents which, upon doping, is supplanted in favor of superconductivity. The dopings discussed herein allow us to tune through the phase diagram, beginning with long range ordered parents and ending with optimally doped superconductors with short range magnetic correlations.

For $BaFe_2As_2$, the excitations in the ordered state are strongly damped and persist up to 300meV. Low energies excitations are centered around Q_{AMF} and disperse towards the zone boundary with increasing energy. Only scattering above 100meV is effected when warming above T_N. In underdoped x = 0.04 $BaNi_xFe_{2-x}As_2$, we find an order of magnitude reduction in the coupling between layers and a corresponding crossover from 3D to 2D magnetism. In coauthor work on optimal doped x = 0.1 $BaNi_xFe_{2-x}As_2$ we establish the existence of a 3D resonance mode in the superconducting state. Excitations at optimal doping above the resonance are very similar to the paramagnetic scattering observed in the parent and consists of diffuse scattering below 100meV while above this threshold the signal has similar dispersion, linewidths, and intensity as the ordered state.

For FeTe, I discuss our existing efforts and data collection aimed at addressing issues associated with calculating the effective moment from Q,E-integrated data. Tuning through the phase diagram to the x = 0.3 underdoped $FeSe_xTe_{1-x}$ system we find filamentary superconductivity with magnetic spectral weight sitting at both the AFM and nesting vector. Upon reaching x = 0.4 optimal doping, the scattering completely transfers over to the nesting vector and a 2D resonance mode appears below T_c.

Contents

List of Figures **xii**

1 Introduction **1**

1.1 Introduction to Conventional Superconductivity 1

1.2 Introduction to Unconventional Superconductivity 3

1.2.1 The Cuprates 3

1.2.2 The Fe-based Superconductors 5

1.2.3 The Heavy Fermions 8

1.3 Magnetism in Unconventional Superconductors 9

1.3.1 Localization, Itinerancy, and Everything In between: An Introduction 9

1.3.2 Magnetism in the Cuprates 10

1.3.3 Magnetism in the Fe-based Superconductors 16

1.3.4 Magnetism in the Heavy Fermions 24

1.4 Neutron Scattering 28

1.4.1 Scattering Cross-Sections 28

1.4.2 Nuclear Scattering Cross-Section 33

1.4.3 Magnetic Scattering Cross-Section 35

1.4.4 Fluctuation Dissipation Theorem 37

1.5 Data Analysis 41

1.5.1 Transformations between Unit Cells 41

1.5.2 Normalization of Data to Absolute Units 44
1.5.3 Resolution Calculations and Model Convolution 46
1.6 Motivation of Thesis 52

2 Pnictides **54**
2.1 Magnetic Excitations in the $BaFe_2As_2$ Parent 54
2.1.1 Introduction 54
2.1.2 7K Data and Model 56
2.1.3 Resolution Convolved Model Fitting 63
2.1.4 Magnetic Excitation across the Phase Transition; 125K and 150K 71
2.1.5 Conclusion 76
2.2 Magnetic Excitations in Under Doped $BaFe_2As_2$ 82
2.2.1 Introduction 82
2.2.2 Spin Wave Scattering with 2D Character in the Ordered State 83
2.2.3 Conclusion 92
2.3 Magnetic Excitations in Optimal Doped $BaFe_2As_2$ 93
2.3.1 Mapping out the Resonance 93
2.3.2 Comparison of High Energy Magnetic Excitations in the Parent and Optimal Doped $BaFe_2As_2$ 105

3 Chalcogenides **113**
3.1 Parent and Underdoped 113
3.1.1 Introduction 113
3.1.2 Local, Itinerant, Frustration... 114
3.1.3 Conclusion 118
3.2 Optimal Doped 121
3.2.1 Introduction 121
3.2.2 Characterization of the Resonance Mode Energy 125
3.2.3 Conclusions 137

4 Looking Back, Looking Forward **140**

4.1 Ongoing Work 140

4.1.1 Temperature Dependence of the Effective Moment in FeTe . . 140

4.1.2 High Temperature Study of Magnetic Excitations in $BaFe_2As_2$ 143

4.2 Future Work 145

4.3 Concluding Remarks 148

Vita **164**

List of Figures

1.1 a) Chemical structure of the parent (x=0) $La_{2-x}Sr_xCuO_{4-y}$ (figure taken from http://www.physics.ubc.ca/ berciu/RESEARCH/). b) Doping replaces La^{3+} with Sr^{2+}, the reduction of oxidation state draws electrons from the CuO_2 layers and effectively hole dopes these planes. c) The antiferromagnetic order in the copper oxide planes is of simple G-type order and with sufficient doping this long range order is replaced by a dome of superconductivity in the phase diagram as depicted in d). Fig 1d reproduced from Damascelli, *et al.* 4

1.2 a) Q-integrated local susceptibility as a function of T_c for overdoped $La_{2-x}Sr_xCuO_{4-y}$ with x = 0.25, 0.27, 0.28, and 0.30 [123]. The linear correlation suggests that superconductivity is contingent on the presence of magnetic excitations. Inset provides a measure of T_c via the superconducting dielectric response for the dopings studied. b) The energy about which a superconducting resonant gain in magnetic intensity appears can be linearly correlated to the T_c of the system [139]. c) A similar linear dependence exists between the resonant energy and the superconducting gap [139]. The points correspond to different dopings across multiple classes including the cuprates, pnictides, and heavy Fermion systems. Thus, these features appear to be ubiquitous to unconventional superconductivity where magnetism is present. 6

1.3 Crystal structure of the four Fe-based families [75]: a) LaFeAsO, b) $SrFe_2As_2$, c) LiFeAs, and d) $Fe_{1+x}Te$. The stripe antiferromagnetic (AFM) order of the Fe spins is depicted for LaFeAsO and $SrFe_2As_2$. AFM order in the (111) class was originally found to be absent. However, experiments now demonstrate an identical magnetic ordering [62] as the (1111) and (122) classes with weak magnetic moments that are quickly suppressed due to Li evaporation. In $Fe_{1+x}Te$, stripe AFM ordering is also present, however the spin alignment is rotated 45 degrees away with respect to AFM order in the other classes. Inhomogeneity in the form of excess iron Fe(2) is also present in these systems and can effect the magnetic ordering of the system [3]. 7

1.4 Time of flight neutron scattering data for spin wave scattering in the cuprate parent $LaCuO_4$ with fits to the Heisenberg Hamiltonian given in Eq. 1.8. a) Extracted dispersion along the path in reciprocal space described by the subpanel in c). The red line is a fit to the model. b) A 2-D data slice of the same dispersion path with the intensity of the scattering included as a color profile. c) The intensity corresponding to the dispersion in panel a). d) The ratio of the experimental intensity over the model intensity demonstrates that the model fits very well everywhere except at the wave vector (1/2, 0) where the spin wave lifetime damps out due to a decay process discussed in the body of text. e) In general the Heisenberg model gives an hour glass dispersion propagating out of the long-range ordering wave vector, the exact structure and spin band width depend on the exchange couplings of the systems. Panel f) describes the different exchange couplings used to fit the data. Note that the copper and oxygen orbitals spacial character support a hopping that would reduce J_2 while simulateously enhance a cyclic exchange. Panels taken from figures in [44, 16] 14

1.5 (a) Incommensurability in the magnetic scattering of hole doped LSCO. Insets are cartoons describing the direction of the incommensurability about the AFM wave vector. At the metal to insulator transition the incommensurability rotates by 45 degrees from a diagonal to parallel alignment with the unit cell. (b) Upon doping the short range fluctuations left over from broken long range order remain dispersive, however an hourglass feature is introduced at low energies in the dispersion. Figures taken from [110] and comprise the work of several papers. Refer to this work (Ch. 6) for references to original data. . . 16

1.6 a) Spin-split bands separated by an energy Δ. b) The susceptibility of an electron gas. c,d) The corresponding nesting conditions associated with panel b. Panels are reconstructed from figures appearing in [6, 39]. 18

1.7 a,b) Phase diagram for electron and hole doping of $BaFe_2As_2$ including information for the structural, magnetic, and superconducting phases. The acronyms IC-AF, C-AF correspond to incommensurate and commensurate elastic scattering while IC-SF corresponds to incommensurate inelastic scattering. The incommensurate structure is dependent on the doping type and depicted as insets on the respective sides of the phase diagram. c-e) Geometry of the Fermi surface where the role of doping enlarges and/or shrinks pockets depending on doping type. e-f) Structure of inelastic excitations due to the off-nesting that results from doping. Panels taken from a forthcoming publication in Nature Physics Review article [18]. 21

1.8 a) Qualitative regions of phase space based off of Hubbard model calculations with the yellow ellipse corresponding to region where experiment agrees well with theory. b) DMFT vs RPA calculations of the distribution of the fluctuating moment across energy transfer. Comparing this with inelastic neutron scattering data c) we find that the DMFT calculations, which can capture stronger electronic correlations than RPA, lead to much better agreement between experiment and theory. d) A qualitative sketch of the Hubbard model as a function of electron correlation with a guess as to where the pnictides fall between the two extremes of localized and itinerant magnetism. Panels taken from [18, 67] 23

1.9 Possible ground states resulting from the competition between the Kondo and RKKY interactions. T_m is the ordering temperature and JN is the f-d exchange coupling times the f density of states at the Fermi energy. [105] 25

1.10 a) Confirmation of T^* given by the intersite RKKY interaction for a variety of Kondo lattice materials; c = 0.45. b) Updated Doniach diagram for Kondo lattice materials. [29] 28

1.11 Definition of Unit Cells: a) The black box defines the tetragonal unit cell corresponding to the lattice symmetry for temperatures above the structural phase transition. In the tetragonal state, the magnetic moments associated with the iron atoms are disordered as represented by the black arrows. b) Below the phase transition, the tetragonal cell undergoes an inplane angular distortion leading to the monoclinic unit cell defined in red. The low temperature phase can also be described by an orthorhombic unit cell (dashed green line) which consists of 4 neighboring diagonals of the monoclinic cell. The structural distortion is accompanied by a long range ordering of the magnetic moments with the the spins aligning antiferromagnetically and ferromagnetically along the orthorhombic a and b axis respectively. 42

1.12 Fourier Transform of the Structure: a) Superposition of the real space orthorhombic (dashed green) and tetragonal (solid blue) cells. b) Fourier transform of cells. c) Relationship between the lattice vectors of the two cells. Given that the distortion is extremely small, its effects have been ignored in the figure, ie: $a_O = b_O$ with axis 90° apart and $\theta = 45^o$ 43

1.13 a) Example of an experimental determination of elastic energy resolution based on an E-scan of the elastic line about E=0. b) Triple axis spectrometer with labeled quantities that contribute to the resolution: 4 collimations, 3 mosaics, 2 neutron wave vectors, 1 spectrometer handedness. c) Example of two resolution ellipses at equivelant positions along an acoustic phonon dispersion centered on an (0,0,4) nuclear Bragg peak. d) The resulting intensity and linewidth difference of the two equivalent peaks results from one resolution ellipse lying more or less perpendicular to the dispersion line while the other lies along it. 48

1.14 Time of flight spectrometer with labeled quantities that contribute to the resolution: 3 spacial spans, 2 flight paths, 2 pulse widths, 2 energies 50

2.1 a) Constant energy cuts of the spin wave excitations at 7K for $BaFe_2As_2$ and $CaFe_2As_2$ in absolute units within the first Brillouin zone. The data for $CaFe_2As_2$ and $BaFe_2As_2$ are from Ref. [40] and [144] respectively. 57

2.2 a) 2D Constant-energy slices of spin wave data in $CaFe_2As_2$. Each consecutive panel shows a slice at a higher energy transfer. At energies below 50meV (top left panel) the scattering is centered at the AFM wave vector, as the energy transfer increases the scattering spreads out into well formed ellipses that track the cone like dispersion of spin waves. Upon approach of the zone boundary at 175meV (bottom right panel) the scattering becomes very diffuse with maxima at the zone edge. The third panel in the top row includes an arrow showing the direction that 1D cuts were made in b) The lines overplotting the data in b) are global fits to the Heisenberg model described in the text with a Q-isotropic damping $\Gamma = \Gamma_0 + (\text{slope}) \cdot E$ [144]. 59

2.3 Constant energy slices of the 7K spin wave data for $BaFe_2As_2$. a) At lower energies the scattering forms an ellipse centered around the AFM wave vector much like $CaFe_2As_2$. b) At intermediate energy transfers the scattering breaks apart along the H-direction to form two mirror image rods (ie: L independent) of scattering above and below the H-axis. These rods translate along the K-direction with increasing energy transfer. c) At high energies the scattering combines with contributions from twinned domains to form a ringlike excitation about the zone boundary. Above the zone boundary (not shown) the scattering stretches out in a long damping tail and fills in to form a single center of scattering at (1,1). 60

2.4 a) Comparison of a normalized RPA calculation from Ref. [52] and our data. Given the normalization correction, RPA appears to fit the data. 61

2.5 (Figure on next page.) a) The AF Fe spin ordering in $BaFe_2As_2$ with the magnetic exchange couplings J_{1a} , J_{1b}, J_2 along different directions. b) Temperature dependence of the resistivity in detwinned $BaFe_2As_2$ (from Ref. [12]). The inset is a plot of the resistivity for the twinned sample used in our neutron measurements with the blue points corresponding to T = 7, 125, and 150 K. (c) Color plots describing qualitatively how the spin wave scattering evolves from Q = (1, 0) to (1, 1) as a function of energy using an anisotropic damping Γ. The solid black contours are an overlay of the same model with identical exchange coupling parameters but with no damping. The exchange couplings used are from best fits of the data. d) Color plot of the anisotropic damping Γ, which is much stronger along the H direction than along the K direction. (e) Spin wave dispersion along the (1, K) direction as determined by energy and Q cuts of the raw data below and above T_N. The solid line is a Heisenberg model calculation using anisotropic exchange couplings $SJ_{1a} = 59.2 \pm 2.0$, $SJ_{1b} = -9.2 \pm 1.2$, $SJ_2 = 13.6 \pm 1.0$, $SJ_c = 1.8 \pm 0.3$ meV determined by fitting the full cross-section. The dotted line is a Heisenberg model calculation assuming isotropic exchange coupling $SJ1a = SJ_{1b} = 18.3 \pm 1.4$, $SJ_2 = 28.7 \pm 0.5$, and $SJ_c = 1.8$ meV. f) Dispersion along the (H, 0) direction; data points beyond H = 1.4 could not be reliably obtained due to strong damping at higher energies. The red shading stresses how the damping grows as a function of H. Error bars are systematic and represent the difference between Q and E cut dispersion points. The statistical error of the Q and E cuts are much smaller. 64

2.6 Control flow describing the three fitting paths and starting parameters used to determine the final parameters of best fit for the anisotropic Heisenberg model used. Details about each route are described in the text. 67

2.7 (Figure on next page.) Wave vector dependence of the spin waves for energy transfers of (a) $E = 26 \pm 10$ meV [$E_i = 450$ meV and Q = (H, K, 1)]; (b) $E = 81 \pm 10$ meV [$E_i = 450$ meV and Q = (H, K, 3)]; (c) $E = 113 \pm 10$ meV [$E_i = 450$ meV and Q = (H, K, 5)]; (d) $E = 157 \pm 10$ meV [$E_i = 600$ meV and Q = (H, K, 5)]; e) $E = 214 \pm 10$ meV [$E_i = 600$ meV and Q = (H, K, 7)] f) The projection of the spin waves on the energy transfer axis and (1, K) direction (with integration of H from 0.8 to 1.2 rlu) after subtracting the background integrated from $1.8 < H < 2.2$ and from $-0.25 < K < 0.25$ with $E_i = 450$ meV. The color bar scales represent the absolute spin wave intensity in units of mbarn·sr^{-1}·meV^{-1}·f.u.$^{-1}$ and the dashed boxes indicate zone boundaries. The missing low-energy data in (f) is due to imperfect data subtraction. (g)-(l) Model calculation of identical slices as in (a)-(f) using anisotropic exchange couplings from best fits and convolved with the instrumental resolution. 68

2.8 (a)-(c) Spin waves of $E = 50 \pm 10$ meV; (d)-(f) $E = 75 \pm 10$ meV; (g)-(i) $E = 125 \pm 10$ meV; and (j)-(l) $E = 150 \pm 10$ meV for temperatures of T = 7, 125, and 150 K. The dashed curves show fixed reciprocal space sizes at different temperatures. 72

2.9 (Figure on next page.) The blue diamonds in (a)-(d) are constant-Q cuts at Q = (1, 0.05), (1, 0.2), (1, 0.35), and (1, 0.5), respectively, at T = 7 K. The green squares and red circles in (a)-(d) are identical constant-Q cuts at T = 125 and 150 K, respectively. The dashed lines are guides to the eye for the observed paramagnetic scattering. (e) and (f) Q dependence of the spin wave excitations below and above T_N obtained through constant-E cuts at $E = 19 \pm 5$ and 128 ± 5 meV. The solid lines in (a)-(f) are fits to the anisotropic spin-wave model discussed in the text, and the horizontal bars represent the instrumental energy (E)/wave vector (Q) resolution. (g) Energy dependence of the dynamic spin-spin correlation lengths below and above T_N obtained by Fourier transform of constant-E cuts similar to (e) and (f). 74

2.10 (a)-(d) Results from an isotropic $J_1 - J_2 - K$ Heisenberg model [141]. Consecutive panels are of increasing energy transfer following the dispersion of magnetic excitations from the (1, 0) zone center at low energy (panel a) to the (1, 1) zone boundary at high energies (panel d). (e) and (f) are reproductions of zone center and zone boundary data from Fig. 2.7. 77

2.11 (a) Different unit cells in the real space of the crystal: Solid black is Fe sublattice required by RPA, red and blue are the tetragonal and orthorhombic cells respectively. (b) Corresponding Brillioun zones in reciprocal space. Taken from [27]. 79

2.12 (a) Structure of scattering as a function of increasing energy based on DMFT calculations. (b) Structure of scattering from our measurement. Figure taken from [90]. 81

2.13 (a) Diagram of the parent compound $BaFe_2As_2$ with Fe spin ordering and magnetic exchange couplings depicted. (b) Electronic phase diagram from Ref. [7]. (c) Temperature dependence of the resistance showing anomalies at T_s, T_N, and T_c. (d) Temperature dependence of the Meissner and shielding signals on a small crystal (field cooled $4\pi\chi = -0.001$ at 4.5 K) and the (1, 0, 1) magnetic Bragg peak intensity. (e) The structural distortion of the lattice as determined by tracking the width of the (2, 0, 0) nuclear Bragg peak using $\lambda/2$ scattering without Be filter. (f) Magnetic order parameter determined by Q scans around the (1, 0, 1) magnetic Bragg peak above background. The solid line shows an order parameter fit using $(1 - T/T_N)^{2\beta}$ with $T_N = 91.3 \pm 0.7$ K and $\beta = 0.3 \pm 0.02$. 84

2.14 (Figure on next page.) (a) Energy scans at $Q = (1, 0, 1)$ and $Q = (1, 0, 0)$ above and below T_c. (b) $\chi''(\mathbf{Q}, \omega)$ at $Q = (1, 0, 1)$. (c) Energy scans at higher temperatures and, (d) the corresponding $\chi''(\mathbf{Q}, \omega)$. The solid lines in (b) and (d) are guides to the eye. (e) Q scans along the [H, 0, 1] direction at 4 meV. At 86 K, the Gaussian peak has FWHM $= 0.098 \pm 0.006$ rlu which corresponds to minimum correlation lengths of $\xi = 57 \pm 4\mathring{A}$. (f) Estimated $\chi''(\mathbf{Q}, \omega)$ at 4 meV. (g) $\chi''(\mathbf{Q}, \omega)$ at 7 meV with FWHM $= 0.103 \pm 0.013$ rlu and minimum correlation length of $\xi = 54 \pm 6\mathring{A}$. (h) Low temperature Q scans along the [1, 0, L] direction (c axis) at 4 meV (FWHM $= 0.58 \pm 0.06$ rlu) and 7 meV (FWHM $= 0.9 \pm 0.3$ rlu) correspond to $\xi = 14 \pm 5$ and $21 \pm 2\mathring{A}$, respectively. The solid curves in e-h) are Gaussian fits with centers fixed at (1, 0, 1) rlu. 86

2.15 (Figure on next page.) (a) Energy scans at $Q = (1, 0, 0)$ and $Q = (1.4, 0, 0)$ from 0.5 meV to 7 meV at 3.5 K and 18 K. (b) Background corrected $\chi''(\mathbf{Q}, \omega)$ showing clear evidence for a 4 meV spin gap. (c) Temperature dependence of the signal $[Q = (1, 0, 0)]$ and background $[Q = (1.4, 0, 0)]$ scattering at various temperatures. (d) $\chi''(\mathbf{Q}, \omega)$ at different temperatures. The solid lines in (b) and (d) are guides to the eye. (e) Q scans along the [H, 0, 0] direction at 4 meV and different temperatures. (f) Background corrected $\chi''(\mathbf{Q}, \omega)$. (g) Temperature dependence of the Q scans along the [H, 0, 0] direction at 6 meV (FWHM $= 0.10 \pm 0.01$ rlu). (h) Temperature dependence of the $\chi''(\mathbf{Q}, \omega)$ at 6 meV. Gaussian fits to the data in (e-h) have fixed centers at $Q = (1, 0, 1)$ rlu. 88

2.16 ((a) Temperature dependence of the 1 meV scattering at the signal $Q = (1, 0, 0)$ and background $Q = (1.4, 0, 1)$ positions. The inset shows Q scans along the [H, 0, 0] at 1 meV and different temperatures. The scattering shows no anomaly across T_c but clearly peaks at T_N. (b) Temperature dependence of the scattering at 4 meV and $Q = (1, 0, 1)$ again peaks at T_N. 91

2.17 a), b) Neutron scattering data on a powder sample of $Ba_{0.6}K_{0.4}Fe_2As_2$ at T = 5K (superconducting) and T = 50K (non superconducting) respectively. In the SC state, a sharp increase in scattering is visible at 14meV, indicative of the presence of a resonance. c) A temperature scan of the 14meV anomaly reveals that intensity follows an order parameter in temperature, with suppression at T_c. d) (left panel) Q-integrated energy scan of the resonance at T = 7K demonstrating that the intensity peaks at $\omega_R = 14$meV. (right panel) The T = 7K energy scan compared to an identical scan at T = 50K reveals that the resonant excitation disappears in the normal state. Data from [10]. . 94

2.18 Constant-energy scans around the (1, 0, 0) and (1, 0, 1) positions for E = 2, 6, and 8.5 meV. (a-c) Q scan along the [H, 0, 0] direction at 30 and 3 K. The inset in (a) shows the temperature difference plot and a Gaussian fit to the data. The missing low-Q data for scans in (b) and (c) are due to kinematic constraint. (d) Q scan along the [1, 0, L] direction for E = 8.5 meV at 3 K. Note two clear peaks centered at (1, 0, -1) and (1, 0, 1), respectively. 97

2.19 (a) Energy scans at Q = (1, 0, 0) from 5 to 13 meV at 30 and 3 K. (b) The temperature difference scattering between 3 and 30 K shows a clear resonant peak at E = 9.1 ± 0.4 meV. (c) Energy scans at Q = (1, 0, -1) from 2 to 13 meV at 30 and 3 K. (d) The temperature difference plot confirms that the mode has now moved to 7.0 ± 0.5 meV. (e) Wave vector dependence of the scattering at 30 and 3 K for E = 7 meV, confirming that the resonance intensity gain occurs at Q = (1, 0, -1). (f) Temperature dependence of the scattering at Q = (1, 0, -1) and E = 7 meV shows a clear order-parameter-like increase below T_c. 99

2.20 Summary of electron-doping dependence of the neutron spin resonance energies at $Q = (0.5, 0.5, 0)$ and $(0.5, 0.5, 1)$ as a function of T_c. Solid lines are linear fits to the data. Figure taken from [125] with data for $BaFe_{2-x}Ni_xAs_2$ and $BaFe_{2-x}Co_xAs_2$ compiled from multiple papers. Refer to [125] for these references. 100

2.21 (a) Energy cuts of the resonance in underdoped $Ba(Fe_{1-x}Co_x)_2As_2$ (Co=4.7%) for a range of L values throughout the Brillouin zone. (b) Comparison of the resonance for under (4.7%) and optimal (8%) dopings at different L. (c) Dispersion of the resonant peak energy as a function of L. Figure taken from [96]. 102

2.22 Resonance in $YBa_2Cu_3O_{6.85}$ for both the odd (a,b) and even (c,d) channels. L-scans in (b) and (d) reveal explicitly the sine squared and cosine squared intensity modulation for the odd and even channels respectively. Figure taken from [89]. 104

2.23 (Figure on next page.) **a**, AF spin structure of $BaFe_2As_2$ with Fe spin ordering. The effective magnetic exchange couplings along different directions are shown. **b**, RPA and LDA+DMFT calculations of $\chi''(\omega)$ in absolute units for $BaFe_2As_2$ and $BaFe_{1.9}Ni_{0.1}As_2$. **c**, The solid lines show the spin wave dispersions of $BaFe_2As_2$ for $J_{1a} \neq J_{1b}$, along the $[1, K]$ and $[H, 0]$ directions obtained in [42]. The filled circles and triangles are the spin excitation dispersions of $BaFe_{1.9}Ni_{0.1}As_2$ at 5 K and 150 K, respectively. **d**, The solid line shows the low-energy spin waves of $BaFe_2As_2$. The horizontal bars show the full-width at half-maximum of spin excitations in $BaFe_{1.9}Ni_{0.1}As_2$. **e**, Energy dependence of $\chi''(\omega)$ for $BaFe_2As_2$ (filled blue circles) and $BaFe_{1.9}Ni_{0.1}As_2$ below (filled red circles) and above (open red circles) T_c. The solid and dashed lines are guides to the eye. The vertical error bars indicate statistical errors of one standard deviation. The horizontal error bars in **e** indicate the energy integration range. Figure taken from the coauthor work [67]. 106

2.24 Constant-energy images of the spin excitations as a function of increasing energy for $BaFe_{1.9}Ni_{0.1}As_2$ and $BaFe_2As_2$ in units of mbarns/sr/meV/f.u.(a)$E = 33 \pm 3$, (b)43 ± 3, (c)60 ± 10, (d)81 ± 10, (e)113 ± 10, (f)135 ± 10, (g)157 ± 10, and(h)214 ± 10 meV. 111

3.1 Constant energy slices of the spin waves as a function of increasing energy at 10 K for $Fe_{1.05}Te$. All data are normalized to absolute units with a vanadium standard. (a)(c) Collected with incident neutron energy E_i = 90 meV on ARCS, (d)(f) E_i = 350 meV on MAPS, (g),(h) E_i = 500 meV on MAPS. The dashed line in (a) shows a crystallographic BZ. Figure taken from [64]. 115

3.2 Contour plot of combined cuts for the T = 1.5 K data in the (a) [0.5,K] direction and (b) the [H,1 - H] direction through (0.5,0.5) as a function of energy. Both figures are plotted on the same energy scale so that the correspondence between the two excitations can be seen. Figure taken from [8]. Note that this figure uses tetragonal units whereas the body of my thesis uses orthorhombic units throughout. 117

3.3 a)-d) The first momentum in energy as a function of momentum transfer is illustrated for the interstitial iron concentrations investigated. The solid curves are fits to the Hohenberg-Brinkman sum rule described in the original paper from which this figure was taken [116]. e) Peak position of the magnetic spectrum in momentum. f) Mean energy position. (g) Total integrated intensity in energy and momentum as a function of interstitial iron concentration. All of the data is presented for $T = 2$ K. 119

3.4 a), c) Energy scans of the resonance at different temperatures. b), d) Energy of the resonance obtained by fits to the data from panels a) and c) respectively. Panels a), b) taken from [49] and panels c), d) taken from [33]. 123

3.5 (a) Diagram of the Fe spin ordering with the shaded region defining the magnetic unit cell. (b) Cartoon of the scan directions though the $(1/2, 1/2, L)$ nesting vector. The inset illustrates the direction in the $[H, K]$ plane that scans were confined to. Excitations at $(1/2, 1/2, L)$ in $FeTe_{1-x}Se_x$ consist of two incommensurate peaks that spread away from one another in the transverse direction. The red circles in the inset depict these excitations with the radius of the circles equal to twice the FWHM of the (1/2, 1/2, 0), 7.5 meV resonance peaks measured on crystals from the same batch on a different experiment. The separation of their centers is set to agree with the dispersion mapped out in this previous experiment [63] (c-e) Energy scans about the 7 meV resonance position above and below T_c for $L = 0, 1/2, 1$. Clear intensity gain is observed inside the superconducting state. The background at $L = 0$ is plotted above and below T_c and is found to be identical, allowing direct temperature subtraction of the scans with no need for background correction. (f) Temperature subtraction of energy scans shown in panels (c-e) demonstrating no observable dispersion of the resonance energy along L. 127

3.6 (Figure on next page.)(a) Raw data for energy scans at $Q = (1/2, 1/2, 1/2)$ for multiple temperatures below T_c. At 2 K the 7 meV resonance is clearly present. A strong reduction in scattering for energies below 4 meV is also visible, indicating the opening of a gap in the system. Subsequent Q-scans, however, show that this is not a true gap. As the temperature increases to T_c the resonance suppresses and the partial gap closes up. (b) Temperature subtraction of scans shown in panel (a). All of the data is fit with a Gaussian leaving the center energy as a free parameter to be determined. (c) Position of the resonance energy vs temperature as determined from the fits in panel b), note that circle above T = 15K are meant to indicate that the resonance has been completely suppressed. The temperature dependence of the superconducting gap [93] is also graphed, explicitly demonstrating that the resonance does not shift in energy as a function of temperature so as to remain inside 2Δ as required by the spin exciton scenario. 128

3.7 (a,b) Raw Q-scan data along $[H, H]$ and L respectively at $E_R = 6.5$meV at several temperatures. (c,d) $\chi''(Q, \omega)$ is determined by subtraction of the background and correcting for the Bose factor. In c) the 100 K data was used as a final background subtraction in order to remove a spurion at (0.45, 0.45, 0.5) and a phonon tail for points near (0.7, 0.7, 0.5). (d) The intensity gain due to the resonance is determined by subtraction of the 2 K and 20 K data. The resulting signal is very broad and fits well to the Fe^{2+} form factor; a testament to the 2D nature of the resonant mode. (e,f) Temperature dependence of the resonance for $Q = (1/2, 1/2, 1/2)$ and $E = 6.8$ meV. The resonance suppresses as an order parameter as T_c is approached. 131

3.8 (a,b) Q-scan data along the $[H, H]$ direction for $L = 1$ and $E = 3$ meV. The scattering becomes stronger as T_c is approached from higher temperatures, upon entering the superconducting state the intensity drops significantly by 2 K but does not fully gap. (c) Temperature dependence at 3 meV inside of the pseudo spin gap region reveals that near T_c a gap begins to form but never fully forms by base temperature. (d) $S(Q, \omega)$ of the temperature scan as determined by interpolating and subtracting the background collected using A3 rocking curves. Yellow diamonds correspond to cross checks with fitted Q-scans from panels (a,b). Since the Q-scans and temperature scan were collected on different experiments, the data sets were not normalized to one another by monitor count but rather shifted to coincide at 20 K. 132

3.9 (a) Raw Q-scan data along the $[H, H]$ direction for $L = 1$ and $E = 11$ meV. (b) $\chi''(Q, \omega)$ determined by background subtraction and correcting for the Bose factor. The resonance is no longer visible, instead the scattering at 2 K is nearly identical to 20 K. Upon entering the normal state, the intensity begins dropping monotonically with increasing temperature but remains robust up to 100 K. (c,d) Temperature scan at (1/2, 1/2, 1/2) for $E = 11$ meV. Red stars correspond to cross checks with fitted peak intensities from Q-scans in panel a) that have been form factor corrected and normalized by monitor count. 135

3.10 (a) Energy scans focusing on temperatures above T_c. (b) The background subtraction of $\chi''(Q, \omega)$ is determined from Q-scans. Aside from the resonance in the 2 K data, all other energy scans follow a similar linear trend; fanning out as a function of temperature. 136

4.1 (a) $\chi''(\mathbf{Q},\omega)$ as a function of energy for $\mathbf{Q} = (0, 0.45)$ at 10 K, 80 K and 300 K. (b) Temperature dependence of S(E), excluding Bragg scattering. (c) Square of the effective magnetic moment obtained by integrating the S(E), as a function of temperature. Upper (blue) symbols show the total response, bottom (red) symbols are the Bragg contribution, green symbols are the quasi elastic contribution. Figure taken from [143]. 141

4.2 (a)-(e) Temperature dependence of S(E), excluding Bragg scattering. (f) Overplot at all temperatures of the empirical fits used to integrate out the moment. (g) Square of the effective magnetic moment as a function of temperature. Figure taken from unpublished work by our group. 144

4.3 Screen shot of Lslice, a developmentary software for improving the functionality, user friendliness, and integration of existing time of flight software. 147

Chapter 1

Introduction

1.1 Introduction to Conventional Superconductivity

The definitive text describing superconductivity, BCS Theory [4], provides both a microscopic model for qualitatively understanding the formation of this phase and a fully non-relativistic quantum mechanical framework that establishes a quantitative basis for calculating measurable parameters. The applicability of BCS theory is constrained primarily to spatially isotropic systems. In cases where spatial inhomogeneity must be taken into account, an ever present concern in type II superconductivity, the microscopic BCS model becomes cumbersome and must be replaced with a limiting form, Ginzberg-Landau (GL) theory [35]. Taken together, these two theories stand as a crowning achievement in condensed matter physics and provide an excellent description of the superconducting state.

In 1956, a year prior to the publication of BCS Theory, Cooper demonstrated that a net positive attraction between two electrons will generate a gapped ground state and, as a result, the Fermi sea becomes unstable against electron pair formation [17]. In conventional BCS theory, this electronic phase transition is driven by an attractive potential between two electrons mediated via electron-lattice coupling.

This mediating interaction dictates the form of the gap via the self consistency gap equation

$$\Delta_{\mathbf{k}} = -\frac{1}{2}\sum_{\mathbf{k}'} \frac{\Delta_{\mathbf{k}'}}{(\Delta_{\mathbf{k}}^2 + \xi^2)^{1/2}} V_{\mathbf{k}\mathbf{k}'} \tag{1.1}$$

where ξ is the difference between the single particle energy and the Fermi energy $\xi = \epsilon_{\mathbf{k}} - \epsilon_F$. Since the superconducting state is governed by the gap, this implies that the nature of the mediating interaction has profound consequences on the observed properties of the system. In the case of electron-lattice coupling, the matrix components of the Fourier transformed interaction energy, $V_{\mathbf{k}\mathbf{k}'} = \Omega^{-1}\int V(\mathbf{r})e^{i(\mathbf{k}'-\mathbf{k})}d\mathbf{r}$ can be well described as a constant (-V) in a thin shell of thickness $\hbar\omega_c$ around the Fermi surface and zero elsewhere. Converting the sum in (1.1) to an integral and taking ω_c to be the Debye phonon cutoff frequency leads to

$$\Delta = \frac{\hbar\omega_D}{\sinh[1/(N_F V)]} \tag{1.2}$$

Upon inspection of Eq. 1.2, it is clear that the isotropic nature of the electron-lattice interaction energy translates into an isotropic gap sitting at the Fermi surface with a phonon frequency dependent magnitude. Working through the details of BCS theory within this simplified s-wave framework yields several quantitative parameters that can be checked directly [121]. In particular, the ratio of the superconducting gap and T_c is a constant in value:

$$\frac{\Delta(0)}{kT_c} = 1.764 \tag{1.3}$$

Measurement of the gap over a wide range of conventional superconductors lead to values distributed very closely around this BCS value of 1.764. Moreover, these measurements have been checked along different directions in k-space and yield the same universal value, providing direct evidence of an s-wave symmetry. As well, since the phonon frequencies depends on mass as $M^{-1/2}$ we find that the superconducting properties of chemically identical samples consisting of different isotopes tend to renormalize in response to variations in isotopic mass [81]. These observations,

among others, provide a large and consistent body of evidence identifying phonons as the appropriate mediating quasiparticle binding Cooper pairs in a conventional superconducting lattice.

1.2 Introduction to Unconventional Superconductivity

1.2.1 The Cuprates

In 1986 Bednorz and Muller discovered a new class of unconventional superconductors now known as the cuprates [5]. Unlike their predecessors which tended to be chemically simple, metallic systems, this new class is comprised of ceramic insulators with a much more complicated chemical structure. Interestingly, both the isotope effect [34] and an s-wave gap are absent. Although it is possible for the gap symmetry of conventional superconductors to manifest as lower than s-wave, this reduction is due solely to the gap following the symmetry of the lattice. However, in the cuprates, these systems display a d-wave gap with sign reversal on opposing lobes which reflects a symmetry lower than the underlying tetragonal lattice [131, 122, 80]. The anomalously high T_c of some of these systems, as high as 134K in $HgBa_2Ca_2Cu_3O_{1+x}$ [109], also suggests that a binding interaction stronger than phonons is likely required to reach such high transition temperatures. Despite these striking differences with conventional superconductors, both BCS and GL Theory provide satisfactory descriptions of these systems upon substitution of the observed T_c, crystal anisotropy, Fermi velocity, and density of states [121]. Thus, it is expected that BCS and GL theory can provide a broader, first principles understanding of unconventional superconductivity by substitution of the correct set of $V_{\mathbf{kk}'}$ matrix elements. As a result, there now exists an extensive effort by the condensed matter community to identify the interaction responsible for Cooper pairing with much evidence at present pointing towards magnetic excitations as the most likely candidate [86].

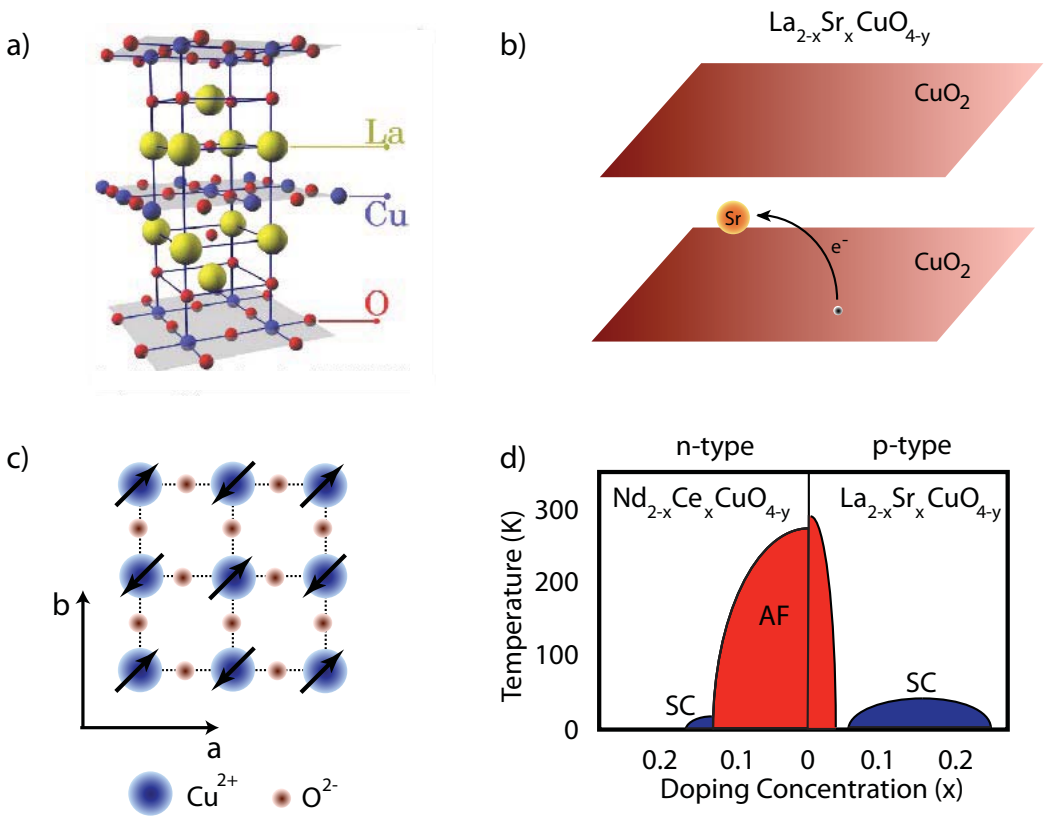

Figure 1.1: a) Chemical structure of the parent (x=0) $La_{2-x}Sr_xCuO_{4-y}$ (figure taken from http://www.physics.ubc.ca/ berciu/RESEARCH/). b) Doping replaces La^{3+} with Sr^{2+}, the reduction of oxidation state draws electrons from the CuO_2 layers and effectively hole dopes these planes. c) The antiferromagnetic order in the copper oxide planes is of simple G-type order and with sufficient doping this long range order is replaced by a dome of superconductivity in the phase diagram as depicted in d). Fig 1d reproduced from Damascelli, *et al.*

The cuprates as a family consist of 2D antiferromagnetically aligned Copper-Oxide planes separated by buffer layers. These buffer layers act as a charge reservoir which, upon doping, destroy the long range antiferromagnetic order. As a result, the spin waves of the parent are supplanted by loosely correlated spin fluctuations (Fig. 1.1). One of the most important features of these superconductors is that they are all derived from the doping of their antiferromagnetically ordered parents. Without doping, the compounds are well-described as antiferromagnets with long-range three-dimensional order due to a weak inter-plane coupling between spins. As

charge carriers (holes or electrons) are doped into the planes, these high-Tc systems evolve from long range antiferromagnets (AF) into superconductors. Even though the static AF order is destroyed upon carrier doping toward the SC phase, strong AF spin fluctuations persist into superconducting concentrations. This persistence of AF spin fluctuations into the SC phase has led to theories seeking a magnetic role in the pairing mechanism [108]. Of particular interest is a resonant mode in the spin excitation spectrum [32, 102]. This mode appears upon entering the superconducting state and is evidenced by a sharp climb in spectral weight about a particular energy (E_R). The resonance intensity (I) as a function of temperature takes the form of an order parameter that tracks T_c as $I(T) \propto (T - T_c)^{-\alpha}$. Furthermore, systematic studies over a wide range of samples reveal that the energy of the resonance displays a strong linear correlation with T_c [128] and the superconducting gap [139]. With sufficient overdoping, the magnetism becomes completely uncorrelated and superconductivity is suppressed.

In the case of overdoped $La_{2-x}Sr_xCuO_{4-y}$ (LSCO) it has been shown that the local susceptibility, $\int \chi''(\mathbf{Q}, \omega)\mathbf{dQ}$, of the spin excitation spectrum reduces linearly with T_c with full suppression of these two phases concomitant with doping (Fig. 1.2) [123]. Taken together, the antiferromagnetic ground state, resonant mode, and correlation between the local susceptibility and T_c provide clear evidence that superconductivity is closely coupled to magnetism in the cuprates. However, despite this strong level of correlation, the exact relationship between these phases and determining if magnons are indeed the correct excitation driving Cooper pair formation has remained elusive.

1.2.2 The Fe-based Superconductors

In 2008 a new class of unconventional Fe-based superconductors was discovered upon doping Fluorine into LaFeAsO [51]. This new class breaks down further into four distinct families, all of which are structurally very similar to the cuprates (Fig. 1.3). The first three, known as the pnictides, consist of quasi-2D FeAs planes to which the

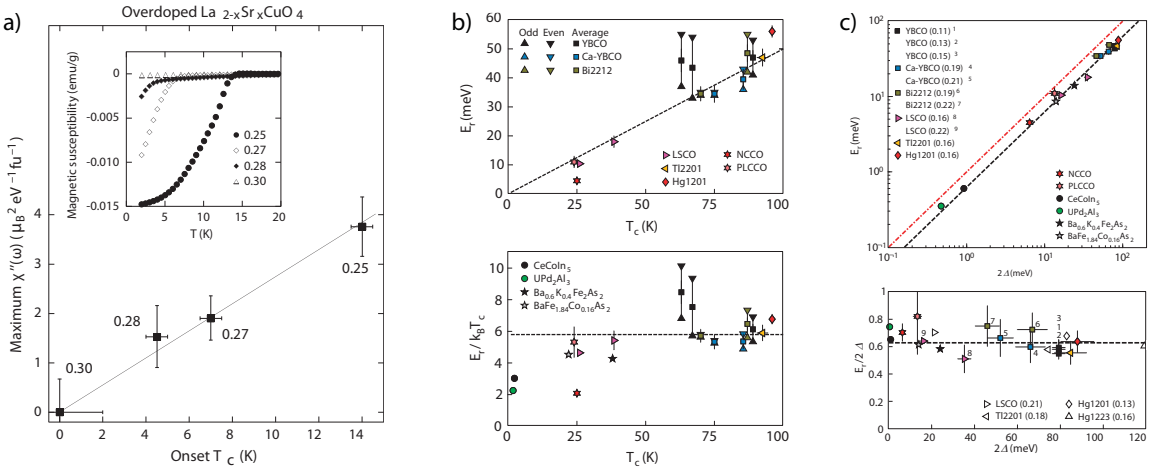

Figure 1.2: a) Q-integrated local susceptibility as a function of T_c for overdoped $La_{2-x}Sr_xCuO_{4-y}$ with x = 0.25, 0.27, 0.28, and 0.30 [123]. The linear correlation suggests that superconductivity is contingent on the presence of magnetic excitations. Inset provides a measure of T_c via the superconducting dielectric response for the dopings studied. b) The energy about which a superconducting resonant gain in magnetic intensity appears can be linearly correlated to the T_c of the system [139]. c) A similar linear dependence exists between the resonant energy and the superconducting gap [139]. The points correspond to different dopings across multiple classes including the cuprates, pnictides, and heavy Fermion systems. Thus, these features appear to be ubiquitous to unconventional superconductivity where magnetism is present.

superconductivity is confined with buffer layers in between. Archtypical examples of these groups are $BaFe_2As_2$, LaFeAsO, and NaFeAs which are often referenced simply by their stoichiometry; (122), (1111), and (111) respectively. The last family, the chalcoginides (11), consists of quasi-2D FeTe/(Se) planes stacked directly upon one another with no separating layer. At the time of this writing, a new (122) chalcogonide family has just emerged which also contains FeSe layers but with K, Rb, or Cs intercalated between and a much more complicated nuclear and magnetic structure due to ordered Fe vacancies within the FeSe layers and unordered vacancies in the intercalated buffer layer [126, 134].

In many respects, the phase diagrams of the Fe-based families are qualitatively similar to the cuprates and consist of an antiferromagnetic ground state [21] that is

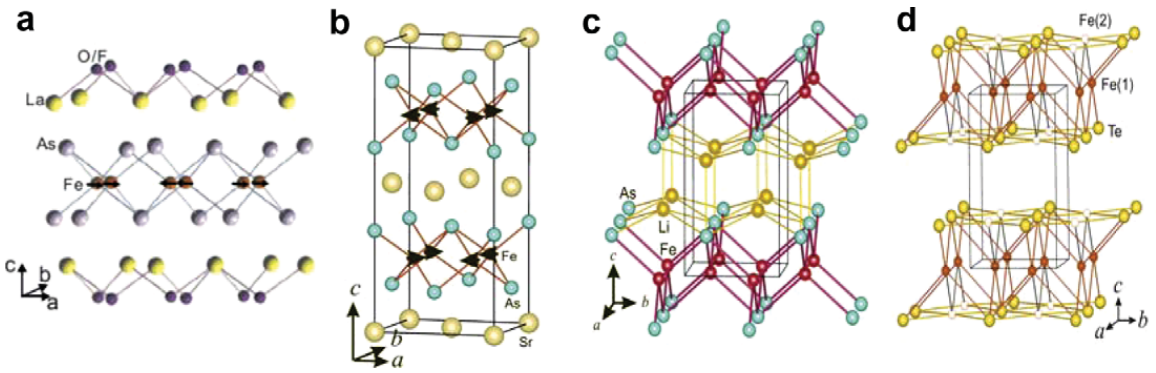

Figure 1.3: Crystal structure of the four Fe-based families [75]: a) LaFeAsO, b) $SrFe_2As_2$, c) LiFeAs, and d) $Fe_{1+x}Te$. The stripe antiferromagnetic (AFM) order of the Fe spins is depicted for LaFeAsO and $SrFe_2As_2$. AFM order in the (111) class was originally found to be absent. However, experiments now demonstrate an identical magnetic ordering [62] as the (1111) and (122) classes with weak magnetic moments that are quickly suppressed due to Li evaporation. In $Fe_{1+x}Te$, stripe AFM ordering is also present, however the spin alignment is rotated 45 degrees away with respect to AFM order in the other classes. Inhomogeneity in the form of excess iron Fe(2) is also present in these systems and can effect the magnetic ordering of the system [3].

replaced in favor of superconductivity upon doping [48, 145]. Studies of the magnetic excitations have revealed that the resonant excitation is also present in these material and scales with T_c and the superconducting gap with a similar linear dependence (Fig. 1.2b) [10]. However, the Fe-based superconductors are distinctly different from the cuprates in several fundamental ways. To begin, the simple G-type AFM order of the cuprates is replaced by a colinear order consisting of antiferromagnetically aligned spins along the a-axis and ferromagnetically aligned spins along the b-axis. Second, whereas the magnetism in the cuprates is described in terms of a local moment picture derived from a Mott insulating ground state, the Fe-based superconductors are semi-metallic with the AFM order potentially itinerant in nature. A further difference is that in the cuprates, doping of the CuO_2 planes is realized by substitutions in the buffer layers which results in electron or hole doping of the planes, while in the Fe-based systems, superconductivity can be achieved by way of electron, hole, or isostructural substitutions with the sites often existing in-plane. Thus, it

appears that the electronic groundstate and form of doping are flexible features of the superconducting systems, with the ubiquitous feature in the superconducting phase being short range magnetic fluctuations left over from a broken long range ordered magnetic state.

1.2.3 The Heavy Fermions

The story of unconventional superconductivity actually began in 1979, seven years before the cuprates, when superconductivity was discovered in $CeCu_2Si_2$ [114] with a transition temperature of 0.5K. The normal state properties of this system revealed an effective carrier mass two orders of magnitude larger than a free electron. Such systems, known as heavy Fermions, form a class of materials typically containing magnetic ions with f-electrons in their outer valency. In conventional superconductors, the inclusion of magnetic ions act as pair breakers and suppress the superconducting state. Thus, this system was a first indication that a non-conventional electronic pairing mechanism could be at play in some materials. Superconductivity was subsequently discovered over a wide range of heavy Fermion material, however the T_c of these systems is typically on the order of 1K. As a result, most research on these systems was abandoned when the cuprates, with their much higher transition temperatures were discovered. Nonetheless, the magnetic properties of these systems (ordered groundstates, resonance feature [107, 115], and loosely correlated fluctuation upon doping) help establish a broad and consistent framework identifying a strong coupling of the spin degrees of freedom to the superconducting state.

1.3 Magnetism in Unconventional Superconductors

1.3.1 Localization, Itinerancy, and Everything In between: An Introduction

The origin and phenomenology of magnetism can arise from two opposite extremes. On the one hand, valence electrons tightly bound to their host will lead to a non-zero spin. In this picture, the resulting lattice of localized magnetic ions will take on different ground states, ie: paramagnetic, ordered, spin glass, etc., depending on the details of the magnetic exchange couplings between sites. At the other extreme, analogous groundstates can be derived from the non-site specific conduction electrons as they move through the lattice. However, this dichotomy between localized and itinerant magnetism is in no way mutually exclusive. Indeed, the parents of the cuprates are understood in terms of fully localized magnetic systems whose long range order dissolves as itinerancy is favored due to doping. Thus these systems follow a classic Heisenberg model securely tethered to a fully localized picture of magnetism with no Fermi surface present in the insulating parent state. However with increased doping Fermi arcs appear and this local moment picture blurs into an intermediate regime with the exact state unclear before finally reemerging on the overdoped side as an itinerant paramagnet with properties governed by the fully formed Fermi surface. To compare with the case of the pnictides, it has been established that the local moment Heisenberg model can also fit the parent data very well if a damping parameter is included to account for itinerant electron-electron interactions. Despite this quasi-local moment fit, the Fe-based superconductors are known to be semimetallic with a Fermi surface topology that supports itinerant descriptions for some, but not all, of the observed magnetic properties. To date, the debate between itinerant and localized descriptions of the Fe-based superconductors is ongoing with the correct picture likely a mixture of these two states.

In this section, details of fully local moment magnetism will be discussed in terms of the groundstate of the cuprates while the details of itinerant magnetism will be relegated to the ongoing discussion of the appropriate groundstate for the pnictides. Thus, these two classes, the cuprates and pnictides, provide a natural stage for discussing the two opposing ends of magnetic interaction. Interestingly, magnetism in the heavy Fermions is now understood in terms of a mixture of localized and itinerant components in the form of Kondo and RKKY interactions respectively. Thus, these systems provide a good bridge for discussing the details of how the overall magnetic properties of a system can be governed by contributions from both a localized and itinerant channel.

1.3.2 Magnetism in the Cuprates

What's past is prologue....

-William Shakespeare *The Tempest*

In the undoped Cuprate parents, the $3d^9$ Hund's filling of the copper states dictate that there should exist a single half-filled hole band. As a result, the naive expectation is that these systems should be band metals. In practice, however, a strong on site Coulombic repulsion (U) tightly binds the electrons onto their respective ions thereby driving the system into a Mott insulating state. This on-site repulsion is responsible for a band splitting that leaves the Fermi energy sitting inside a large gap. Each site carries a single unpaired electron which, collectively, form an antiferromagnetically aligned lattice of magnetic moments. Since a band metal picture fails for the Cuprates, the simplest correction to the electronic groundstate is to include a Coulombic potential energy to the tight-binding model. The resulting Hamiltonian, known as the Hubbard Model is given by

$$\mathscr{H} = -t \sum_{\langle i,j \rangle, \sigma} c^{\dagger}_{i,\sigma} c_{j,\sigma} + U \sum_{i} n_{i\uparrow} n_{i\downarrow} \tag{1.4}$$

where i,j are sites on the lattice with $\langle i, j \rangle$ dictating that the sum is only over neighboring sites, t is an overlap integral for neighboring orbitals on the the lattice, $c^{\dagger}_{i,\sigma}$ and $c_{j,\sigma}$ are creation and annihilation operators respectively, σ is the spin of the electron (up or down), U is the onsite potential energy, and $n_{i,\sigma} = c^{\dagger}_{i,\sigma} c_{i,\sigma}$ is the number operator (either 0 or 1). The first term in the Hubbard model is a kinetic energy term associated with electron hopping between sites. The second term sums through all sites and adds an energy cost of U whenever double occupation is encountered. Hopping will generally lead to a reduction in the kinetic energy of the system. This can be qualitatively understood by comparison with the quantum particle in a box, here the energy is proportional to L^{-2}. Thus, as the box becomes larger the energy of the system reduces. For a lattice, site hopping effectively increases the 'box size' that the electron occupies. However, since the copper d-orbitals are exactly half filled, off-site hopping neccissarily leads to double occupation. Thus, the kinetic and potential energy terms directly compete. In the parents of the cuprates the on-site repulsion dominates, reducing the hopping drastically and driving the system into a Mott insulating state. With the system sufficiently localized, the resulting electrostatic Hamiltonian can be rewritten in terms of spin operators $\mathbf{S}$ weighted by a site-to-site exchange coupling J. The resulting simplification is known as the Heisenberg Hamiltonian and for the case of only nearest neighbor exchange can be written as

$$\mathscr{H} = J \sum_{\langle i,j \rangle} \mathbf{S_i} \cdot \mathbf{S_j} \tag{1.5}$$

where again $\langle i, j \rangle$ refers to summation of only nearest neighbor sites and $J = 4t^2/U$. Since magnetetic moments do not feel the Coulombic force, at first glance it seems peculiar that a purely electrostatic potential can be recast in terms of moment operators. The key to unraveling this mystery can be understood by considering a two particle system. Here the expectation of the square of the separation distance between the two electrons depends on whether the particles wave function combine

symmetrically or antisymmetrically [38].

$$\langle (x_1 - x_2)^2 \rangle_\pm = \langle x^2 \rangle_a + \langle x^2 \rangle_b - 2\langle x \rangle_a \langle x \rangle_b \mp 2|\langle x^2 \rangle_{ab}|^2 \tag{1.6}$$

where $\psi_a(x)$ and $\psi_b(x)$ refer to the wave functions of the two electrons and $\langle x \rangle_{ab} = \int x\psi_a^\dagger(x)\psi_b(x)$. Since, the distance between electrons directly effects the resultant Coulomb energy, this provides a mechanism for aligning spins either ferromagnetically or antiferromagnetically in order to reduce the total energy of the system. Indeed, in the two body case it is customary to write the exchange coupling in terms of the difference in energy between the single and triplet state

$$J = \frac{E_- - E_+}{2} = \int \psi_a^\dagger(\mathbf{r}_1)\psi_b^\dagger(\mathbf{r}_2)U\psi_a(\mathbf{r}_1)\psi_a(\mathbf{r}_1)d\mathbf{r}_1 d\mathbf{r}_2 \tag{1.7}$$

From this we see that the sign of the exchange coupling determines whether the singlet (antiferromagnetism) or triplet state (ferromagnetism) is favored, ie: a negative J implies $E_- < E_+$ while a positive J implies $E_- > E_+$. Although the multibody case is much more complicated, the basic idea remains the same with the sign of the exchange coupling governing the magnetic ordering.

The Heisenberg Hamiltonian describes the Goldstone modes (spin waves) resulting from the symmetry breaking operation of establishing a long range ordered magnetic groundstate within the lattice. The solution can be obtained from linear spin wave theory. In the presence of solely spin wave excitations, the pair-correlation tensor $\langle S_0^\alpha S_t^\beta \rangle$ governing the structure of the dynamical susceptibility and (equivalently) the cross-section for neutron scattering (see the following neutron scattering section for details), gives off-diagonal elements of zero while the diagonal elements consist of two transverse terms that carry the inelastic spectral weight and one longitudinal term that carries the elastic signal. (Technically this is only true for linear spin-wave theory, higher order terms in the expansion bring with it inelastic multi-magnon processes

that transfer inelastic spectral weight from the transverse channel to the longitudinal channel [69].)

In the Cuprates, linear spin wave theory has been used to accurately model the both the dispersion and intensity across all of $S(\mathbf{Q}, \omega)$ using a Heisenberg model that includes nearest, next nearest, next next nearest neighbor exchange couplings and a ring exchange coupling four spins [44, 16]

$$\begin{gathered}\mathscr{H} = J_1 \sum_{\langle i,j \rangle} \mathbf{S}_i \cdot \mathbf{S}_j + J_2 \sum_{\langle i,i' \rangle} \mathbf{S}_i \cdot \mathbf{S}_{i'} + J_3 \sum_{\langle i,i'' \rangle} \mathbf{S}_i \cdot \mathbf{S}_{i''} + \\ J_c \sum_{\langle i,j,k,l \rangle} \{(\mathbf{S}_i \cdot \mathbf{S}_j)(\mathbf{S}_k \cdot \mathbf{S}_l) + (\mathbf{S}_i \cdot \mathbf{S}_l)(\mathbf{S}_k \cdot \mathbf{S}_j) - (\mathbf{S}_i \cdot \mathbf{S}_k)(\mathbf{S}_j \cdot \mathbf{S}_l)\}\end{gathered} \tag{1.8}$$

Inclusion of exchange to further neighbors indicates a coherent hopping of electrons across increasingly large length scales which is, in large part, due to the ring exchange that results from hybridization of in plane orbitals creating a charge transfer path across copper plaquettes of four neighboring ions (see panel f in Fig 1.4) [16].

In acquiring a fit of the data to the Heisenberg model, the exchange couplings are treated as fitting parameters. In $LaCuO_4$ these values are determined to be around $J_1 \approx 140$meV, $J_2 = J_3 \approx 2$meV, and $J_c \approx 50$meV. The exchange couplings are quantitatively related to ratio's of hopping t and Hubbard U to increasing order for more distant J [120, 101]. Thus, model fits provide a means for backing out the Hubbard parameters describing the competing physics of the system. Comparison of these values with those determined from photoemission [55] and optical spectroscopy [111] are in good agreement.

Electron or hole doping of the CuO_4 planes in the Cuprates can be achieved by substitutions of ions sitting in the out-of-plane buffer layers with elements of a higher or lower valence respectively. Here I will focus exclusively on hole doped compounds since they have been studied much more extensively than their electron doped counterparts. The Mott insulating state derives not solely from the strong on-site Coulomb repulsion. Of equal importance, the $3d^9$ copper orbital corresponds to an exactly half filled state. As a result, for every copper atom their is exactly

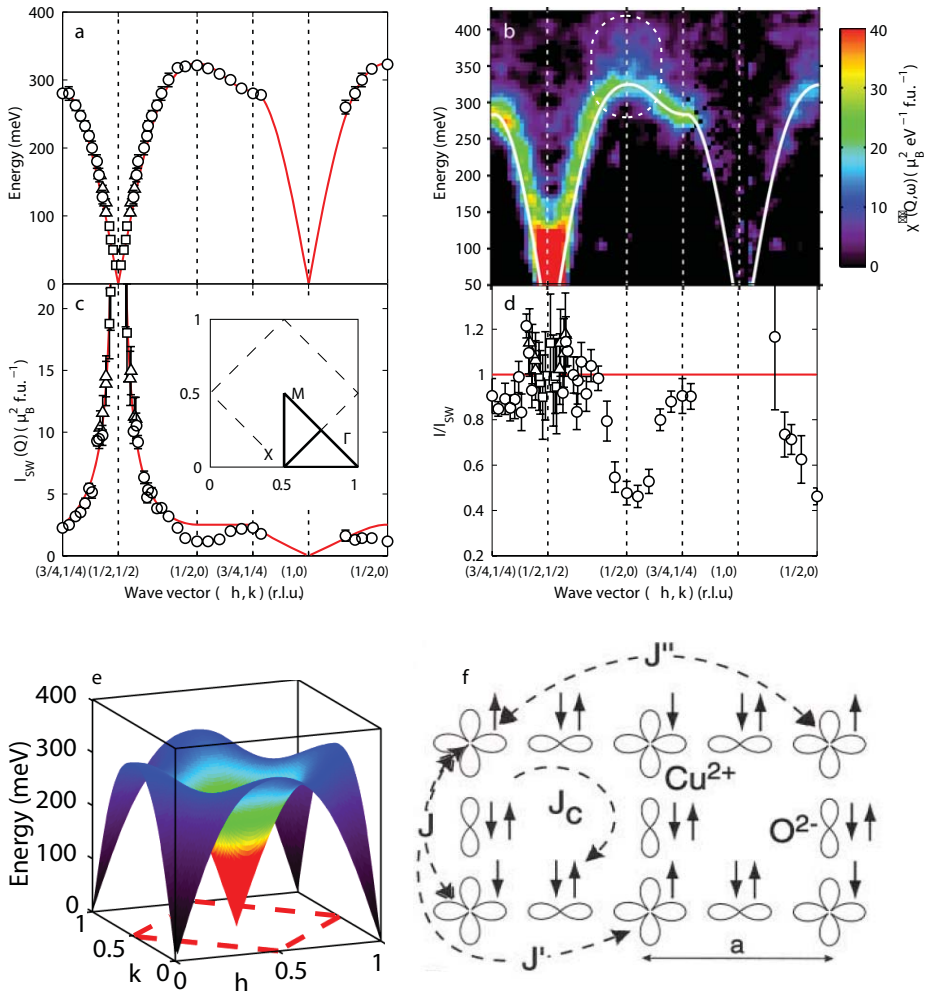

Figure 1.4: Time of flight neutron scattering data for spin wave scattering in the cuprate parent $LaCuO_4$ with fits to the Heisenberg Hamiltonian given in Eq. 1.8. a) Extracted dispersion along the path in reciprocal space described by the subpanel in c). The red line is a fit to the model. b) A 2-D data slice of the same dispersion path with the intensity of the scattering included as a color profile. c) The intensity corresponding to the dispersion in panel a). d) The ratio of the experimental intensity over the model intensity demonstrates that the model fits very well everywhere except at the wave vector (1/2, 0) where the spin wave lifetime damps out due to a decay process discussed in the body of text. e) In general the Heisenberg model gives an hour glass dispersion propagating out of the long-range ordering wave vector, the exact structure and spin band width depend on the exchange couplings of the systems. Panel f) describes the different exchange couplings used to fit the data. Note that the copper and oxygen orbitals spacial character support a hopping that would reduce J_2 while simulateously enhance a cyclic exchange. Panels taken from figures in [44, 16]

one unpaired electron. These electrons spread uniformly across the lattice in order to remove the cost of double occupation. Qualitatively, the introduction of holes in the lattice allows electrons to hop without double occupation onto these empty sites thereby reducing the total energy. With sufficient doping, the system evolves from an insulating to metallic state and long range ordered magnetism dissolves. The short range magnetic fluctuations within the system remain dispersive and centered about the AFM wave vector much like in the parents with the bandwidth of the doped systems proportional to their magnetic exchange J. However, the excitations are split incommensurately about Q_{AFM} due to a fluctuating order associated with doped holes collecting into 1D stripe configurations. The alignment of these stripes rotate by 45 degrees across the metal to insulator transition resulting in a corresponding rotation of the incommensurate signal. As well, the dispersion in doped samples display an hour glass-feature not present in the parents and as they are tuned to optimal doping the total spectral weight given by $(\mathbf{Q}, \omega)$ integration of the data decreases [110].

Theoretical models for describing the magnetic fluctuations in doped cuprates can be constructed using either the strongly correlated parent or the weakly correlated, heavily overdoped side of the phase diagram as the appropriate starting point. In the former case, Anderson proposed early on a valence band model where, upon loss of long range order, electrons remained bound in singlet pairs due to a residual exchange force left over from the parent. As the system is doped into a metal, superconductivity forms directly from these preformed singlet pairs. Thus, in this picture, the same electrons that participate in long range order in the parent also participate in superconductivity in doped samples [2]. From the other extreme, with heavy doping the cuprates are a weakly correlated metal. Thus the magnetic properties are thought to be derived from particle-hole excitations across the Fermi-surface. RPA on the bandstructure is then the natural starting point for modeling the dynamic response of the systems. Although both these methods have had some success in describing doped cuprates, neither provide a satisfactory description in

the intermediate regime of the diagram and, to date, this remains an area of active research.

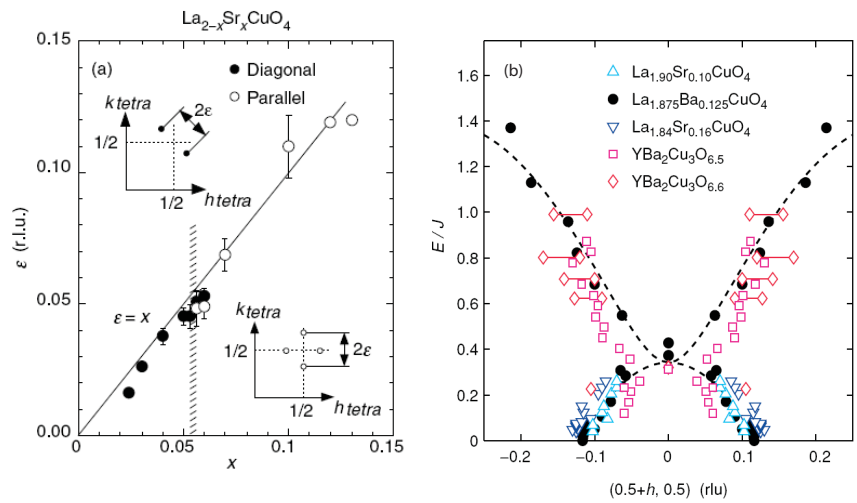

Figure 1.5: (a) Incommensurability in the magnetic scattering of hole doped LSCO. Insets are cartoons describing the direction of the incommensurability about the AFM wave vector. At the metal to insulator transition the incommensurability rotates by 45 degrees from a diagonal to parallel alignment with the unit cell. (b) Upon doping the short range fluctuations left over from broken long range order remain dispersive, however an hourglass feature is introduced at low energies in the dispersion. Figures taken from [110] and comprise the work of several papers. Refer to this work (Ch. 6) for references to original data.

1.3.3 Magnetism in the Fe-based Superconductors

Introduction to Itinerant Magnetism

In general, the magnetic moment operator is given by $\hat{\mu} = g\mu_B(\hat{L} + \hat{S})$. Assuming no orbital contribution to the moment, the Landé g-factor $g \approx \frac{3}{2} + \frac{S(S+1)-L(L+1)}{2J(J+1)}$ becomes 2 and we can write the total moment as

$$\mu^2 = 4\mu_B^2 S(S+1) \tag{1.9}$$

In localized systems dominated by Hund's exchange, the size of the moment is dictated by the Hund's filling of the orbitals. In the case of bulk iron, the $3d^6$ electrons should give a spin $S = 2$ and, according to Eq. 1.9, a corresponding moment of $m^2 = 24\mu_B^2$ on each ion in the lattice. Instead, experimentally we find a much smaller moment of $m^2 = 4.9\mu_B^2$. From this, it is clear that the moment based on orbital filling of atomic iron is effected dramatically when these atoms are combined in bulk. The origin of this phenomenon is associated with the splitting of discrete atomic orbitals into effectively continuous energy bands as individual iron atoms bond into a metallic long range ordered lattice. In a metal, each momentum state in a band allows for two electrons: one up and one down. These fill in equal number to the Fermi energy. However, the application of a magnetic field B will create two separate spin-split subbands separated by a small energy of $2\mu_B B$. Thus, the electrons no longer fill in equal number (Fig. 1.6) resulting in a small net moment appearing in the system. Even outside of an externally applied field the band can still spin split spontaneously due to a run away effect of microscopic spin flip fluctuations across the bands. In this picture, a spin flip process creates a local field, this field in turn polarizes other electrons adding to the field. This cycle continues until the energy reduction due to magnetization is balanced by the kinetic energy gain associated with taking electrons at the Fermi surface from one spin band and depositing them in a larger free energy state in the other band [6].

This so called 'Stoner enhancement' in the magnetism can be recast in terms of instabilities appearing in the susceptibility. A perturbation ϕ to the free electron gas can be treated within linear response theory, allowing us to write the induced density as

$$\rho^{ind}(\mathbf{q}) = \chi(\mathbf{q})\phi(\mathbf{q}) \tag{1.10}$$

where $\chi(\mathbf{q})$ is given by [39]

$$\chi(\mathbf{q}) = \int \frac{d\mathbf{k}}{(2\pi)^d} \frac{f_k - f_{k+q}}{E_k - E_{k+q}} \tag{1.11}$$

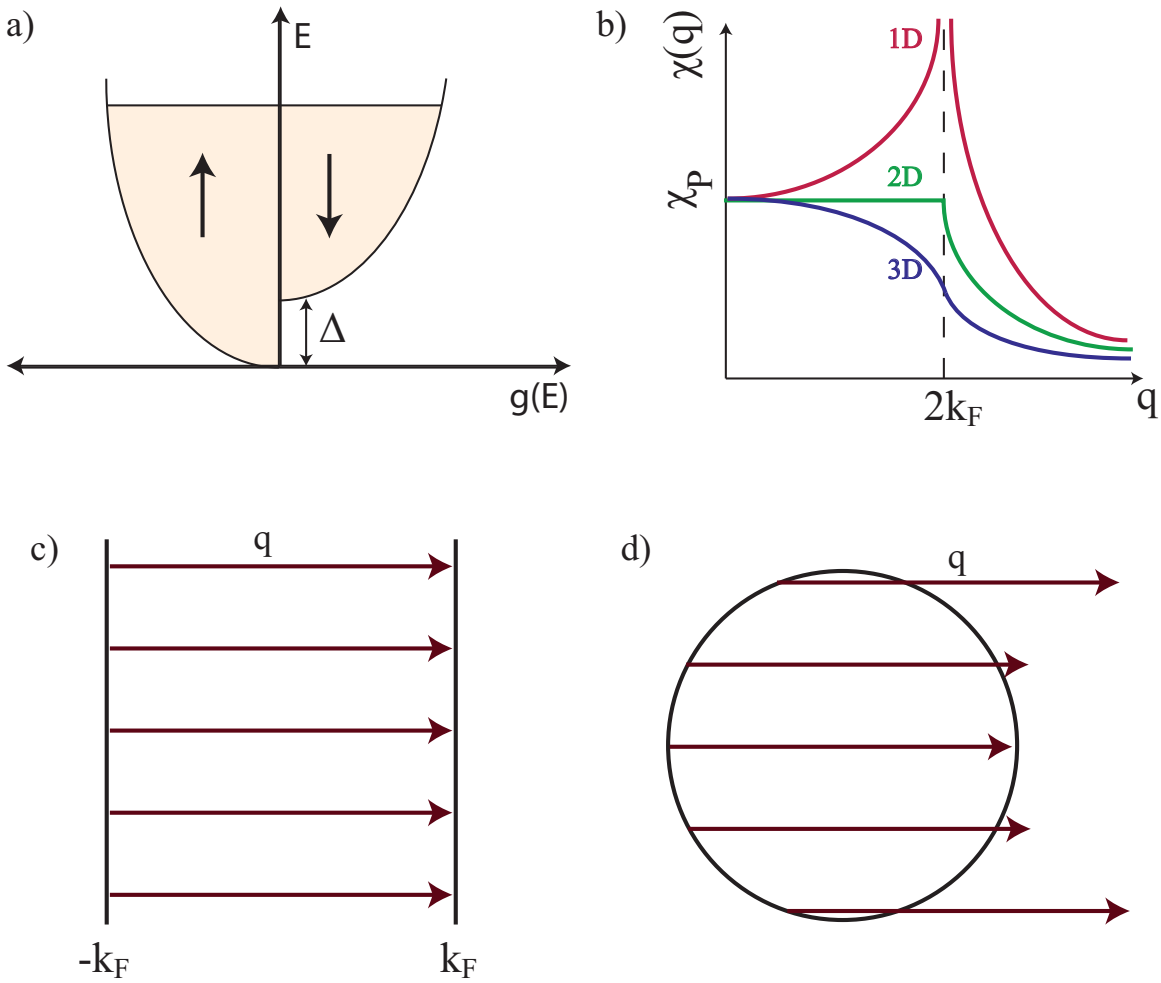

Figure 1.6: a) Spin-split bands separated by an energy Δ. b) The susceptibility of an electron gas. c,d) The corresponding nesting conditions associated with panel b. Panels are reconstructed from figures appearing in [6, 39].

here d is the dimensionality of the system, f_k is the Fermi function and $E(k)$ is the electron dispersion. On inspection, we see that the integrand diverges whenever $E_k = E_{k+q}$. If for a given $\mathbf{q}_{\text{order}}$ there exist many $\mathbf{k}$ that satisfy this condition, then it is possible for the susceptibility to form an instability at this 'nesting vector' $\chi(\mathbf{q}_{\text{order}})$ and, by extension, the density $\rho(\mathbf{q}_{\text{order}})$. Fourier transforming this back to real space gives a long range modulation of the lattice with a period defined by $(2\pi)/(\mathbf{q}_{\text{order}})$. Physically, this corresponds to a strong enhancement in band scattering between empty and filled states at the Fermi energy due to a nesting condition associated with the geometry of the Fermi surface that generates multiple paths for a scattering process with momentum transfer $\mathbf{q}_{\text{nesting}}$ to proceed. A trivial example of this is a 1D free electron gas. Here the Fermi 'surface' consists of only 2 points $-k_F$ and k_F. Thus the entire surface is well nested and leads to long range ordering of the lattice at T=0 (for finite temperatures the reduced dimensionality of the system makes it unstable against fluctuations and order cannot be maintained.) In a 2D electron gas the Fermi surface is a single circle and the nesting condition is lost, leading to a non-divergent susceptibility Fig. 1.6, but an enhancement for $q < 2k_F$ (the Fermi surface diameter), since these $\mathbf{q}$ will always connect some states.

A Case for Itinerant Magnetism in the Fe-based superconductors

Since itinerant magnetism is derived from perturbation theory starting with an electron gas, this implies that it is only valid for weakly correlated materials. Unlike the cuprate parents, which are strongly correlated insulators, the pnictides are semi-metallic [51, 103]. Thus, from the outset their was speculation that the magnetism in these systems could be described within the Stoner model. Moreover, band structure calculations from DFT predicted before experiment that the Fermi surface of these systems consisted of hole pockets at the zone center that were well nested by $\mathbf{q} = (1, 0, L_{\text{odd}})_{ort}$ to electron pockets at the zone boundary . Subsequent measurements by angle resolved photoemission spectroscopy confirmed the geometry of the Fermi surface [100] predicted by theory and neutron diffraction measurements

determined that, in the case of pnictide, the parents developed colinear long range AFM order consistent with the nesting condition present on the Fermi surface and with a moment of $\approx 1\mu_B$/Fe [21, 62], much smaller than what would be expected in a local moment picture. In terms of magnetic excitations, RPA can be used as an indicator of how well a nesting picture works for scattering in the inelastic channel. Here, the expected structure of the magnetic fluctuations based off band structure is captured well by RPA since this method calculates the dynamic linear response of a system from superpositions of particle hole excitations. Moreover, these RPA calculations have been carried out on band structure for parent, electron and hole doped systems [91, 36], allowing for a systematic comparison of theory and experiment across both sides of the phase diagram. It was found that the effect of doping on the geometry of the Fermi surface follows naive expectations. Namely, electron doping enlarges the electron pockets at the zone boundary while simultaneously shrinking the hole pockets in the center, with hole doping the reverse effect is observed. The resulting mismatch of nested pockets due to doping leads to short range magnetic fluctuations that are transversely elongated in the case of electron doping while for hole doping the reversed pocket mismatch leads to an elongations that is rotated 90 degrees, Fig. 1.7. All of these features are observed from neutron scattering measurement of parent [144], electron [91] and hole doped [58] $BaFe_2As_2$ compounds. Thus, at first blush, nesting provides a simple and intuitive picture for the origin and evolution of magnetism in these systems and is in line, qualitatively, with much of what has been observed experimentally.

A case for local moments in the Fe-based Superconductors

Although nesting has proven useful for describing many of the magnetic properties of the Fe-based superconductors, there is now mounting evidence that it is insufficient to fully account for the magnetism. Indeed the (11) chalcogenides are composed of an identical quasi 2D chemical structure as the pnictides but with Te (instead of As) tetrahedrally coordinated with Fe. Thus, it came as no surprise that the

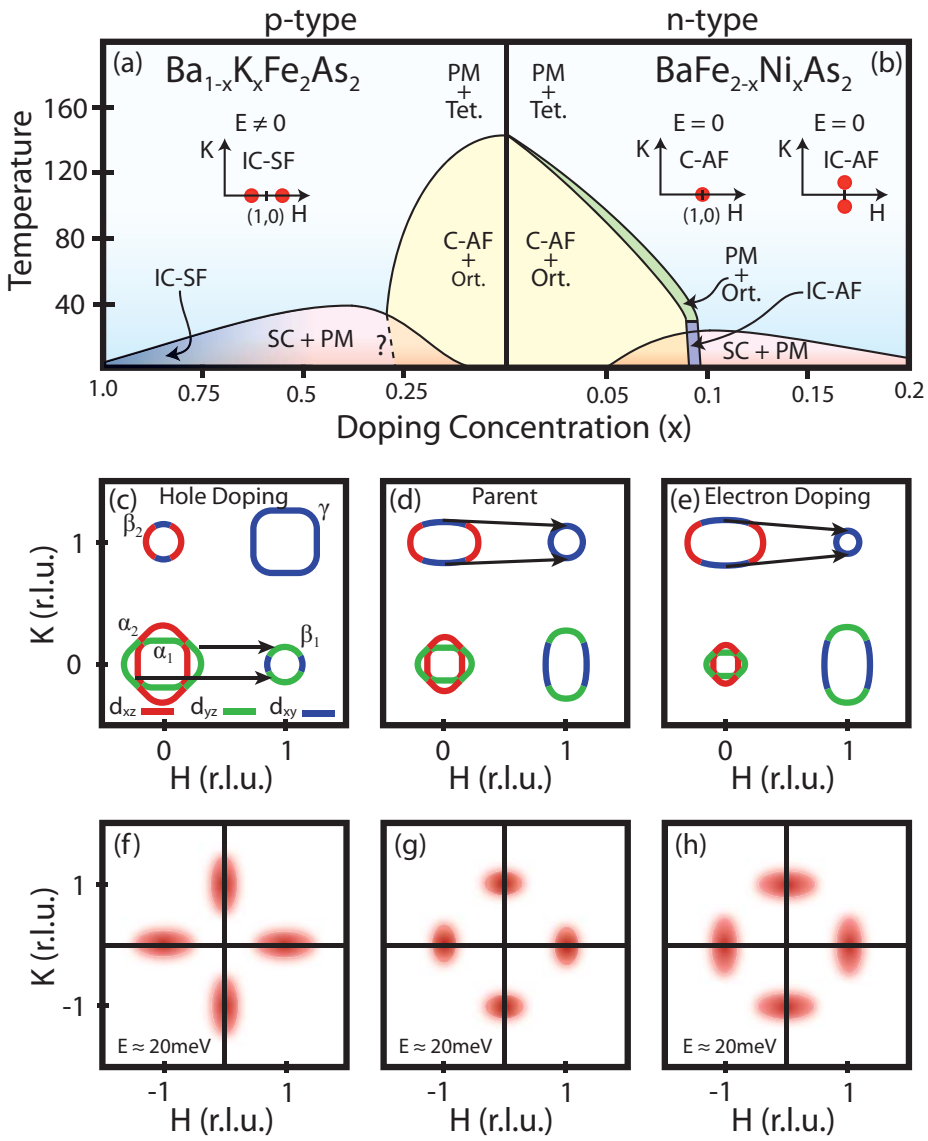

Figure 1.7: a,b) Phase diagram for electron and hole doping of $BaFe_2As_2$ including information for the structural, magnetic, and superconducting phases. The acronyms IC-AF, C-AF correspond to incommensurate and commensurate elastic scattering while IC-SF corresponds to incommensurate inelastic scattering. The incommensurate structure is dependent on the doping type and depicted as insets on the respective sides of the phase diagram. c-e) Geometry of the Fermi surface where the role of doping enlarges and/or shrinks pockets depending on doping type. e-f) Structure of inelastic excitations due to the off-nesting that results from doping. Panels taken from a forthcoming publication in Nature Physics Review article [18].

(11)'s have nearly identical Fermi surfaces as their pnictide counterparts. What was surprising though is that the long range order in these systems does not correspond to the nesting vector connecting zone and boundary Fermi pockets and therefore a Stoner model of itinerant magnetism fails immediately. Moreover, even in the case of the pnictides where a nesting picture meets with some success, the total moment as determined by integration of neutron data in both the elastic and inelastic channel gives a moment that is much too small to be fully local, but also larger than what is expected from a fully itinerant picture [90]. To make matters worse, the magnetism in the (122) systems is a factor of 3 greater than the (1111) systems even though the latter have better nested Fermi surfaces. The fact that calculations in the virtual field approximation demonstrate that the dimensionality of the (122) systems is more 3D than the 1111 suggest that interlayer coupling has more to do with the onset and magnitude of the magnetism rather than the Fermiology [82]. As well, electron spin resonance measurements (ESR) on $LaFeAsO_{1-x}F_x$, which is capable of dynamically probing the local moment, indicate that local moments are present and interact with itinerant electrons at higher temperatures. Further support for a strongly coupled system is evidenced by the ESR determined spin susceptibility which follows a Curie Weiss behavior in the parent [132]. Later x-ray emission spectroscopy measurement confirmed that local moments existed at room temperature in the paramagnetic state [37].

It is important to keep in mind that the local and itinerant pictures fall on opposite ends of a broad spectrum of physically realizable systems. This spectrum of possibilities can be characterized in terms of a ratio of the Hubbard parameters U/W where again, U is the Hubbard repulsion and W is the bandwidth which is directly related to the hopping coefficient t describing the kinetic energy term in the Hamiltonian. This parameterization is effectively a measure of how correlated the electrons are with very small U/W describing weakly correlated metals in the perturbation regime where the Stoner model is appropriate while very large U/W describes strongly correlated insulators where local moments govern the magnetic

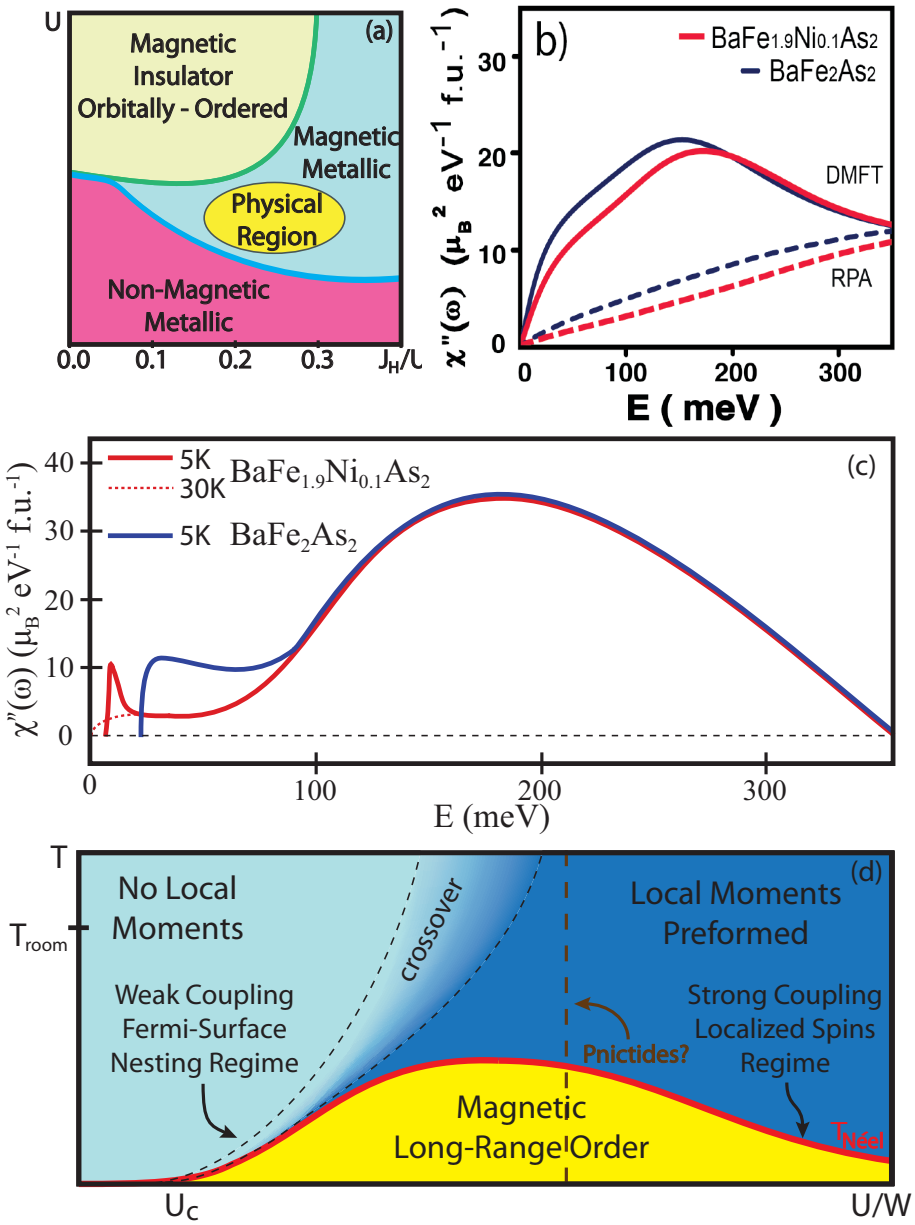

Figure 1.8: a) Qualitative regions of phase space based off of Hubbard model calculations with the yellow ellipse corresponding to region where experiment agrees well with theory. b) DMFT vs RPA calculations of the distribution of the fluctuating moment across energy transfer. Comparing this with inelastic neutron scattering data c) we find that the DMFT calculations, which can capture stronger electronic correlations than RPA, lead to much better agreement between experiment and theory. d) A qualitative sketch of the Hubbard model as a function of electron correlation with a guess as to where the pnictides fall between the two extremes of localized and itinerant magnetism. Panels taken from [18, 67]

properties. Hubbard model calculations, though difficult due to the multi-orbital nature of the systems, have been performed and comparison with neutron and ARPES data suggest that the Fe-based superconductors inhabit a region of phase space that is in close proximity to both a magnetic insulator and non-magnetic metallic phase (Fig. 1.8 a) with an intermediate $U/W \approx 0.3 - 0.4$ [72, 140]. The idea that these systems can be characterized as 'correlated metals' is backed further by the fact that they are poor metals with Haas van Alphen measurements reporting effective elecron masses up to a factor of 7 larger than the bare electron mass. Dynamic mean field theory (DMFT) calculations that are able to incorporate much stronger interactions than are captured by RPA, have proven successful at obtaining effective masses similar to those measured in experiment [136], can qualitatively track the evolution of spin excitations as a function of energy in the $BaFe_2As_2$ parent [90], and quantitatively track the distribution of neutron spectral weight [67] (e.g. time resolved fluctuating moment) to a much higher degree of accuracy than RPA, Fig. 1.8 b,c. Taken together, the ontology of magnetism in this new class of materials is still an open question. However, it has become clear that the simple picture of nesting must be replaced with something that, although much more messier, is also much richer and interesting in terms of physics.

1.3.4 Magnetism in the Heavy Fermions

Heavy Fermion systems are a collection of materials whose properties are governed by a lattice that carries f-electron magnetic ions at crystallographic sites [45]. The electrons within these f-orbitals interact magnetically with conduction electrons within the system. This state of affairs is reminiscent of the single ion Kondo problem that arises in other systems. In single ion Kondo systems, magnetic impurities are injected into the system which then interact with passing conduction electrons. This results in a direct exchange coupling J forming between the localized spin impurities and those of the itinerant conduction electrons.

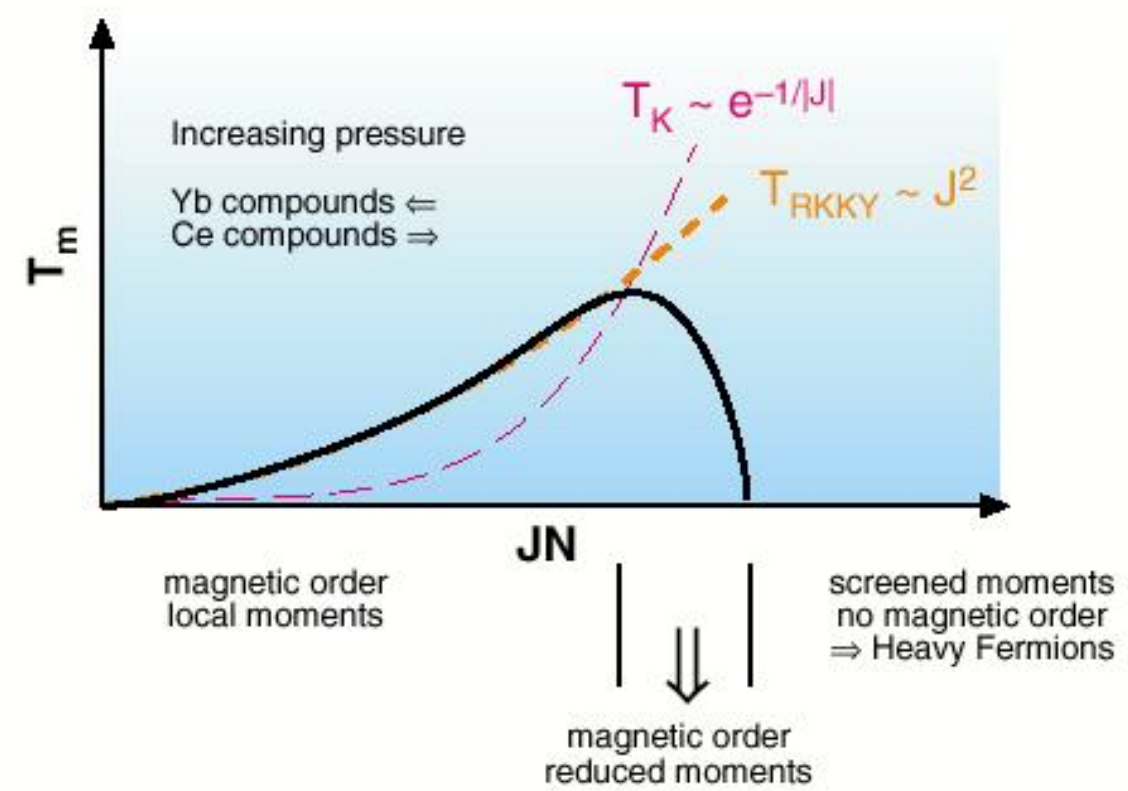

Figure 1.9: Possible ground states resulting from the competition between the Kondo and RKKY interactions. T_m is the ordering temperature and JN is the f-d exchange coupling times the f density of states at the Fermi energy. [105]

A direct consequence of this interaction is that resistivity within these systems breaks from standard Fermi liquid theory at very low temperatures . Moreover, with decreasing temperature the coupling can screen out the spin impurities by binding conduction electrons to them to form a singlet state. The temperature at which this screening occurs is referred to as the Kondo Temperature, T_K. Jun Kondo was the first to solve this problem and provide a logarithmic correction term to the resistivity [57]. This term accurately accounted for the peculiar upturn in resistivity at low temperatures but also asymptotically diverged as the temperature was suppressed to absolute zero. Further work by others succeeded in fixing the divergence and today

the solution to the Kondo problem stands as an impressive achievement in solid state physics.

A fundamental and very important difference between single ion Kondo systems and heavy Fermion systems is that in the former, the ions exist as impurities scattered within the system and, as a result, interactions are isolated short range events. However, in heavy electron systems, the f-orbitals are part of the crystallographic structure and form a Kondo lattice of magnetic ions. Although this may at fist appear to be a direct extension of the original Kondo problem, in practice a solution is much less tractable. Moreover, due to the periodicity of the magnetic lattice, an indirect exchange coupling mediated by the conduction electrons is established between the sites; the so-called RKKY interaction [104, 53, 138]. Indeed, many models of heavy Fermion systems are treated as a competition between a RKKY interaction that acts to set up long range magnetic order at a temperature T_{RKKY} and a Kondo effect that begins screening the sites as the temperature drops below T_K. In the Kondo effect the onset of magnetic screening is given by

$$T_K = \rho^{-1} e^{-\frac{1}{\rho J}} \tag{1.12}$$

where ρ is the density of states at the Fermi surface and J is the exchange coupling between the conduction electrons and the localized magnetic f-orbitals. However, the onset temperature for magnetic ordering due to the RKKY interaction goes as

$$T_{RKKY} \propto J^2 \rho \tag{1.13}$$

Consequently, as the temperature is suppressed, the moments associated with the long range magnetic order will begin to be screened away (Fig 1.9) as the Kondo interaction begins to dominate the system.

Aside from T_{RKKY} and T_K, there exists a third temperature that plays a vital role in determining the onset of property changes within heavy Fermion systems. This

temperature, which is referred to as T^*, corresponds to a point where the bound f-electrons become (at least partially) itinerant. Interestingly, it is for temperatures below T^* that the f-electrons begin to unbind. T^* is typically very low, around 1-10K depending on the system [31]. A calculation of the change in entropy over this temperature range reveals a sharp climb which is attributed to this unbinding process. The magnitude of this change is fairly consistent from system to system, around $Rln(2)$ where R is Rydbergs constant, and is accompanied by significant changes in properties such as reduced resistivity, modified spin susceptibility, an observed Knight shift, etc [30]. Because of this, it is convenient to define T^* as

$$\Delta S = \int_0^{T_*} \gamma dT = Rln(2) \tag{1.14}$$

Recent work [29] has demonstrated that T^* can be modeled very well as

$$T^* = cJ^2\rho \tag{1.15}$$

where c is a parameter to be determined. Combining this with Eq. 1.12 gives the relation:

$$[ln(T_K\rho)]^{-1} = \sqrt{c^{-1}T^*\rho} \tag{1.16}$$

A value of c = 0.45 was determined by fitting Eq. 1.16 to experimental values of T^*, T_K, and γ for a variety of Kondo lattices (Fig. 1.10a). From this, a modified version (Fig. 1.10b) of the Doniach diagram [Doniach] was generated that relates the general phase diagram behavior of the system to the fundamental quantities that drive this behavior.

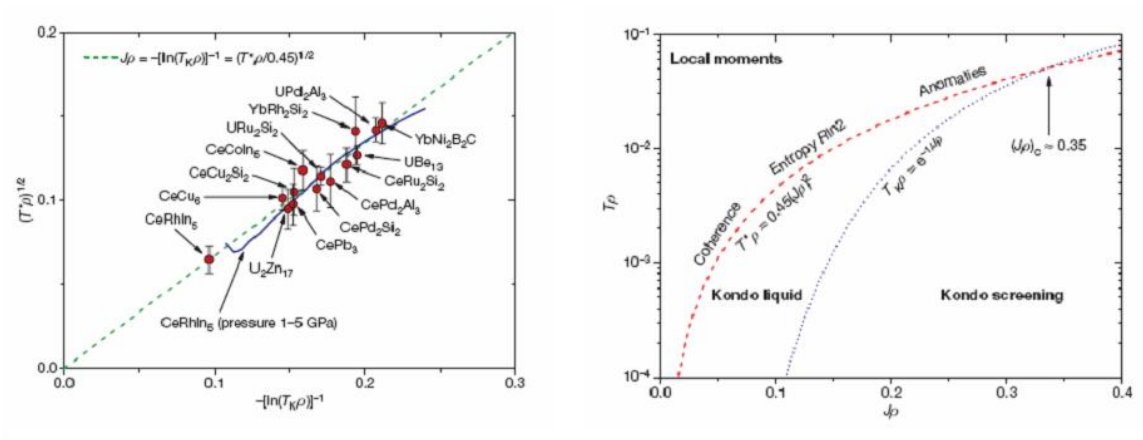

Figure 1.10: a) Confirmation of T^* given by the intersite RKKY interaction for a variety of Kondo lattice materials; c = 0.45. b) Updated Doniach diagram for Kondo lattice materials. [29]

1.4 Neutron Scattering

1.4.1 Scattering Cross-Sections

Thermal neurons are a unique tool for studying materials for several reasons. First, due to lack of charge, neutrons are able to pass through the sample without Coulombic screening. As a result, they are able to penetrate deeply and provide a measure of the bulk properties. As well, the lack of a Coulombic barrier allows neutrons to pass very close to and interact directly with the nucleus. Second, although neutrons lack charge, as Fermions they carry a spin 1/2 moment which allows them to probe the magnetic properties of the system. Indeed, neutron scattering is the sole direct method available for determining the $(\mathbf{Q}, \omega)$ dependence of the the magnetic excitations in condensed matter. Third, the wavelength of thermal neutrons is on the same order as the interatomic spacing of atoms within a crystalline lattice. Thus, as neutrons travel through the sample the resulting interference creates Bragg conditions that carry information about the systems structure. Finally, many of the excitations within a system are on the same order as the energy of thermal neutrons which makes it much easier to determine the energy transfer between the neutron and the sample.

The key elements of a neutron scattering experiment consist of sending a neutron into a sample with an incident momentum $\mathbf{k}$ and energy $E = \frac{\hbar^2 k^2}{2m_n}$ and then measure the final momentum $\mathbf{k}'$ and energy $E' = \frac{\hbar^2 k'^2}{2m_n}$ upon leaving. Through energy and momentum conservation, we can then determine the energy $E = \hbar\omega = E - E'$ and momentum $\boldsymbol{\kappa} = \mathbf{k} - \mathbf{k}'$ of the excitation responsible for the scattering event. By collecting the scattering for different energy and momentum transfers it is then possible to create a map of the excitations in reciprocal space. In order to interpret and quantitatively model this spectra, it is first necessary to have in hand the partial differential cross-section for scattering of neutrons in condensed matter.

A complete derivation of the scattering cross-section requires a considerable amount of mathematical detail. Thus, what follows is only a basic outline of the construction following primarily the approach of Squires [113]. To begin, a given incident flux multiplied into the partial differential scattering cross-section $\Phi \frac{d^2\sigma}{d\Omega dE'}$ measures the number of neutrons scattered per second into the solid angle $d\Omega$ with final energy between E' and $E' + dE'$. Thus, the cross-section effectively represents a transition rate for processes within the sample. Hence, we can write:

$$\left(\frac{d\sigma}{d\Omega}\right)_{\sigma\lambda\to\sigma'\lambda'} = \frac{1}{\Phi}\frac{1}{d\Omega}\sum_{\mathbf{k}' \text{ in } d\Omega} W_{\mathbf{k},\sigma\lambda\to\mathbf{k}',\sigma'\lambda'} \tag{1.17}$$

where $W_{\mathbf{k},\sigma\lambda\to\mathbf{k}',\sigma'\lambda'}$ is the number of transitions per second taking the neutron from the momentum and spin state $\mathbf{k}, \sigma$ to $\mathbf{k}', \sigma'$ and the scattering system from the state λ to λ'. In this form, we can make use of Fermi's Golden Rule to calculate the transition rate:

$$\sum_{\mathbf{k}' \text{ in } d\Omega} W_{\mathbf{k},\sigma\lambda\to\mathbf{k}',\sigma'\lambda'} = \frac{2\pi}{\hbar}\rho_{\mathbf{k}'}\left|\langle \mathbf{k}'\sigma'\lambda' \mid V \mid \mathbf{k}\sigma\lambda\rangle\right|^2 \tag{1.18}$$

where V is the potential that the neutron travels through and $\rho_{\mathbf{k}'}$ is the number of momentum states in $d\Omega$ per unit energy range for neutrons in the state $\mathbf{k}'$. Both ρ and Φ are readily calculatable. As well, since we are considering a specific transition from $\lambda \to \lambda'$, the energy dependence can be appended to the cross-section as a delta

function. All together this gives:

$$\left(\frac{d^2\sigma}{d\Omega dE'}\right)_{\sigma\lambda\to\sigma'\lambda'} = \frac{k'}{k}\left(\frac{m}{2\pi\hbar^2}\right)^2 |\langle \mathbf{k}'\sigma'\lambda' \mid V \mid \mathbf{k}\sigma\lambda\rangle|^2 \,\delta(E_\lambda - E_{\lambda'} + \hbar\omega) \tag{1.19}$$

This is the general result for the scattering cross-section. However, the present form is incomplete since it still only considers a single state transition form $\sigma\lambda \to \sigma'\lambda'$. When solving the cross-section down further in the presence of a nuclear or magnetic scattering process, the standard treatment in both cases is to rewrite the energy delta function in integral form:

$$\delta(E_\lambda - E_{\lambda'} + \hbar\omega) = \frac{1}{2\pi\hbar}\int_{-\infty}^{\infty} \exp\{i(E_\lambda - E_{\lambda'})t/\hbar\}\exp(-i\omega t)dt \tag{1.20}$$

Since $\exp(-iHt/\hbar)|\lambda\rangle = \exp(-iE_\lambda t/\hbar)|\lambda\rangle$ the integrand can be drawn into the matrix elements and incorporated to give time dependent Heisenberg operators in the cross-section of the general form:

$$\mathbf{A}(t) = \exp(iHt/\hbar)\mathbf{A}\exp(-iHt/\hbar) \tag{1.21}$$

It should be clarified at this point that the potential V is not the potential associated with the Hamiltonian H. V corresponds to the potential the neutron feels as it travels through the material while H corresponds to the Hamiltonian of the system. For instance, in nuclear scattering V is due to the nuclear force centered around the nuclei. However, the Hamiltonian of the lattice describes the motion of the nuclei about equilibrium, ie: phonon excitations.

Going from $\left(\frac{d^2\sigma}{d\Omega dE'}\right)_{\sigma\lambda\to\sigma'\lambda'}$ to $\frac{d^2\sigma}{d\Omega dE'}$ requires summing the cross-section over all states λ' keeping λ fixed, and then averaging over all λ. This generally leads to thermal averages of operators appearing in the cross-section

$$\langle \mathbf{A}\rangle = \sum_\lambda p_\lambda \langle \lambda \mid \mathbf{A} \mid \lambda\rangle \tag{1.22}$$

where p_λ is the probability that the system is in a given state λ. The details of the above two steps (writing the delta function as an integral and performing the sum/average) are carried out differently when working out the magnetic vs nuclear cross-section and will not be discussed. A final general result stemming from the form of Eq.1.19 is that the squaring of the matrix elements $|M|^2 = |\langle \mathbf{k}'\sigma'\lambda' \mid V \mid \mathbf{k}\sigma\lambda\rangle|^2$ leads to a calculation of the form $M^\dagger M$ and, combined with the above two general properties, gives a cross-section dominated by thermally averaged Heisenberg operator products of the form $\langle \mathbf{A}_i(0)\mathbf{A}_j(t)\rangle$. This important result identifies the scattering as a pair correlation process. Indeed, we find that nuclear scattering is dominated by terms of the form $\langle \exp\{i\boldsymbol{\kappa}\cdot\mathbf{R}_{j'}(0)\}\exp\{i\boldsymbol{\kappa}\cdot\mathbf{R}_j(t)\}\rangle$ where R_j is the distance to site j. From this it follows that $j = j'$ corresponds to incoherent scattering, ie: the correlation between the position of the same nucleus at different times, while $j \neq j'$ leads to coherent scattering of different sites at different times due to interference effects. As well, the relationship between peak width and ordering length scale arises naturally from considering the effect of this product pair on the cross-section. As an example, in (purely) magnetic scattering we find that the cross-section is dominated by terms of the form

$$\sum_l \exp(i\boldsymbol{\kappa}\cdot\mathbf{l})\langle \mathbf{S}_0^\alpha(0)\mathbf{S}_l^\beta(t)\rangle \tag{1.23}$$

where $\mathbf{S}_l^\beta$ is the operator corresponding to the β component of spin for the ion l. In the far limit of elastic paramagnetic scattering we have that the time dependence drops out. Also, in a paramagnetic there is no correlation between the spins of different ions. Therefore, for $l \neq 0$

$$\exp(i\boldsymbol{\kappa}\cdot\mathbf{l})\langle \mathbf{S}_0^\alpha\mathbf{S}_l^\beta\rangle = \exp(i\boldsymbol{\kappa}\cdot\mathbf{l})\langle \mathbf{S}_0^\alpha\rangle\langle \mathbf{S}_l^\beta\rangle = 0 \tag{1.24}$$

with each spin factor equaling zero due to the thermal averaging of randomly oriented spins. For $l = 0$

$$\exp(i\boldsymbol{\kappa} \cdot \mathbf{0})\langle \mathbf{S}_0^\alpha \mathbf{S}_0^\beta \rangle = \langle (\mathbf{S}_0^\alpha)^2 \rangle = \frac{1}{3}\langle \mathbf{S}^2 \rangle = \frac{1}{3}S(S+1) \tag{1.25}$$

as a result we find that there is no paramagnetic scattering due to spin correlations between different sites, however the onsite $l = 0$ cross-section for individual spins leads to a constant magnitude, momentum independent scattering intensity. Thus we see that uncorrelated elastic scattering can be interpreted as an infinitely broadened peak in reciprocal space. In stark contrast, if we now consider elastic scattering from infinitely long range ferromagnetically ordered spins then this corresponds to $t \to \infty$ with

$$\lim_{t\to\infty} \langle \mathbf{S}_0^\alpha(0)\mathbf{S}_l^\beta(t) \rangle = \langle \mathbf{S}_0^\alpha \rangle \langle \mathbf{S}_l^\beta \rangle \tag{1.26}$$

if we set the spin ordering along the z direction then $\langle \mathbf{S}_l^x \rangle = \langle \mathbf{S}_l^y \rangle = 0$ and $\langle \mathbf{S}_l^z \rangle = \langle \mathbf{S}^z \rangle$ and we get that

$$\sum_l \exp(i\boldsymbol{\kappa} \cdot \mathbf{l})\langle \mathbf{S}_0^\alpha(0)\mathbf{S}_l^\beta(t) \rangle = \langle \mathbf{S}^z \rangle \sum_l \exp(i\boldsymbol{\kappa} \cdot \mathbf{l}) = \frac{(2\pi)^2}{\nu_0}\langle \mathbf{S}^z \rangle \sum_{\boldsymbol{\tau}} \delta(\boldsymbol{\kappa} - \boldsymbol{\tau}) \tag{1.27}$$

Here we see that the interference terms ($l \neq 0$) lead to delta functions in the cross-section, ie: a peak width of zero, when the spin-spin product is the same on each site pair. If, on the other hand, a glassy component was introduced, then the spin-spin product for site pairs would vary leading to different amplitudes on the complex exponentials $\exp(i\boldsymbol{\kappa} \cdot \mathbf{l})$. This would result in phase decoherence and broadening of the peak in the cross-section.

In the following sections I will lay out the more complete cross-sections that result from solving the matrix elements for the nuclear and magnetic potential. Although the end result is quite complicated in both cases, it is useful to keep in mind that the intrinsic properties of the system are carried in the matrix elements which distill out into thermally averaged pair-pair correlation functions, in the form of Heisenberg

operators. Extrinsic properties are pulled out as a trivial prefactor and consist of the neutron mass, magnitude of incident and final neutron momentum, and several constants as a byproduct of the derivation.

1.4.2 Nuclear Scattering Cross-Section

The potential for scattering of neutrons off the ions in the lattice is governed by the nuclear force. Working out the cross-section quantitatively for this potential is daunting. However, because the nuclear force is very short ranged with respect to the distance between sites in the lattice, the potential at a given site can be approximated as $V(\mathbf{r}) = \alpha\delta(\mathbf{r})$. The task then is to determine the value of α. Since the scattering lengths $b^2 = \frac{d\sigma}{d\Omega}$ can be measured experimentally, this allows us to solve the differential cross-section in the presence of the delta function potential

$$\frac{d\sigma}{d\Omega} = \left(\frac{m}{2\pi\hbar^2}\right)^2 \left| \int V(\mathbf{r}) \exp(i\boldsymbol{\kappa} \cdot \mathbf{r}) d\mathbf{r} \right|^2 = \left(\frac{m}{2\pi\hbar^2}\right)^2 a^2 \tag{1.28}$$

and set it equal to b^2, from this we get

$$V(\mathbf{r}) = \frac{2\pi\hbar^2}{m} b\delta(\mathbf{r}) \tag{1.29}$$

This result is known as the Fermi psuedopotential. In solving the full cross-section this approximation is scaled up to include the entire lattice

$$V = \sum_j \frac{2\pi\hbar^2}{m} b_j \delta(\mathbf{r} - \mathbf{R}_j) \tag{1.30}$$

where $\mathbf{r}$ is the distance to the neutron from the origin and $\mathbf{R}_j$ is the distance to the jth nucleus from the origin. Solving the matrix elements under this potential gives

the following results for coherent nuclear scattering

$$\left(\frac{d^2\sigma}{d\Omega dE'}\right)_{\text{coh}} = \frac{\sigma_{\text{coh}}}{4\pi}\frac{k'}{k}\frac{1}{2\pi\hbar}\sum_{j,j'}\int_{-\infty}^{\infty}\langle\exp\{i\boldsymbol{\kappa}\cdot\mathbf{R}_{j'}(0)\}\exp\{i\boldsymbol{\kappa}\cdot\mathbf{R}_j(t)\}\rangle\exp(-i\omega t)dt \tag{1.31}$$

with

$$\sigma_{\text{coh}} = 4\pi(\bar{b})^2 \tag{1.32}$$

It is possible to extend this result even further and capture the thermal motion of the nuclei by setting the Hamiltonian of the crystal equal to the sum of harmonic oscillator Hamiltonians representing the normal modes. In this case, $\mathbf{R_l} = \mathbf{l} + \mathbf{u_l}$ where $\mathbf{l}$ is the equilibrium position for nucleus l and $\mathbf{u_l}$ is the displacement from equilibrium to be expressed as the sum of displacements due to a set of normal modes. Specifically, $\mathbf{u_l}$ is effectively a sum of complex exponentials weighted by the creation and annihilation operators for harmonic oscillators. From this it can be shown that the coherent cross-section can be written as

$$\left(\frac{d^2\sigma}{d\Omega dE'}\right)_{\text{coh}} = \frac{\sigma_{\text{coh}}}{4\pi}\frac{k'}{k}\frac{N}{2\pi\hbar}\exp\langle\mathbf{U}^2\rangle\sum_{\mathbf{l}}\exp(i\boldsymbol{\kappa}\cdot\mathbf{l})\int_{-\infty}^{\infty}\exp\langle\mathbf{UV}\rangle\exp(-i\omega t)dt \tag{1.33}$$

where $\exp(\mathbf{U}^2)$ is the Debye-Waller factor that picks up an intensity drop due to thermal motion, N is the number of unit cells and $\mathbf{U}$ and $\mathbf{V}$ are the operators

$$\mathbf{U} = -i\boldsymbol{\kappa}\cdot\mathbf{u}_0(0), \mathbf{V} = -i\boldsymbol{\kappa}\cdot\mathbf{u_l}(t) \tag{1.34}$$

The standard treatment from here is to rewrite the exponential $\exp(\mathbf{UV})$ as a Taylor series. This is referred to as the phonon expansion of the cross-section with the nth term describing the n-phonon scattering cross-section. Thus the zeroth term, 1, describes elastic nuclear scattering and we get

$$\left(\frac{d\sigma}{d\Omega}\right)_{\text{coh el}} = \frac{\sigma_{\text{coh}}}{4\pi}N\frac{(2\pi)^3}{\nu_0}\exp(\mathbf{U}^2)\sum_{\boldsymbol{\tau}}\delta(\boldsymbol{\kappa}-\boldsymbol{\tau}) \tag{1.35}$$

while the next term, $\langle \mathbf{UV} \rangle$ describes the 1-phonon process

$$\left(\frac{d^2\sigma}{d\Omega dE'}\right)_{\text{coh}} = \frac{\sigma_{\text{coh}}}{4\pi}\frac{k'}{k}\frac{(2\pi)^3}{\nu_0}\frac{1}{2M}\exp(\mathbf{U}^2)\sum_s\sum_{\boldsymbol{\tau}}\frac{(\boldsymbol{\kappa}\cdot\mathbf{e}_s)^2}{\omega_s}\langle n_s{+}1\rangle\delta(\omega{+}\omega_s)\delta(\boldsymbol{\kappa}{+}\mathbf{q}{-}\boldsymbol{\tau}) \tag{1.36}$$

where s stands for the double index q, j; $\mathbf{q}$ is the wave vector of the phonon mode and $j = 1, 2, 3$ is the polarization index, $\mathbf{e}_s$ is the polarization vector. The sum over s is over the N values of $\mathbf{q}$ in the 1st Brillouin zone, and over the three values of j. M is the mass of the atom.

For the multiphonon processes, the scattering no longer leads to sharp peaks in $(\boldsymbol{\kappa}, \omega)$ due to the large number of ways that the neutron can scatter from the first event to the second event. Hence, this higher order scattering contributes to the background channel.

1.4.3 Magnetic Scattering Cross-Section

As a neutron passes through a system, its spin couples to the magnetic field produced by electrons. There are two sources for the magnetic field. First, there is a field produced by the electrons magnetic dipole moment $\boldsymbol{\mu}_e = -2\mu_B\mathbf{s}$ where $\mathbf{s}$ is the spin angular momentum operator and, in the case of electrons, carries eigenvalues of $\pm 1/2$ for its components. Second, an electron with momentum $\mathbf{p}$ will produce a field due to the Biot-Savart law. Thus the total field is

$$\mathbf{B} = \mathbf{B}_s + \mathbf{B}_L = \frac{\mu_0}{4\pi}\left\{\text{curl}\left(\frac{\boldsymbol{\mu}_e \times \hat{\mathbf{R}}}{R^2}\right) - \frac{2\mu_B}{\hbar}\frac{\mathbf{p}\times\hat{\mathbf{R}}}{R^2}\right\} \tag{1.37}$$

The potential is then given by dotting the moment of the neutron with the field $V = -\boldsymbol{\mu}_N \cdot \mathbf{B}$. Putting this into the cross-section, the matrix elements can be solved down to give

$$\left(\frac{d^2\sigma}{d\Omega dE'}\right)_{\sigma\lambda\to\sigma'\lambda'} = (\gamma r_0)^2\frac{k'}{k}\left|\langle\sigma'\lambda' \mid \boldsymbol{\sigma}\cdot\mathbf{Q}_\perp \mid \sigma\lambda\rangle\right|^2\delta(E_\lambda - E_{\lambda'} + \hbar\omega) \tag{1.38}$$

From this we get the important result that neutrons only measure the component of the electron moment $\mathbf{Q}_\perp$ that is perpendicular to the momentum transfer of the neutron.

$$\mathbf{Q}_\perp = -\frac{1}{2\mu_B}\hat{\boldsymbol{\kappa}} \times (\mathbf{M}(\boldsymbol{\kappa}) \times \hat{\boldsymbol{\kappa}}) \tag{1.39}$$

Here $M(\boldsymbol{\kappa})$ is the Fourier transformed magnetization operator. When the matrix elements are dotted with their complex conjugates, the fact that we measure only a component of the electron's moment translates into directionality factors in the cross-section of the form

$$\mathbf{Q}_\perp^\dagger \cdot \mathbf{Q}_\perp = \sum_{\alpha\beta}(\delta_{\alpha\beta} - \hat{\kappa}_\alpha\hat{\kappa}_\beta)Q_\alpha^\dagger Q_\beta \tag{1.40}$$

where α and β are the x, y, and z directions and $\hat{\kappa}$ is the unit vector associated with the momentum transfer of the neutron $\boldsymbol{\kappa}$. After writing the delta function as an integral and performing a sum/average over final and initial states, the general form for the cross-section section can be written as

$$\frac{d^2\sigma}{d\Omega dE'} = \frac{(\gamma r_0)^2}{2\pi\hbar}\frac{k'}{k}\sum_{\alpha\beta}(\delta_{\alpha\beta} - \hat{\kappa}_\alpha\hat{\kappa}_\beta)\int \langle Q_\alpha(-\boldsymbol{\kappa},0)Q_\beta(\boldsymbol{\kappa},t)\rangle \exp(-i\omega t)dt \tag{1.41}$$

In the case of a localized system, the cross-section can be cleanly separated into nuclear $I_{jj'}(\boldsymbol{\kappa},t)$ and magnetic contributions $J_{jj'}^{\alpha\beta}(t)$ where

$$I_{jj'}(\boldsymbol{\kappa},t) = \langle \exp\{-i\boldsymbol{\kappa}\cdot\mathbf{R}_{l'd'}(0)\}\exp\{i\boldsymbol{\kappa}\cdot\mathbf{R}_{ld}(t)\}\rangle \tag{1.42}$$

$$J_{jj'}^{\alpha\beta}(t) = \langle \mathbf{S}_{l'd'}^\alpha(0)\mathbf{S}_{ld}^\beta(t)\rangle \tag{1.43}$$

here j is the combination l, d that singles out ion d in the lth unit cell and $\mathbf{S}_{ld}^\beta$ is the operator corresponding to the β component of spin for that ion. To simplify the results for a Bravias crystal the subscript d can be suppressed. These terms can be

further separated into elastic ($t = \infty$) and inelastic (time varying) contributions

$$I_{jj'}(\boldsymbol{\kappa}, t) = I_{jj'}(\boldsymbol{\kappa}, \infty) + I'_{jj'}(\boldsymbol{\kappa}, t) \tag{1.44}$$

$$J^{\alpha\beta}_{jj'}(t) = J^{\alpha\beta}_{jj'}(\infty) + J'^{\alpha\beta}_{jj'}(t) \tag{1.45}$$

The final magnetic scattering cross-section is then

$$\begin{aligned} \tfrac{d^2\sigma}{d\Omega dE'} &= \tfrac{(\gamma r_0)^2}{2\pi\hbar}\tfrac{k'}{k}\sum_{\alpha\beta}(\delta_{\alpha\beta} - \hat{\kappa}_\alpha\hat{\kappa}_\beta)\sum_{jj'}\tfrac{1}{4}g_{d'}g_d F^\dagger_{d'}(\boldsymbol{\kappa})F_d(\boldsymbol{\kappa}) \\ &\times \textstyle\int_{-\infty}^{\infty}\{I_{jj'}(\boldsymbol{\kappa}, \infty) + I'_{jj'}(\boldsymbol{\kappa}, t)\}\{J^{\alpha\beta}_{jj'}(\infty) + J'^{\alpha\beta}_{jj'}(t)\}\exp(-i\omega t)dt \end{aligned} \tag{1.46}$$

The cross terms break the scattering into four different contributions:

$I_{jj'}(\boldsymbol{\kappa}, \infty)J^{\alpha\beta}_{jj'}(\infty)$ - Elastic magnetic scattering

$I_{jj'}(\boldsymbol{\kappa}, \infty)J^{\alpha\beta}_{jj'}(t)$ - Inelastic magnetic scattering by

$I_{jj'}(\boldsymbol{\kappa}, t)J^{\alpha\beta}_{jj'}(\infty)$ - Magnetovibrational scattering, ie: phonon processes mediated by the magnetic interaction; elastic in the magnetic channel, inelastic in the nuclear channel.

$I_{jj'}(\boldsymbol{\kappa}, t)J^{\alpha\beta}_{jj'}(t)$ - Inelastic scattering in both channels

1.4.4 Fluctuation Dissipation Theorem

When a neutron passes through a sample it probes the magnetic properties associated with the systems Hamiltonian $\mathscr{H}$. In the state ψ with energy E the total moment of the system is given by

$$\mathbf{M}V = -\left\langle \psi \left| \frac{\partial \mathscr{H}}{\partial \mathbf{H}} \right| \psi \right\rangle \tag{1.47}$$

where $\mathbf{H}$ is the applied field and $\mathbf{M}$ is the magnetization. This allows us to define the total system magnetic moment operator

$$\mathscr{M} = -\frac{\partial \mathscr{H}}{\partial \mathbf{H}} \tag{1.48}$$

Table 1.1: Properties of a scattering system that simplify the dependencies associated with the susceptibility

Linear Medium	Susceptibility is Independent of Field
Stationary Medium	$\Omega = \omega$
Medium is Translationaly Invariant	$\mathbf{q} = \mathbf{k}$

which can be projected out to give the magnetic moment per unit volume, see for instance White [127]. Using the density matrix approach [15], the magnetization $\mathbf{M}(\mathbf{r})$ of the system can then be found by taking the ensemble average

$$\mathbf{M}(\mathbf{r}) = \langle \mathscr{M}(\mathbf{r}) \rangle = tr \rho \mathscr{M}(\mathbf{r}) \tag{1.49}$$

In linear response theory the magnetization of a system is taken to be directly proportional to the perturbing magnetic field and the susceptibility χ is the coefficient of proportionality relating these two quantities. The real space structure $(\mathbf{r}, t)$ of the field and magnetization can be rewritten in terms of Fourier components as

$$\mathbf{M}(\mathbf{r}, t) = \frac{1}{2\pi V} \sum_{\mathbf{k}} \int d\Omega \mathbf{M}(\mathbf{k}, \Omega) \exp\{i(\mathbf{k} \cdot \mathbf{r} - \Omega t)\} \tag{1.50}$$

$$\mathbf{H}(\mathbf{r}, t) = \frac{1}{2\pi V} \sum_{\mathbf{q}} \int d\Omega \mathbf{H}(\mathbf{q}, \omega) \exp\{i(\mathbf{q} \cdot \mathbf{r} - \omega t)\} \tag{1.51}$$

and from this the generalized susceptibility takes the form

$$M_\nu(\mathbf{k}, \Omega) = \sum_{\mathbf{q}} \int d\omega \sum_{\mu} \chi_{\nu\mu}(\mathbf{k}, \mathbf{q}; \Omega, \omega) H_\mu(\mathbf{q}, \omega) \tag{1.52}$$

where ν and $\mu = x, y, z$. In general, the temporal frequency and spacial modulation of the field $(\mathbf{q}, \omega)$ can be different from that of the resulting magnetization $(\mathbf{k}, \Omega)$. As well, the susceptibility also depends on the particular form of the field. However, Table 1.1 list properties of a system that simplify this general susceptibility considerably. Since the systems under consideration satisfy all of these conditions, we can reduce

the complexity from that of a field dependent $\boldsymbol{\chi}(\mathbf{k}, \mathbf{q}; \Omega, \omega)$ to a field independent $\boldsymbol{\chi}(\mathbf{q}, \omega)$.

Because the magnetic response of the system can be out-of-phase with the perturbing field, the susceptibility is complex in nature

$$\boldsymbol{\chi}(\mathbf{q}, \omega) = \boldsymbol{\chi}'(\mathbf{q}, \omega) + i\boldsymbol{\chi}''(\mathbf{q}, \omega) \tag{1.53}$$

The imaginary part of the susceptibility describes simultaneously both the fluctuations and the dissipation when the system is driven away from equilibrium. To see this, it is worth while to compare the magnetic response of a system to that of a damped driven harmonic oscillator. The differential equation describing harmonic motion is given by

$$\ddot{x} + 2\beta\dot{x} + \omega_0^2 x = A\cos(\omega t) \tag{1.54}$$

where 2β captures the dissipation and ω_0 is the restoring force of the system. The non-transient motion is given by the particular solution of this equation

$$x_p(t) = \frac{A}{\sqrt{(\omega_0^2 - \omega^2)^2 + 4\omega^2\beta^2}} cos(\omega t - \delta) \tag{1.55}$$

with

$$\delta = \tan^{-1}\left(\frac{2\omega\beta}{\omega_0^2 - \omega^2}\right) \tag{1.56}$$

from this we see that the difference in phase between the driving force and the resultant motion is given by δ. Moreover, the magnitude of δ is directly related to the dissipation in the system 2β. This also holds true for our magnetic system where a complex susceptibility $\chi = \chi' + i\chi'' = |\chi|\exp(i\delta)$ multiplied into a driving magnetic field $H_0\exp(i\omega t)$ leads to an offset magnetization $H_0|\chi|\exp(i(\omega t + \delta))$. The true importance of this result lies in the fact that the dissipation is related in a fundamental manner to fluctuations in the system away from its equilibrium state. This was first demonstrated for liquids where the viscosity (describing dissipation due

to the collisions of molecules during fluid flow) was related directly to the fluctuations encapsulated in the Brownian motion of an equilibrium (non-flowing) fluid due to equivilent collision processes. In comparison, whereas the non-equilibrium properties in a fluid are quantified by its coefficient of viscosity, in a magnetic system they are quantified by the imaginary part of the susceptibility (dynamic susceptibility) $\boldsymbol{\chi}''(\mathbf{q},\omega)$. A powerful result from statistical mechanics known as the fluctuation-dissipation theorem [94] allows us to quantify the relationship between the response of a system and the spectrum of inelastic excitations representing fluctuations away from equilibrium. In the case of magnetic systems this response is, again, the dynamic susceptibility and the fluctuations under consideration are thermal fluctuations in the magnetization with the relationship given by [127]

$$\int_{-\infty}^{\infty} dt \langle \{\mathscr{M}_\nu(\mathbf{q},t)\mathscr{M}_\mu(-\mathbf{q})\}\rangle e^{i\omega t} = \frac{2\hbar V}{1-e^{-\frac{\hbar\omega}{k_B T}}}\chi''_{\mu\nu}(\mathbf{q},\omega) \tag{1.57}$$

Given that neutron scattering measures the magnetic fluctuations within a system, it comes as no surprise that the pair correlation function in the fluctuation dissipation theorem is equivalent to the one appearing in the inelastic magnetic scattering cross-section. Indeed, it can be shown that for a Bravais lattice this cross-section can be rewritten as

$$\left(\frac{d^2\sigma}{d\Omega dE_f}\right)_{\text{mag inel}} = (\gamma r_0)^2 \frac{k_f}{k_i} N \left[\frac{1}{2} g F(\mathbf{q})\right]^2 \exp(U^2) \sum_{\nu\mu} (\delta_{\nu\mu} - \hat{q}_\nu \hat{q}_\mu) \frac{1}{\pi g^2 \mu_B^2} \frac{1}{1-\exp(-\frac{\hbar\omega}{k_B T})} \chi''_{\nu\mu}(\mathbf{q},\omega) \tag{1.58}$$

From this we see that the neutron scattering cross-section directly probes the structure of the dynamic susceptibility. Moreover, the Kramer-Kronig relations provide a method for obtaining the real part of the susceptibility $\boldsymbol{\chi}'(\mathbf{q},\omega)$ when the imaginary part is completely known. Thus, neutron scattering is capable of mapping out the total response function.

1.5 Data Analysis

1.5.1 Transformations between Unit Cells

The parents of the Fe-based superconductors undergo a tetragonal to orthorhombic phase transition as the temperature is reduced. This transition is quickly suppressed as a function of doping leaving a single tetragonal phase over all temperatures. As a result, the existing literature on these systems contains analysis performed in the tetragonal unit cell for some papers and the orthorhombic unit cell for others. Although most of our data is collected in the tetragonal unit cell, our final analysis is typically converted to and published in the orthorhombic cell in order to facilitate easy comparison across all of our studies. Nonetheless, due to the common usage of both systems within the literature, a geometric understanding of the difference between these two unit cells and a coordinate transformation between them will be useful at times.

We will consider a simplified picture consisting only of the in plane Fe atoms from which the magnetic properties originate. As seen in Fig 1.11, the structural phase transition is not a direct stretching along the lattice vectors that define the tetragonal unit cell. Rather, within this cell the lattice parameters remain equal across the phase transition, $a = b$, with a monoclinic distortion of the lattice occurring within the ab-plane. Although the monoclinic unit cell is the primitive cell of the lattice, it is generally rejected in favor of a larger orthorhombic unit cell. Geometrically, the boundary of the real space orthorhombic cell consists of 4 neighboring diagonals of the monoclinic cell. It should be noted that this orthorhombic cell is accessible if and only if a_m and b_m remain the same. The benefits of this larger cell are two fold. First, mirror reflections are restored in the orthorhombic cell giving it a higher degree of symmetry. Second, although the monoclinic cell corresponds to the primitive cell of the nuclear structure, the orthorhombic cell corresponds to the smallest magnetic cell

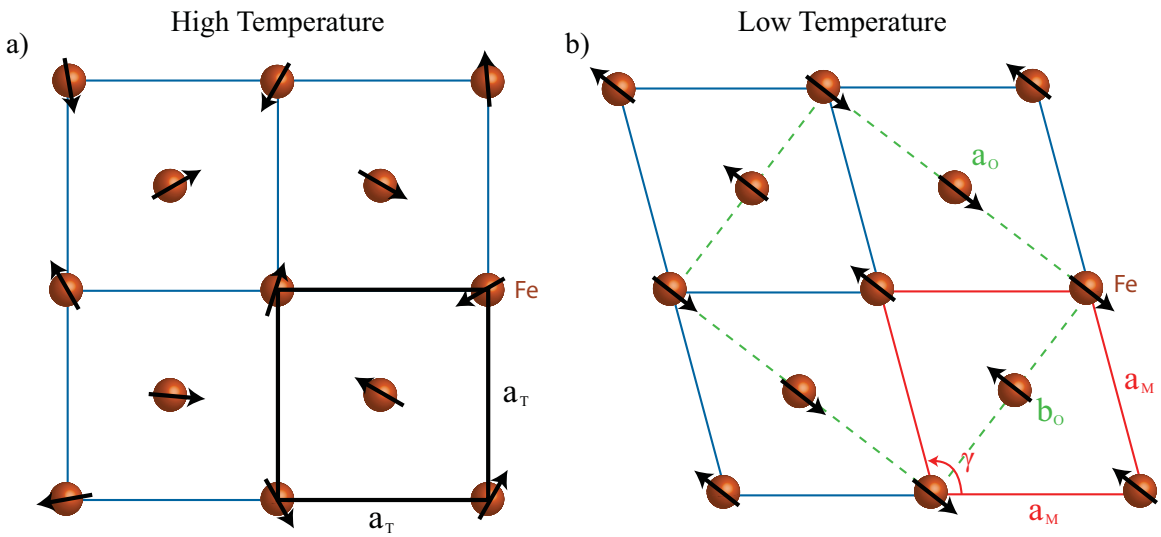

Figure 1.11: Definition of Unit Cells: a) The black box defines the tetragonal unit cell corresponding to the lattice symmetry for temperatures above the structural phase transition. In the tetragonal state, the magnetic moments associated with the iron atoms are disordered as represented by the black arrows. b) Below the phase transition, the tetragonal cell undergoes an inplane angular distortion leading to the monoclinic unit cell defined in red. The low temperature phase can also be described by an orthorhombic unit cell (dashed green line) which consists of 4 neighboring diagonals of the monoclinic cell. The structural distortion is accompanied by a long range ordering of the magnetic moments with the the spins aligning antiferromagnetically and ferromagnetically along the orthorhombic a and b axis respectively.

associated with the ordered antiferromagnetic phase that is concomitant (or in close proximity) to the structural phase transition.

In deriving the transformation from tetragonal to orthorhombic units, we use the approximation that the monoclinic distortion is small enough to be neglected. This approximation is more than justified given that the angular distortion is less than 1%. Fig. 1.12 a) shows a single tetragonal and orthorhombic cell (solid blue and dashed green lines respectively), with the latter shifted such that it encomapasses the tetragonal cell. When Fourier transformed into reciprocal space, the orthorhombic cell shrinks within the tetrogonal cell, Fig 1.12 b), while the angles between the lattice vectors remains unchanged. Specifically, each systems set of reciprocal lattice vectors

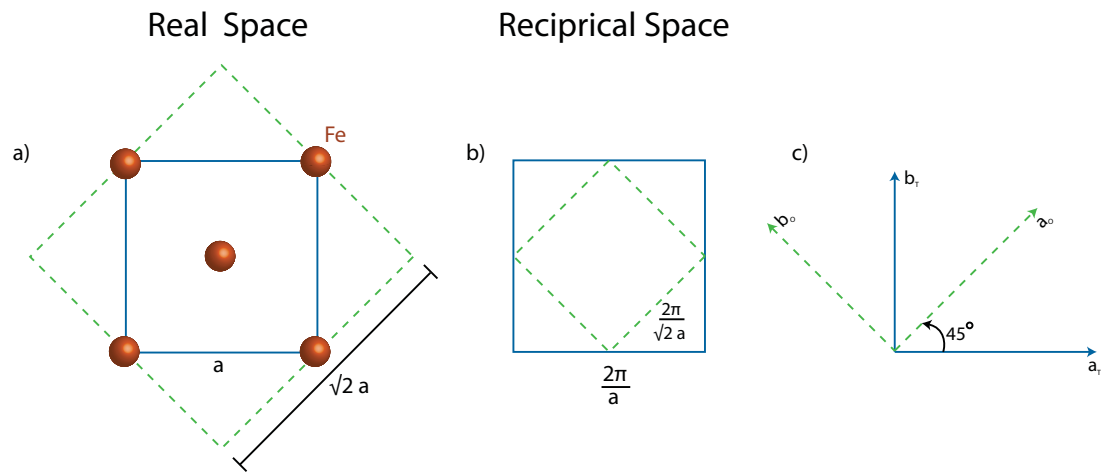

Figure 1.12: Fourier Transform of the Structure: a) Superposition of the real space orthorhombic (dashed green) and tetragonal (solid blue) cells. b) Fourier transform of cells. c) Relationship between the lattice vectors of the two cells. Given that the distortion is extremely small, its effects have been ignored in the figure, ie: $a_O = b_O$ with axis 90° apart and $\theta = 45^o$

is orthogonal with an offset angle of 45° between the two systems. As a result, the coordinate transformation in reciprical space can be expressed as a rotation matrix with $\theta = 45^o$. Moreover, given that the rotation is within the ab-plane we know immediately that $Q_z^O = Q_z^T$ and, as a result, we need only to consider a 2D rotation matrix.

$$\begin{pmatrix} \cos\theta & \sin\theta \\ \sin\theta & -\cos\theta \end{pmatrix} \begin{pmatrix} Q_x^T \\ Q_y^T \end{pmatrix} = \begin{pmatrix} Q_x^O \\ Q_y^O \end{pmatrix} \Rightarrow \begin{cases} \frac{1}{\sqrt{2}} Q_x^T + \frac{1}{\sqrt{2}} Q_y^T = Q_x^O \\ \frac{1}{\sqrt{2}} Q_x^T - \frac{1}{\sqrt{2}} Q_y^T = Q_y^O \end{cases} \tag{1.59}$$

Since the tetragonal and orthorhombic cells are of size a and $\sqrt{2}a$ respectively, when expressed in terms of reciprocal lattice units, $\mathbf{Q^T}$ and $\mathbf{Q^O}$ differ in prefactor only by a $\sqrt{2}$ in the denominator, ie: $(Q_x^T, Q_y^T) = (\frac{2\pi}{a} H_T, \frac{2\pi}{a} K_T)$ whereas $(Q_x^O, Q_y^O) =$

$(\frac{2\pi}{\sqrt{2}a}H_O, \frac{2\pi}{\sqrt{2}a}K_O)$. When combined with Eq. 1.59 we get the desired final result:

$$\begin{cases} H_O = H_T + K_T \\ K_O = H_T - K_T \\ \quad L_O = L_T \end{cases} \tag{1.60}$$

Technical Note: The rotation matrix is written with the negative out of place. It should be assigned to the $\sin\theta$ in the second row in order to correctly represent a coordinate transformation associated with a counter clockwise rotation. However, by mirror symmetry of the orthorhombic cell, we are free to identify the negative without impunity to K_T rather than H_T which gives a slightly cleaner looking result.

1.5.2 Normalization of Data to Absolute Units

Often in neutron scattering experiments, calibration of intensities to absolute units is of very little importance and therefore not performed. At triple axis facilities this is very often the case since it is not customary for the facility to have a standard operating procedure in place to normalize intensities for the user at the end of an experiment. As a result, intensities are reguraly reported in terms of arbitrary units consisting of the number of detector counts collected over a given period of time. eg: counts/min. Although reporting arbitrary units in terms of a collection time is common practice, in reality, the total flux incident on a sample over a given length of time varies with the chosen incident energy of the spectrometer, upstream collimation, and, to a lesser degree, the variation in the output of the reactor. To account for this, an upstream detector measures flux pre-sample and scans are set to collect each data point up to a predefined monitor count. As a result, the reported collection time typically only provides a ball park measure of how long it took to collect up to a preset total incident flux. Often measurements forgo reporting in terms of time altogether and instead use units of counts/(x monitor counts) where x is the total incident flux measured for each point by the upstream detector. Since

different scans on the same experiment often carry different counting times, a trivial normalization can be performed whereby the intensity of each scan point is multiplied by the appropriate prefactor such that these intensities would all correspond to the same total incident flux. For example, scan intensities collected for 20,000, 30,000 and 60,000 monitor counts could, for instance, be multiplied by 3, 2, and 1 respectively. Such a procedure allows the experimenter to arbitrarily normalize the data set so that it is possible to fairly cross compare the intensities of different scans within that particular experiment(though not with others.)

When absolute units are desired on triple axis data, then the most often used approach is to map out a transverse acoustic low energy phonon and use the known differential one-phonon scattering cross-section in the long wavelength limit to normalize the data [112]:

$$\frac{\partial^2\sigma}{\partial\Omega\partial E} = A\frac{\hbar^2 N}{2E(\mathbf{q})}\frac{k_f}{k_i}(n(\omega)+1)(\boldsymbol{\kappa}\cdot\mathbf{e_{qs}})^2 e^{-2W}\frac{1}{M}\left|G(\boldsymbol{\tau}\right|\partial(E-E(\mathbf{q})) \tag{1.61}$$

where the momentum transfer of the neutron $\boldsymbol{\kappa}$ and the reduced wave vector $\mathbf{q}$ are related by the lattice vector of the associated phonon mode by $\boldsymbol{\kappa} = \boldsymbol{\tau} + \mathbf{q}$, N is the number of unit cells, M is the mass of an individual unit cell, k_i and k_f are incident and final neutron wavelengths, $\mathbf{e}_{qs}$ is a unit vector in the direction of the displacement of the atoms for the phonon mode, E($\mathbf{q}$) is the energy of the phonon mode, $(n(\omega)+1)$ is the Bose population factor, e^{-2W} is the Debye-Waller factor (approximated as 1), G($\boldsymbol{\tau}$)is the nuclear structure factor and A is the spectrometer dependent constant to be determined.

Once A has been determined, this value can be used in the cross-section for paramagnetic scattering to calculate the dynamic susceptibility in absolute units:

$$\frac{\partial^2\sigma}{\partial\Omega\partial E} = A\frac{(\gamma r_0)^2}{4}\frac{k_f}{k_i}N\left|f(\boldsymbol{\kappa})\right|^2 e^{-2W}(n(\omega)+1)\frac{2}{\pi\mu_B^2}\chi''(\boldsymbol{\kappa},\omega) \tag{1.62}$$

where $f(\boldsymbol{\kappa})$ is the isotropic, magnetic form factor for (in our work) Fe^{2+}.

At ISIS, where all of the time of flight data within this thesis was performed, collected data is normalized by the local contact to a vanadium standard as standard operating procedure. The benefit of vanadium is that the scattering cross-section is dominated by the incoherent contribution, $\frac{\sigma^V_{inc}}{\sigma^V_{coh}} = 250$ (whereas, for comparison, the ratio for iron is $\frac{\sigma^{Fe}_{inc}}{\sigma^{Fe}_{coh}} = 0.035$.) Moreover, since the elastic incoherent total scattering cross-section for vanadium is well known $(\frac{\sigma_{inc}}{4\pi})^V = 404\frac{mbarn}{s.r.}$ this provides us with a straight forward means of normalizing to absolute units the scattering from the sample $AN^{sample}S(\mathbf{Q},\omega) = I(\mathbf{Q},\omega)^{sample}$ using the elastic incoherent cross-section of the vanadium $AN^{van}(\frac{\sigma_{inc}}{4\pi})^{van} = I^{van}$. Where, N^{van} and N^{sample} are the number of unit cells in the vanadium standard and the sample respectively, I^{van} and I^{sample} are the spectrometer intensities, and A is the spectrometer dependent constant to be removed. Equating these gives:

$$S(\mathbf{Q},\omega) = \left(\frac{\sigma_{inc}}{4\pi}\right)^{van} \frac{N^{van}}{N^{sample}} \frac{I_{sample}(\mathbf{Q},\omega)}{I_{van}} \tag{1.63}$$

Since the spectrometer prefactor A is a function of both E_i and chopper frequency ω, this requires that monochromatic vanadium scans be performed for all of combinations of E_i and ω that data was collected at. As well, a single white beam vanadium scan is used to account for variation in the detector efficiencies.

1.5.3 Resolution Calculations and Model Convolution

Resolution is an important concern in neutron scattering. Especially given that many measurements correspond to scattering processes characterized by infinite lifetimes, such as undamped spin waves, or infinite spacial correlation, such as long range ordered magnetic Bragg peaks. As a result, the ($\mathbf{Q}$, ω) dependence takes the form of delta functions in the associated cross-sections. Thus, in the far limit of infinite correlation, we see that such measurements return resolution limited peak widths. More generally, resolution must be taken into account in order to correctly separate

resolution broadening from intrinsic broadening processes (damping, disorder, glass phases, etc.) when fitting models to the data.

A simple, experimental estimate of the energy resolution can be obtained at ($\mathbf{Q}$, 0) by performing an energy scan centered at E=0. Since the elastic background scattering is orders of magnitude stronger than inelastic background scattering, this results in a resolution limited peak at E=0, Fig. 1.13. Likewise, a similar experimental estimate of the Q-resolution can often be obtained at ($\mathbf{Q}_B$, 0) where Q_B is a resolution limited Bragg peak. In order to determine the resolution at a general location in ($\mathbf{Q_0}, \omega_0$), resolution calculations are required.

In triple axis experiments, the resolution function is described by a 4D Gaussian distribution with dimensions ($\omega, \mathbf{Q}$) projected into the 4-vector $\mathscr{L} = \left(\frac{m_n}{\hbar Q}\omega, Q_\parallel, Q_\perp, Q_z\right)$ and parameterized in terms of the spectrometer quantities that contribute to the resolution width: mosaics of the sample, monochromator and analyzer crystals, the full-width at half maximum of the transmission functions associated with the collimators, incident and final neutron average wave vectors, and the "'handedness"' of the spectrometer configuration. The resolution function can be written in the form of a matrix multiplied on either side by the 4-vector $\Delta\mathscr{L}$[112]:

$$R(\omega - \omega_0, \mathbf{Q} - \mathbf{Q_0}) = R_0 \exp\left(-\frac{1}{2}\Delta\mathscr{L} M \Delta\mathscr{L}\right) \tag{1.64}$$

where

$$\Delta\mathscr{L} = \left(\frac{m_n}{\hbar Q_0}(\omega - \omega_0), Q_\parallel - Q_0, Q_\perp, Q_z\right) \tag{1.65}$$

Here ω_0 and $\mathbf{Q_0}$ define the location where the resolution is calculated. For the components of $\mathbf{Q_0}$ inside the scattering plane, $Q_\parallel$ is defined as the in plane component along $\mathbf{Q_0}$ and $Q_\perp$ as the in plane component perpendicular to $\mathbf{Q_0}$, Q_z is the out of plane component. M is a 4x4 matrix (see appendix A of [112]) and m_n is the mass of the neutron. Constant intensity contours are given by fixing the argument of the exponential in Eq. 1.64. These contours take the form of 4D ellipses which can be projected out onto the scattering plane to establish resolution widths at a particular

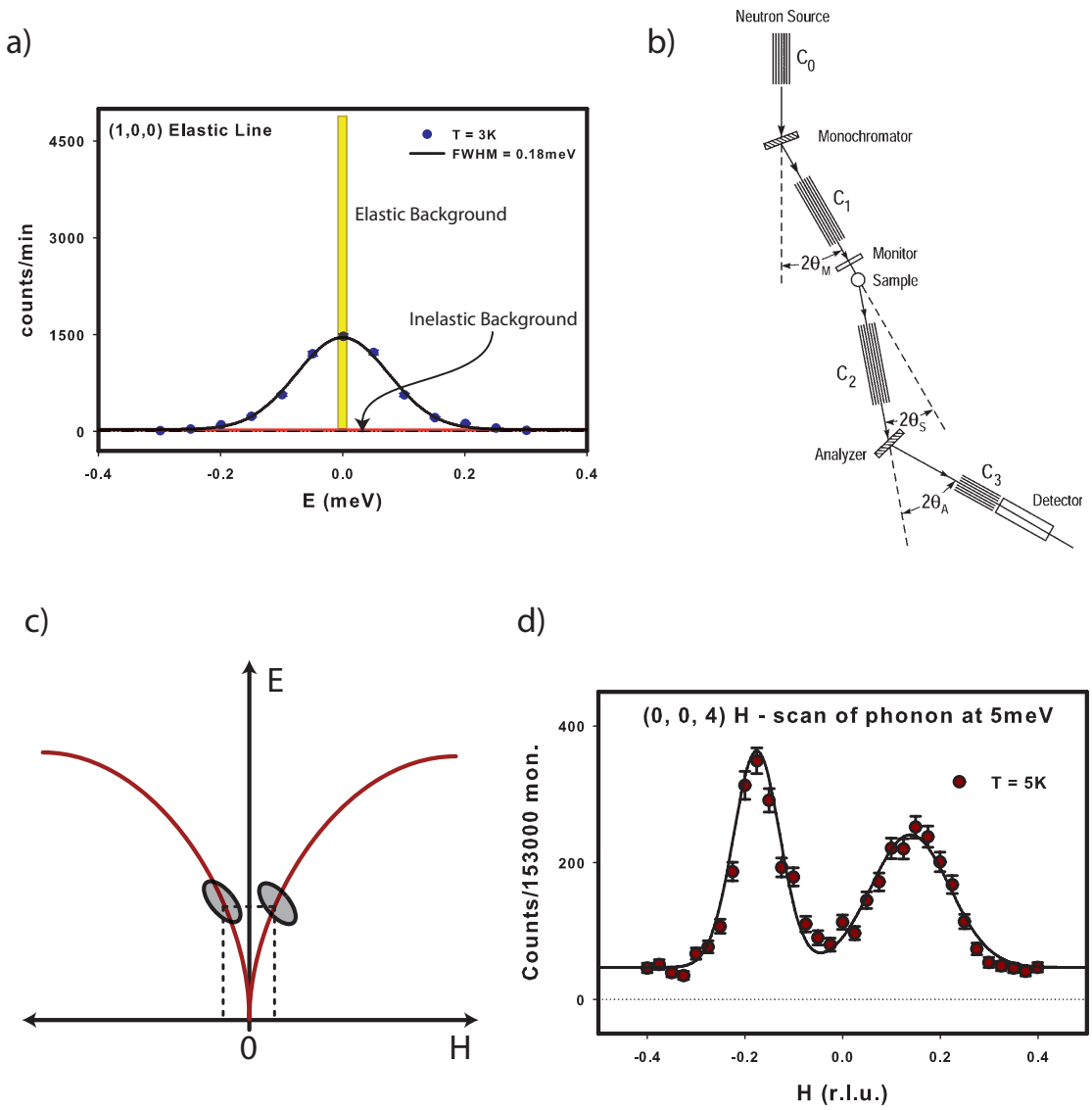

Figure 1.13: a) Example of an experimental determination of elastic energy resolution based on an E-scan of the elastic line about E=0. b) Triple axis spectrometer with labeled quantities that contribute to the resolution: 4 collimations, 3 mosaics, 2 neutron wave vectors, 1 spectrometer handedness. c) Example of two resolution ellipses at equivelant positions along an acoustic phonon dispersion centered on an (0,0,4) nuclear Bragg peak. d) The resulting intensity and linewidth difference of the two equivalent peaks results from one resolution ellipse lying more or less perpendicular to the dispersion line while the other lies along it.

$(\mathbf{Q_0}, \omega_0)$ or, leaving the argument unfixed, the resolution function can be convolved

with a fitting model to describe the observed flux at the detector $F_d(\omega_0, \mathbf{Q_0})$:

$$F_d(\omega_0, \mathbf{Q_0}) = \phi(\bar{k}_i) \int d\omega d\mathbf{Q} R(\omega - \omega_0, \mathbf{Q} - \mathbf{Q_0}) S(\mathbf{Q}, \omega) \tag{1.66}$$

where $\phi(k)d\mathbf{k}$ is the number of neutrons incident on C_0 (see Fig. 1.13) and $\bar{k}_i$ is the average incident neutron wave vector.

Since the 4x4 matrix M contains non-vanishing off diagonal terms, this results in the axis of the resolution ellipses and axes defined by ω_0 and $\mathbf{Q_0}$ to lay at non-parallel angles. In general, the orientation of the resolution ellipse can have a pronounced effect on the observed intensities and line widths since they effectively represent an integration volume. Acoustic phonon measurements are a good example of this in practice. Measurements at two equivelant positions along the phonon dispersion at low energies would give two nearly identical resolution ellipses. However, the orientation of the ellipses will integrate a different length of the dispersion at these equivalent positions, thereby leading to non-equivalent line widths and intensities, Fig. 1.13. Presently, there are several software packages that allow the user to input the resolution parameters and quickly extract out resolution widths or perform model convolution.

In time of flight analysis, model convolution is complicated by the size of the task. Unlike a triple axis spectrometer which consists of a single analyzer, time of flight spectrometers consist of several thousand position sensitive, time resolved detectors covering a large region of $(\mathbf{Q}, \omega)$ space. For a given detector, kinematic formulas relating pulse widths, flight times, flight paths and incident energies allow for fairly straightforward calculations of the resolution. Additional contributions to the resolution stem from the finite size of the detectors, moderator, and sample. It is also possible to include the mosaic of the crystal in the calculation, although it was not included in our work and does not contribute substantially. The chopper and moderator contributions can be summed in quadrature to get the total energy

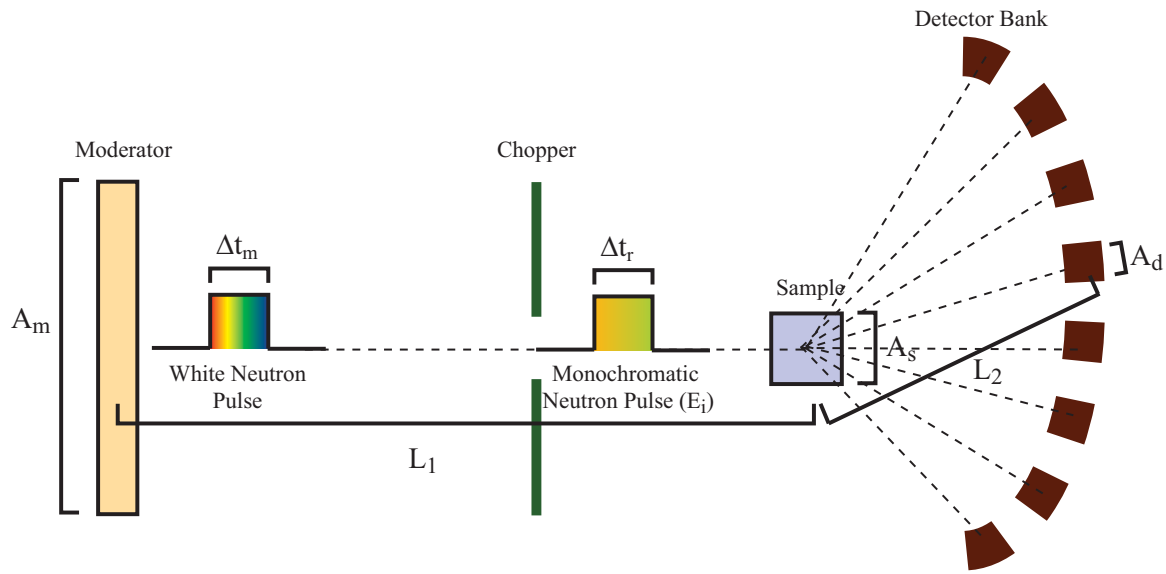

Figure 1.14: Time of flight spectrometer with labeled quantities that contribute to the resolution: 3 spacial spans, 2 flight paths, 2 pulse widths, 2 energies

resolution [130]:

$$\Delta E = \sqrt{(\Delta E^m)^2 + (\Delta E^r)^2} \tag{1.67}$$

where

$$\frac{\Delta E^m}{E_i} = \frac{2}{L_1}\left(\frac{2E_i}{m_n}\right)^{\frac{1}{2}} \Delta t_m \tag{1.68}$$

and

$$\frac{\Delta E^r}{E_i} = \frac{2}{L_1}\left(\frac{2E_i}{m_n}\right)^{\frac{1}{2}} \Delta t_r \left[1 + \left(\frac{E_i - E}{E_i}\right)^{\frac{3}{2}} \frac{L_1}{L_2}\right] \tag{1.69}$$

here Δt_m and Δt_r are the durations of the moderator and chopper neutron pulses respectively, L_1 and L_2 are the moderator to sample and the sample to detector distances respectively, and m_n is the mass of the neutron.

Resolution broadening of models is achieved using a Monte-Carlo approach. In brief, to calculate the convolved model at S($\mathbf{Q}$, E), we begin by considering a given detector with nominal energy transfer, E, and wave vector $\mathbf{Q}$. Since the data is collected and sorted into energy bins, a random energy transfer, E', is chosen from a uniform distribution with length equal to the energy bin size. A random deviation in

the incident energy, ΔE_i, is chosen from a Gaussian distribution centered about the nominal E_i with a width equal to the energy resolution at the sample. A deviation from the final energy ΔE_f can be calculated from ΔE_i based off of results from Eq. 1.68. The actual energy transfer is then given by $E'' = E' + \Delta E_i - \Delta E_f$. Positions on the moderator, detector and crystal are then chosen from a uniform distribution and used along with the above energy results to calculate the actual momentum transfer $\mathbf{Q}'$ using the appropriate kinematics and geometry. A single Monti Carlo point is then constructed by passing $\mathbf{Q}'$ and E'' into the model $\mathrm{S}_n(\mathbf{Q}'_n,E''_n)$. Additional Monti Carlo points for the detector can be collected by starting the entire procedure all over again. The convolved cross-section at detector d is then taken as the mean of the Monti Carlo points: $\mathrm{S}_d(\mathbf{Q},E)$=mean[$\mathrm{S}_n(\mathbf{Q}'_n,E''_n)$]. After this process loops over all detectors, the results are binned into pixels in reciprocal space and the model is then ready to be passed, along with the data, into a fitting routine.

Due to the sheer number of detectors, this iterative Monti Carlo procedure is very costly in terms of processor time. As a result, fitting complicated, non-analytic models cannot always be achieved due to the time required for convergence of the fitting routine to minima in reduced χ^2. In such cases, one is relegated to searching through parameter space by hand, using an unconvolved cross-section, in order to approximate the correct parameters and then convolve the cross-section with these parameters fixed. In my first author work, we considered a Heisenberg model with an analytic form. Hence, we were able to run fits with a convergence time of roughly 5 minutes. However, on coauthor work, the system at hand required that for each location in reciprocal space, we diagonalize an 8x8 matrix to extract out the intensity of the four doubly degenerate dispersion branches at that location. In this case, overnight runs were still insufficient to achieve convergence.

To get a single resolution width at a particular location, ($\mathbf{Q}_0$, ω_0), in reciprocal space, we convolve a Gaussian centered at ($\mathbf{Q}_0$, ω_0) with a FWHM set extremely close to zero. We then taken the resulting broadened FWHM of the convolved Gaussian

as our resolution. For our time of flight data analysis, the software TobyFit [95] was used for model convolution and fitting.

1.6 Motivation of Thesis

Within this introduction I have discussed in some detail the aspects of the Fe-based systems that make them highly interesting for neutron scattering studies. First, superconductivity exists in close proximity to long range antiferromagnetic order with tuning between phases achieved via doping. Second, the short range magnetic excitations that persist into the SC phase contain a resonant excitation that is strongly correlated to T_c. The fact that these two features are also present in both the heavy Fermions and the cuprates provides strong evidence that the unconventional superconductivity observed in all these systems is coupled in a fundamental manner to the magnetic degrees of freedom. However, beyond this general statement lies a host of details that can potentially vary from system to system: What differences exist between superconductivity derived from an itinerant magnet versus a local moment system? How do different long range orders (G-type AFM vs. stripe AFM vs FM, etc.) affect the magnetic excitations and, in turn, the superconductivity? Can the source of differences between families be identified and categorized with respect to one another, ie: pnictides vs closely related chalcogenides vs less related cuprates vs even more distantly related heavy Fermions? How important is dimensionality to unconventional superconductivity?

In order to answer these broader questions, it is first necessary to answer more immediate questions associated with the Fe-based superconductors. At the start of my thesis, very little was known about the physics of these system. Early on, Fermi surface nesting and the metallicity suggested that the magnetism was itinerant in origin. However, since then, it has become increasingly clear that corellations play an important role in defining the magnetic groundstate. Moreover, at the start of my work, there existed no systematic studies of the effect of doping on the magnetic

excitations. Thus, neither the origin of the magnetism nor the evolution of magnetic excitations in doped derivatives were in hand. This is equally true for both the Chalcogenides and Pnictides. Hence, similar studies on both of these classes were needed in order to acquire a comprehensive picture of the Fe-based superconductors. Only after these measurements had been performed and there results compiled would it be possible to do a sweeping review covering commonalities and differences between the cuprates, heavy Fermions, and Fe-based systems.

As more has been learned about these new systems, the motivation to study their properties has stretched beyond attempts to only fit the Fe-based superconductors into a larger canvas consisting of multiple unconventional superconducting families. It has been said that the asymptotic solutions come quickly and the deeper physics lies in between. This is never truer than in magnetism where the (fairly well understood) local and itinerant end solutions are situated in between a broad spectrum of potential magnetic states that offer a rich variety of physics. It now appears that somewhere within this middle lies the correct mix of driving interactions that give rise to the magnetism the Fe-based systems. Thus, the chance to explore part of this more complex realm and shed light on the underlying physics is of interesting in itself.

Chapter 2

Pnictides

2.1 Magnetic Excitations in the $BaFe_2As_2$ Parent

2.1.1 Introduction

By the start of my work on the Ba(122) parent, a host of neutron scattering experiments had been carried out on the pnictides. A large portion of these studies had focused on the Ba-based (122) family. However, almost all of these experiments studied spin excitations in either optimally or under doped superconductors [10, 70, 9], with little investigation given to the spin wave excitations in the parent compound [26, 79]. A comprehensive study of spin excitations up to the zone boundary had been hindered due to the difficulty in growing the large amounts of single crystals required for inelastic neutron scattering experiments.

Understanding the magnetic exchange coupling and fundamental Hamiltonian of the parent compound of FeAs-based superconductors is extremely important, because such information will lay the foundation from which to analyze the evolution of spin excitations as the parent is doped away from its long range ordered groundstate. For example, as discussed in the introduction, spin waves in the parent compound of cuprates can be described very well by local moment Heisenberg Hamiltonian [16]. Since the parent compound of FeAs-based superconductors are semimetals,

much has been debated about the microscopic origin of the magnetism in these materials. Although recent measurements by our group on $CaFe_2As_2$ at the MERLIN spectrometer at ISIS [144] suggested that spin excitations in this material have both local and itinerant features, it is not clear that these features are a general property of all parent compounds of pnictides. Indeed, studies of pressure induced superconductivity in AFe_2As_2 have demonstrated that the maximum T_c of the parents, as well as the range of pressures that sustain superconductivity, increases with the ionic size of A. Studies by Kimber et. al. and others provide evidence that the structural effects of applying pressure are identical to those that result from chemical doping. Namely, both methods of tuning into superconductivity suppress the structural phase transition and decrease the As-Fe-As bond angle as well as the Fe-Fe distance with the end result being that the structural changes to the FeAs layer reduces nesting and destabilizes the SDW ground state [56]. Given that Ba, Sr, and Ca all have very different sizes and in light of the existing relationships between ionic size, Tc, and structural distortions, cross studies of all (122) parents would be very interesting in order to sort out how spin excitations differ between them. As such, our study would also probe the lattice effect on magnetic exchange couplings along the c-axis and since Ba is considerably larger than Ca, it would be important to determine whether Ba(122) has a weaker or stronger c-axis coupling compared with Ca(122).

Additional motivation for studying $BaFe_2As_2$ arose because the existing triple-axis work on single crystals [79] was not fully consistent with time-of-flight measurements on powder samples [26]. Specifically, triple axis measurements up to 30meV energy transfer by Matan et. al. found evidence of anisotropic scattering that they attributed to electron hole excitations at the edge of the Stoner continuum [79]. No such Stoner excitations were observed in time of flight Ba(122) powder measurements that extend to 100meV or time of flight Ca(122) [144] measurements up to 300meV. Since we had grown and coaligned 25g of single crystals, we had the necessary mass to probe excitations all the way to the zone boundary and conclusively settle this discrepancy

in the literature, fully determine the effective exchange couplings, and compare our Ba(122) results with existing similar data on Ca(122).

For our experiment we grew our single crystals at the Institute of Physics in Bejing and coaligned these using the triple axis spectrometer HB-1 attached to the High Flux Isotope reactor at Oak Ridge National Laboratories. Time of flight data was then collected using the MAPS spectrometer attached to ISIS at the Rutherford Appleton Laboratories. The sample was aligned with the c-axis parallel to the beam allowing for four folding of data in-plane at the expense of spectrometer coupling of the energy transfer and the out of plane direction L. The sample was placed in a closed cycle refrigerator and data collection was carried out at three different temperatures, 7K, 125K, and 150K corresponding to scattering deep inside the ordered state, and scattering 10% below and 10% above T_N respectively.

2.1.2 7K Data and Model

Upon review of our data it became immediately clear that the spin wave scattering in $BaFe_2As_2$ in the low temperature, long range magnetically ordered state was very different in character from that observed in $CaFe_2As_2$ [40]. To illustrate the dramatic difference, we show in Fig. 2.1 constant-energy images of the spin waves for these two materials. Since the AF structure, twinning, and lattice structure of $BaFe_2As_2$ and $CaFe_2As_2$ are identical, one would naively expect that the structure of the scattering and effective AF exchange couplings in these materials would be similar. Inspection of Fig. 2.1 reveals that instead, at higher energies the spin waves of $BaFe_2As_2$ at $E = 144 \pm 15$meV no longer form a ring centered around the AF ordering wave vector as in the case of $CaFe_2As_2$.

Previous modeling of the spin wave data in $CaFe_2As_2$ was performed using a Heisenberg Hamiltonian consisting of effective in-plane nearest-neighbors [Fig. 2.5, J_{1a} and J_{1b}], next-nearest-neighbor [Fig. 2.5, J_2], and out-of-plane (J_c) exchange

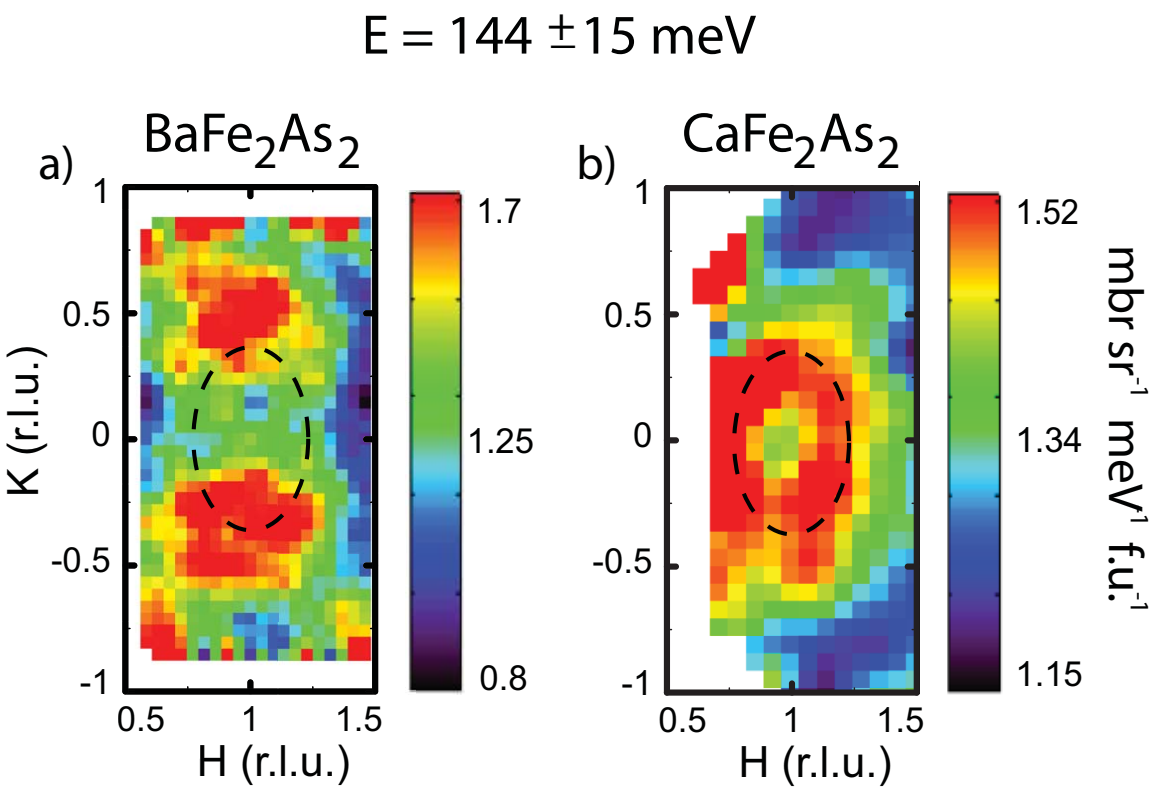

Figure 2.1: a) Constant energy cuts of the spin wave excitations at 7K for $BaFe_2As_2$ and $CaFe_2As_2$ in absolute units within the first Brillouin zone. The data for $CaFe_2As_2$ and $BaFe_2As_2$ are from Ref. [40] and [144] respectively.

interactions. The dispersion relations are given by

$$E(q) = \sqrt{A_q^2 - B_q^2} \tag{2.1}$$

with

$$\begin{aligned} A_q &= 2S\{J_{1b}[\cos(\pi K) - 1] + J_{1a} + J_c + 2J_2 + J_s\} \\ B_q &= 2S[J_{1a}\cos(\pi H) + 2J_2\cos(\pi H)\cos(\pi K) + J_c\cos(\pi L)] \end{aligned} \tag{2.2}$$

here J_s is the single ion anisotropy constant, and q the reduced wave vector away from the AF zone center. The neutron scattering cross section can be written as

$$\frac{d^2\sigma}{d\Omega dE}\frac{k_f}{k_i}\left(\frac{r_0}{2}\right)^2 f^2(Q)e^{-2W}\sum_{\alpha\beta}(\delta_{\alpha\beta} - Q_\alpha Q_\beta)S^{\alpha\beta}(\mathbf{Q}, E) \tag{2.3}$$

$(r_0/2)^2 = 72.65mb/sr$, g is the g factor ($\approx$2), $f(Q)$ the magnetic form factor of iron Fe^{2+}, e^{2W} the Debye-Waller factor ($\approx$ 1 at 10 K), Q_α the α component of a unit vector in the direction of $\mathbf{Q}$, $S^{\alpha\beta}(\mathbf{Q}, E)$ the response function that describes the $\alpha\beta$ spin-spin correlations, and k_i and k_f incident and final wave vectors of the neutron, respectively. Assuming that only the transverse correlations contribute to the spin-wave cross section, and finite excitation lifetimes can be described by a damped simple harmonic oscillator with inverse lifetime Γ, we have

$$S_{yy}(\mathbf{Q}, E) = S_{zz}(\mathbf{Q}, E) = S_{\text{eff}} \frac{(A_q - B_q)}{E_0(1 - e^{E/k_{BT}})} \frac{4}{\pi} \frac{\Gamma E E_0}{(E^2 - E_0^2)^2 + 4(\Gamma E)^2} \tag{2.4}$$

where k_B is the Boltzmann constant, E_0 the spin-wave energy, and S_{eff} the effective spin. In general, the Heisenberg model forms a cone like dispersion propagating out of the AFM wave vector that folds over at the zone boundary (see Fig. 1.4 e). As a result the in-plane scattering forms ellipses centered around Q_{AFM} that grow larger with increasing energy transfer. In $CaFe_2As_2$ this is exactly what was observed and the above model was used with great success to fit the intensity across all of $(\mathbf{Q}, E)$ Fig. 2.2 [144]. Although the low energy excitations in $BaFe_2As_2$ below 100meV also form similar rings, above this energy transfer the excitations break apart into two separate regions of scattering that then translate along the K-direction with increasing energy transfer until finally forming a ring around the zone boundary at $(1, 1)$ along with equivalent scattering regions from the twin domain (Fig. 2.3).

A staightforward way to interpret these data is to assume that spin waves along the $(1, 0)$ direction are heavily damped and no longer observable for $BaFe_2As_2$. Assuming isotropic spin wave inverse lifetime Γ, we were unable to find any effective exchange couplings that will describe the entire spin wave spectra as shown in Fig. 2.3. To resolve this problem, we have used an anisotropic spin wave damping Γ assuming

$$\Gamma(H, K) = \Gamma_0 + \Gamma_1 E + A[\cos(\frac{\pi H}{2})]^2 + B[\cos(\frac{\pi K}{2})]^2 \tag{2.5}$$

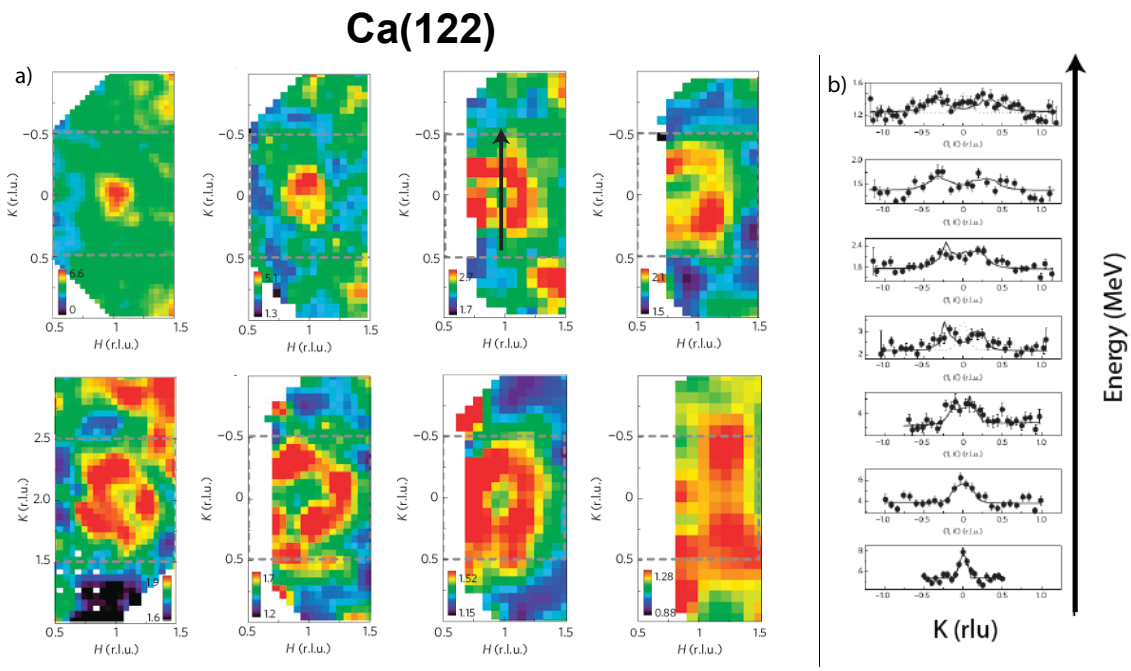

Figure 2.2: a) 2D Constant-energy slices of spin wave data in $CaFe_2As_2$. Each consecutive panel shows a slice at a higher energy transfer. At energies below 50meV (top left panel) the scattering is centered at the AFM wave vector, as the energy transfer increases the scattering spreads out into well formed ellipses that track the cone like dispersion of spin waves. Upon approach of the zone boundary at 175meV (bottom right panel) the scattering becomes very diffuse with maxima at the zone edge. The third panel in the top row includes an arrow showing the direction that 1D cuts were made in b) The lines overplotting the data in b) are global fits to the Heisenberg model described in the text with a Q-isotropic damping $\Gamma = \Gamma_0 + (\text{slope}) \cdot E$ [144].

where A and B are parameters controlling the magnitude of the spin wave damping. For the best fit to the spin wave data, we have $\Gamma_0 = 32 \pm 10.6$, $\Gamma_1 \to 0$, $A = 51.9 \pm 9.0$, $B = 27.8 \pm 7.3$ with magnetic exchange couplings as listed elsewhere in the main text.

In general, the spin wave cross-section is resolution limited (ie: spin waves propagate with infinite lifetime) for a fully local moment system where the Heisenberg model is the true microscopic Hamiltonian describing the physics of the system. This is observed in the Cuprates everywhere in (Q, E) except at $(1/2, 0)$ [44] where the spin waves were predicted prior to measurement to decay into spin 1/2 quasiparticles at sufficiently high energy (Fig. 1.4 b,d) due to the coexistence of the Neel order with

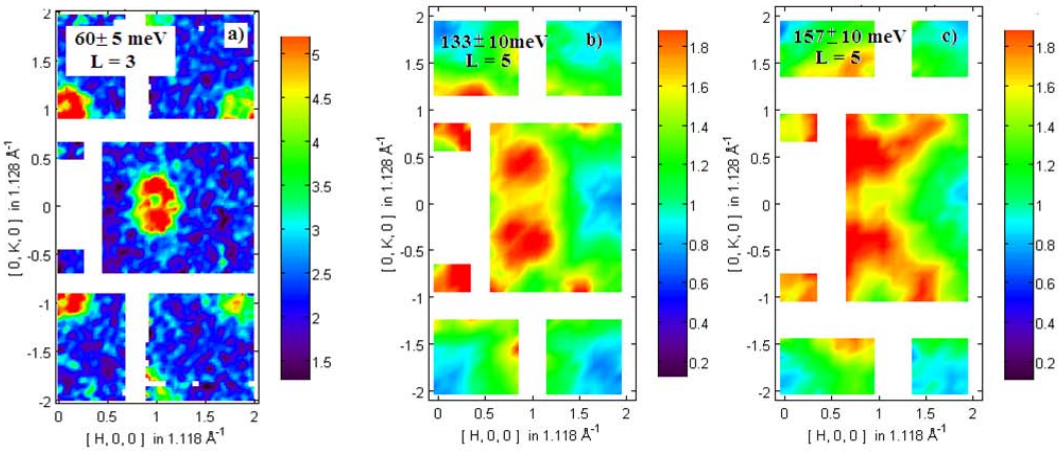

Figure 2.3: Constant energy slices of the 7K spin wave data for $BaFe_2As_2$. a) At lower energies the scattering forms an ellipse centered around the AFM wave vector much like $CaFe_2As_2$. b) At intermediate energy transfers the scattering breaks apart along the H-direction to form two mirror image rods (ie: L independent) of scattering above and below the H-axis. These rods translate along the K-direction with increasing energy transfer. c) At high energies the scattering combines with contributions from twinned domains to form a ringlike excitation about the zone boundary. Above the zone boundary (not shown) the scattering stretches out in a long damping tail and fills in to form a single center of scattering at (1,1).

other magnetic correlations not captured by spin wave theory [1, 106, 46]. Due to the itinerant nature of the pnictides it is expected that electron-electron interactions will create multiple decay paths for the spin waves at all (Q, E). For $CaFe_2As_2$ it was sufficient to replace the spin wave delta function in the cross-section with a damped harmonic oscillator and use a damping Γ that was isotropic in Q but grew linearly with increasing energy. For a given 2D (H, K) constant-energy slice, this damping takes the elliptical pattern of scattering and smears it isotropically so that the overall structure of the scattering is preserved but only broader. Since $BaFe_2As_2$ damps much heavier along H, the isotropic form failed and we were require to incorporate an anisotropic damping. The form chosen was purely empirical and consisted of appending to the original isotropic damping $\Gamma_0 + \Gamma_1 E$ two new terms whose form was chosen to be as

simple as possible within the restrictions that it satisfy the periodicity of the magnetic scattering and take only non-negative values: $A[\cos(\frac{\pi H}{2})]^2 + B[\cos(\frac{\pi K}{2})]^2$. Surprisingly, even this very simplistic inclusion of damping anisotropy resulted in dramatically better fits of the data. Comparison of Fig. 2.3 and Fig. 2.5 c) demonstrates how the ring like scattering is broken up and follows an identical pattern as observed in our data when this anisotropic damping is included. Although our form for the

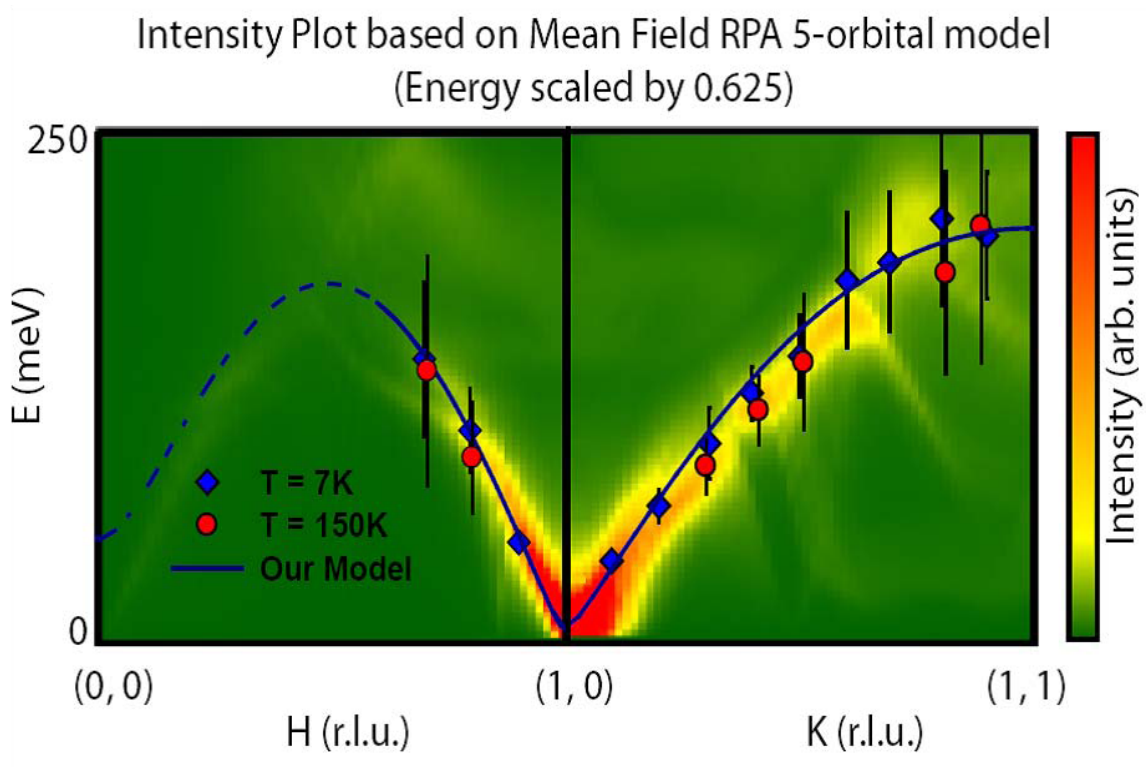

Figure 2.4: a) Comparison of a normalized RPA calculation from Ref. [52] and our data. Given the normalization correction, RPA appears to fit the data.

anisotropic damping is completely empirical, the origin can be understood in terms of excitations across the Fermi surface. Recent RPA calculations (Ref. [52]) of the particle-hole excitation spectrum reveal that these excitations are also anisotropic; however, they are suppressed below 200 meV due to a partially opened gap in the density of states at the Fermi energy. In $BaFe_2As_2$, we found experimentally that the anisotropic damping switches on around 100 meV. This would imply that the

200-meV pseudogap is overestimated by about a factor of two in their study. Thus, by renormalizing the particle-hole excitation spectrum to this experimental threshold value and taking the damping intensity to be in correspondence with this particle-hole spectrum, it may be possible to replace our phenomenological damping function with a more theoretically sound counterpart. To test this relationship, the energy of the RPA calculation was scaled by 0.6, and the spin-wave band intensity was determined along the H and K directions. Upon direct comparison with our data, we find that both the dispersion and anisotropic intensity are in excellent agreement with theory (see Fig. 2.4). Hence, this implies that the pseudogap in the density of states strongly influences the observed spin-wave scattering. Indeed, in $CaFe_2As_2$, a similar threshold value of 100 meV was originally determined but with strong Q-isotropic damping $\Gamma(E)$ appearing above this energy (Ref. [24]), leading the authors to conclude that the pseudogap may have provided a low energy window for the formation of local moment excitations that can be well described by the Heisenberg model, but that above this value the excitations quickly evolved into a Stoner picture. Later studies on $CaFe_2As_2$ revealed that well-defined spin-waves could still be observed out to the zone boundary, thereby ruling out a quick evolution into a Stoner continuum above 100 meV (Ref. 7). Nonetheless, both studies support an increase in itinerancy as a function of energy, consistent with the idea that the pseudogap drives a transition from local moment to itinerant physics, but with particle-hole excitations favoring the AF direction. Since no damping anisotropy was observed in $CaFe_2As_2$, it is possible that the pseudogap is larger than the spin-wave bandwidth in this system. As a result only Q-isotropic damping from electron-magnon interactions are visible. In regards to $SrFe_2As_2$, after finishing the present work, we became aware of a related neutron scattering work on this compound, where strong magnetic anisotropy was also reported. Although the authors prefer to use an itinerant approach to interpret their data, the central conclusion is consistent with results present in our paper.

2.1.3 Resolution Convolved Model Fitting

Describing our data with an effective Heisenberg model required fitting simultaneously 11 parameters: Intensity I, the in-plane nearest neighbor exchange coupling J_{1a}, the in-plane next nearest neighbor exchange coupling J_{1b}, the in-plane next next nearest neighbor exchange coupling J_2, the out of plane exchange coupling J_c, the anisotropy gap J_s, the linear coefficients for an isotropic damping contribution Γ_0 and Γ_1, the trigonometric coefficients for an anisotropic damping contribution A and B, and finally a possible additional gap parameter appended to the dispersion Δ. Due to this exceedingly large number of parameters, it would be extremely time intensive and virtually impossible to run fits based on random starting parameters. This is exacerbated by the fact that each fit is performed globally over approximately 50 cuts through S(Q,E) all of which must be convolved with the instrument resolution in advance. To manage this task, the fitting was carried out systematically from three different starting points. The control flow for each process is shown in Fig. 2.6 and are labeled as A, B, and C. To begin, an unconvolved model was built in Matlab that allowed all parameters to be fixed but one. The model could then run as a movie where each frame corresponded to a slight increase in this free parameter. In this way, it was possible to get an overview on how each parameter effected the model. This approach, corresponding to Route B in the control flow, allowed us to get a first estimate of parameters from scratch. As well, it was discovered that J_s has virtually no effect on the model. As a result, this parameters value was set to the value of J_s = 0.084 meV determined by an earlier group studying powders up to ≈100meV [26]. Also, the gap parameter Δ only effected the scattering at extremely low energies, and as such, had little effect on the exchange couplings whose values were governed by scattering over a much larger range of energies. Moreover, the model is often written excluding this gap parameter and since our time of flight data was mostly lacking in the range where this value contributed the most we began by setting it to $\Delta = 0$. After the full analysis had been done, this parameter was then freed up at multiple

Figure 2.5: (Figure on next page.) a) The AF Fe spin ordering in $BaFe_2As_2$ with the magnetic exchange couplings J_{1a} , J_{1b}, J_2 along different directions. b) Temperature dependence of the resistivity in detwinned $BaFe_2As_2$ (from Ref. [12]). The inset is a plot of the resistivity for the twinned sample used in our neutron measurements with the blue points corresponding to T = 7, 125, and 150 K. (c) Color plots describing qualitatively how the spin wave scattering evolves from Q = (1, 0) to (1, 1) as a function of energy using an anisotropic damping Γ. The solid black contours are an overlay of the same model with identical exchange coupling parameters but with no damping. The exchange couplings used are from best fits of the data. d) Color plot of the anisotropic damping Γ, which is much stronger along the H direction than along the K direction. (e) Spin wave dispersion along the (1, K) direction as determined by energy and Q cuts of the raw data below and above T_N. The solid line is a Heisenberg model calculation using anisotropic exchange couplings $SJ_{1a} = 59.2 \pm 2.0$, $SJ_{1b} = -9.2 \pm 1.2$, $SJ_2 = 13.6 \pm 1.0$, $SJ_c = 1.8 \pm 0.3$ meV determined by fitting the full cross-section. The dotted line is a Heisenberg model calculation assuming isotropic exchange coupling $SJ1a = SJ_{1b} = 18.3 \pm 1.4$, $SJ_2 = 28.7 \pm 0.5$, and $SJ_c = 1.8$ meV. f) Dispersion along the (H, 0) direction; data points beyond H = 1.4 could not be reliably obtained due to strong damping at higher energies. The red shading stresses how the damping grows as a function of H. Error bars are systematic and represent the difference between Q and E cut dispersion points. The statistical error of the Q and E cuts are much smaller.

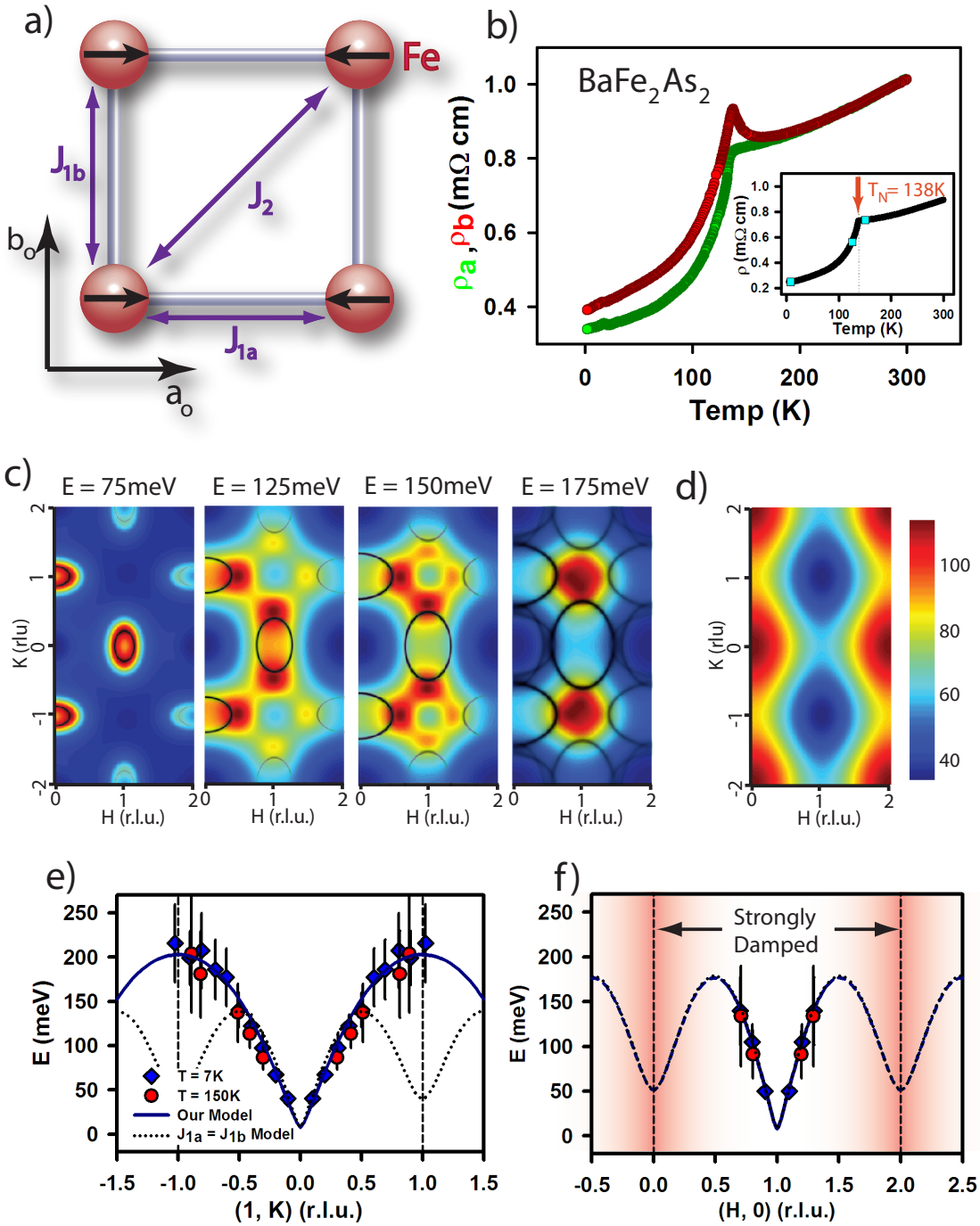

Figure 2.5: Caption on previous page.

steps in the fitting procedure and we discovered that the convergence of χ^2 was only improved by 1%. Thus, we chose to discard the very small χ^2 reduction in favor of a simplified model with one less parameter.

To handle the remaining 9 parameters, the fitting procedure was broken up into two parts. First, dispersions were extracted from Q-cuts (Route A) and E-cuts (Route C) along both the high symmetry (H,0) and (1,K) directions. Since the dispersions are intensity and damping independent, this allowed us to perform unconvolved global fits of them using only the 4 exchange couplings as free parameters. The exchange couplings determined from earlier powder measurement up to ≈100meV on $BaFe_2As_2$ [26] were used as starting parameters. This was cross-checked using the exchange couplings on single crystals of $CaFe_2As_2$ up to ≈200 meV as the starting parameters. Both sets of starting parameters converged to the same values. These dispersion fitted exchange couplings were then passed back into the unconvolved Matlab model and estimates of the intensity, J_c, and damping coefficients were determined by hand. In this way, it was possible to put together three sets of starting parameters to use in the resolution convolved fitting that was carried out globally over the approximately 50 cuts: starting parameters based primarily on A) E-cut dispersions, B) Estimations by hand, C) Q-cut dispersions. Tobyfit was used to carry out the final resolution convolved fitting in each case. It was found that Route A and B gave almost identical results while Route C converged to a different best fit with a higher χ^2. It was expected in advance that the starting parameters based off of Q-cut dispersions would lead to a poorer fit since Q-cuts cannot resolve the roll-over of the dispersion at the zone boundary due to a large damping tail that extends up to 300meV. Fitting parameters from route A were chosen as our reporting values since they corresponded to the fitting path that relied on the least adjustments by hand. Figs. 2.7a) - e) show two-dimensional constant-energy (E) images of spin-wave excitations of $BaFe_2As_2$ in the (H, K) scattering plane for several Brillouin zones at L = 1, 3, 5, and 7. For energy transfers of $E = 26 \pm 10$ [Fig. 2.7 a)] and 81 ± 10 meV [Fig. 2.7 b)], spin waves are still peaked at Q = (1, 0) in the center of the Brillouin zone, shown as

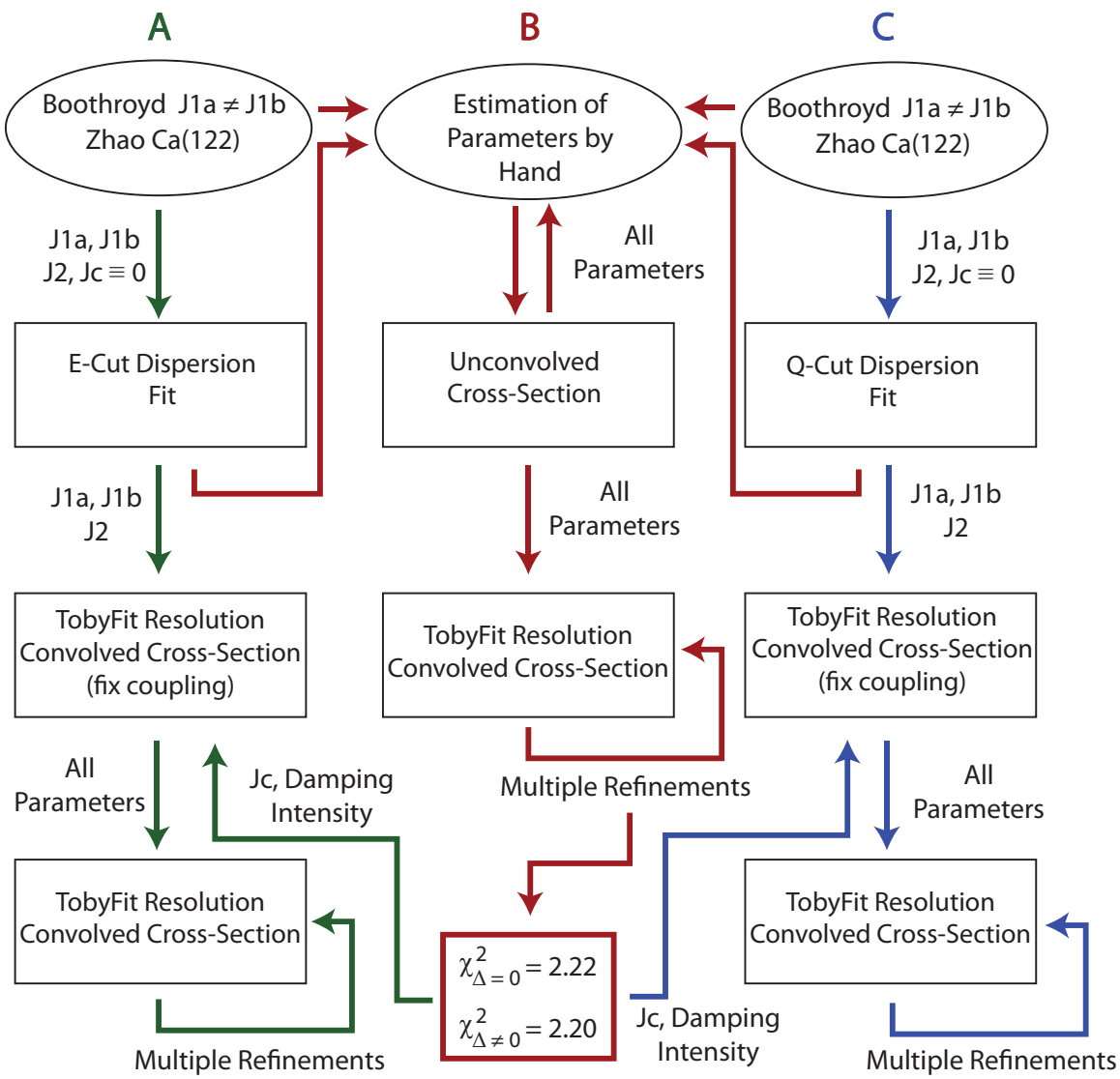

Parameters of Best Fit

Route	Int	J1a	J1b	J2	Jc	Δ	Γ_0	Γ_1	A	B	χ^2
A	248.1	59.2	-9.26	13.6	1.85	0	32.0	0.01	51.9	27.8	2.22
A	267.8	56.8	-11.9	11.4	0.47	9.1	32.0	0.01	51.9	27.8	2.20
B	242.1	57.7	-8.64	14.0	1.72	0	27.0	0.01	52.5	30.8	2.22
B	260.8	56.9	-11.0	12.1	0.63	7.0	29.1	0.01	52.5	30.8	2.20
C	293.5	64.5	-16.0	10.5	3.73	0	85.9	0.01	55.8	-17.5	2.53
C	338.9	66.6	-26.0	3.65	0.18	18.6	85.9	0.01	55.8	-17.5	2.46

Figure 2.6: Control flow describing the three fitting paths and starting parameters used to determine the final parameters of best fit for the anisotropic Heisenberg model used. Details about each route are described in the text.

Figure 2.7: (Figure on next page.) Wave vector dependence of the spin waves for energy transfers of (a) $E = 26 \pm 10$ meV [$E_i = 450$ meV and Q = (H, K, 1)]; (b) $E = 81 \pm 10$ meV [$E_i = 450$ meV and Q = (H, K, 3)]; (c) $E = 113 \pm 10$ meV [$E_i = 450$ meV and Q = (H, K, 5)]; (d) $E = 157 \pm 10$ meV [$E_i = 600$ meV and Q = (H, K, 5)]; e) $E = 214 \pm 10$ meV [$E_i = 600$ meV and Q = (H, K, 7)] f) The projection of the spin waves on the energy transfer axis and (1, K) direction (with integration of H from 0.8 to 1.2 rlu) after subtracting the background integrated from $1.8 < H < 2.2$ and from $-0.25 < K < 0.25$ with $E_i = 450$ meV. The color bar scales represent the absolute spin wave intensity in units of mbarn·sr^{-1}·meV^{-1}·f.u.$^{-1}$ and the dashed boxes indicate zone boundaries. The missing low-energy data in (f) is due to imperfect data subtraction. (g)-(l) Model calculation of identical slices as in (a)-(f) using anisotropic exchange couplings from best fits and convolved with the instrumental resolution.

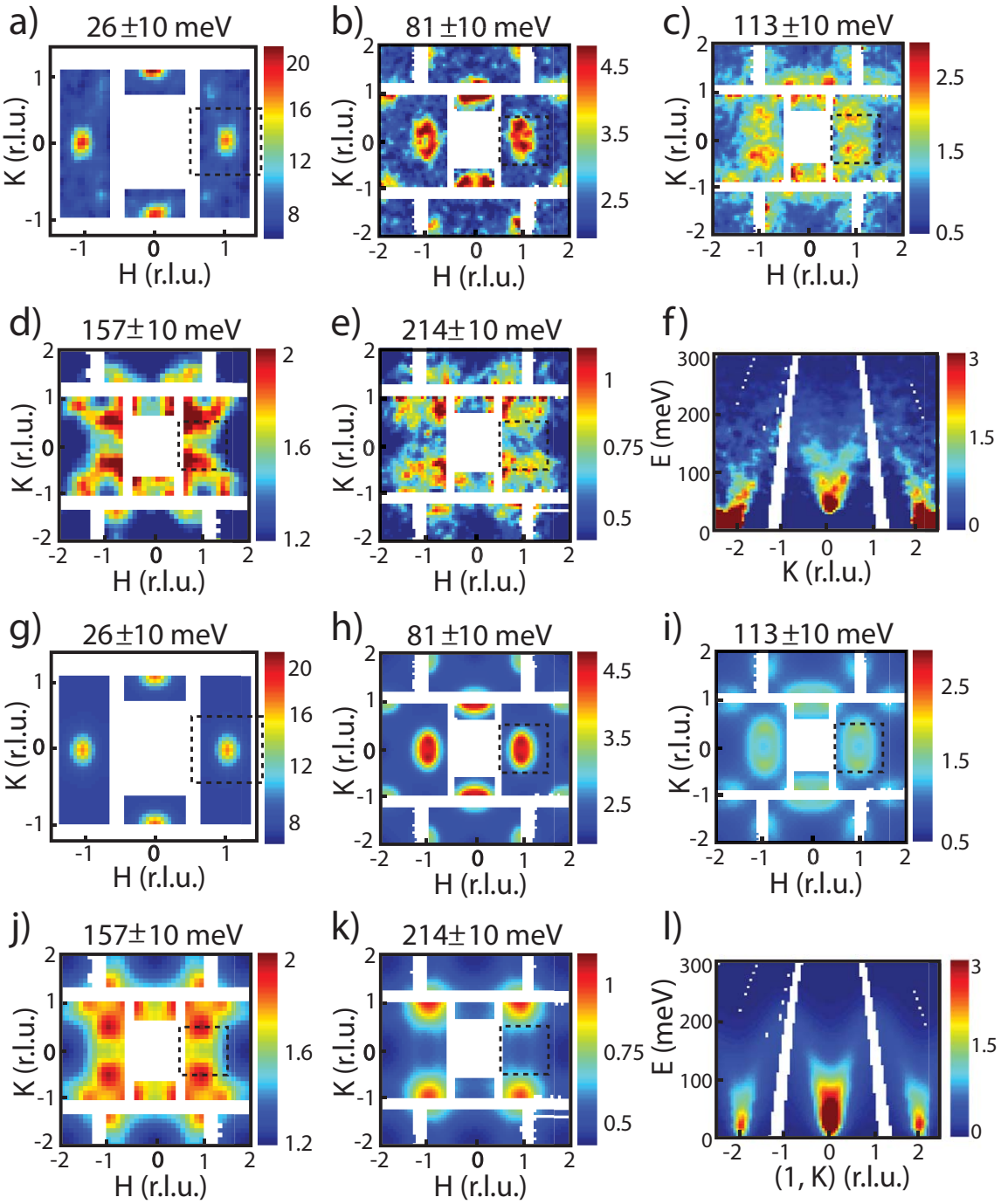

Figure 2.7: Caption on previous page.

dashed square boxes. As the energy increases to $E = 113 \pm 10$ [Fig. 2.7 c)], 157 ± 10 [Fig. 2.7 d)], and 214 ± 15 meV [Fig. 2.7 e)], spin waves no longer form ellipses centered around Q = (1, 0). Instead, they start to split along the K direction and form an anisotropic and asymmetric ring around $Q = (\pm 1, \pm 1)$, in stark contrast with the spin waves at similar energies seen in $CaFe_2As_2$ [Fig. 2.2 a)]. To understand the low-temperature spin waves in $BaFe_2As_2$, we cut through the two-dimensional images similar to Fig. 2.2. Figures 2.5 e) and f) show spin wave dispersions along the (1, K) and (H, 0) directions, respectively. Figure 2.7 f) shows the background subtracted scattering for the $E_i = 450$ meV data projected in the wave vector (Q = [1, K]) and energy space. Similar to spin waves in $CaFe_2As_2$ [144], we can see three clear plumes of scattering arising from the in-plane AF zone centers Q = (1, -2), (1, 0), and (1, 2) extending up to about 200 meV. After failing to fit the entire spin wave spectra in Fig. 2.7 using a Heisenberg Hamiltonian with an isotropic spin wave damping parameter Γ [black curves in Fig. 2.5 c)] we included the anisotropic spin wave damping discussed above [Fig. 2.5 d)] that produced an energy dependence of the spin wave profiles [color plots in Fig. 2.5 c)] that is qualitatively similar to what we observe [Figs. 2.7 a)-e)]. Using the Q-dependent damping Γ(H, K), we were able to fit the entire measured spin wave excitation spectra in absolute units by convolving the neutron scattering spin-wave cross section with the instrument resolution. The effect of twin domains is taken into account by a/b averaging. Consistent with earlier results on $CaFe_2As_2$ [144], we find that the Heisenberg Hamiltonian with $SJ_{1a} \approx SJ_{1b} \approx \frac{1}{2}SJ_2$ fails to describe the zone boundary data [Fig. 2.5 e)]. Our best fits to both the low-energy and zone boundary spin waves are shown as solid lines in Fig. 2.5 e), f) and color plots in Fig. 2.7 g) - l) with $SJ_{1a} = 59.2 \pm 2.0$, $SJ_{1b} = 9.2 \pm 1.2$, $SJ_2 = 13.6 \pm 1.0$, and $SJ_c = 1.8 \pm 0.3$ meV. Comparing the above fitted results for $BaFe_2As_2$ with those for $CaFe_2As_2$, we see that while the in-plane effective magnetic exchanges (SJ_{1a}, SJ_{1b}) are very similar in these two materials, there is 30% reduction in SJ_2 when Ca is replaced by the larger Ba and the c-axis exchange coupling is reduced considerably (from $SJ_c = 5.3 \pm 1.3$ meV for $CaFe_2As_2$). In brief, while one can see clear spin

wave ellipses centered around Q = (1, 0) in $CaFe_2As_2$ at all energies, spin waves in $BaFe_2As_2$ are heavily damped along the a-axis direction and become hardly observable for energies above 100 meV, consistent with the random phase approximation (RPA) calculations discussed earlier [52]. This leads to very different scattering profiles between these two parents. However, despite their distincly different patterns, the same model can be used after inclusion of an anisotropic damping with the final exchange couplings that are quite similar in the two systems.

2.1.4 Magnetic Excitation across the Phase Transition; 125K and 150K

Having demonstrated that $BaFe_2As_2$ exhibits a large spin anisotropy in the low temperature orthorhombic, magnetically ordered phase (LTO), it is important to determine if this spin anisotropy also exists in the high-temperature tetragonal phase, where the underlying crystal lattice structure has C4 rotational symmetry. In a recent work on $CaFe_2As_2$, spin excitations in the paramagnetic tetragonal phase were found to have a similar spatial line shape as those of the low-temperature spin waves below 60 meV (Ref. [23]). These anisotropic short-range AF fluctuations can be interpreted as frustrated paramagnetic scattering. If the observed large anisotropy of SJ_{1a} and SJ_{1b} for $BaFe_2As_2$ (Figs. 2.5 and 2.7) and $CaFe_2As_2$ (Ref. [144]) in the LTO phase becomes isotropic ($SJ_{1a} = SJ_{1b}$) in the paramagnetic tetragonal phase, one would expect a huge softening of the zone boundary spin waves upon entering into the tetragonal phase [see dotted lines in Fig. 2.5(e)], which we do not observe. Figure 2.8 summarizes the temperature dependence of the spin wave excitations at temperatures of $0.05T_N$, $0.93T_N$, and $1.09T_N$. For spin wave energies of $E = 50 \pm 10$ and 75 ± 10 meV, we confirm the earlier result [23] on $CaFe_2As_2$ and find that spin excitations above T_N are weaker and broader than the spin waves below T_N [Figs. 2.8(a) - (f)]. However, spin waves at energies of $E = 125 \pm 10$ and 150 ± 10 meV have virtually no temperature dependence of their intensity and line shape across

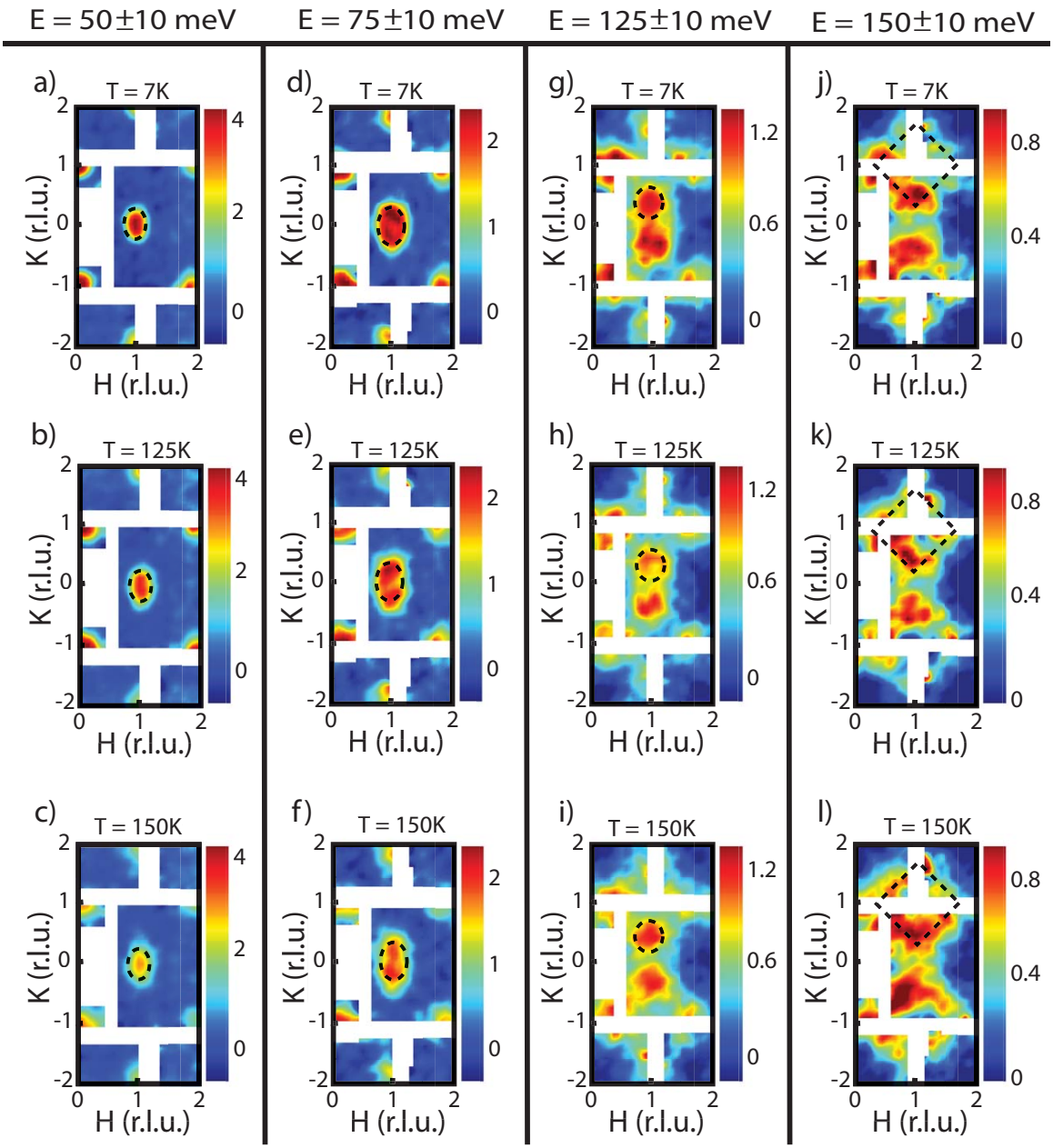

Figure 2.8: (a)-(c) Spin waves of $E = 50 \pm 10$ meV; (d)-(f) $E = 75 \pm 10$ meV; (g)-(i) $E = 125 \pm 10$ meV; and (j)-(l) $E = 150 \pm 10$ meV for temperatures of T = 7, 125, and 150 K. The dashed curves show fixed reciprocal space sizes at different temperatures.

the AF orthorhombic-to-paramagnetic tetragonal phase transition [Figs. 2.8(g) - (l)]. Therefore, spin excitations near the zone boundary do not exhibit huge softening in the paramagnetic state, which implies that the large in-plane exchange anisotropy persists above T_N without spin frustration. To test whether the observed scattering above T_N indeed arises from localized spin excitations similar to the spin waves below T_N and not from paramagnetic scattering centered at zero energy, we carried out energy cuts of the spin excitations at different positions of the dispersion, as shown in the inset of Fig. 2.9(a).

Near the Brillouin zone center at Q = (1, 0.05) and (1, 0.2), well-defined spin waves are observed at E = 32 and 50 meV, respectively [blue diamonds in Figs. 2.9(a) and (b)], in the AF ordered state. Upon warming to the paramagnetic tetragonal state $T = 1.09T_N$, the spin wave peaks disappear, and spin excitations become purely paramagnetic with their highest intensity centered at zero energy [red circles in Figs. 2.9(a) and (b)]. Moving closer to the zone boundary at Q = (1, 0.35), the spin wave peaks at 90 meV are virtually unchanged on warming from $0.05T_N$ to $0.93T_N$ and decrease only slightly in intensity at $1.09T_N$ [Fig. 2.9(c)]. At Q=(1, 0.5), spin wave peaks at E=125 meV are temperature independent below and above T_N [Fig. 2.9(d)]. Figures 2.9(e) and (f) show the Q-dependence of the magnetic scattering at $E = 19 \pm 5$ and 128 ± 5 meV, respectively. Consistent with Fig. 2.8, the spin waves at low energies become broad paramagnetic spin excitations above T_N, while they stay unchanged at high energies near the zone boundary [Figs. 2.9(e) and (f)]. The energy dependence of the dynamic spin-spin correlation lengths below and above T_N in Fig. 2.9(g) suggests that short-range spin excitations at energies above $\sim$ 100 meV are not sensitive to the orthorhombic-to-tetragonal phase transition and do not reflect the C4 symmetry. The effective magnetic exchange couplings SJ_{1a} and SJ_{1b} in spin clusters of sizes $\xi = 15 \pm 3\mathring{A}$ must be anisotropic and therefore locally break the C4 tetragonal symmetry.

Figure 2.9: (Figure on next page.) The blue diamonds in (a)-(d) are constant-Q cuts at Q = (1, 0.05), (1, 0.2), (1, 0.35), and (1, 0.5), respectively, at T = 7 K. The green squares and red circles in (a)-(d) are identical constant-Q cuts at T = 125 and 150 K, respectively. The dashed lines are guides to the eye for the observed paramagnetic scattering. (e) and (f) Q dependence of the spin wave excitations below and above T_N obtained through constant-E cuts at $E = 19 \pm 5$ and 128 ± 5 meV. The solid lines in (a)-(f) are fits to the anisotropic spin-wave model discussed in the text, and the horizontal bars represent the instrumental energy (E)/wave vector (Q) resolution. (g) Energy dependence of the dynamic spin-spin correlation lengths below and above T_N obtained by Fourier transform of constant-E cuts similar to (e) and (f).

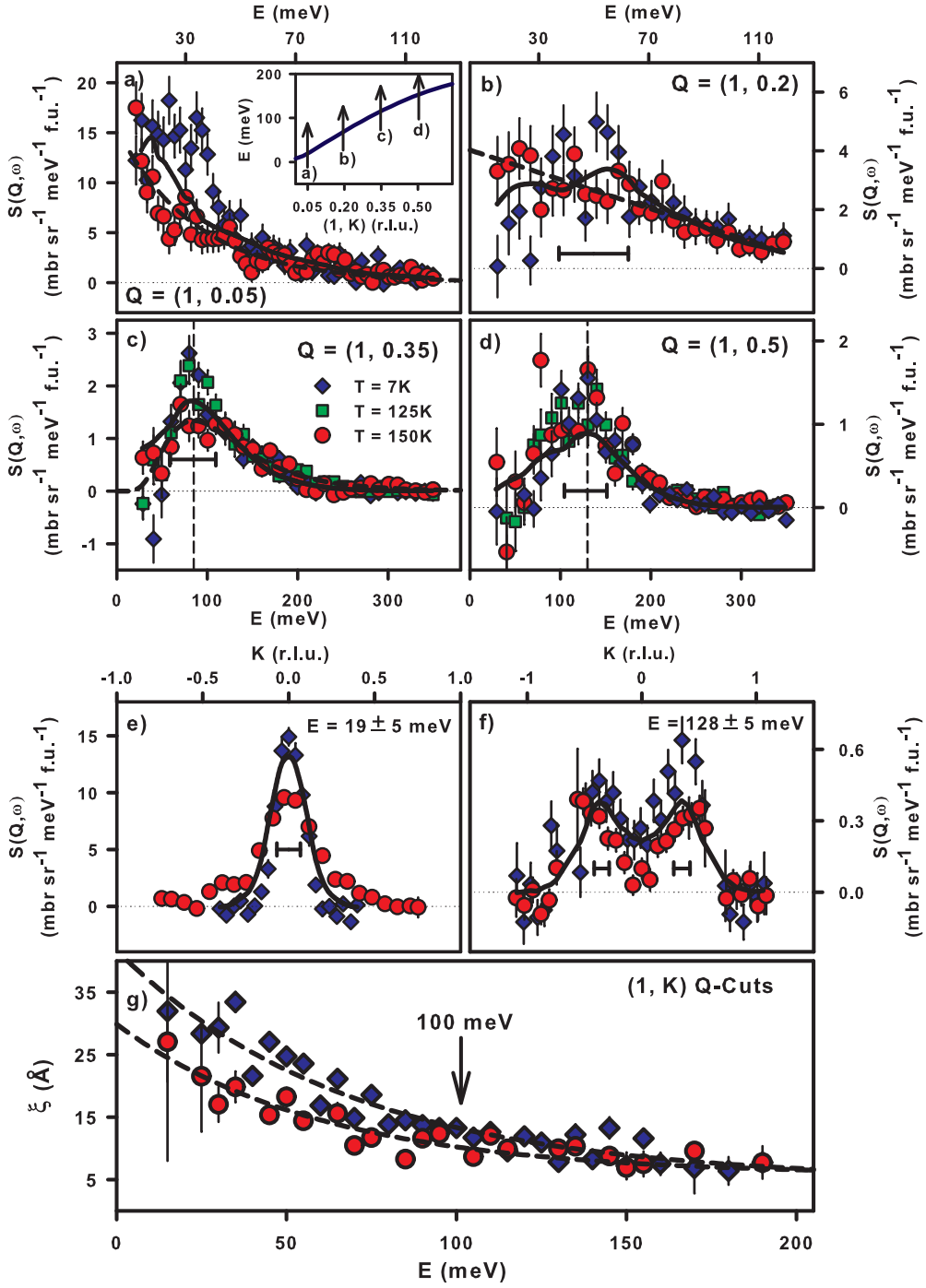

Figure 2.9: Caption on previous page.

2.1.5 Conclusion

We have discovered that the spin waves in $BaFe_2As_2$ are highly anisotropic with a large damping along the metallic AF a-axis direction in the LTO phase (Figs. 2.5 and 2.7). On warming to the paramagnetic tetragonal phase, the low-energy spin waves near the zone center evolve into paramagnetic scattering, while the anisotropy of the high-energy spin excitations near the zone boundary persists (Figs. 2.8 and 2.9). This means that the short-range effective magnetic exchange couplings in $BaFe_2As_2$ are anisotropic and unchanged across T_N, consistent with a nematic spin fluid that breaks the C4 symmetry of the tetragonal phase. In previous observations of electronic nematic phases in different materials, there is usually a symmetry breaking field present, such as an external magnetic field, uniaxial pressure, or an orthorhombic crystalline lattice,[135, 14, 12] which is not the case here. The persistence of spin anisotropy in the paramagnetic phase has obvious implications for the nature of the magnetism in pnictides, which in turn has potentially profound implications for the origin of superconductivity. Anisotropy in the resistivity has been seen to persist for Co-doped $BaFe_2As_2$ samples into the region of the phase diagram where superconductivity exists [12]. Moreover, the existence of a spin resonance in the superconducting state of Ni-doped $BaFe_2As_2$, which is a doublet rather than a triplet, is also consistent with local spin nematicity [65]. Since the spin excitations at short length scales are intrinsically nematic in the paramagnetic tetragonal phase, the AF phase transition and lattice distortion are likely induced by nematic spin fluctuations. On the other hand, if orbital ordering were driving the spin nematicity, one would expect a gradual change of spin anisotropy across T_N depending on the strength of spin-orbital coupling, contrary to our observations. Since the spin nematicity leads to an enormous anisotropy in the near-neighbor exchange couplings, this could have a profound impact on the nature of the superconducting electron pairing interaction.

Since publication of our results, there have been several studies done by separate groups offering either explanations or alternatives to spin nematic behavior in

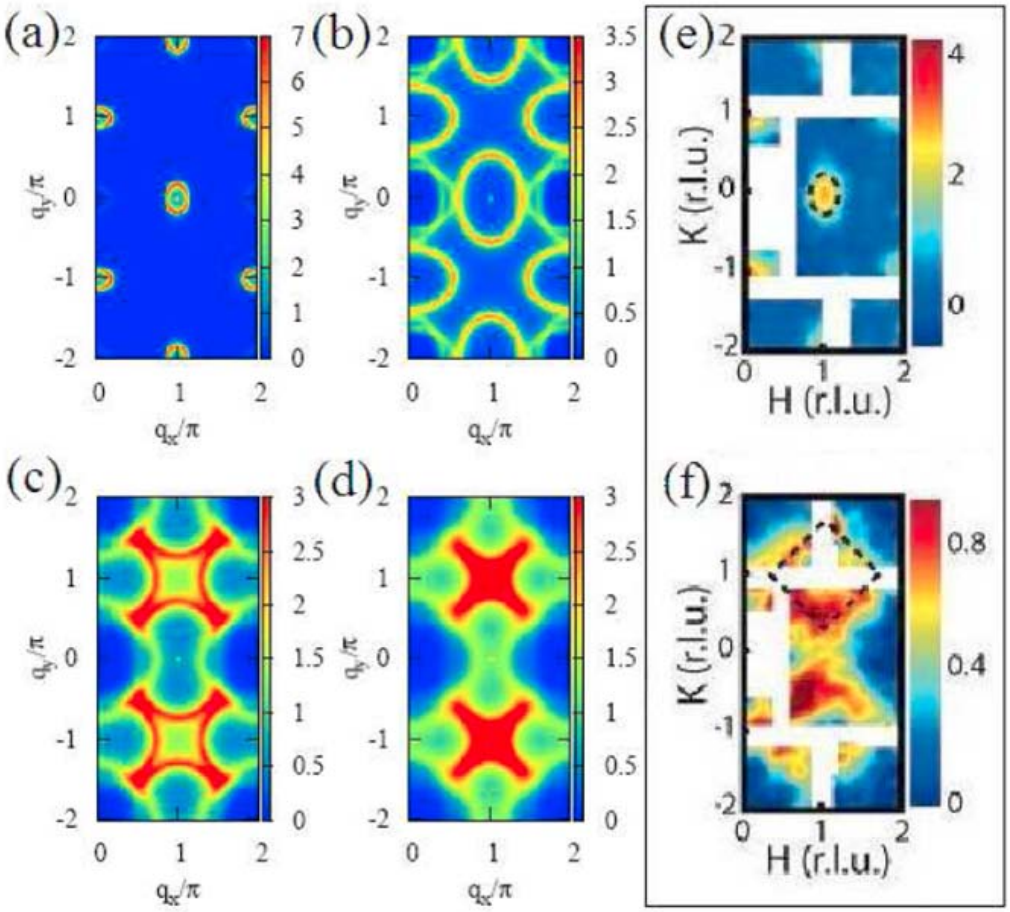

Figure 2.10: (a)-(d) Results from an isotropic $J_1 - J_2 - K$ Heisenberg model [141]. Consecutive panels are of increasing energy transfer following the dispersion of magnetic excitations from the (1, 0) zone center at low energy (panel a) to the (1, 1) zone boundary at high energies (panel d). (e) and (f) are reproductions of zone center and zone boundary data from Fig. 2.7.

$BaFe_2As_2$. Local, itinerant, and mixed states have all been selected as starting points. In terms of a local moment picture, attempts to build a Heisenberg model that respects the C4 symmetry of the lattice have met with some success by considering an isotropic J_1 and J_2 exchange but with the extra inclusion of a biquadratic exchange term[141, 133].

$$\mathscr{H} = J_1 \sum_{\langle i,j \rangle} \mathbf{S}_i \cdot \mathbf{S}_j + J_2 \sum_{\langle\langle i,j \rangle\rangle} \mathbf{S}_i \cdot \mathbf{S}_j - K \sum_{\langle i,j \rangle} (\mathbf{S}_i \cdot \mathbf{S}_j)^2 \tag{2.6}$$

where J_1 and J_2 are the nearest neighbor and next-nearest neighbor antiferromagnetic exchange couplings and K is the biquadratic exchange for nearest neighbors. As can be seen in Fig. 2.10 this model captures the most salient features of the scattering. Namely, low energy elliptical scattering centered at the (1, 0) AFM wave vector that evolves into scattering centered around the (1, 1) zone boundary at high energies. It has been shown clearly that increasing the biquadratic exchange K results in a corresponding decrease in the zone boundary softening [133]. In the absence of a biquadratic term, an anisotropic Heisenberg model is required since this reduction in zone softening is achieved via a corresponding reduction in J_{1b} towards negative values. Although both the anisotropic damping and lack of zone boundary softening are both present in this isotropic spin model, the overall in-plane profile of the scattering only roughly matches experiment. As well, there is no measure of how well the model intensity could follow the experimental intensity across all $(\mathbf{Q}, E)$. Nonetheless, this model does offer some evidence that it could be possible to build a full fitting spin model that respects the symmetry of the lattice.

The spin nematic description has also been studied starting from the itinerant end as well. Similar studies of $SrFe_2As_2$ carried out at the same time as ours by a different group also found that this system does not fit well to a $J_{1a} - J_{1b} - J_2$ model when only isotropic damping is considered [27]. In our study we retained the local moment model and included an anisotropic damping to fix this problem; appealing to RPA for a microscopic justification in terms of an anisotropic particle

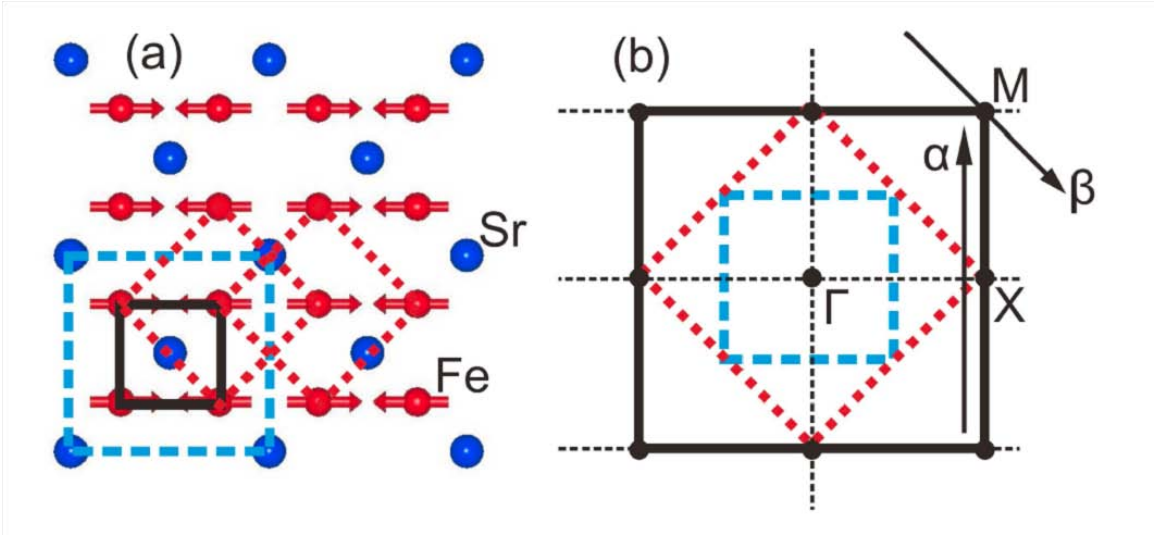

Figure 2.11: (a) Different unit cells in the real space of the crystal: Solid black is Fe sublattice required by RPA, red and blue are the tetragonal and orthorhombic cells respectively. (b) Corresponding Brillioun zones in reciprocal space. Taken from [27].

hole excitation spectra. The authors of the $SrFe_2As_2$ study preferred instead to abandon the Heisenberg model altogether in favor of an itinerant RPA description. In RPA, the calculation is carried out over the unit cell corresponding to four irons in each corner. This leads to an enlarged Brillouin zone. As a result, whereas zone boundary softening of the Heisenberg model at (1, 1) is required by symmetry when $J_{1a} = J_{1b}$, in the RPA on the Fe sublattice (1, 1) and (0, 0) do not correspond to equivalent zone centers, but, rather, inequivalent zone corner and center locations, respectively (Fig. 2.11). Thus, the softening is not a necessary symmetry requirement for itinerant magnetic scattering in the tetragonal state. Although RPA can explain unsoftened paramagnetic scattering reaching to the zone boundary, the model predicts an incommensurate signal for low energy scattering at the (1, 0) position most likely associated with the partial nesting derived from the band structure used. Furthermore, it runs afoul when attempting to account for the large spectral weight sitting at high energies. This goes back to the original problem of itinerant models

predicting total moments that are smaller than observation. Thus, mean field RPA cannot account for the full signal observed by neutrons.

Attempts to go beyond RPA have modeled the scattering in terms of dynamical mean field theory which is capable of capturing contributions from both the itinerant and localized spins within the system. From this analysis, all aspects of the neutron scattering signal were much better accounted for as shown in Fig. 2.12 and Fig. 1.8. A key point of consideration is that the interaction strength required by DFMT to reproduce the data is large enough to place it within the incoherent spectrum. As a result, this implies that there exist electron correlations strong enough to drive local moment physics within the system [83].

The nematic phase has also been explained using a mixed magnetic state consisting of an isotropic local Heisenberg Hamiltonian with the addition of a double exchange between local and itinerant electrons parameterized in terms of Hunds J and hopping t, respectively. It is then shown that this can be mapped onto a purely local anisotropic Heisenberg model similar to what we use. In this picture, the exchange coupling of the local moments are indeed anisotropic and the fact that $J_{1a} > J_{1b}$ is a byproduct of ferro-orbital ordering which leads to a much stronger double exchange coupling of itinerant and local electrons along the ferromagnetic direction [74]. It has been pointed out within this picture that the observed anisotropic magnetic exchange in our experiments does not signal a truly nematic state. All that is needed is a fluctuating nematic/orbital order. Within the correlation length, there will be a favorable nematic/orbital order (d_{xz} or d_{yz}), and consequently either $J_{1a} > J_{1b}$ or $J_{1a} < J_{1b}$. By summing over the whole sample, a C4 symmetric result is obtained, which matches the raw data of our INS experiment. The analysis of our INS result is the reverse of the above process, and the result of strong magnetic anisotropy simply follows [73].

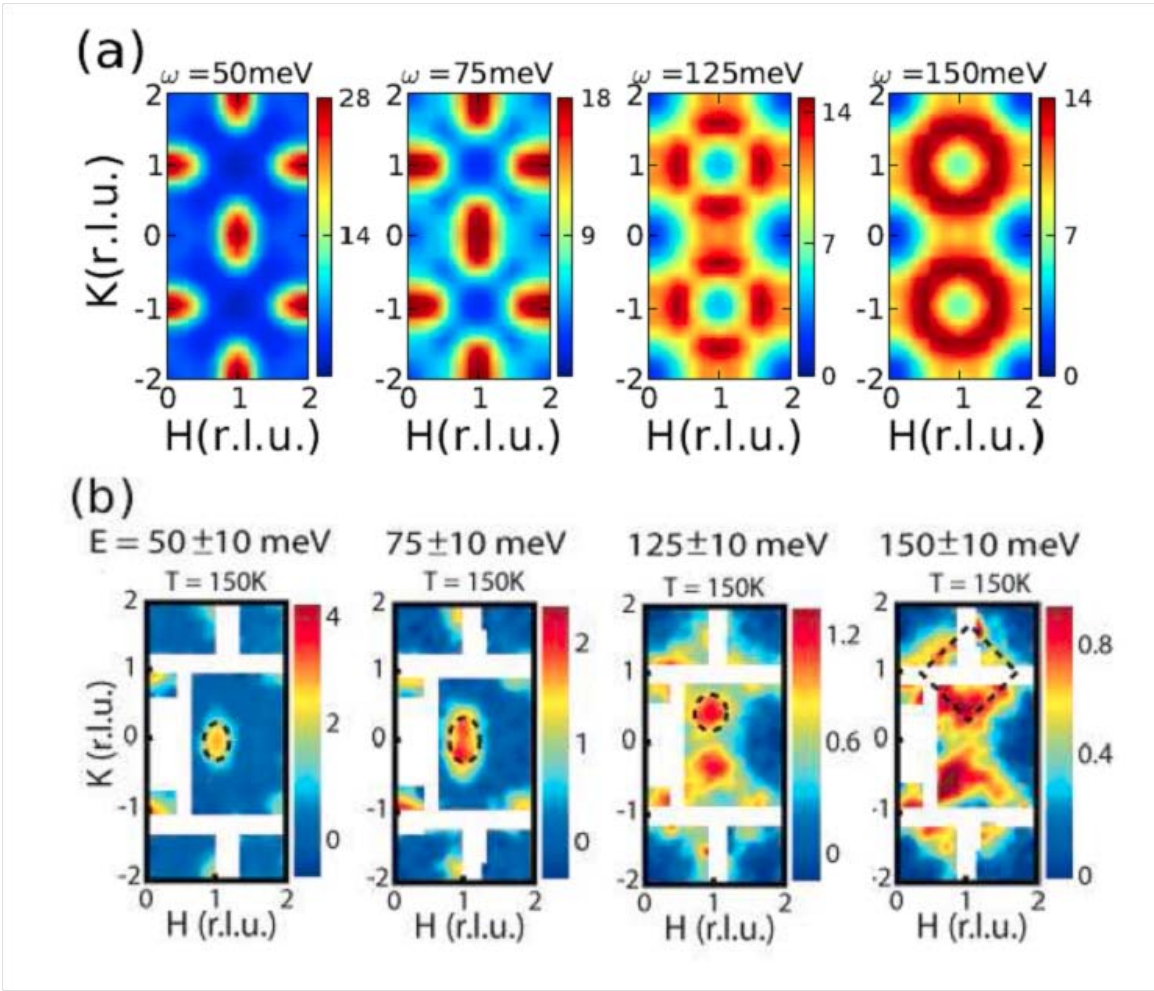

Figure 2.12: (a) Structure of scattering as a function of increasing energy based on DMFT calculations. (b) Structure of scattering from our measurement. Figure taken from [90].

2.2 Magnetic Excitations in Under Doped $BaFe_2As_2$

2.2.1 Introduction

The previous section focused on spin excitations in the superconducting parent of $BaFe_2As_2$. However, understanding the doping evolution of spin excitations is important because high-transition temperature (high-T_c) superconductivity arises from electron or hole doping the antiferromagnetic (AF) parent compounds. For undoped iron arsenides such as AFe_2As_2 (A = Ba, Sr, Ca) with a spin structure of Fig. 2.13(a), spin waves consist of a large anisotropy gap at the AF zone center and excitations extend up to ∼200 meV [40, 27, 144]. Upon doping to reach optimal superconductivity, the gapped spin wave excitations are replaced by a gapless continuum of scattering in the normal state and a neutron spin resonance below T_c [10, 9, 70, 61]. Since spin fluctuations may play a crucial role in the superconductivity of iron arsenides [82, 28, 124] it is imperative to determine the doping evolution of spin dynamics of the parent compounds. In the undoped state, $BaFe_2As_2$ exhibits simultaneous structural and magnetic phase transitions below $T_s = T_N = 143K$ [47]. Upon Co-doping to induce electrons onto the FeAs plane, the combined AF and structural phase transitions are split into two distinct transitions and the electronic phase diagram in the lower Co-doping region displays coexisting static AF order with the superconductivity [87, 13]. Although neutron scattering experiments confirmed that the upper transition is structural and the AF order occurs at a lower temperature [11, 97] it is unknown why the structural and magnetic phase transitions should be separated upon doping. More importantly, it is unclear what happens to the spin waves of $BaFe_2As_2$ when electrons are doped into these materials. At the time that I began this work, neutron scattering studies of the pnictides were just beginning to appear in the literature with the majority of the experiments focused on Co-doped samples where static AF order coexists with bulk superconductivity [11, 97]. Thus, we chose to study lightly electron-doped $BaFe_{1.96}Ni_{0.04}As_2$ (where

Ni concentration is nominal) without the influence of bulk superconductivity [Fig. 2.13(b)] [7]. Although resistivity on our $BaFe_{1.96}Ni_{0.04}As_2$ suggested $T_c \approx 15$ K [Fig. 2.13(c)], susceptibility measurement [Fig. 2.13(d)] showed a weak Meissner effect indicating a superconducting volume fraction of less than 0.2%. These results are consistent with the electronic phase diagram of $BaFe_{2-x}Ni_xAs_2$ in Fig. 2.13(b), where no bulk superconductivity heat capacity anomaly was found for $x \leq 0.05$ [7].

2.2.2 Spin Wave Scattering with 2D Character in the Ordered State

Using the self-flux method [60], we grew a ∼1 gram single crystal of $BaFe_{1.96}Ni_{0.04}As_2$ with an in-plane and out-of-plane mosaic of 1.74^o and 2.20^o full width at half maximum (FWHM, measured by doing rocking curves), respectively. We defined the wave vector Q at (q_x, q_y, q_z) as $(H, K, L) = (q_x a/2\pi, q_y b/2\pi, q_z c/2\pi)$ reciprocal lattice units (rlu) using the orthorhombic magnetic unit cell (space group Fmmm), where $a = 5.5\mathring{A}$, $b = 5.4\mathring{A}$, and $c = 12.77\mathring{A}$. We performed our neutron scattering experiment on the PANDA cold triple-axis spectrometer at the FRM II, TU Munchen, Germany. Our sample was aligned in the [H, 0, L] zone inside a closed cycle refrigerator. Since our work focused on mapping out spin excitations using a cold triple axis spectrometer, we were constrained to collecting only 1D cuts through the magnetic scattering at energies not to exceed 10meV. Thus, it was not possible to obtain the more comprehensive profile of the scattering across all of $(\mathbf{Q}, \omega)$ such as was determined in our parent study using time of flight spectroscopy. However, despite this limitation, cold triple axis provides an advantage of over time of flight in that it can collect scans at much lower energy with no spectrometer coupling of the L momentum transfer to the energy transfer. As well, there is much more freedom to move around in temperature; allowing us to collect identical scans at multiple temperatures and also sit at a specific spot in $(\mathbf{Q}, \omega)$ and collect temperature scans to determine how the scattering evolves across gaps and phase transitions.

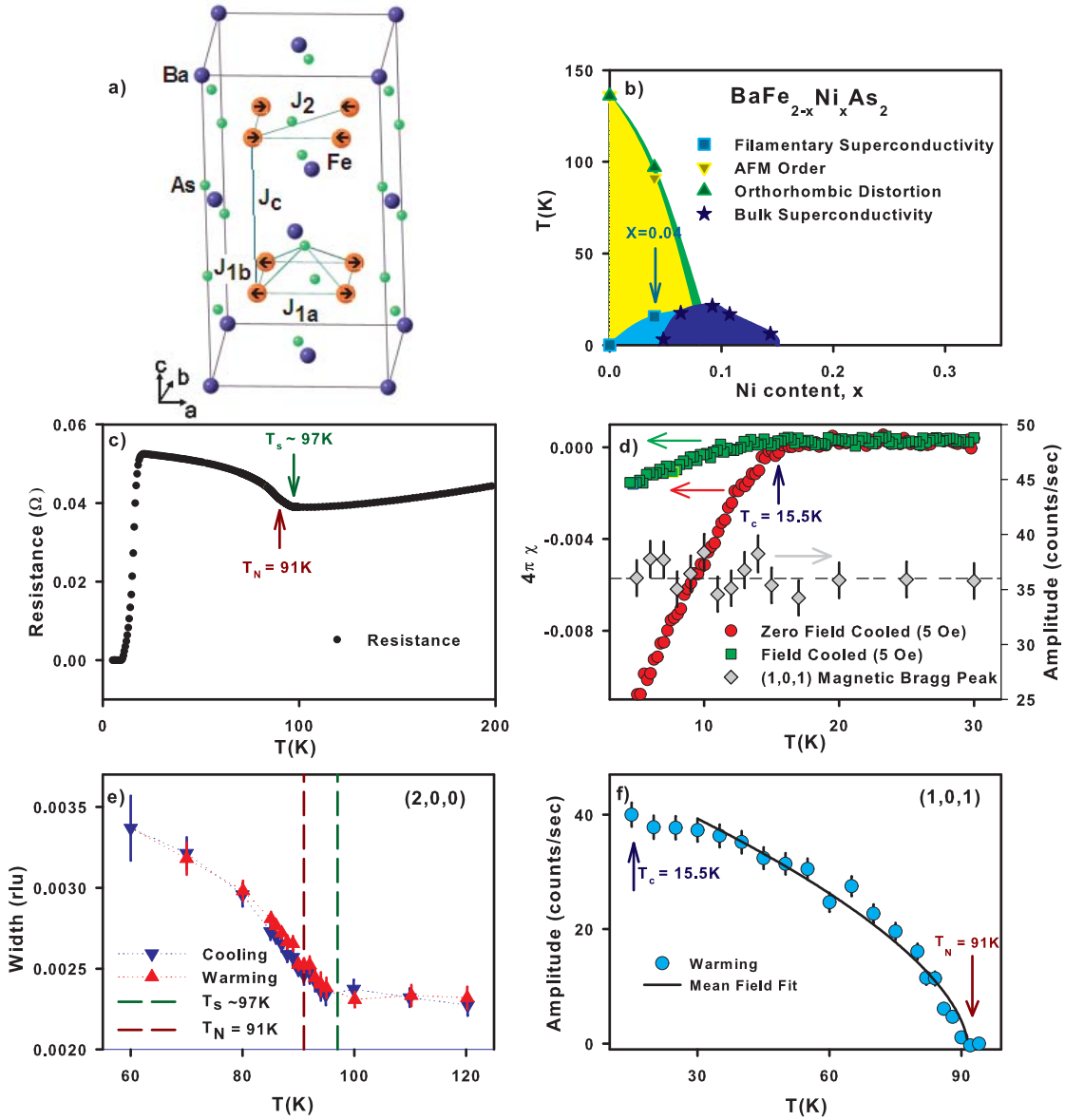

Figure 2.13: (a) Diagram of the parent compound $BaFe_2As_2$ with Fe spin ordering and magnetic exchange couplings depicted. (b) Electronic phase diagram from Ref. [7]. (c) Temperature dependence of the resistance showing anomalies at T_s, T_N, and T_c. (d) Temperature dependence of the Meissner and shielding signals on a small crystal (field cooled $4\pi\chi = -0.001$ at 4.5 K) and the (1, 0, 1) magnetic Bragg peak intensity. (e) The structural distortion of the lattice as determined by tracking the width of the (2, 0, 0) nuclear Bragg peak using $\lambda/2$ scattering without Be filter. (f) Magnetic order parameter determined by Q scans around the (1, 0, 1) magnetic Bragg peak above background. The solid line shows an order parameter fit using $(1 - T/T_N)^{2\beta}$ with $T_N = 91.3 \pm 0.7$ K and $\beta = 0.3 \pm 0.02$.

As a result, we were able to acquire a great deal of insight about the effect of doping from a very focused set scans. Specifically, we find that the effect of electron doping is to significantly reduce the c-axis exchange coupling and change the three-dimensional (3D) spin waves of $BaFe_2As_2$ into quasi two-dimensional (2D) spin waves. These results suggest that the separated structural and magnetic phase transitions in $BaFe_{1.96}Ni_{0.04}As_2$ may be associated with the diminishing spin anisotropy gap and the 3D to 2D transition of the spin excitations [43]. Since $BaFe_{1.96}Ni_{0.04}As_2$ is not a bulk superconductor [Figs. 1(b) and 1(d)] [6], it is not surprising that superconductivity has negligible influence on the static AF order [Figs. 2.13(d) and (f)]. To show that the scattering does indeed originate from spin waves associated with the long ranged magnetic ordered state, panels (a)-(d) from figures 2.14 and 2.15 compare energy scans at the (1, 0) AFM wave vector at different temperatures. After correcting for the Bose population factor, all of these scans fall on a universal line as to be expected for spin wave scattering. As a final check, we show in Fig. 2.16(a) the temperature dependence of the 1 meV scattering at the $Q = (1, 0, 0)$ (signal) and $Q = 1.4, 0, 0$ (background) positions. While the background scattering only increases slightly with increasing temperature and shows no anomaly across T_N, the scattering at $Q = (1, 0, 0)$ clearly peaks at T_N. Q scans along the [H, 0, 0] direction at 1 meV confirm these results [Fig. 2.16(c)].

Of particular interest in the scattering profile of the spin waves is the magnitude of the normal state gap. It is known that in undoped $BaFe_2As_2$, spin waves have an anisotropy gap of about 8 meV at $Q = (1, 0, 1)$ [$\Delta(1, 0, 1) = 8$ meV] [26, 79]. For optimally Co and Ni doped materials, spin excitations are gapless in the normal state [70, 9] and superconductivity induced spin gaps open below T_c [61]. Figure 2.14(a) shows the constant-Q scans at the $Q = (1, 0, 1)$(signal) and $Q = (1.2, 0, 1)$ (background) positions above and below T_c for $BaFe_{1.96}Ni_{0.04}As_2$. Figure 2.14(b) plots the imaginary part of the dynamic susceptibility $\chi''(\mathbf{Q}, \omega)$ after correcting for background and Bose population factor. We find that $\chi''(\mathbf{Q}, \omega)$ has a 2 meV normal state spin gap.

Figure 2.14: (Figure on next page.) (a) Energy scans at $Q = (1, 0, 1)$ and $Q = (1, 0, 0)$ above and below T_c. (b) $\chi''(\mathbf{Q}, \omega)$ at $Q = (1, 0, 1)$. (c) Energy scans at higher temperatures and, (d) the corresponding $\chi''(\mathbf{Q}, \omega)$. The solid lines in (b) and (d) are guides to the eye. (e) Q scans along the [H, 0, 1] direction at 4 meV. At 86 K, the Gaussian peak has FWHM $= 0.098 \pm 0.006$ rlu which corresponds to minimum correlation lengths of $\xi = 57 \pm 4\mathring{A}$. (f) Estimated $\chi''(\mathbf{Q}, \omega)$ at 4 meV. (g) $\chi''(\mathbf{Q}, \omega)$ at 7 meV with FWHM $= 0.103 \pm 0.013$ rlu and minimum correlation length of $\xi = 54 \pm 6\mathring{A}$. (h) Low temperature Q scans along the [1, 0, L] direction (c axis) at 4 meV (FWHM $= 0.58 \pm 0.06$ rlu) and 7 meV (FWHM $= 0.9 \pm 0.3$ rlu) correspond to $\xi = 14 \pm 5$ and $21 \pm 2\mathring{A}$, respectively. The solid curves in e-h) are Gaussian fits with centers fixed at (1, 0, 1) rlu.

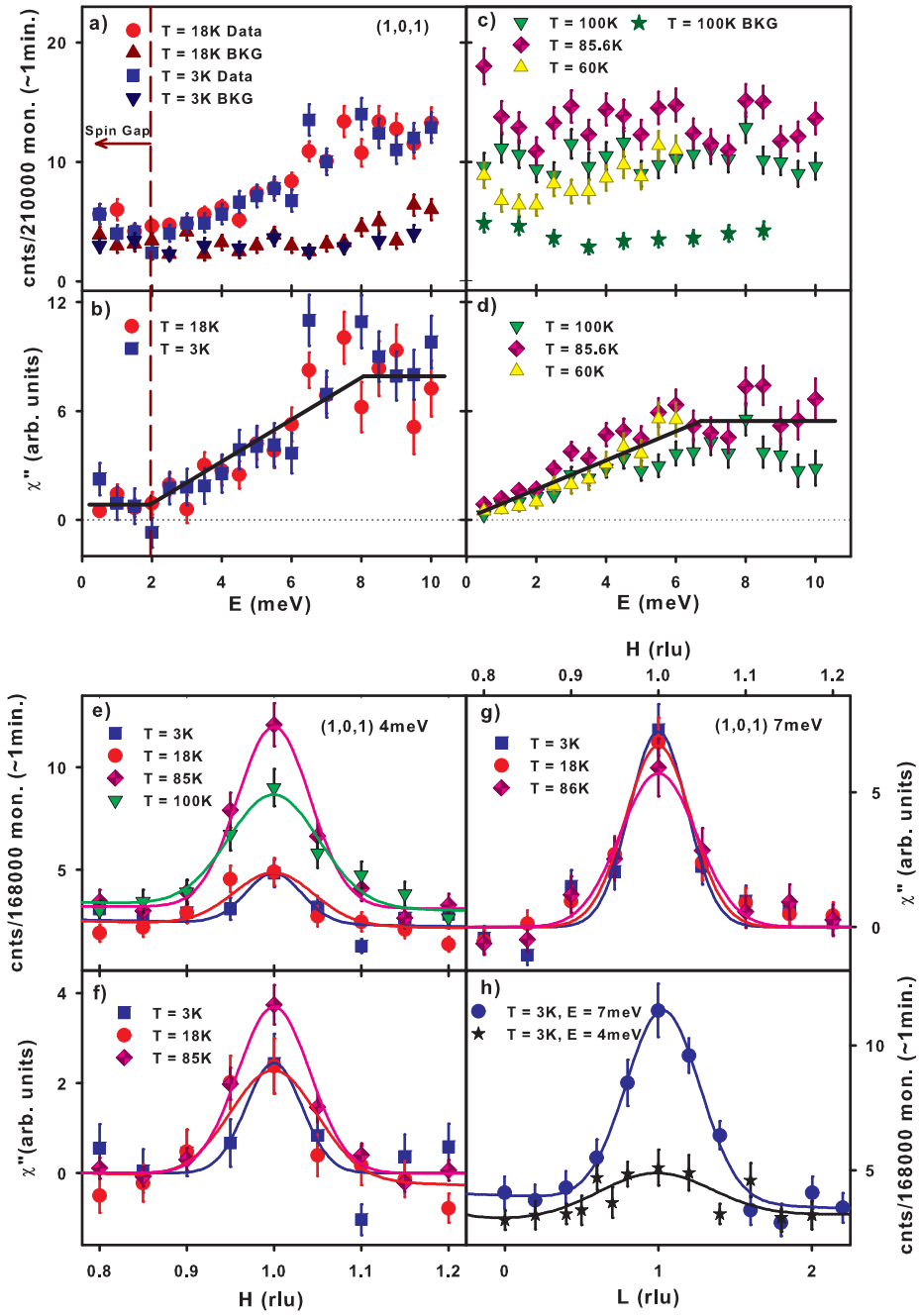

Figure 2.14: Caption on previous page.

Figure 2.15: (Figure on next page.) (a) Energy scans at $Q = (1, 0, 0)$ and $Q = (1.4, 0, 0)$ from 0.5 meV to 7 meV at 3.5 K and 18 K. (b) Background corrected $\chi''(\mathbf{Q}, \omega)$ showing clear evidence for a 4 meV spin gap. (c) Temperature dependence of the signal $[Q = (1, 0, 0)]$ and background $[Q = (1.4, 0, 0)]$ scattering at various temperatures. (d) $\chi''(\mathbf{Q}, \omega)$ at different temperatures. The solid lines in (b) and (d) are guides to the eye. (e) Q scans along the [H, 0, 0] direction at 4 meV and different temperatures. (f) Background corrected $\chi''(\mathbf{Q}, \omega)$. (g) Temperature dependence of the Q scans along the [H, 0, 0] direction at 6 meV (FWHM $= 0.10 \pm 0.01$ rlu). (h) Temperature dependence of the $\chi''(\mathbf{Q}, \omega)$ at 6 meV. Gaussian fits to the data in (e-h) have fixed centers at $Q = (1, 0, 1)$ rlu.

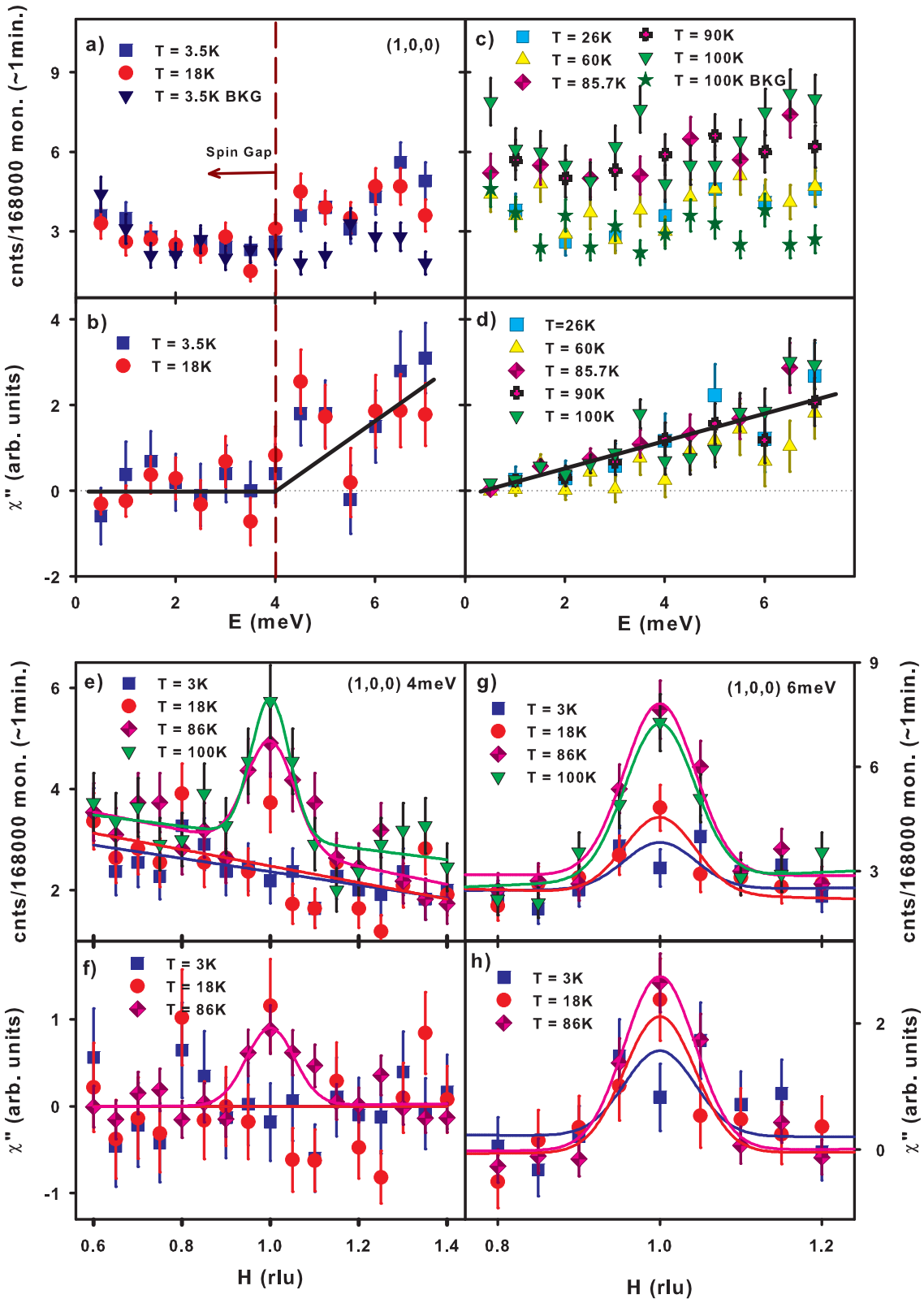

Figure 2.15: Caption on previous page.

Figures 2.14(c) and (d) reveal that the magnetic intensity increase with increasing temperature below T_N is due mostly to the Bose population factor. These results are confirmed by Q scans along the [H, 0, 1] direction at different temperatures [Figs. 2.14(e)(g)], which display well-defined peaks at $Q = (1, 0, 1)$ that have similar widths to the undoped $BaFe_2As_2$ at 10 meV [79]. Figure 2.14(h) shows Q scans along the c axis [1, 0, L] direction. Fourier transforms of the wave vector scans in Figs. 2.14(g) and (h) suggest that spins are only correlated around two unit cells ($\sim 20\AA$) along the c axis, much smaller than the 10 unit cell correlations ($\sim 50\AA$) of in-plane spin excitations. Therefore, spin excitations in $BaFe_{1.96}Ni_{0.04}As_22$ are not entirely 2D like those of optimally doped material [70].

Further evidences for quasi-2D spin excitations in $BaFe_{1.96}Ni_{0.04}As_2$ are summarized in Fig. 2.15. Assuming spin excitations in $BaFe_{2-x}Ni_xAs_2$ can be described by an effective Heisenberg Hamiltonian, the spin anisotropy gaps at $Q = (1, 0, 1)$ and $Q = (1, 0, 0)$ are $\Delta(1, 0, 1) = 2S[(J_{1a} + 2J_2 + J_c + J_s)^2 - (J_c + J_{1a} + 2J_2)^2]^{1/2}$ and $\Delta(1, 0, 0) = 2S[(2J_{1a} + 4J_2 + J_s)(2J_c + J_s)]^{1/2}$, respectively [145, 26, 79, 144]. Here S is the magnetic spin (=1); J_{1a}, J_2, J_c are effective in-plane nearest-neighbor, next nearest-neighbor, and c-axis magnetic couplings, respectively [Fig. 2.15(a)]. J_s represents the magnetic single ion anisotropy. From our time of flight data on $BaFe_2As_2$, we report a J_c value of 1.8 meV and estimate that the zone center ($\Delta(1, 0, 1)$) and zone boundary ($\Delta(1, 0, 0)$) gaps are ~ 10 and ~ 50 meV respectively. More recently triple axis work by Kiemer's group claims that this value is overestimated and that the true value is closer to $J_c = 0.22$ with a corresponding zone boundary gap value of $\Delta(1, 0, 0) = 20$meV [92]. It should be noted that in our data analysis, the globally fitted Q-cuts were for odd L values above ~ 25 meV. To get a more accurate estimate of J_c it would have been necessary to collect lower energy data over a broader range of E_i's and sample alignments with an inclusion of cuts at even L values since this would give a better measure J_c due to the gap modulation along L at low energies. As well, since our parent data became L independent above roughly 40meV, there was only a small 15meV window where it was possible to

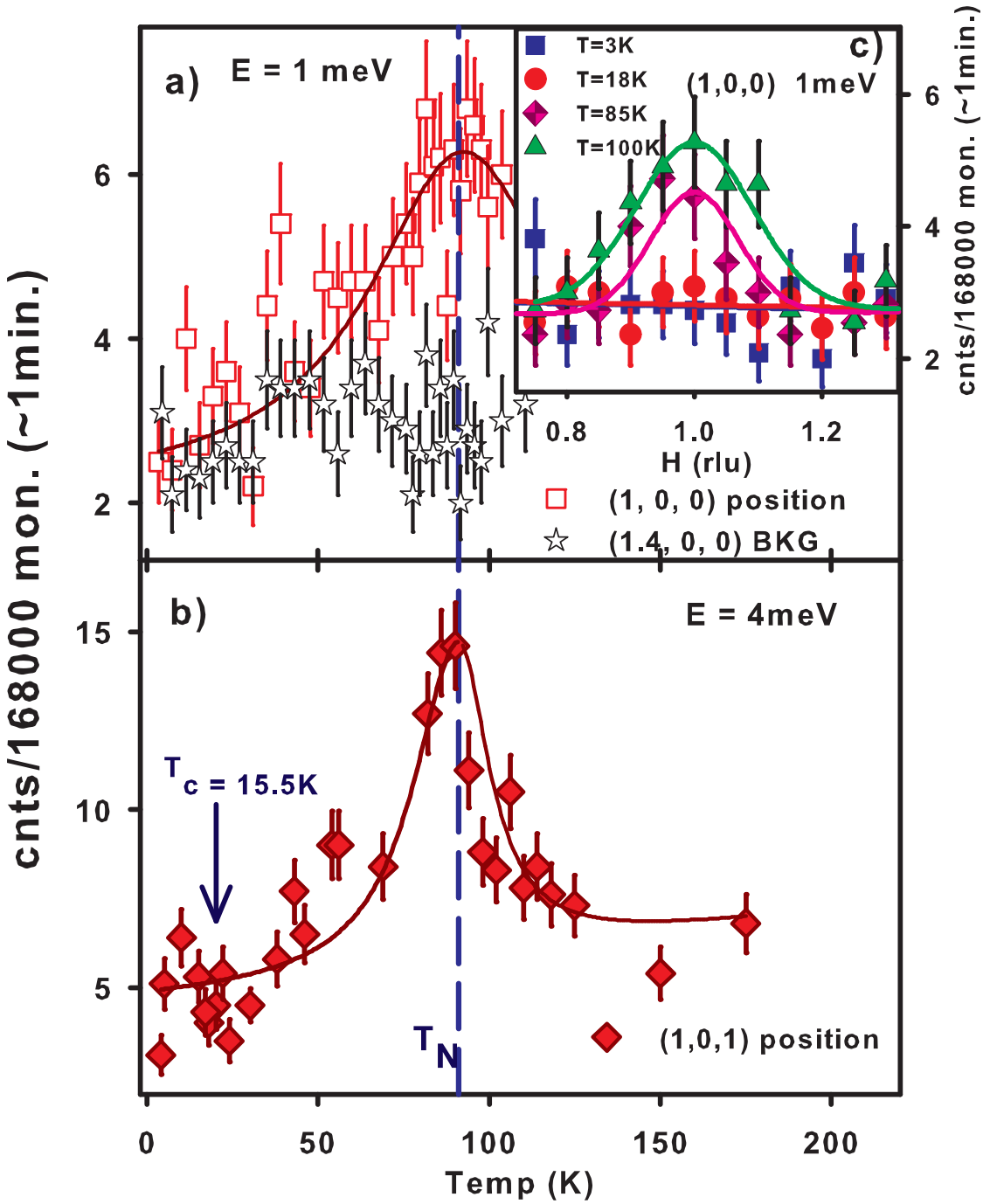

Figure 2.16: ((a) Temperature dependence of the 1 meV scattering at the signal $Q = (1, 0, 0)$ and background $Q = (1.4, 0, 1)$ positions. The inset shows Q scans along the [H, 0, 0] at 1 meV and different temperatures. The scattering shows no anomaly across T_c but clearly peaks at T_N. (b) Temperature dependence of the scattering at 4 meV and $Q = (1, 0, 1)$ again peaks at T_N.

analyzing the L-dependence. As a result, it would not be surprising if the correct J_c value in the parent $BaFe_2As_2$ is closer to 0.22 as opposed to our TOF estimation of $J_c = 1.8$ meV. Regardless, upon electron doping to form $BaFe_{1.96}Ni_{0.04}As_2$, these spin gap values have been reduced to $\Delta(1,0,1) = 2$ meV and $\Delta(1,0,0) = 4$ meV [Figs. 2.14(b) and 2.15(b)]. Since such electron doping hardly changes the in-plane Q-scan widths compared to that of the undoped $BaFe_2As_2$ [Figs. 2.14(e)(g), 2.15(e), and (g)] [26, 79], it should only slightly modify the in-plane exchange couplings. Assuming that J_{1a} and J_2 are unchanged in $BaFe_{1.96}Ni_{0.04}As_2$, the observed $\Delta(1,0,1) = 2$ meV and $\Delta(1,0,0) = 4$ meV would correspond to $J_c = 0.01$ meV and $J_s = 0.007$ meV, suggesting a rapid suppression of c-axis exchange coupling and magnetic single ion anisotropy with electron doping.

2.2.3 Conclusion

We have shown that the most dramatic effect of electron doping in $BaFe_2As_2$ is to transform the 3D anisotropic spin waves into quasi-2D spin excitations. Similar dimension reduction on the electronic states of 122 materials has also been observed in angle resolved photoemission spectroscopy [142, 66]. As well, within the effective $J_1 - J_2 - J_c$ model it is possible to understand the separated structural and magnetic phase transitions for $BaFe_{1.96}Ni_{0.04}As_2$ since the separation in temperature of these two phases is controlled by the value of J_c [28]. When J_c is large there is only one transition temperature. However, a finite separation between the two transition temperatures occurs when J_c/J_2 is reduced to the order of 10^{-3}. Our experimental result of $J_c/J_2 \sim 0.5 \times 10^{-3}$ is consistent with this picture. In closing, the apparent reduction in dimensionality is in line with the idea that the loss of long range order is not due (primarily) to a loss of nesting as the system is doped away from the parent state. Rather, it is a general consequence of quantum disorder due to a reduction in dimensionality [82]. As well, the seperation of the structural and magnetic phase transitions is a natural consequence of a vanishing coupling between layers. While the

microscopic origin of such dimension reductions upon doping is unclear, these results suggest that reduced dimensionality in spin excitations of iron arsenides is important for the separated structural and magnetic phase transitions in these materials, and also possibly the occurrence of bulk superconductivity.

2.3 Magnetic Excitations in Optimal Doped $BaFe_2As_2$

2.3.1 Mapping out the Resonance

Introduction and Earlier Studies of the Resonance in the Pnictides

Given the strong correlation between superconductivity and magnetism in the cuprates, it comes as no surprise that immediately after the discovery of unconventional superconductivity in the pnictides, one of the primary questions was whether or not magnetism was also present in these new systems as well. The first confirmation came when it was shown that the ground state of the parent (x = 0) $LaO_{1-x}F_xFeAs$ consisted of a long range antiferromagnetic order [21] that was suppressed in favor of superconductivity upon doping [48]. The strong parallel between the pnictides and the cuprates could not be missed (ie: superconductivity existing in close proximity to a long range ordered parent with tuning between phases achieved via doping) and motivated a host of new studies focused on determining how closely magnetism and superconductivity were correlated in these systems. With a magnetic structure in the parent firmly established, attention quickly turned to determining if a resonance magnetic excitation was present in doped superconducting samples. As discussed in the introduction, the resonant mode, already observed in both the cuprates [32, 102] and the heavy fermions [107, 115], is a feature that appears when the spin waves associated with the long range order have been supplanted by short range magnetic excitations that persist in proximity to the ordered state. The mode is distinguished by an anomalous climb in spectral weight at a specific location in $S(q, \omega) = S(q_R, \omega_R)$ and is coupled to superconductivity in two distinct ways.

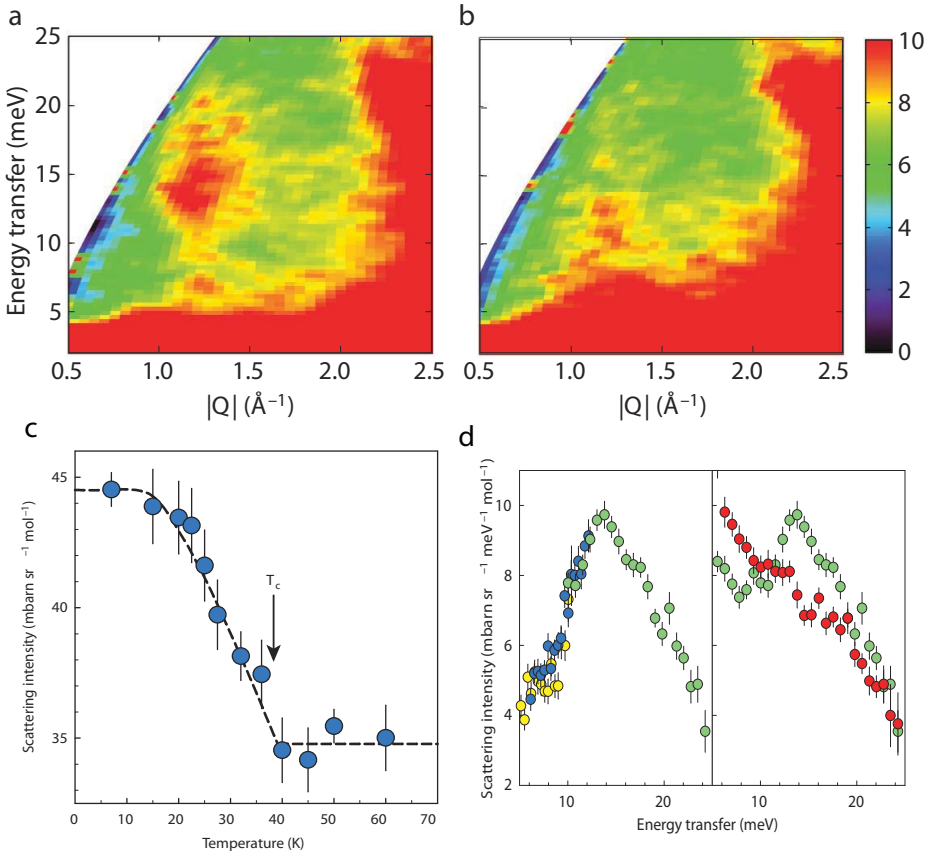

Figure 2.17: a), b) Neutron scattering data on a powder sample of $Ba_{0.6}K_{0.4}Fe_2As_2$ at T = 5K (superconducting) and T = 50K (non superconducting) respectively. In the SC state, a sharp increase in scattering is visible at 14meV, indicative of the presence of a resonance. c) A temperature scan of the 14meV anomaly reveals that intensity follows an order parameter in temperature, with suppression at T_c. d) (left panel) Q-integrated energy scan of the resonance at T = 7K demonstrating that the intensity peaks at ω_R = 14meV. (right panel) The T = 7K energy scan compared to an identical scan at T = 50K reveals that the resonant excitation disappears in the normal state. Data from [10].

First, the resonance is only present in the superconducting state with the intensity following an order parameter in temperature and full suppression coinciding with the transition T_c. Second, the resonance energy, ω_R, is linearly correlated to the superconducting transition temperature T_c [128] and (in many cases) the superconducting gap 2Δ [139]. Moreover, magnetic field measurements of YBCO revealed that the resonance was sensitive to applied field, acting as a potential probe of the phase coherence time (resonance width) and superfluid density (integrated intensity)[19]. Given the importance of the resonance in other unconventional superconductors, establishing its existence and mapping it out in the pnictides was the natural starting point for my thesis focusing on the role of magnetic excitations in iron based superconductors.

Within a few short months after a magnetic groundstate was discovered in the 1111 system (x = 0) $LaO_{1-x}F_xFeAs$, powder measurements of the 122 compound $Ba_{0.6}K_{0.4}Fe_2As_2$ (Fig. 2.17) by another group revealed the presence of a resonance in the pnictides for the first time [10]. By comparison of panels 2.17 (a) T = 5K (superconducting) and 2.17(b) T = 50K (nonsuperconducting), the resonance appears as a diffuse signal gain in the 2D powder dispersions. 1D Temperature and energy scans (2.17 (c) and (d) respectively) confirm that the resonance switches on a T_c with a mode energy centered at 14meV. However, since the experiment was carried out on powders, only the mod Q dependence of the excitation could be determined. In order to verify the existence of the resonance and resolve its location and dependence on Q, our group mapped out the spin excitations in optimal doped $BaNi_{0.1}Fe_{1.9}As_2$. As well, since the earlier powder measurement was on a hole doped derivative of $BaFe_2As_2$, our confirmation of its existence in $BaNi_{0.1}Fe_{1.9}As_2$ would demonstrate that, like the cuprates, the resonance is a common feature for both n and p type doping.

Discovery of a 3D resonance (L-dependent) in $BaNi_{0.1}Fe_{1.9}As_2$

Our neutron scattering experiments were performed on the PANDA cold triple-axis spectrometer at the Forschungsneutronenquelle Heinz Maier-Leibnitz (FRM II),

TU Munchen, Germany. We used pyrolytic graphite (0,0,2) as monochromator and analyzer without any collimator. We defined the wave vector Q at (q_x, q_y, q_z) as $(H, K, L) = (q_x a/2\pi, q_y b/2\pi, q_z c/2\pi)$ reciprocal lattice units (rlu) using the orthorhombic magnetic unit cell of the parent undoped compound (space group Fmmm, a = 5.564, b = 5.564, and c = 12.77 $\mathring{A}$). We choose this reciprocal space notation (although the actual crystal structure is tetragonal) for easy comparison with previous spin wave and elastic measurements on the parent compound, where magnetic Bragg peaks and low-energy spin waves are expected to occur around (1, 0, 1) and (1, 0, 3) rlu positions. For the experiment, the $BaNi_{0.1}Fe_{1.9}As_2$ crystal assembly was mounted in the [H, 0, L] zone inside a closed cycle refrigerator. The final neutron wave vector was fixed at either $k_f = 1.55\mathring{A}^{-1}$ with a cold Be filter or at $k_f = 2.662\mathring{A}^{-1}$ with a pyrolytic graphite filter in front of the analyzer.

We first searched for possible static AF order in our samples. For undoped $BaFe_2As_2$, magnetic Bragg peaks are expected at the (1, 0, 1) and (1, 0, 3) positions with the associated low-temperature spin waves of the ordered state gapping below about 9.8 meV [79]. Our elastic Q scans through these expected AF Bragg peak positions were featureless, confirming the absence of static long range order above 30 K. Thus, the inelastic scattering observed is no longer derived from spin waves propagating along a long range ordered lattice, but instead is due to strongly correlated paramagnetic excitations.

Figure 2.18 (a)-(c) summarizes constant energy scans along $(H, 0, 0)$ at 3 K (well below T_c) and at 30 K (above T_c) at E = 2, 6, and 8.5 meV. Recall that in the parent, the zone boundary gap $\Delta(1, 0, 0)$ is at least 20 meV [92] while upon light electron doping it reduces greatly to $\sim$ 4meV [43]. From Fig. 2.18 (a) we observe at 30 K a clear peak centered at the in-plane AF wave vector (1, 0, 0) demonstrating that upon reaching optimal doping, the normal state gap is completely suppressed. Fourier transforms of the Gaussian peaks in Figs. 2.18(a) and (b) gave the minimum dynamic spin correlation lengths of $\xi = 16 \pm 4$ and 21 ± 4 $\mathring{A}$ for E = 2 and 6 meV, respectively. In comparison, the spin-spin correlations extend only to several chemical

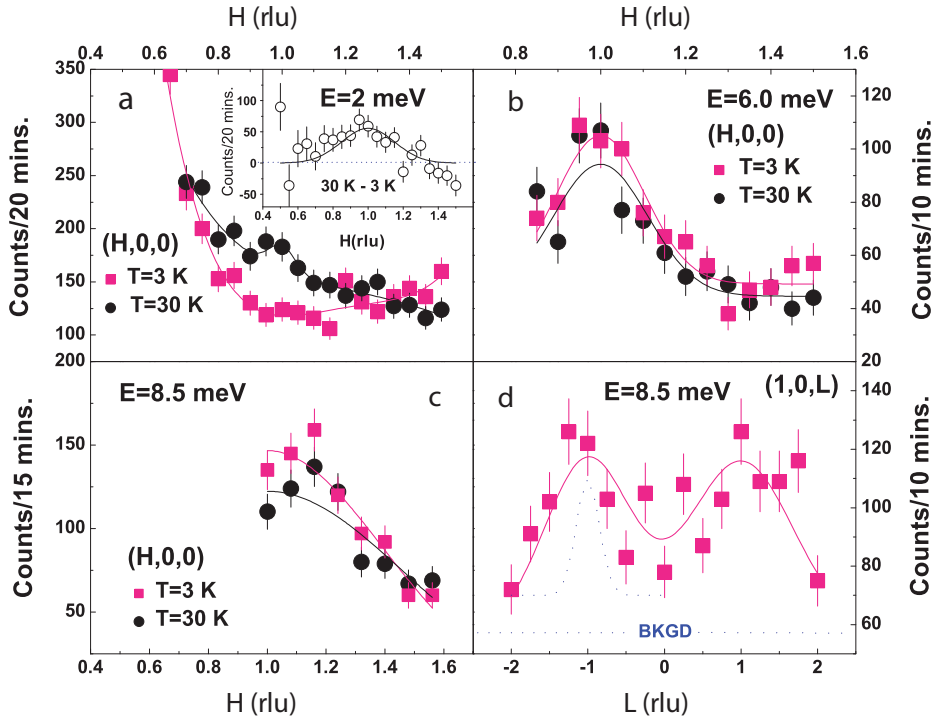

Figure 2.18: Constant-energy scans around the (1, 0, 0) and (1, 0, 1) positions for E = 2, 6, and 8.5 meV. (a-c) Q scan along the [H, 0, 0] direction at 30 and 3 K. The inset in (a) shows the temperature difference plot and a Gaussian fit to the data. The missing low-Q data for scans in (b) and (c) are due to kinematic constraint. (d) Q scan along the [1, 0, L] direction for E = 8.5 meV at 3 K. Note two clear peaks centered at (1, 0, -1) and (1, 0, 1), respectively.

unit cells and are much smaller than the $\xi = 80 \pm 10$ $\mathring{A}$ at E = 1.5 meV obtained for electron-doped cuprate superconductor $Pr_{0.88}LaCe_{0.12}CuO_4$. On cooling from 30 to 3 K, the Gaussian peak at E = 2 meV vanishes and suggests the opening of a spin gap [Figs. 2.18(a)]. In contrast, the Gaussian peaks at E = 6 meV hardly change across T_c [Fig. 2.18(b)], whereas the scattering at (1, 0, 0) for E = 8.5 meV actually increases below T_c [Fig. 2.18(c)]. Taken together these results immediately suggest that the static, long range, antiferromagnetic order and associated spin waves of the parent are replaced by short range correlations only a few unit cells in length for doped superconducting derivatives. Likewise, the spin wave gap in the non superconducting parent closes upon doping as long as the superconducting compound is above T_c, however when the system is cooled into the superconducting state a new spin gap at a much lower energy appears. Energy scans at (1, 0, 0) reveal that the gap opens at 4meV, likewise a temperature scan of the gap reveals a dramatic drop in intensity at T_c, directly tying the appearance of this gap with the superconducting transition.

Our initial scans focused on the (1, 0, 0) wave vector. From the energy scan above and below T_c at (1, 0, 0) in Fig. 2.19 (a) it is clear that a resonant gain in signal appears upon entering the superconducting state at $E_R = 9.1$ meV. However from Fig. 2.18(d) it is clear that the intensity actually peaks at the 3D antiferromagnetic wave vector (1, 0 , 1)/(1, 0 , -1) with (1, 0 ,0) sitting in a minima. Thus, we carried out additional measurements to search for a resonance at (1, 0, -1). The outcome in Fig. 2.19(c) shows a large magnetic intensity gain below T_c at E = 7 meV, clearly different from the 9.1 meV resonance at Q = (1, 0, 0). To further confirm that the intensity gain at E = 7 meV is indeed the resonance occurring at Q = (1, 0, -1), we carried out constant-energy scans around (1, 0, -1) and the outcome shows that the intensity gain below T_c arises from scattering at the 3D AF ordering position [Fig. 2.19(e)]. Finally, in Fig. 2.19(f) we plot the temperature dependence of the scattering at (1, 0, -1) and $E_R = 7$ meV. The scattering increases dramatically below the onset of T_c and is remarkably similar to that of the resonance in high-Tc copper oxides. If the resonance is a measure of electron pairing correlations in high-Tc

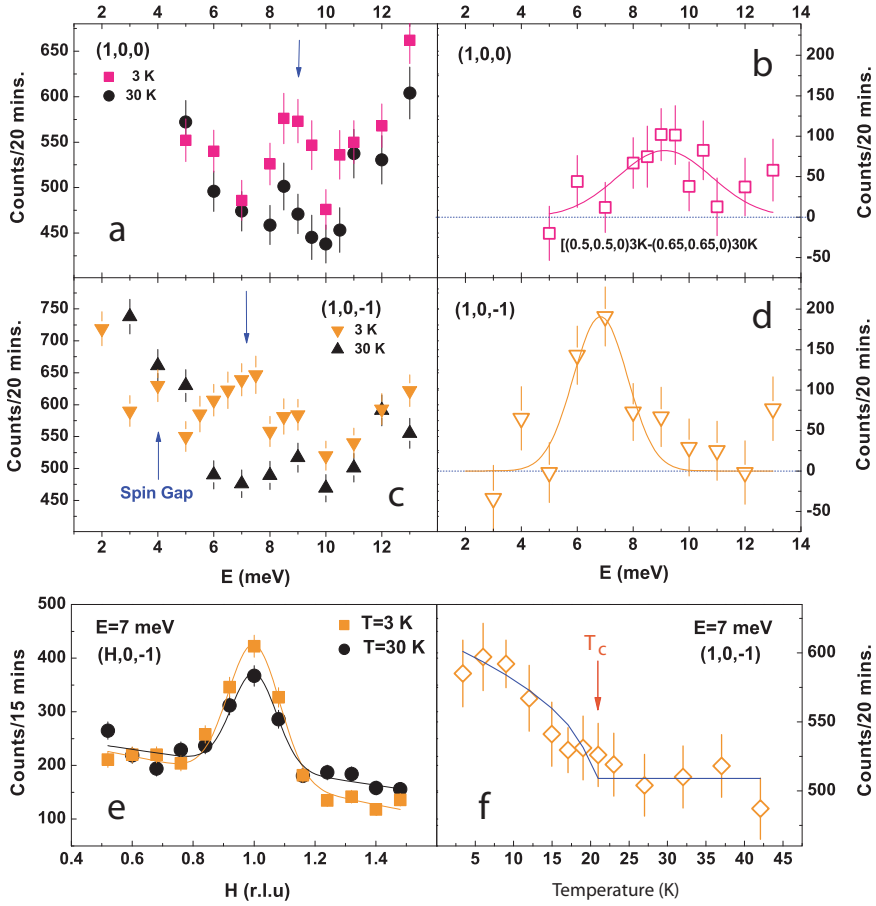

Figure 2.19: (a) Energy scans at Q = (1, 0, 0) from 5 to 13 meV at 30 and 3 K. (b) The temperature difference scattering between 3 and 30 K shows a clear resonant peak at E = 9.1 ± 0.4 meV. (c) Energy scans at Q = (1, 0, -1) from 2 to 13 meV at 30 and 3 K. (d) The temperature difference plot confirms that the mode has now moved to 7.0 ± 0.5 meV. (e) Wave vector dependence of the scattering at 30 and 3 K for E = 7 meV, confirming that the resonance intensity gain occurs at Q = (1, 0, -1). (f) Temperature dependence of the scattering at Q = (1, 0, -1) and E = 7 meV shows a clear order-parameter-like increase below T_c.

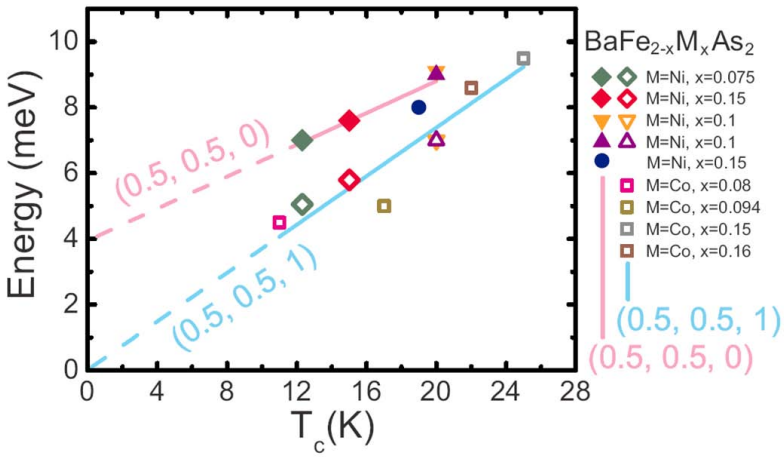

Figure 2.20: Summary of electron-doping dependence of the neutron spin resonance energies at $Q = (0.5, 0.5, 0)$ and $(0.5, 0.5, 1)$ as a function of T_c. Solid lines are linear fits to the data. Figure taken from [125] with data for $BaFe_{2-x}Ni_xAs_2$ and $BaFe_{2-x}Co_xAs_2$ compiled from multiple papers. Refer to [125] for these references.

superconductors [19], the observed 3D resonance dispersion in $BaFe_{1.9}Ni_{0.1}As_2$ would suggest a variation of the superconducting gap Δ along the c axis, similar to those in UPd_2Al_3. This is quite different from the high-T_c copper oxides, where Δ is strictly 2D and independent of the c axis modulations.

Conclusion and Later studies of the Resonance in the Pnictides

After the discovery of resonances in both optimally hole [10] and electron doped $BaFe_2As_2$ [9, 70], further work on both the under and overdoped sides of the phase diagram revealed that the mode was a ubiquitous feature of the superconducting phase. Moreover, as with the cuprates, the location of the mode is linearly correlated with the T_c of the doped derivatives [125]. Tracking the resonances across the phase diagram at both the (1, 0, 1) and (1, 0, 0) positions reveal that the energy transfer of both of these modes shift linearly as function of doping, but with each following a different slope. This has been shown in Fig. 2.20 which is primarily composed of compounds taken from the underdoped side of the phase diagram. Thus, the lower

T_c values in Fig. 2.20 correspond to subsequently lower levels of doping. From this, it is then clear that the separation distance of the resonances at (1, 0, 0) and (1, 0, 1) decreases as the system is tuned towards optimal doping. The natural corrallary is that the 3D nature of the resonance reduces in dimensionality as the system is doped away from the parent. This is consistent with the discovery of a strong reduction in J_c upon light nickel doping as discussed in the previous section.

A leading theory ascribes the origin of the resonance as an enhancement in scattering below T_c due to the superconducting coherence factor. For quasiparticle transitions across sign-revised s-wave electron (Δ_e^0) and hole (Δ_h^0) superconducting gaps (s^{+-}), the coherence factor should enhance scattering at an energy equal to $|\Delta_e^0 + \Delta_h^0|$ (or slightly less). Thus, the discovery of the resonance provided strong support for identifying the superconducting state in the pnictides as unconventional. Moreover, within this picture, the L-modulation of the resonance can be naturally understood in terms of associated L-modulation in the superconducting gap sizes. Indeed, although our original work on the 3D nature of the spin resonance in optimal nickel doped $BaFe_2As_2$ only mapped out the resonance at (1, 0, 0) and (1, 0, 1), it was expected that given an L modulation in the superconducting gaps of the form $\Delta_e(k_z) = \Delta_e^0 + \delta\cos(k_z)$ and $\Delta_h(k_z) = \Delta_h^0 + \delta\cos(k_z)$ then the resonance would appear at all (1, 0, L) positions with a modulation that could be empirically fit by

$$E_R(L) = E_R^0 + W|\cos(\pi L/2)| \tag{2.7}$$

Where E_R^0 is the resonance energy at the AFM wave vector (1, 0, 1) and W is the bandwidth of the dispersive resonance. A careful study of the L dependence in under and optimal Co doped $BaFe_2As_2$ by McQueeney's group [96] confirmed that the resonance does indeed follow this cosine modulation, with the the bandwidth reducing considerably at optimal doping where the physics are expected to be more two dimensional (Fig. 2.21).

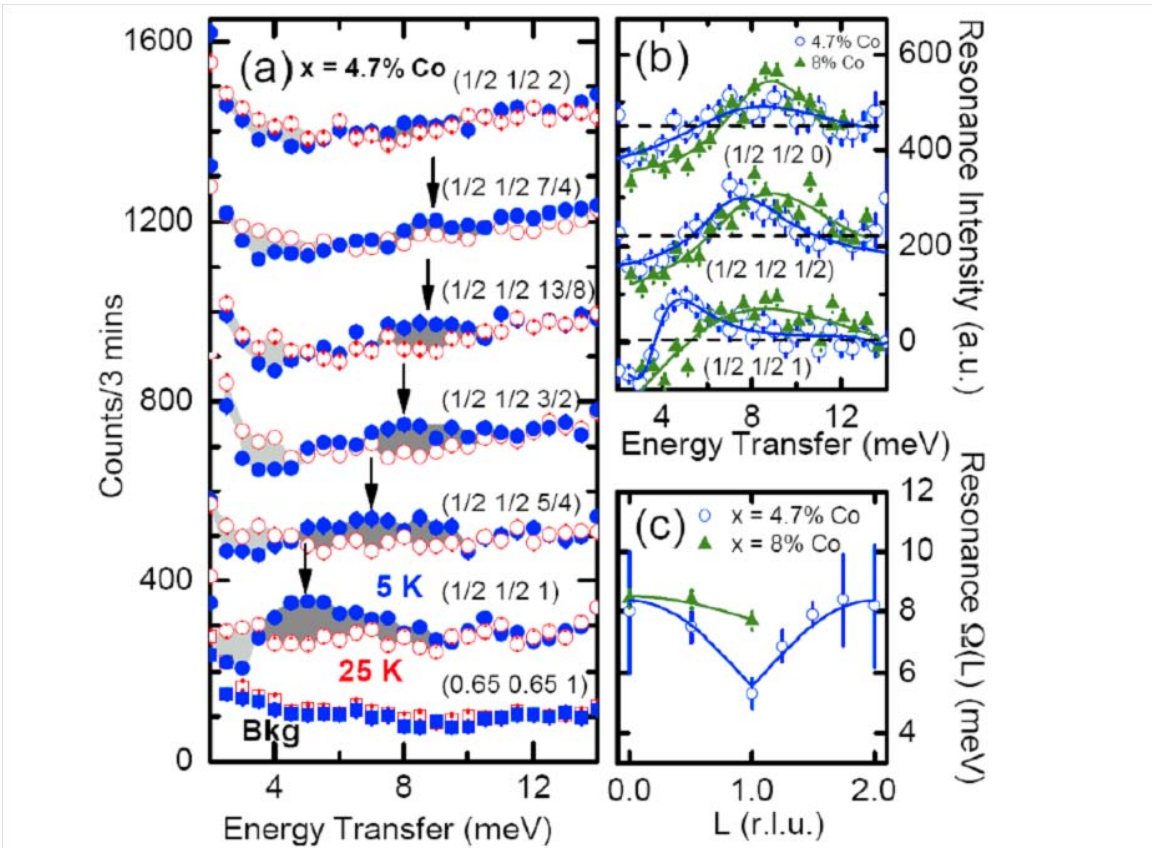

Figure 2.21: (a) Energy cuts of the resonance in underdoped $Ba(Fe_{1-x}Co_x)_2As_2$ (Co=4.7%) for a range of L values throughout the Brillouin zone. (b) Comparison of the resonance for under (4.7%) and optimal (8%) dopings at different L. (c) Dispersion of the resonant peak energy as a function of L. Figure taken from [96].

To contrast this quickly with other families of unconventional superconductors, a similar L dispersion of the resonance has been observed in heavy fermionic systems but not in the cuprates. However, it should be noted that in the bilayer cuprates, symmetry under exchange of planes within a bilayer leads to only two independent components in the dynamic susceptibility $\chi_{||} \equiv \chi_{11} = \chi_{22}$ and $\chi_{\perp} \equiv \chi_{33}$ and, subsequently, the cross-section can be partitioning into 'even' and 'odd' components of the form

$$\frac{d\sigma^2}{d\Omega dE} \sim F^2(Q)\left[\sin^2\left(\frac{Q_z d}{2}\right)\chi''_o(\mathbf{Q},\omega) + \cos^2\left(\frac{Q_z d}{2}\right)\chi''_e(\mathbf{Q},\omega)\right] \tag{2.8}$$

where d is the distance between CuO_4 planes within a bilayer, $F^2(Q)$ is the Cu^{2+} form factor, and the even and odd components are defined as

$$\begin{aligned} \chi''_e(\mathbf{Q},\omega) &= \chi''_{||}(\mathbf{Q},\omega) + \chi''_{\perp}(\mathbf{Q},\omega) \\ \chi''_o(\mathbf{Q},\omega) &= \chi''_{||}(\mathbf{Q},\omega) - \chi''_{\perp}(\mathbf{Q},\omega) \end{aligned} \tag{2.9}$$

(see [25] for a more detailed discussion.) Within this framework it was discovered that both the even and odd components carried a resonance at a different energy [89]. In general, the susceptibility is a superposition of the even and odd components. However, by scanning at the appropriate L value such that $\sin^2(Q_z d/2) = 1$ and $\cos^2(Q_z d/2) = 0$ (or vice versa), it is possible to isolate an individual component Fig. 2.22. Thus, there is a limited form of L-dependence on E_R in the cuprates. However, it is neither dispersive in nature nor associated with a modulation of the superconducting gap (which is 2D).

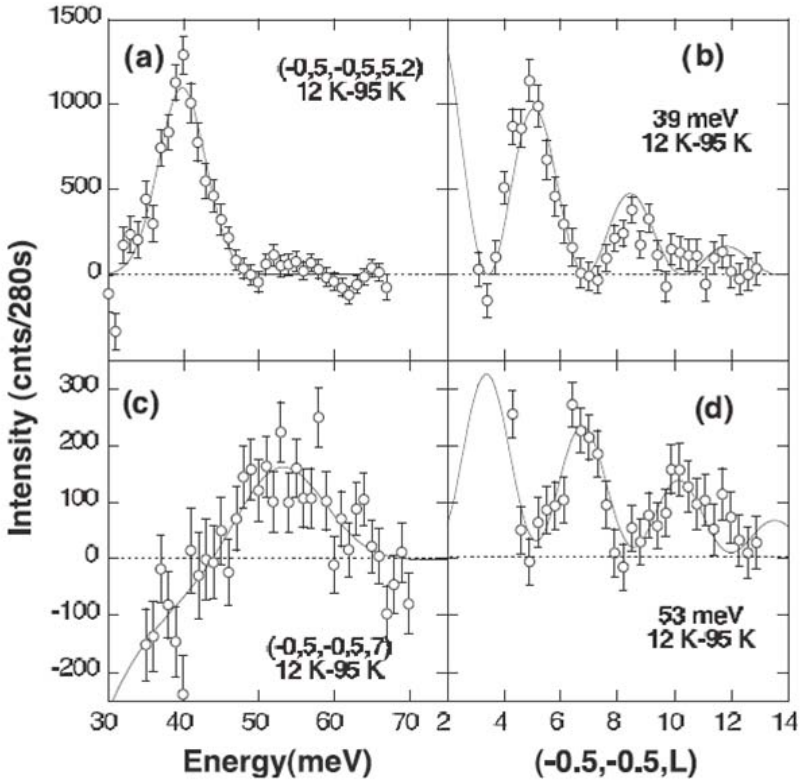

Figure 2.22: Resonance in $YBa_2Cu_3O_{6.85}$ for both the odd (a,b) and even (c,d) channels. L-scans in (b) and (d) reveal explicitly the sine squared and cosine squared intensity modulation for the odd and even channels respectively. Figure taken from [89].

2.3.2 Comparison of High Energy Magnetic Excitations in the Parent and Optimal Doped $BaFe_2As_2$

Introduction

From the above discussions of the parent ($x = 0$), under ($x = 0.4$) and optimal doped ($x = 0.1$) $BaFe_{2-x}Ni_xAs_2$ pnictide systems it is clear that the magnetic state is dramatically affected at low energies upon doping. In the parent, the spins form a long range order with magnetic fluctuations consisting of spin waves propagating through this ordered spin lattice. Below 10meV, the excitations are gapped at the AFM wave vector and with increasing temperature the scattering follows the Bose population factor with critical scattering forming a peak at the Neèl temperature. In contrast, even a very modest amount of doping (x = 0.04) leads to an order of magnitude reduction of the dimensionality (as characterized by J_c) and upon reaching optimal doping the long range spin lattice is completely dissolved with spin waves replace by correlated paramagnetic fluctuations centered diffusely around the AFM wave vector. In the normal state the spin gap is completely closed, however upon cooling below T_c a superconducting spin gap emerges with spectral weight shoveled into a resonance at energies directly above this newly formed gap.

Based off of the striking disparity between the magnetic state at low energies for these different systems, it is natural to naively expect that the scattering profile across the entire energy spectrum is completely restructured upon doping. However, the lack of spin excitation data at higher energies in absolute units for doped compounds precludes a full comparison with spin waves in undoped $BaFe_2As_2$. Only the absolute intensity measurements in the entire Brillouin zone can reveal the effect of electron doping on the overall spin excitation spectra. By comparing spin excitations in $BaFe_{1.9}Ni_{0.1}As_2$ and $BaFe_2As_2$ throughout the Brillouin zone, we were able to probe how electron doping and superconductivity affect the overall spin excitation spectra. We demonstrate that whereas the low-energy spin excitations are affected, the high-energy excitations show only a very weak temperature and doping

Figure 2.23: (Figure on next page.) **a**, AF spin structure of $BaFe_2As_2$ with Fe spin ordering. The effective magnetic exchange couplings along different directions are shown. **b**, RPA and LDA+DMFT calculations of $\chi''(\omega)$ in absolute units for $BaFe_2As_2$ and $BaFe_{1.9}Ni_{0.1}As_2$. **c**, The solid lines show the spin wave dispersions of $BaFe_2As_2$ for $J_{1a} \neq J_{1b}$, along the $[1, K]$ and $[H, 0]$ directions obtained in [42]. The filled circles and triangles are the spin excitation dispersions of $BaFe_{1.9}Ni_{0.1}As_2$ at 5 K and 150 K, respectively. **d**, The solid line shows the low-energy spin waves of $BaFe_2As_2$. The horizontal bars show the full-width at half-maximum of spin excitations in $BaFe_{1.9}Ni_{0.1}As_2$. **e**, Energy dependence of $\chi''(\omega)$ for $BaFe_2As_2$ (filled blue circles) and $BaFe_{1.9}Ni_{0.1}As_2$ below (filled red circles) and above (open red circles) T_c. The solid and dashed lines are guides to the eye. The vertical error bars indicate statistical errors of one standard deviation. The horizontal error bars in **e** indicate the energy integration range. Figure taken from the coauthor work [67].

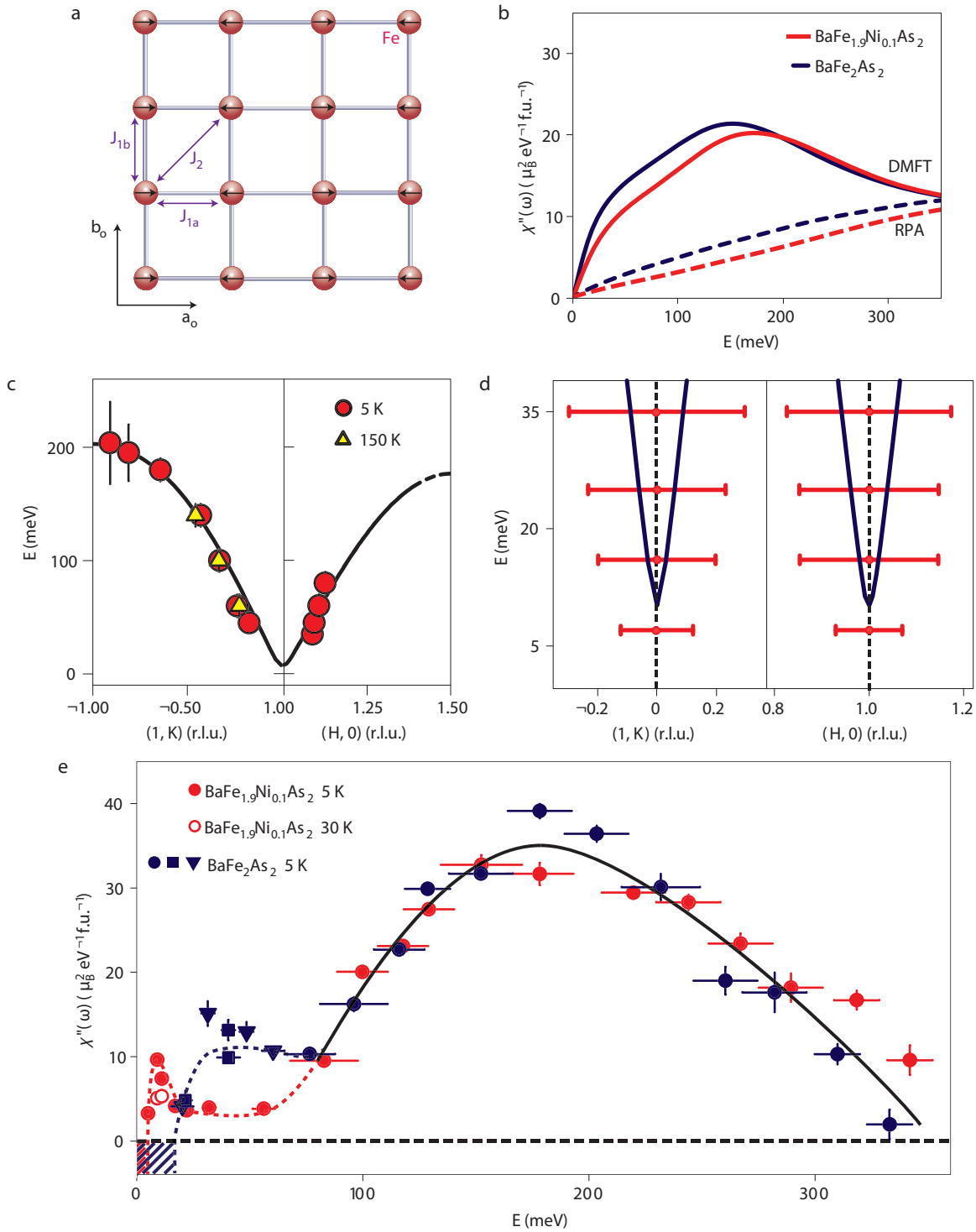

Figure 2.23: Caption on previous page.

dependence. Comparison of our results with various theories suggests that neither a fully itinerant nor a localized picture explains the magnetic excitation spectrum. However, a combination of density functional theory (DFT) and dynamic mean field theory (DMFT) provides a natural way to improve on both these pictures.

Based off of the striking disparity between the magnetic state at low energies for these different systems, it is natural to naively expect that the scattering profile across the entire energy spectrum is completely restructured upon doping. However, the lack of spin excitation data at higher energies in absolute units for doped compounds precludes a full comparison with spin waves in undoped $BaFe_2As_2$. Only the absolute intensity measurements in the entire Brillouin zone can reveal the effect of electron doping on the overall spin excitation spectra. By comparing spin excitations in $BaFe_{1.9}Ni_{0.1}As_2$ and $BaFe_2As_2$ throughout the Brillouin zone, we were able to probe how electron doping and superconductivity affect the overall spin excitation spectra. We demonstrate that whereas the low-energy spin excitations are affected, the high-energy excitations show only a very weak temperature and doping dependence. Comparison of our results with various theories suggests that neither a fully itinerant nor a localized picture explains the magnetic excitation spectrum. However, a combination of density functional theory (DFT) and dynamic mean field theory (DMFT) provides a natural way to improve on both these pictures.

High Energy Excitations in $BaFe_{1.9}Ni_{0.1}As_2$

Our experiments were carried out on the MERLIN time-of-flight chopper spectrometer at the Rutherford-Appleton Laboratory, UK [99]. We co-aligned 28 g of single crystals of $BaFe_{1.9}Ni_{0.1}As_2$ (with in-plane mosaic of 2.5^o and out-of-plane mosaic of 4°). The incident beam energies were $E_i = 20, 25, 30, 80, 250, 450, 600$ meV, and mostly with E_i parallel to the c axis. To facilitate easy comparison with spin waves in $BaFe_2As_2$ [40], we defined the wave vector Q at (q_x, q_y, q_z) as $(H, K, L) = (q_x a/2\pi, q_y b/2\pi, q_z c/2\pi)$ reciprocal lattice units (r.l.u.) using the orthorhombic unit cell, where $a = b = 5.564\mathring{A}$, and $c = 12.77\mathring{A}$. The data are normalized to absolute units using a vanadium

standard, which may have a systematic error up to 20% owing to differences in neutron illumination of the vanadium and sample, and time-of-flight instruments.

Figure 2.23 (c)-(e) summarizes our key findings for the electron-doped iron arsenide superconductor $BaFe_{1.9}Ni_{0.1}As_2$ and the comparison with the spin waves in $BaFe_2As_2$. The data points in Fig. 2.23 (c) and (d) show the dispersion of spin excitations for optimally doped $BaFe_{1.9}Ni_{0.1}As_2$ along [1, K] and [H, 0] and the solid lines show the fit of $BaFe_2As_2$ spin waves to an effective Heisenberg $J_{1a} - J_{1b} - J_2$ model [42]. Figure 2.23 (e) shows the local dynamic susceptibility per formula unit (f.u.), which contains two Fe(Ni) atoms, in absolute units, defined as $\chi''(\omega) = \int \chi''(\mathbf{q},\omega)d\mathbf{q}/\int d\mathbf{q}$ [59], where $\chi''(\mathbf{q},\omega) = (1/3)tr(\chi''_{\alpha\beta}(\mathbf{q},\omega))$, at different energies for $BaFe_2As_2$ and $BaFe_{1.9}Ni_{0.1}As_2$. It is clear that electron doping on $BaFe_2As_2$ affects only the low-energy spin excitations by broadening the spin waves below 80 meV, but has no impact on spin waves above 100 meV. Specifically, the distribution of spectral weight integrated across the entire Brillioun zone is nearly identical between the parent and optimal doped systems for energy transfers greater than $\sim$ 100 meV while below this energy transfer the sum intensity is reduced considerably for $BaFe_{1.9}Ni_{0.1}As_2$ Fig. 2.23 e. From a physical point of view, the local susceptibility is a measure of the distribution of the fluctuating moment on different timescales. Thus, we see that whereas doping strongly effects the moment fluctuating on a timescales slower than $t \sim \hbar/(100meV)$, for timescales greater than this there is no change. Indeed, we can estimate the total fluctuating moment, defined as $\langle m^2 \rangle = (3\hbar/\pi)\int \chi''(\omega)d\omega/(1-\exp(-\hbar\omega/kT))$ [59]. Since only a small portion of the total spectral weight sits at energy transfers that are sensitive to doping, we find that the total moment is nearly unchanged with $\langle m^2 \rangle = 3.17 \pm 0.16$ and $\langle m^2 \rangle = 3.2 \pm 0.16$ per Fe(Ni) for $BaFe_2As_2$ and $BaFe_{1.9}Ni_{0.1}As_2$, respectively. Using the formula for the magnetic moment of a spin $\langle m^2 \rangle = (g\mu_B)^2 S(S+1)$ (where $g = 2$; [69]), we find an effective iron spin S of about 1/2, similar to that of $CaFe_2As_2$ [144]. These results also show that superconductivity in electron doped systems hardly changes the total size of the fluctuating moment. In the fully localized (insulating) case, the formal

Fe^{2+} oxidation state in $BaFe_2As_2$ would give a $3d^6$ electronic configuration. Hund's rules would yield $S = 2$ and $\langle m^2 \rangle = 24\mu_B^2$ per Fe. This is much larger than the observed values, suggesting significant hybridization of Fe 3d with pnictide p orbitals and among themselves, which leads to a metallic state where the Hund's coupling is less important than in the atomic limit [119]

Inspection of 2.23 (c) and (d) reveal that the magnetic scattering in both systems follow an identical dispersion but with a FWHM in $BaFe_{1.9}Ni_{0.1}As_2$ broadening considerably at low energies with respect to the parent. To compare the effect of doping on the overall structure of the magnetic excitations in reciprocal space we constructed identical 2D constant-energy [H, K] slices of the scattering across the full spectrum of energy transfer for $BaFe_{1.9}Ni_{0.1}As_2$ and $BaFe_2As_2$, Fig. 2.24. We found that for energies above 100meV there is no discernible difference in the scattering profile. Even at low energy the scattering is quite similar. However, the sharp dispersive character of the parent is replaced upon doping by a more diffuse scattering with weakened intensity centered around the AFM wave vector. It is interesting to note that the effect of doping the system is strikingly similar to the paramagnetic scattering observed in the parent when warmed just above T_N Fig. 2.8. Here a nearly identical threshold energy of 100meV separated the more diffuse scattering at low energy from the dispersive scattering that tracked the spin wave character of the magnetic excitations in the ordered state.

Conclusion

The partitioning of the scattering into a low energy part that is both temperature and doping sensitive, and a high energy part that is indifferent to such tuning can be understood in terms of mixed physics containing local and itinerant elements. The quasiparticles that form within the spin density wave gap are sensitive to the Fermi surface change on doping $BaFe_2As_2$ and, hence, the resulting low-energy itinerant spin excitations change substantially, whereas the higher energy spin excitations are hardly affected. To place this idea on firmer ground, we began by checking if spin excitations

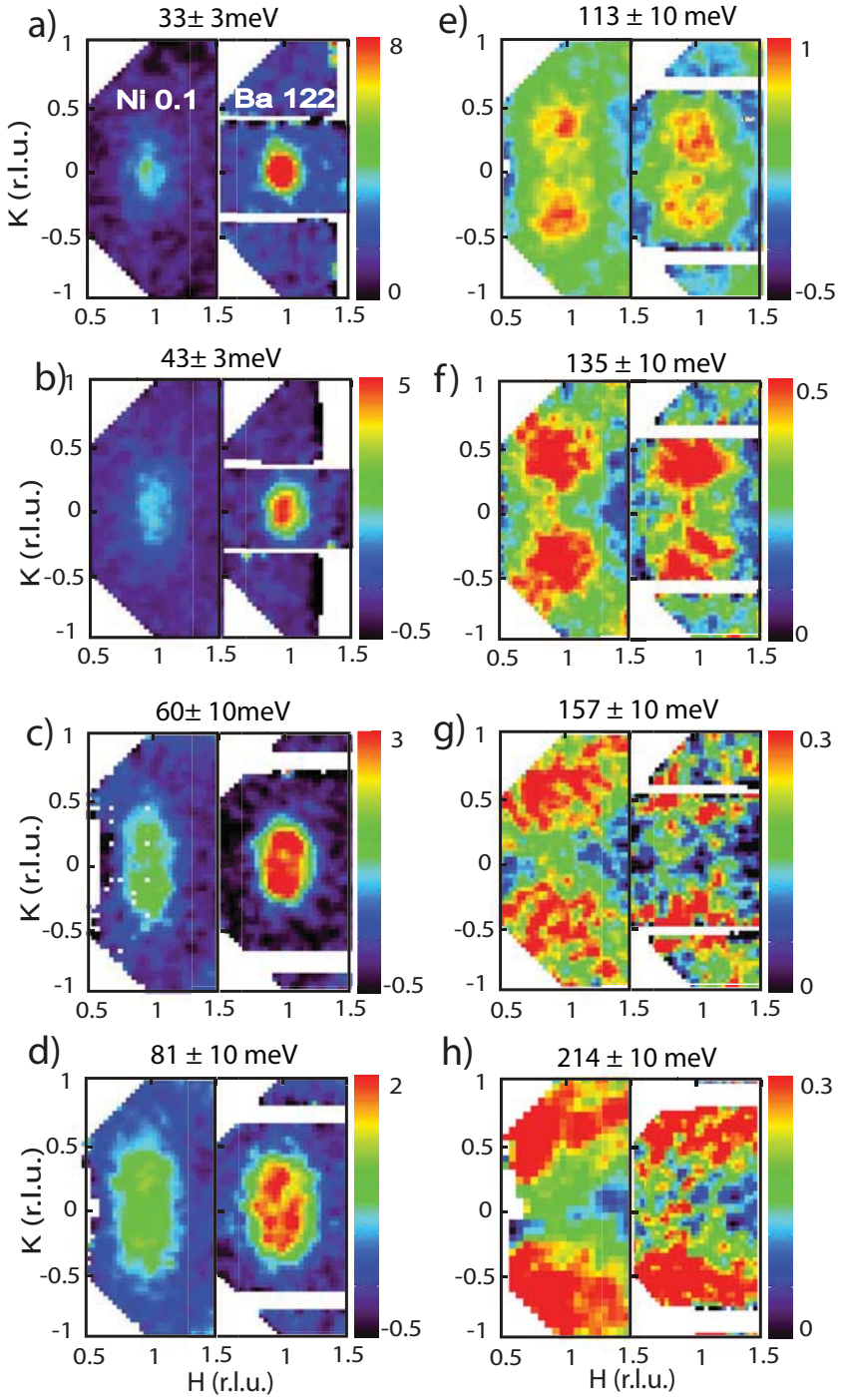

Figure 2.24: Constant-energy images of the spin excitations as a function of increasing energy for $BaFe_{1.9}Ni_{0.1}As_2$ and $BaFe_2As_2$ in units of mbarns/sr/meV/f.u.(a)$E = 33 \pm 3$, (b)43 ± 3, (c)60 ± 10, (d)81 ± 10, (e)113 ± 10, (f)135 ± 10, (g)157 ± 10, and(h)214 ± 10 meV.

in AF $BaFe_2As_2$ and superconducting $BaFe_{1.9}Ni_{0.1}As_2$ can be understood in a purely itinerant picture, we calculate the local susceptibility $\chi''(\omega)$ using the random phase approximation (RPA) based on realistic Fermi surfaces and band structures [90]. Using $\tilde{U} = 1.3$ eV and $\tilde{J} = 0.4$ eV as our screened Coulomb parameters and performing calculations above T_N [90], we find that the RPA estimate of $\chi''(\omega)$ for $BaFe_2As_2$ and $BaFe_{1.9}Ni_{0.1}As_2$ (dashed blue and red lines in Fig. 2.23 b) increases approximately linearly with energy and has absolute values about a factor of three smaller than the observation (Fig. 2.23 e). Although the RPA calculation depends on the Coulomb parameters used, we note that the five-orbital Hubbard model calculation using $\tilde{U}$ = 0.8 eV and $\tilde{J}$ = 0.2 eV produces essentially similar local magnetic spectra [36]. Therefore, a pure RPA-type itinerant model underestimates the absolute spectral weight of the magnetic excitations in iron pnictides.

The solid blue and red lines in Fig. 2.23 (b) show the calculated local susceptibility using a combined DFT and DMFT in the paramagnetic state. By comparing DFT+DMFT and RPA calculations in Fig. 2.23 (b) with data in Fig. 2.23 (e), we see that the former is much closer to the observation. Note that the calculation is done in the paramagnetic state, hence the low-energy modifications of the spectra due to the long range AF order are not captured in this calculation. RPA can describe only the itinerant part of the electron spectra, whereas DFT+DMFT captures the essential aspects of both the quasiparticles and the local moments of iron formed by strong Hund's coupling. The improved agreement of DFT+DMFT thus suggests that both the quasiparticles and the local moment aspects of the electrons of iron are needed to obtain the correct intensity and energy distribution of neutron scattering spectra. It is worth noting that the same abinitio methodology which is here used to compute the magnetic excitation spectra, was previously shown to describe the photoemission, the optical spectra and the magnetic moments of this material [137] in excellent agreement with experiment.

Chapter 3

Chalcogenides

3.1 Parent and Underdoped

3.1.1 Introduction

My work on the $Fe_ySe_xTe_{1-x}$ chalcogenides has been fairly limited, and is relegated primarily to a published triple axis study of the resonance at optimal doping ($x = 0.4$) and non-publishable triple axis work on a non superconducting underdoped derivative ($x = 0.3$). Nonetheless, in order to provide a comprehensive picture of the Fe-based superconductors, it is conducive to include a section describing the more salient magnetic features of the parent and underdoped compounds and to contrast this with the pnictides. As stated in the introduction, the crystal structure of the pnictides and chalcogenides are very similar and consist of stacked quasi-2D planes of Fe tetrahedrally coordinated with As or Te respectively. The fermiologies are also alike with a band structure dominated by Fe orbitals at the Fermi energy with electron and hole Fermi surface pockets sitting at the zone boundary and center respectively [118]. Given these similarities it is somewhat of a surprise that the magnetic ground state of the parent FeTe (which, like the pnictides, nests its electron and hole Fermi surfaces by a (1, 0) wave vector) consists of a 'double stripe' AFM order sitting at $(1/2, 1/2)$ as opposed to $(1, 0)$ [3]. Although the primary source of doping in the chalcogenides is

to isovalently substitute tellurium with selinium, there is a much less controlled, but equally important, interstitial doping of excess iron that has profound consequences on the magnetism within the system [117, 116]. As a result, the doping phase diagram of $Fe_ySe_xTe_{1-x}$ includes an extra degree of freedom: x-y-T. In general, manufacturing samples in stoichiometric proportions lead to a strong variation from the nominal iron content. Moreover, the amount of excess iron is more or less a random variable function of selinium doping with iron tending to approach stoichiometry near optimal Se doping. Thus, the coupling of these two forms of doping, Se and Fe, has made it inherently difficult to diffinitively ascribe the exact role that each plays in modifying the physics of the system and has highlighted the need to check the exact doping level of systems.

3.1.2 Local, Itinerant, Frustration...

In the parent Fe_yTe, the excitations at low energy ($\sim$ 9 meV) have been mapped out on powders for both $y = 1.05$ and 1.1 [117]. Here the increase in iron from 1.05 to 1.1 is sufficient to reduce T_N from 75K to 60K, close a 7meV spin gap in the energy spectrum, and drive the scattering off-center from the commensurate $(1/2, 1/2)$ AFM wave vector. Experiments to high energies at similar doping disparities, $y = 1.057$ [64] and 1.141 [143], appear to give a similar scattering profile (although a direct comparison of in-plane 2D scattering slices to the zone boundary is not readily available) and consist of diffuse scattering centered at the AFM wave vector that broadens above 20meV to such a large degree that it canvases the majority of the Brillouin zone. Although the scattering reaches energy transfers in excess of 200meV, above 20meV peak intensities are drastically reduced with the scattering shifting away from a simple spin wave like dispersive cone centered about the AFM wave vector Fig. 3.1. Attempts to fit the scattering to a Heisenberg model have met with some success but are limited to only acquiring a dispersion fit along the $(1, K)$ and $(H, 0)$ high symmetry directions but with effective exchange couplings that fail to fit the intensity

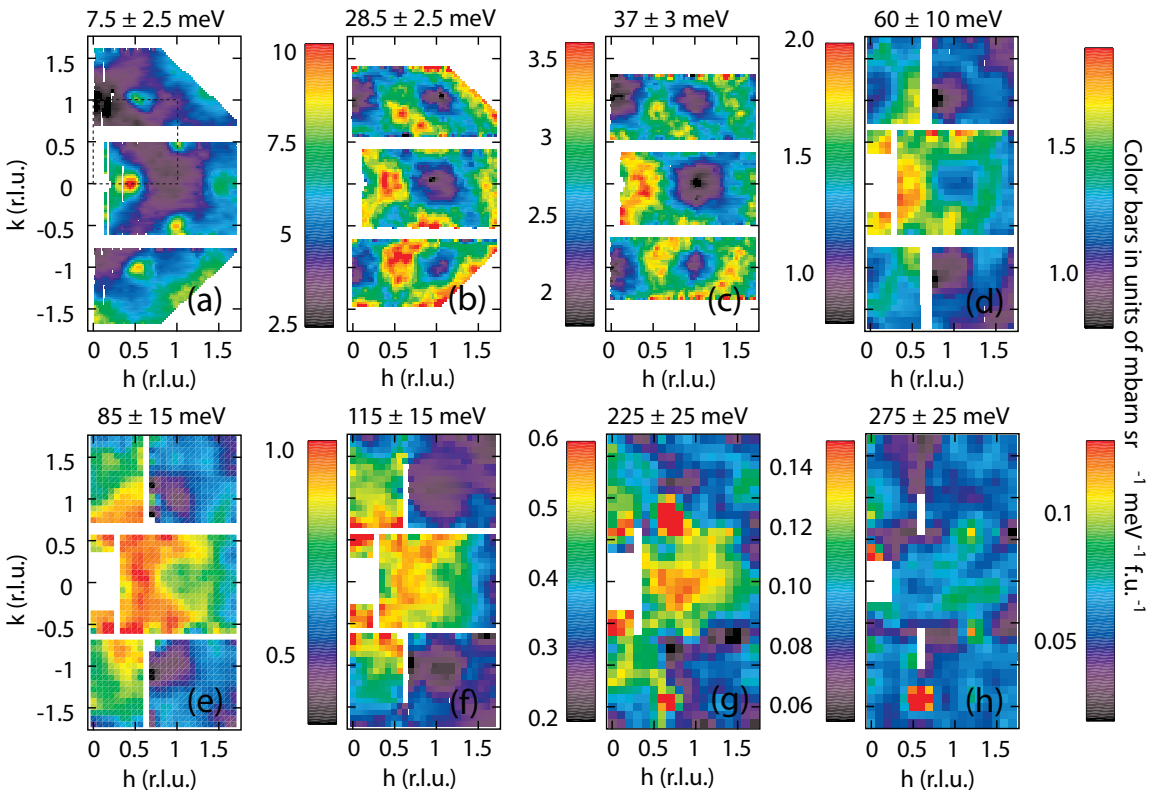

Figure 3.1: Constant energy slices of the spin waves as a function of increasing energy at 10 K for $Fe_{1.05}Te$. All data are normalized to absolute units with a vanadium standard. (a)(c) Collected with incident neutron energy $E_i = 90$ meV on ARCS, (d)(f) $E_i = 350$ meV on MAPS, (g),(h) $E_i = 500$ meV on MAPS. The dashed line in (a) shows a crystallographic BZ. Figure taken from [64].

and evolution of scattering across all of $(\mathbf{Q}, \omega)$ [64]. A separate model ascribes the role of excess iron in Fe_yTe as inducing collective modes on a spin frustrated lattice. In this picture, the excess iron acts as centers driving the condensation of four neighboring localized spins into a ferromagnetic arrangement. These four-spin plaquettes create a new collective degree of freedom that interact antiferromagnetically with neighboring plaquettes [143]. Fits of the data to this checkerboard cluster model have proven to fit the data quite well. In addition, the reduction of the static moment and T_N with increased excess iron [78], along with the exceptionally diffuse nature of the scattering and competition/transfer of spectral weight between the (1/2, 1/2) and (1,0) wave

vectors with doping [68] are all strong indicators that the addition of interstitial iron does directly frustrate the magnetism. Regardless of whether the excess iron does truly drive the moments to form fluctuating plaquettes, it is clear from experiments in both the parent and doped samples that the magnetic properties of the system are very sensitive to this secondary form of doping and complicate attempts to describe the microscopic physics.

As $Fe_ySe_xTe_{1-x}$ is tuned from the parent state to optimal doping $x \approx 0.4$ to 0.5 there is a cross-over of spectral weight at low energies from the AFM wave vector to the nesting wave vector. As well, with increasing doping the magnetic Bragg peaks broaden past the instrumental resolution indicating that the static order picks up a spin glass component with a switch from a long range to short range order [54]. By $x \approx 0.35$ all static order has dissolved and bulk superconductivity begins to emerge.

In underdoped $Fe_ySe_xTe_{1-x}$ the scattering co-exists at both the AFM and nesting wave vectors. At the $(1/2, 1/2)$ AFM position the scattering peaks slightly off center from this commensurate position depending on the amount of excess iron. At $(1, 0)$ the scattering consists of two transversely separated incommensurate peaks centered equidistant from $(1, 0)$ that follow a bell shaped dispersion. In a study on non superconducting $Fe_{1.01}Se_{0.28}Te_{0.72}$ it was shown that the distribution of spectral weight between the $(1, 0)$ and $(1/2, 1/2)$ positions vary as a function of energy. Below 6meV the scattering at $(1/2, 1/2)$ is strongly suppressed while, in contrast, the scattering at $(1, 0)$ only extends up to approximately 6 meV, demonstrating that the loss of spectral weight at one wave vector is offset by a corresponding increase at the other, Fig. 3.2. Temperature scans at E = 1meV at each of these wave vectors reveal that the scattering at both wave vectors follow identical critical scattering behavior with a steep increase in intensity and line width that starts at ∼50K (approximately T_N) before peaking around ∼100K and then dropping gradually off [8].

Time of flight neutron scattering studies of $Fe_{1.04}Se_{0.27}Te_{0.73}$ demonstrate that the high energy excitations in the underdoped region evolve from two incommensurate peaks centered transversely about $(1, 0)$ to a ring of scattering about $(1, 1)$ around

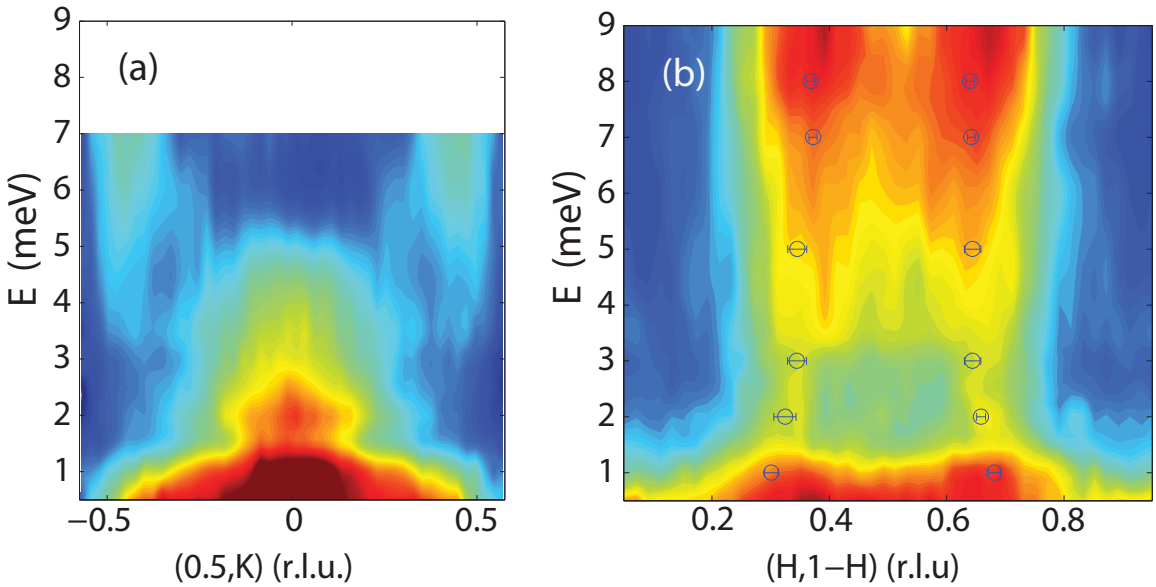

Figure 3.2: Contour plot of combined cuts for the T = 1.5 K data in the (a) [0.5,K] direction and (b) the [H,1 - H] direction through (0.5,0.5) as a function of energy. Both figures are plotted on the same energy scale so that the correspondence between the two excitations can be seen. Figure taken from [8]. Note that this figure uses tetragonal units whereas the body of my thesis uses orthorhombic units throughout.

45meV and, finally, for energies above 100meV this ring fills in completely to form a broad circle of scattering about $(1, 1)$ that survives to energy transfers in excess of 200meV [71]. Interestingly, this scattering profile is more reminiscent of the high energy scattering in $BaFe_2As_2$ (see Fig. 2.7) than the FeTe parent which consists of extremely broad scattering that is not always clearly associated with a particular wave vector at high energies. The same time of flight study also looked at optimal doped $FeSe_{0.49}Te_{0.51}$ and found that the evolution of high energy excitations are nearly identical to that of the underdoped sample. However, at low energies all scattering at the AFM wave vector is suppressed and the 7meV pseudo gap at the nesting vector closes.

The independent role of excess iron in underdoped samples has also been studied by Stock, *et. al* where they made powders of fixed Se content, x = 0.3, and varied the excess iron through the range of $\sim 1.01 - 1.05$ [116]. Low energy neutron scattering

studies revealed that the powder dispersions across the range of samples consist of a broad first moment peak centered at Q_{AFM} for $y \approx 1.05$ that systematically evolves to $Q_{nesting}$ as y is reduced to a near stoichiometric level of $y = 1.01$ Fig. 3.3 a) - d), f). Given that this same wave vector transfer has been observed for Se doping this demonstrates that tuning of excess iron provides a second pathway for destroying the fluctuations at the AFM wave vector. Moreover, the superconducting volume fraction as determined from susceptibility measurements increases from ∼1% at $y = 1.05$ to ∼17% at $y = 1.01$ which supports the conclusion that the Q_{AFM} fluctuations destroy superconductivity and the $Q_{nesting}$ promote it. In panels Fig. 3.3 e), g) we see that increasing the excess iron also systematically reduces the average energy $E_0 = \int E \cdot S(E)dE / \int S(E)dE$ while increasing the total low energy spectral weight $I = \int S(\mathbf{Q}, E)d\mathbf{Q}dE$. This can be understood in terms of the closing of a spin gap when sufficient excess iron is introduced, which brings with it additional intensity in the previously gapped region and, as a direct consequence, drives down the average energy E_0.

3.1.3 Conclusion

From the above discussion it is clear that the physics of the chalchogenide superconductors deviate considerably from those of the pnictides. However, we find that the same discussion of itinerant vs local reemerges, albeit in both form and detail that are distinct from the pnictides. The fact that the $(1, 0)$ nesting vector competes for spectral weight with the $(1/2, 1/2)$ AFM wave vector is strong indication that itinerant electrons and stoner enhancement play a role in shaping the physics of the system. However, the very existence of magnetic scattering at $(1/2, 1/2)$ makes a fully itinerant scenario difficult to defend. Indeed, in a localized $J_1 - J_2 - J_3$ picture, the evolution with doping of magnetic scattering from the AFM wave vector to the nesting vector can be understood in terms of the structural deformation imposed by selenium; this deformation leads to a reduction in chalcogen height and, as a direct consequence,

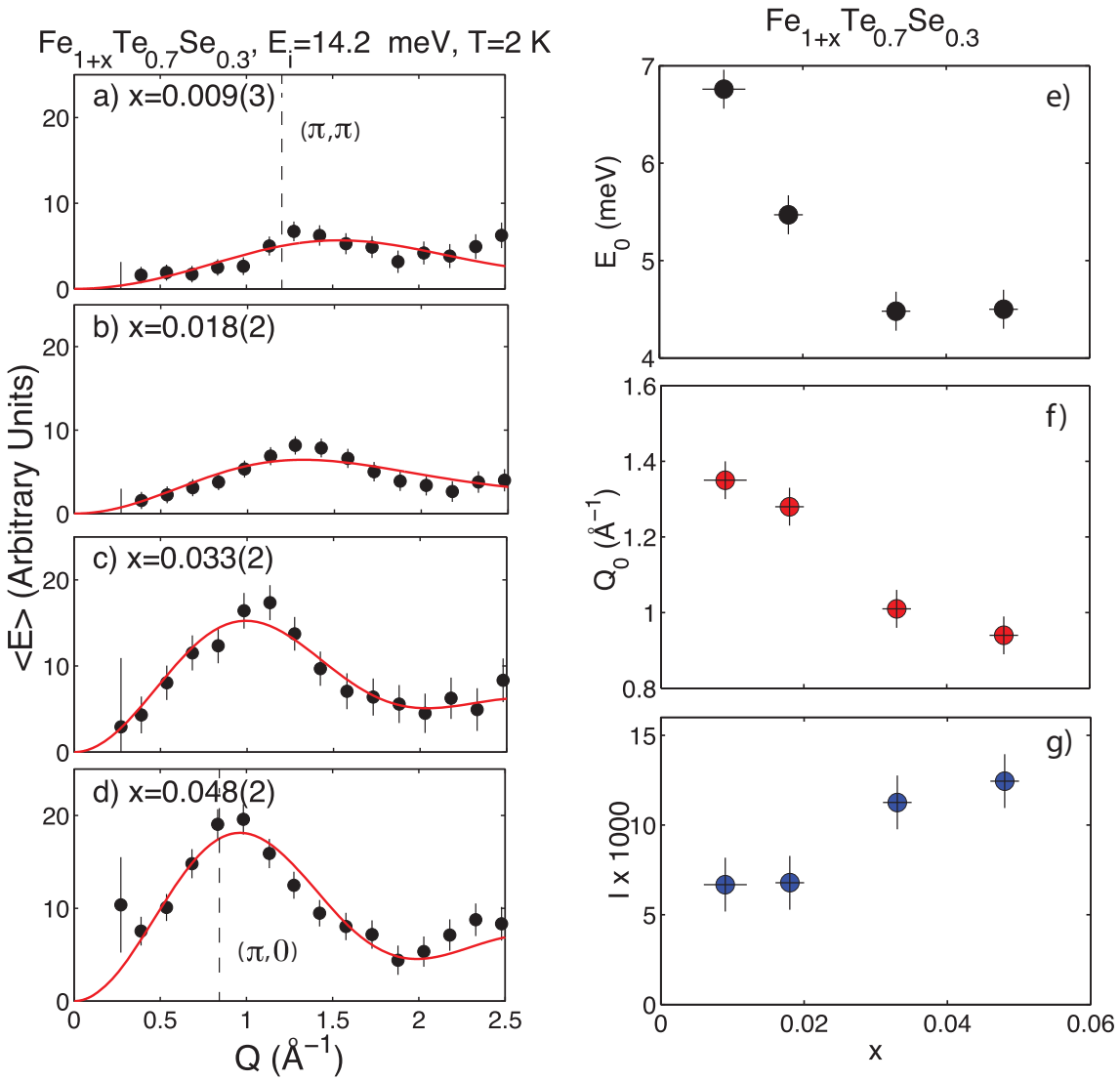

Figure 3.3: a)-d) The first momentum in energy as a function of momentum transfer is illustrated for the interstitial iron concentrations investigated. The solid curves are fits to the Hohenberg-Brinkman sum rule described in the original paper from which this figure was taken [116]. e) Peak position of the magnetic spectrum in momentum. f) Mean energy position. (g) Total integrated intensity in energy and momentum as a function of interstitial iron concentration. All of the data is presented for $T = 2$ K.

a corresponding increase in J_1, J_2, and reduction in J_3. Such a modification to the exchange couplings acts to reduce the bicollinear phase, resulting in a reduction in the energy scale required to suppress scattering at $(1/2, 1/2)$ and transfer spectral weight to the nesting vector [8]. Equally, in resistivity measurements, at low temperatures a sign change in the derivative, dI/dT, as a function of doping has been observed, indicating that there is a cross-over from weakly localized spins to a more metallic state as the doping is increased [68]. It is doubtful that the local and itinerant phases exist independently with no direct interplay other than to grow or shrink at the others expense. As mentioned above, studies of the low energy spectral weight at the two wave vectors follow an identical temperature dependence linking them to the transition from a long range ordered to paramagnetic state; indicating that both types of fluctuations have a common origin. To confound the physics further, a more extensive study of the total sum spectral weight across all $(\mathbf{Q}, \omega)$ reveals that the effective moment is not conserved as a function of temperature in the parent which has lead some to conclude that there is a cross-over of electrons between the local and itinerant channels as the temperature is increased [143]. However, unlike the low energy spectral weight, this temperature dependence is oblivious to the magnetic phase transition (see Section 4.1 for a more complete discussion). Added to all this is the fact that excess interstitial iron acts as a strong source of frustration thus further complicating the mixture of physics already present.

Taken together, it is clear that the rich physics present in $FeSe_xTe_{1-x}$ has lead to many interesting discoveries but an incomplete picture. However, the unique magnetism of this system has provided us with a rare instance to observe the effect of two co-existing magnetic fluctuating orders on an emerging superconducting phase. In this regard, we have found that the weakly localized magnetic order at $(1/2, 1/2)$ hinders the development of superconductivity, while the magnetism at $(1, 0)$ that dominates in the more metallic region of the phase diagram both coexists and couples to the superconducting state. In the non superconducting parent, long range static order and strong fluctuations about the AFM wave vector dominate the system at low

energies and superconductivity is completely suppressed. In the underdoped region filamentary superconductivity can survive in the presence of persisting short range static order with spectral weight sitting at both wave vectors. However, it is not until the static order has completely dissolved and the majority of low energy fluctuations associated with the AFM wave vector have transfered over to the nesting vector that bulk superconductivity can gain a solid foothold within the system.

3.2 Optimal Doped

3.2.1 Introduction

As in the pnictide superconductors, the chalcogenides exhibit a resonant mode in the magnetic spectrum when cooled below T_c [98]. In the s^{+-} picture this resonance is expected to appear at an energy transfer equal to (or slightly smaller than) the superconducting gap 2Δ. This picture was already supported by the 3D nature of the resonance in doped $BaFe_2As_2$, which can be ascribed to an L-modulated 3D superconducting gap [9]. As well, all of the measured base temperature resonance modes mapped out in the Fe-based families are at an energy transfer that is less than 2Δ [140]. However, a more direct test of this picture was performed on optimal Co doped $BaFe_2As_2$ where the mode energy was remeasured over a range of temperatures from base to T_c. Since the superconducting gap reduces in magnitude as an order parameter when T_c is approached, this implies that the resonance energy should shift to lower energy values with increasing temperature in order to remain bounded by the reducing superconducting gap energy. In this experiment, it was discovered that this is indeed the case [49] for the electron doped pnictides. Indeed, with increasing temperature the resonance energy followed an order parameter very similar to that of the superconducting gap and with the reduction in superconductivity met by a corresponding reduction in the intensity of the resonance. A similar

study has also been performed on optimal Ni doped $BaFe_2As_2$, but using an out-of-plane magnetic field instead of temperature as the tuning parameter to reduce the superconducting gap [146]. Likewise, the application of a 14.5T field resulted in a corresponding reduction in the mode energy and intensity. As well, the appearance of the resonance tracked the shift in T_c upon application of the field. Taken together, the above measurements provide strong evidence that the resonance mode is a byproduct of the superconducting coherence factor and linked to sign reversal of nested superconducting gaps.

In contrast, the cuprates also show sign reversal on alternating lobes of the d-wave superconducting gap. However, it has been shown that the resonance energy in fully oxygenated $YBa_2Cu_3O_7$ is insensitive to temperature changes, at least within the range of experimental measurements up to $0.8T_c$ [33]. This strongly suggests that the resonance energy does not remain bounded below the superconducting gap energy as T_c is approached. Given that the resonance is a ubiquitous property of unconventional superconductivity, it stands to reason that the mode would have a common origin in all of the superconducting families. Although other properties of the resonance (ie: dimensionality, line width, intensity, etc.) can and do differ between different systems, a lack of similar behavior in the temperature dependence of the resonance energy is very difficult to justify in a picture describing it as originating from sign-reversal on different parts of the superconducting gap. Since the physics of the cuprates and the pnictides are quite removed from one another, it is highly interesting to retest the temperature dependence of the resonance on the much more closely related $FeSe_xTe_{1-x}$. At the time of our study there was evidence on $FeSe_xTe_{1-x}$ that the picture of a sign reversed scattering enhanced resonance did not work for this system. Specifically, measurements under an in-plane field in optimal doped $FeSe_xTe_{1-x}$ $x = 0.5, (x = 0.4)$ of strength $H = 7T, (H = 14T)$ did not observed any shift in the energy of the resonance. As well, an existing study of the resonance in $FeSe_{0.4}Te_{0.6}$ provides a very nice color plot suggesting that the resonance energy is independent of temperature [98]. However, since the scan resolution of their color

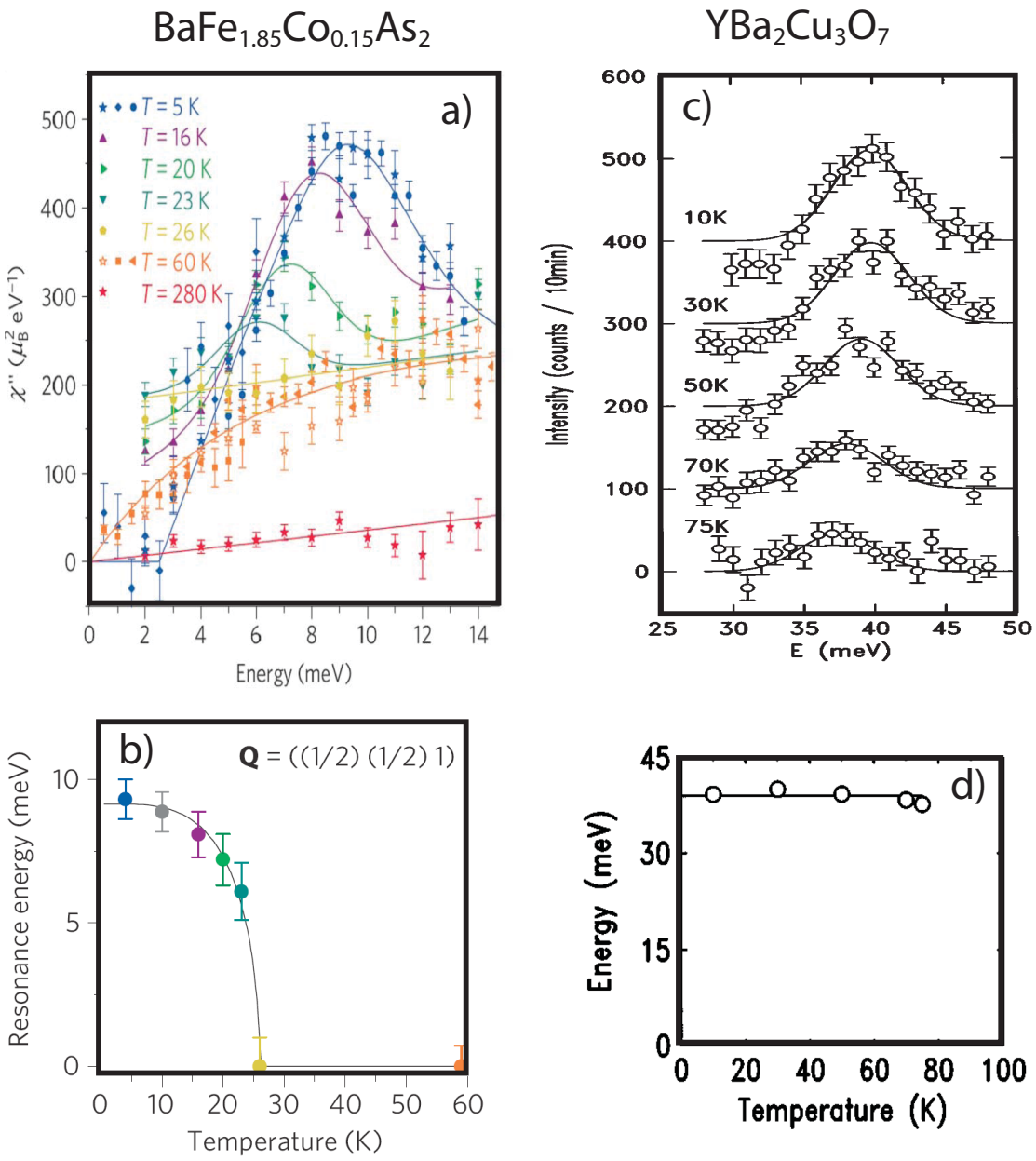

Figure 3.4: a), c) Energy scans of the resonance at different temperatures. b), d) Energy of the resonance obtained by fits to the data from panels a) and c) respectively. Panels a), b) taken from [49] and panels c), d) taken from [33].

profile is unknown, it is possible that the resonance did shift in energy but that this information was lost when interpolated into a color plot. Indeed, in Inosov's paper [49] demonstrating that the energy of the resonance in optimal doped Ba(122) is dependent on temperature, it is his careful analysis of the 1D cuts that are convincing, his 2D mesh of Energy vs Temp is not very suggestive at all. We addressed the above concerns by producing a systematic series of energy scans very close in temperature (separated by only 1-2 degrees) and directly checked each one for a shift in energy.

At the time of our study the 3D L-dependent character of the resonance had already been observed in the pnictides [9, 96]. For the chalcogenides, existing studies suggested that the resonance was completely independent of L, although this had yet been confirmed directly. In our work [41], we report inelastic neutron-scattering studies of superconducting $FeTe_{0.6}Se_{0.4}$ (T_c = 14 K). First, we confirm the earlier work [98] that the mode is purely two dimensional and dispersionless for wave vectors along the c axis, which is different from the dispersive nature of the resonance in electron-doped $BaFe_{2-x}(Co,Ni)_xAs_2$. Second, we extend the earlier work [98] on the temperature dependence of the mode. By carrying out systematic series of energy scans very close and above the superconducting transition temperature T_c, we find that the energy of the mode is essentially temperature independent and collapses at a temperature slightly above T_c, and does not follow the temperature dependence of the superconducting electronic gap as determined from Andreev reflection measurements [93]. Finally, we show that the intensity gain of the resonance is approximately compensated by spectral weight loss at energies below it, and there is a spin gap opening for low-energy spin excitations below T_c. These results suggest that the neutron spin resonance in the $FeTe_{0.6}Se_{0.4}$ system may not be directly coupled to the superconducting electronic gap as those for $BaFe_{2-x}(Co,Ni)_xAs_2$.

3.2.2 Characterization of the Resonance Mode Energy

We carried out neutron-scattering experiments on the HB-3 thermal triple axis spectrometer at the High Flux Isotope Reactor (HFIR), Oak Ridge National Laboratory. We used a pyrolytic graphite PG(002) monochromator and analyzer with a collimation of 48'-monochromator-60'-sample-80'-analyzer-240'-detector. The data were collected in fixed E_f mode at 14.7 meV with a PG filter placed between the sample and analyzer to remove contamination from higher-order reflections. We coaligned two single crystals in the [H,H,L] scattering plane and loaded them in a liquid-He orange cryostat. The total mass was ∼10 g with an in-plane and out-of-plane mosaic of 2.0^o and 2.1^o full width at half maximum (FWHM), respectively. We defined the wave vector Q at (q_x, q_y, q_z) as $(H, K, L) = (q_x a/2\pi, q_y b/2\pi, q_z c/2\pi)$ reciprocal-lattice units (rlu) using the tetragonal unit cell (space group P4/nmm), where $a = 3.8\mathring{A}$, $b = 3.8\mathring{A}$, and $c = 6.0\mathring{A}$. In the earlier sections on the parent and underdoped compounds, all units were reported in th orthorhombic cell which placed the AFM wave vector at $(1/2, 1/2, 1/2)_O$ and the nesting vector at $(1, 0, 0)_O$. However, since our work on $FeTe_{0.6}Se_{0.4}$ was published with the discussion and figures (which are included in my thesis below) in the tetragonal unit cell, I will now break from the usage of orthorhombic units in favor of tetragonal. This corresponds to a 45° vector rotation with the AFM wave vector now sitting at $(1/2, 0, 1/2)_T$ and the nesting vector at $(1/2, 1/2, 0)_T$; the subscripts will be suppressed for the remainder of the discussion.

In the non superconducting $FeTe_{1-x}Se_x$ samples (x = 0.3), spin excitations coexist at both the $(1/2, 0, 1/2)$ AFM wave vector, and the $(1/2, 1/2, L)$ wave vector associated with nesting of electron and hole pockets on the Fermi surface. Upon reaching optimal doping, spin excitations at the AFM wave vector are suppressed, however, they remain strong near the nesting vector and consist of a commensurate resonance mode (in the superconducting state) sitting on top of an incommensurate magnetic signal that follows an hourglass dispersion at low energies [63]. We chose

the [H,H,L] scattering plane for our experiments since this zone gives us full freedom to probe the L dependence of the resonance. In general, the excitations in this system are extremely diffuse and, as a result, much broader than the instrumental resolution. To quantify this, we have calculated the resolution along the $(H, 1-H)$ direction at the $(0.5, 0.5)$ position as a function of energy. The resulting instrumental resolution width in FWHM is roughly 20 times smaller than the incommensurate peak separation. Thus our data collection is a good measure of signal centered directly at the $(0.5, 0.5)$ position.

Although previous measurements suggest that the resonance in $FeTe_{1-x}Se_x$ is two-dimensional [85, 98], there have been no explicit measurements of the resonance at different L- values. With this in mind, we have carried out detailed energy scans of bulk superconducting $FeTe_{0.6}Se_{0.4}$ at the resonance wave vector $(1/2, 1/2, L)$ as a function of temperature and L. Figures 3.5c-e show constant-Q scans at the signal $Q = (0.5, 0.5, 0)$, $(0.5, 0.5, 0.5)$, $(0.5, 0.5, 1)$ and background $Q = (0.65, 0.65, 0)$ positions above and below T_c. Consistent with earlier results [85, 98], we see a clear enhancement of scattering around $E \approx 7$ meV below T_c at the signal wave vectors for all the L values probed. Figure 3.5f over-plots the temperature differences between 2 K and 25 K data for three L values. It is clear that for all L values the resonance energy is the same within the errors of our measurements ($E = 6.95 \pm 0.5$ meV). Therefore, in comparison, we find that the dimensionality of the mode is more like the cuprates (2D) as opposed to the dispersive mode along the c-axis observed in the more closely related electron doped pnictides.

In previous neutron scattering experiments on optimally electron-doped $BaFe_{2-x}Co_xAs_2$, careful temperature dependence measurements revealed that the energy of the resonance with increasing temperature tracks the temperature dependence of the superconducting gap energy [49]. These results, as well as the magnetic field effect of the resonance [146], provided compelling evidence that the resonance energy is intimately associated with the superconducting electronic gap energies. To see if the resonance in $FeTe_{0.6}Se_{0.4}$ behaves similarly, we carried out a series of energy scans

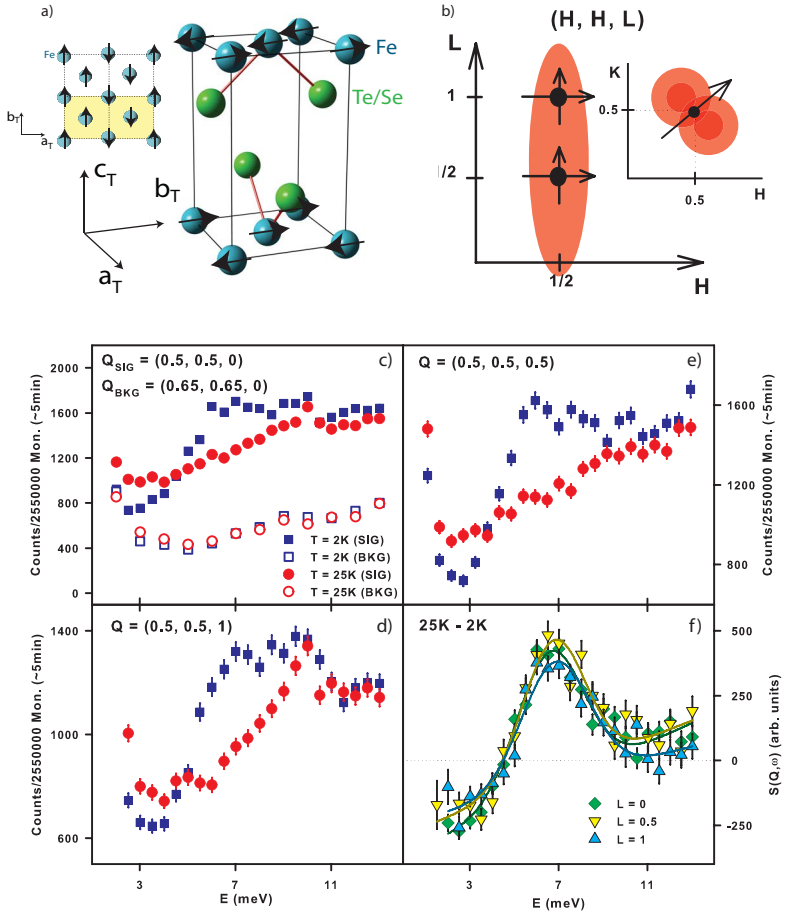

Figure 3.5: (a) Diagram of the Fe spin ordering with the shaded region defining the magnetic unit cell. (b) Cartoon of the scan directions though the $(1/2, 1/2, L)$ nesting vector. The inset illustrates the direction in the $[H, K]$ plane that scans were confined to. Excitations at $(1/2, 1/2, L)$ in $FeTe_{1-x}Se_x$ consist of two incommensurate peaks that spread away from one another in the transverse direction. The red circles in the inset depict these excitations with the radius of the circles equal to twice the FWHM of the (1/2, 1/2, 0), 7.5 meV resonance peaks measured on crystals from the same batch on a different experiment. The separation of their centers is set to agree with the dispersion mapped out in this previous experiment [63] (c-e) Energy scans about the 7 meV resonance position above and below T_c for $L = 0, 1/2, 1$. Clear intensity gain is observed inside the superconducting state. The background at $L = 0$ is plotted above and below T_c and is found to be identical, allowing direct temperature subtraction of the scans with no need for background correction. (f) Temperature subtraction of energy scans shown in panels (c-e) demonstrating no observable dispersion of the resonance energy along L.

Figure 3.6: (Figure on next page.)(a) Raw data for energy scans at $Q = (1/2, 1/2, 1/2)$ for multiple temperatures below T_c. At 2 K the 7 meV resonance is clearly present. A strong reduction in scattering for energies below 4 meV is also visible, indicating the opening of a gap in the system. Subsequent Q-scans, however, show that this is not a true gap. As the temperature increases to T_c the resonance suppresses and the partial gap closes up. (b) Temperature subtraction of scans shown in panel (a). All of the data is fit with a Gaussian leaving the center energy as a free parameter to be determined. (c) Position of the resonance energy vs temperature as determined from the fits in panel b), note that circle above T = 15K are meant to indicate that the resonance has been completely suppressed. The temperature dependence of the superconducting gap [93] is also graphed, explicitly demonstrating that the resonance does not shift in energy as a function of temperature so as to remain inside 2Δ as required by the spin exciton scenario.

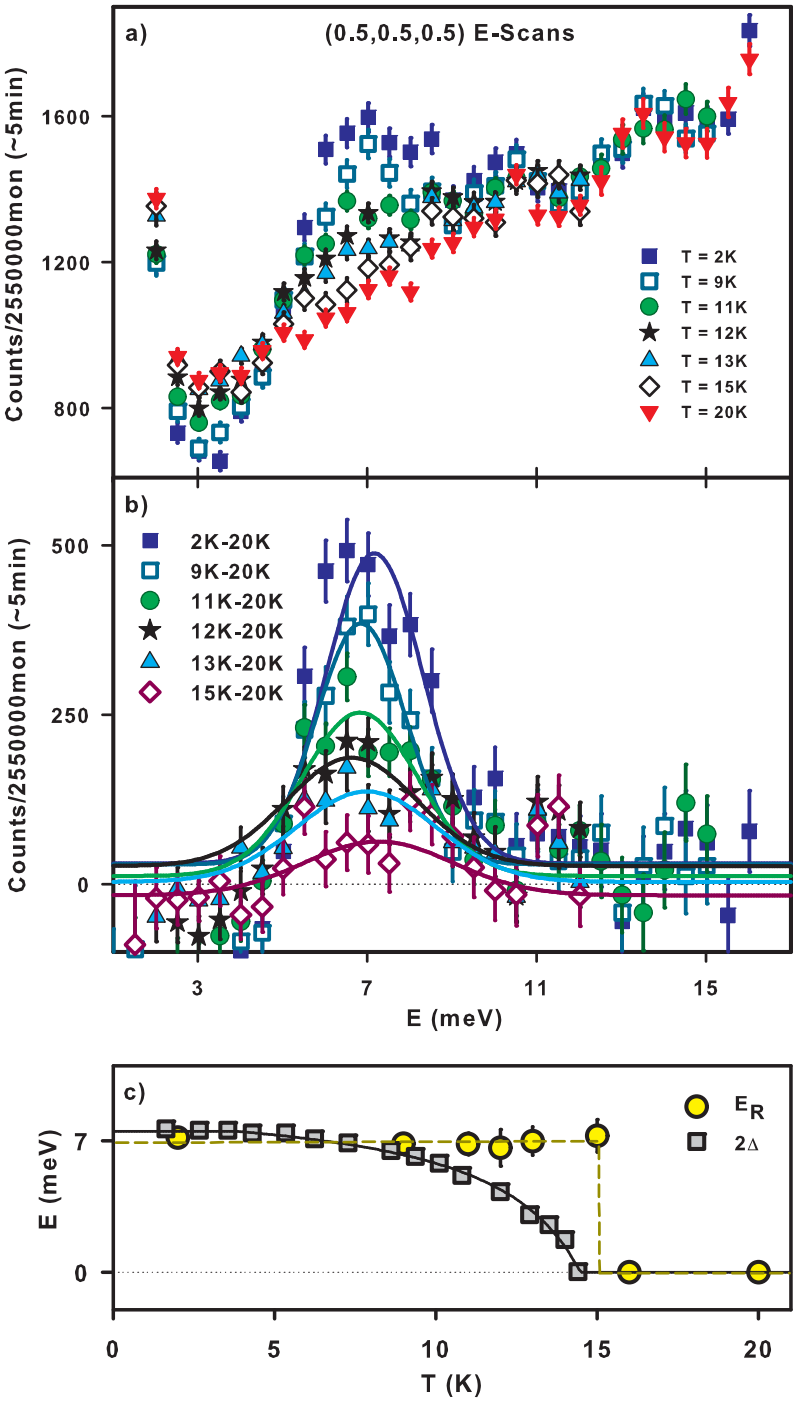

Figure 3.6: Caption on previous page.

from base temperature (2 K) to just above T_c (20 K) at $Q = (0.5, 0.5, 0.5)$ (Fig. 3.6a). As the temperature is increased, we see that the resonance drops monotonically in intensity. To accurately determine the temperature dependence of the mode, the energy scans in the superconducting state were subtracted from the energy scan at 20 K in the normal state. The resulting plots of the resonance intensity gain were then fit to a Gaussian on a linear background with the center left as a free parameter (Fig. 3.6b). By plotting the fitted values of the resonance energy as a function of temperature (Fig. 3.6c), we see that the resonance energy is essentially temperature independent until it abruptly disappears above T_c. This is clearly different from the temperature dependence of the resonance for electron-doped $BaFe_{2-x}Co_xAs_2$ [49] and the temperature dependence of the superconducting gap for $FeTe_{0.6}Se_{0.4}$ as determined from the Andreev reflection measurements (Fig. 3.6c) [93].

To further characterize the resonance, a series of Q-scans were carried out at $E = 6.5$ meV. Scans along the $[H, H]$ direction for $L = 0.5$ confirm that the resonance peaks at the $(0.5, 0.5)$ position with a strong gain in intensity in the superconducting state (Figs. 3.7a and 3.7c). For temperatures above 20 K, the drop in intensity is much more gradual with the peak at $(0.5, 0.5)$ fully suppressed by 100 K. Similar scans along the $[0.5, 0.5, L]$ direction (Fig 3.7d-f) reveal that the scattering is much broader. The intensity gain of the resonance is extracted by subtraction of the 20 K and 2 K data. The L-dependence of the signal fits well to the Fe^{2+} form factor, a further indication that the resonance is purely two-dimensional in nature. A temperature scan at $(0.5, 0.5, 0.5)$ for $E = 6.8$ meV confirmed that the resonance is strongest at base temperatures and then reduces like an order parameter to T_c in good agreement with earlier measurements of the system [85, 98, 63].

Interestingly, the 15K energy scan in Fig. 3.6 b) and the temperature scan of the resonance in Fig. 3.7 e,f) suggest that the resonance mode first forms in the normal state while in close proximity to superconductivity. This behavior was also observed by Qiu [98] in their temperature and energy scans of the resonance in $FeSe_{0.4}Te_{0.6}$. A similar analysis on optimally doped $BaFe_{1.85}Co_{0.15}As_2$ does not display such behavior

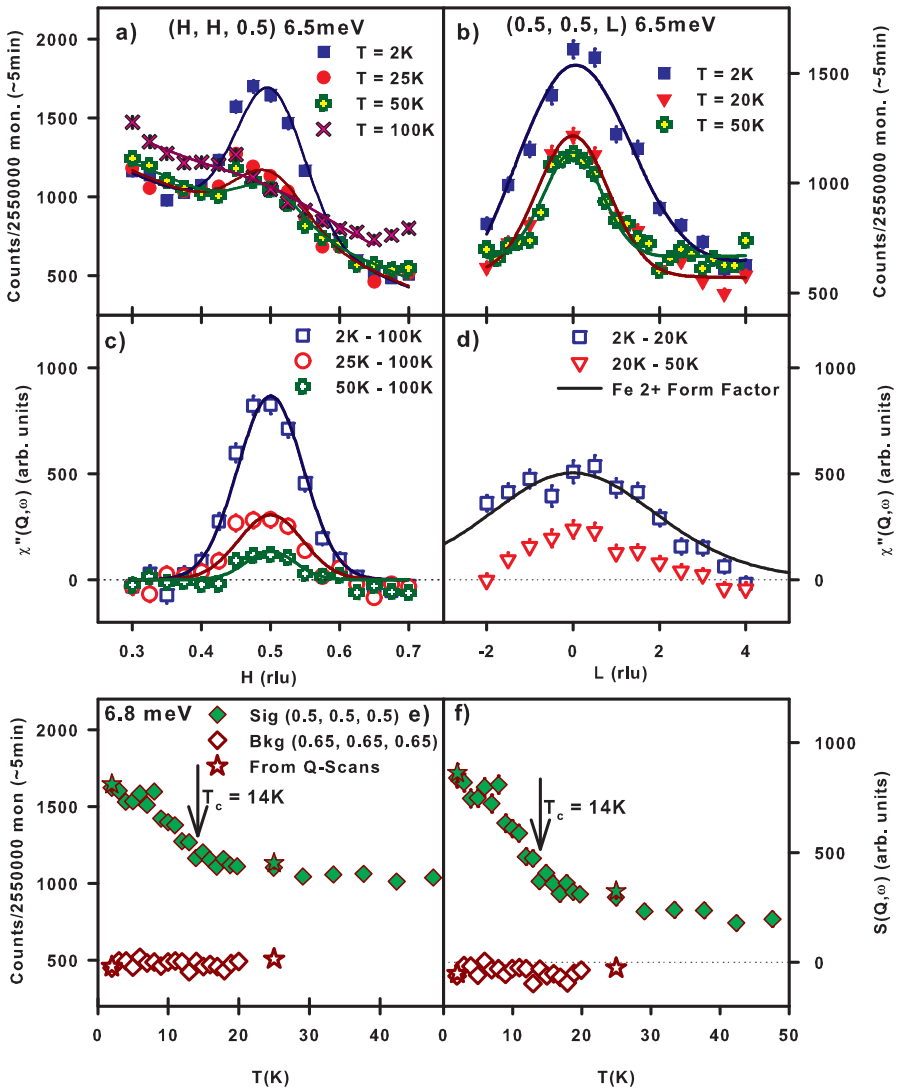

Figure 3.7: (a,b) Raw Q-scan data along $[H, H]$ and L respectively at $E_R = 6.5$meV at several temperatures. (c,d) $\chi''(Q, \omega)$ is determined by subtraction of the background and correcting for the Bose factor. In c) the 100 K data was used as a final background subtraction in order to remove a spurion at (0.45, 0.45, 0.5) and a phonon tail for points near (0.7, 0.7, 0.5). (d) The intensity gain due to the resonance is determined by subtraction of the 2 K and 20 K data. The resulting signal is very broad and fits well to the Fe^{2+} form factor; a testament to the 2D nature of the resonant mode. (e,f) Temperature dependence of the resonance for $Q = (1/2, 1/2, 1/2)$ and $E = 6.8$ meV. The resonance suppresses as an order parameter as T_c is approached.

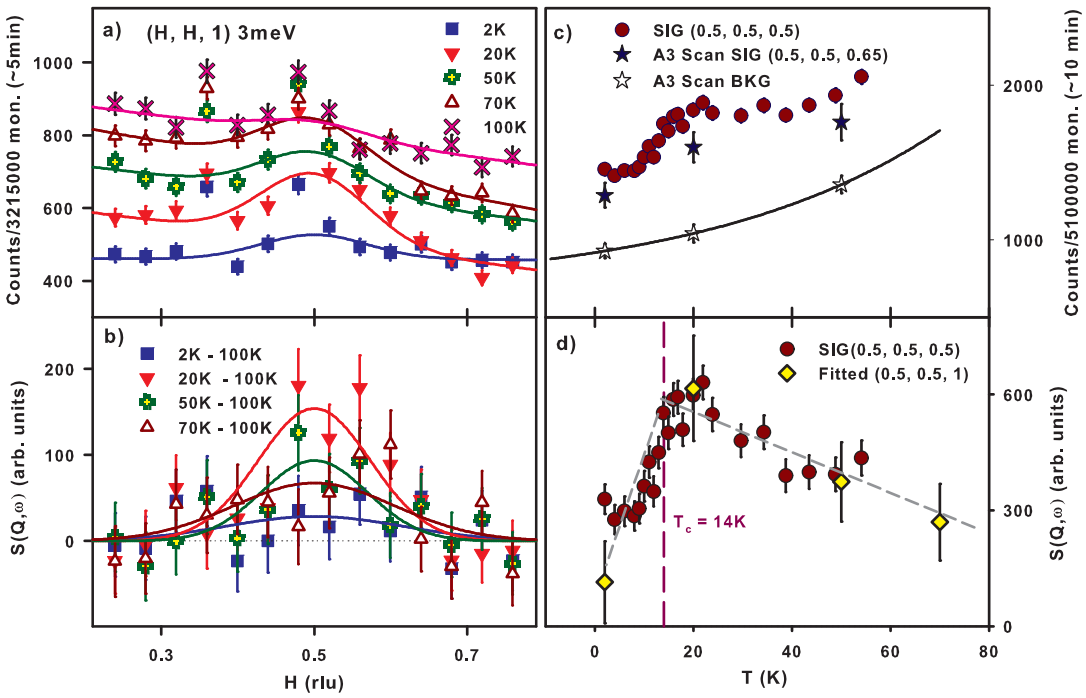

Figure 3.8: (a,b) Q-scan data along the $[H, H]$ direction for $L = 1$ and $E = 3$ meV. The scattering becomes stronger as T_c is approached from higher temperatures, upon entering the superconducting state the intensity drops significantly by 2 K but does not fully gap. (c) Temperature dependence at 3 meV inside of the pseudo spin gap region reveals that near T_c a gap begins to form but never fully forms by base temperature. (d) $S(Q, \omega)$ of the temperature scan as determined by interpolating and subtracting the background collected using A3 rocking curves. Yellow diamonds correspond to cross checks with fitted Q-scans from panels (a,b). Since the Q-scans and temperature scan were collected on different experiments, the data sets were not normalized to one another by monitor count but rather shifted to coincide at 20 K.

[146]. Although the origin of this effect is unclear, it is consistent with the idea of preformed Cooper pairs developing in the normal state prior to establishing long range phase coherence. Indeed, an early onset resonance extending more than 50K above T_c has been associated with the psuedogap region of $YBa_2Cu_3O_{6+x}$ where preformed pairs have been hypothesized as the origin of this state [20].

From Figs. 3.5 and 3.6, we see that the intensity gain of resonance in the superconducting state is accompanied by a loss in signal for energies below 4 meV, suggesting that conservation of spectral weight is satisfied by a reduction of scattering below the resonance energy. However, earlier measurements [63] suggest that the spin gap in $FeTe_{0.6}Se_{0.4}$ is unclean and does not fully open until ∼1 meV. Thus, it is interesting to investigate the temperature dependence of the spin excitations for energies above the spin gap and below the resonance. Figure 3.8a shows Q-scans along the $[H, H, 1]$ direction at different temperatures. With increasing temperature from 2 K, a peak at $(0.5, 0.5, 1)$ above background initially increases at $T_{=}20$ K, then decreases upon further warming until disappearing at 100 K. Assuming that there are only background scattering at 100 K, the temperature difference plots in Fig. 3.8b confirm that the magnetic scattering increases on warming to T_c and then decreases with further increasing temperature. Figure 3.8c shows the detailed temperature dependence data at the signal $Q = (0.5, 0.5, 0.5)$ and background (sample rotated away from the signal position by 30 degrees) position. As we can see, the scattering shows a clear kink at T_c and decreases monotonically above T_c with warming. Figure 3.8 shows the background corrected temperature dependence of the magnetic scattering assuming that the temperature dependence of the background follows the solid line in Fig. 3.8c. The effect of superconductivity is to open a pseudo gap in spin excitations spectrum below T_c.

In the case of electron and hole-doped Ba-122, the enhancement of the resonance occurs at the expense of a full spin gap opening below the resonance. Previously, the situation for Fe(Se,Te) was not completely clear since there are no clean spin gaps for Fe(Se,Te). Furthermore, it was not even clear whether the reduction in magnetic

intensity at energies below the resonance occurs exactly at T_c, when the resonance appears. From our data we see that this is indeed the case, which suggests that the intensity gain of the resonance comes at the expense of spectral weight loss for energies below the resonance. It is worth noting that in terms of lightly doped, non superconducting FeTe, measurements at (0.5, 0.5) also reveal a loss in scattering at 3meV. However, for this underdoped system no resonance is present to suck away spectral weight. Rather, the signal loss is due to the fact that at lower dopings there exists inelastic magnetic scattering at both (0.5,0) and (0.5, 0.5) with a strong crossover of spectral weight between these wave vectors occurring around 3meV [8].

To determine whether spin excitations at energies above the resonance also respond to superconductivity, we carried out a series of constant-energy $E = 11$ meV scans along the $[H, H, 1]$ direction. The outcome shown in Figs. 3.9a and b reveals that magnetic scattering gradually increases in intensity on cooling. However, upon entering the superconducting state, the scattering appears to level off with the 2 K and 20 K Q-scans nearly identical in intensity. Temperature scans at $E = 11$ meV at the signal $[Q = (0.5, 0.5, 0.5)]$ and background $[Q = (0.7, 0.7, 0.5)]$ positions are shown in Fig. 3.9c. The background and Bose factor corrected temperature dependent imaginary part of the dynamic susceptibility, $\chi''(Q, E)$, at $Q = (0.5, 0.5, 0.5)$ and $E = 11$ meV is shown in Fig. 3.9d. It is clear that the magnetic scattering grows with decreasing temperature but essentially saturates at temperatures below $\sim$15 K.

Finally, Figure 3.10a shows the temperature evolution of the constant-Q $[Q = (0.5, 0.5, 0.5)]$ scans from 2 K to 100 K. After correcting for the temperature dependence of the background scattering and Bose population factor, we obtain the temperature dependence of $\chi''(Q, E)$ at $Q = (0.5, 0.5, 0.5)$ (Fig. 3.10b). The $\chi''(Q, E)$ increases linearly with increasing energy, and the resonance appears below T_c together with the opening of a spin gap at lower energies. These results are consistent with earlier work [85, 98].

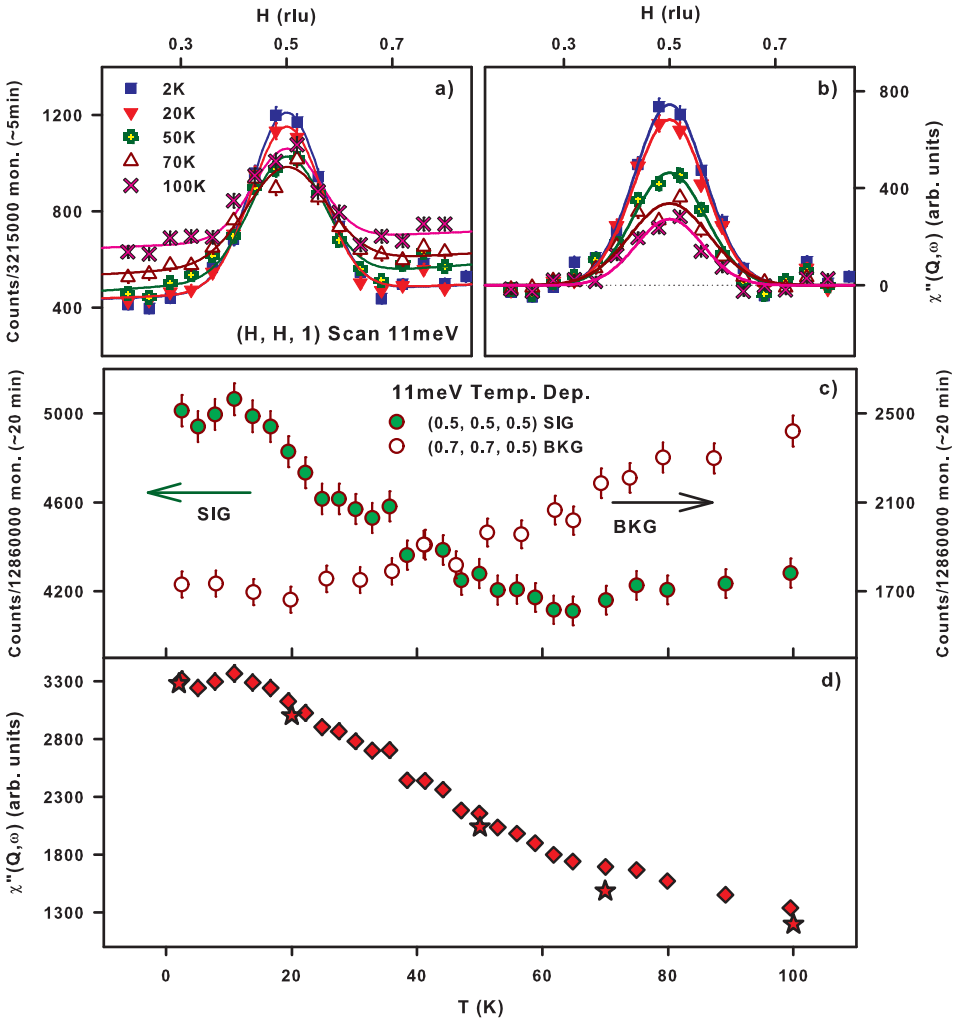

Figure 3.9: (a) Raw Q-scan data along the $[H, H]$ direction for $L = 1$ and $E = 11$ meV. (b) $\chi''(Q, \omega)$ determined by background subtraction and correcting for the Bose factor. The resonance is no longer visible, instead the scattering at 2 K is nearly identical to 20 K. Upon entering the normal state, the intensity begins dropping monotonically with increasing temperature but remains robust up to 100 K. (c,d) Temperature scan at (1/2, 1/2, 1/2) for $E = 11$ meV. Red stars correspond to cross checks with fitted peak intensities from Q-scans in panel a) that have been form factor corrected and normalized by monitor count.

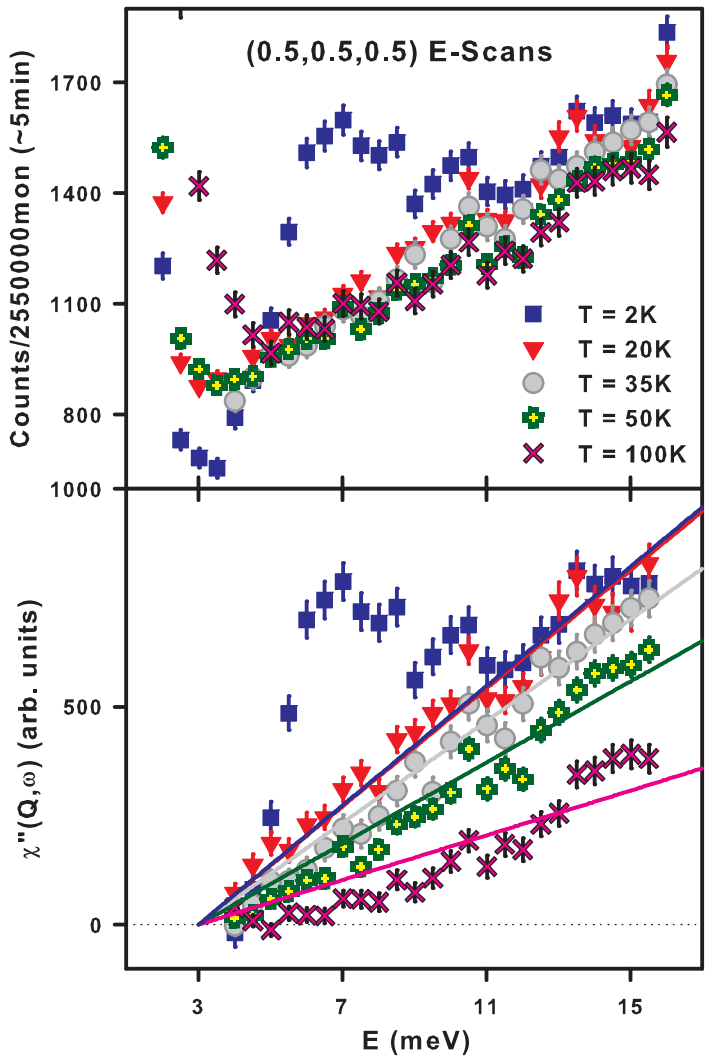

Figure 3.10: (a) Energy scans focusing on temperatures above T_c. (b) The background subtraction of $\chi''(Q,\omega)$ is determined from Q-scans. Aside from the resonance in the 2 K data, all other energy scans follow a similar linear trend; fanning out as a function of temperature.

3.2.3 Conclusions

From our characterization, we find that the resonance in the chalcogenide superconductors deviates considerably from that observed in the pnictides. Interestingly, this resonance is in many ways much more similar to the cuprates, as can be seen from Table 3.1. The presence of a neutron spin resonance in various high-T_c copper oxide

Table 3.1: Comparison of the Resonance Properties in the Pnictides, Chalcogenides, and Cuprates. The precursor resonance refers to a small, gradual, and anomalous increase in spectral weight at the resonance position prior to the onset of superconductivity. The temperature dependence of the resonance refers explicitly to the location of the mode energy as a function of temperature, not its intensity which follows an order parameter in all systems. The dimensionality of the resonance refers to whether the resonance or not the mode energy is (3D) or is not (2D) dispersive along L.

System	Precursor Resonance	Temp. Dep. of E_R	Dimen. of Resonance
$BaM_xFe_{2-x}As_2$	No	Yes	3D
$FeSe_xTe_{1-x}$	Yes	No	2D
$YBa_2Cu_3O_{6+x}$	Yes	No	2D

and Fe-based superconductors has been suggested as the result of a spin-fluctuation mediated electron pairing mechanism [50, 139]. In an earlier work mostly on copper oxide superconductors [139], it was proposed that the resonance energy is universally associated with the superconducting electronic gap Δ via $\hbar\omega_{res}/2\Delta = 0.64$ instead of being proportional to the superconducting transition temperatures T_c [128]. In a more recent summary of neutron scattering data on iron-based superconductors [50], it was found that the energies of the resonance for underdoped $BaFe_{2-x}(Co,Ni)_xAs_2$ deviate from this relationship, particularly for the resonance energy at $L = 0$. For $FeTe_{0.6}Se_{0.4}$, angle resolved photoemission spectroscopy experiments [84] reveal a 4.2 meV gap on the electron Fermi surface and a 2.5 meV gap on the hole Fermi surface. Since the addition of the electron and hole superconducting electronic gap energies is consistent with the energy of the resonance at low temperature, the result has been

interpreted as evidence that the resonance in $FeTe_{0.6}Se_{0.4}$ also arises from electron-hole pocket excitations [84]. However, if we assume that the superconducting gap energy gradually decreases for temperatures approaching T_c, the resonance energy will exceed that of the superconducting gap energy, contrary to the expectation for a spin exciton in the sign revised s-wave electron pairing scenario [77, 76].

If superconductivity in iron-based materials is mediated by orbital fluctuations associated with fully gapped s-wave state without sign reversal (s^{++}-wave state), one would expect a neutron spin resonance at an energy above the addition of the electron and hole superconducting electronic gap energies [88]. Since the superconducting gaps decrease with increasing temperature, one would expect a reduction in the resonance energy with increasing temperature even in this scenario, contrary to the observation.

In the SO(5) theory for high-T_c superconductivity [22], it is postulated that the AF and SC phases in the cuprates share a common microscopic origin. To develop the theory along these lines the 3D AF order parameter (N_x, N_y, N_z) is combined with the 2D superconducting order parameter $(\mathrm{Re}\Delta, \mathrm{Im}\Delta)$ to form a single 5D 'superspin' vector. In this picture, spatial and temporal variations of the superspin are then responsible for the ground state and the dynamics of collective excitations in various phases; ie: rotation of the superspin can tune you from, for instance, a local moment spin ordered insulator into a paramagnetic superconducting state. Since we are dealing with a five-dimensional order-parameter space, the most general rotations are given to us by the SO(5) symmetry group. Thus, it is in a context analogous to the unification of electo-magnetism that the unification of superconductivity and magnetism is developed. Within this theory, the resonance emerges as a Goldstone boson associated with a breaking of the symmetry, and in the full development of the theory it is shown that the resonance is fixed in energy as a function of temperature. Although this is consistent with our present work, it remains unclear how the SO(5) theory originally designed for high-T_c copper oxide superconductors would apply in the case of iron-based superconductors. As well, this theory conflicts with the data for the pnictides which displays a temperature dependent resonance. Hence, our present

work demonstrates that the correct microscopic description of the resonance is both unclear and conflicting, highlighting the need for more work to resolve this problem. It would be of great interest to understand why, in some systems the resonance is clearly linked to the superconducting electronic gap whereas our results on the $FeTe_{0.6}Se_{0.4}$ system suggest that the resonance itself may not be directly associated with Δ.

Chapter 4

Looking Back, Looking Forward

4.1 Ongoing Work

4.1.1 Temperature Dependence of the Effective Moment in FeTe

At the time of this writing it has recently been shown by Zaliznyak, *et. al.* [143] that the effective moment in Fe_yTe, as determined by zone and energy integration of the $S(\mathbf{Q},\omega)$ intensity, is not constant as a function of temperature. In general, conservation of spectral weight implies that the loss of scattering in one region of $(\mathbf{Q},\omega)$ must be offset by a one-to-one increase in scattering in another region. Thus, the total effective moment of the system should remain constant. However, in Fe_yTe the moment appears to climb as a function of temperature from a value of $\mu_{\text{eff}} = 2.7\mu_B$ at T = 10K to $\mu_{\text{eff}} = 3.6\mu_B$ at T = 100K Fig. 4.1c). These values are very close to the moments expected for local spins of S = 1 ($2.8\mu_B$) and S = 3/2 ($3.9\mu_B$). Thus the authors surmise that their is an effective change of 1 electron transferring from the itinerant channel into the local channel.

Previous neutron scattering experiments on FeTe observed excitations extending up to approximately 250meV, Fig. 3.1 [64]. At low energies ($\leq$30meV) the signal is centered around the $(\frac{1}{2},\frac{1}{2})$ ordering wave vector while above this energy the scattering

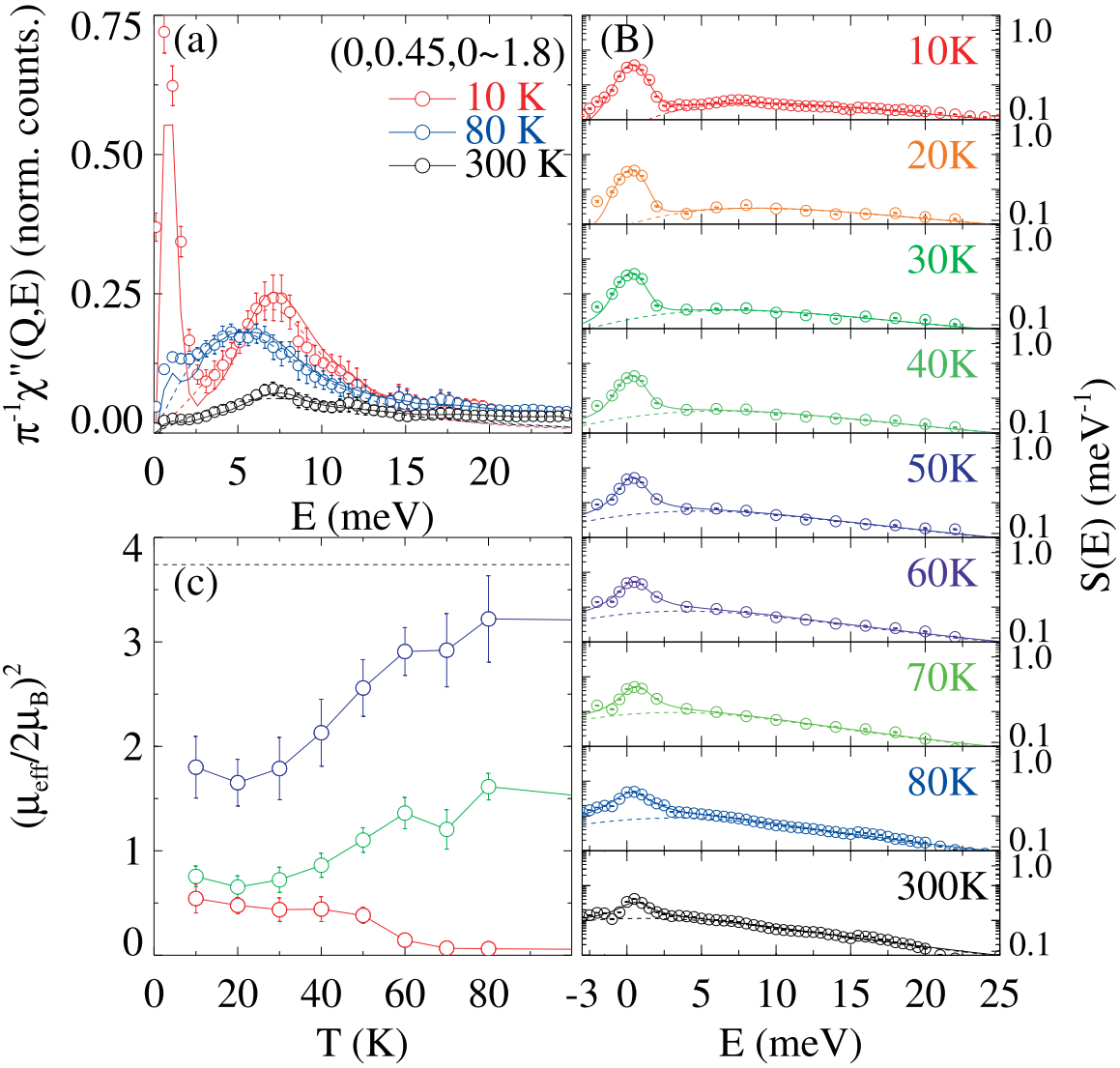

Figure 4.1: (a) $\chi''(\mathbf{Q},\omega)$ as a function of energy for $\mathbf{Q} = (0, 0.45)$ at 10 K, 80 K and 300 K. (b) Temperature dependence of S(E), excluding Bragg scattering. (c) Square of the effective magnetic moment obtained by integrating the S(E), as a function of temperature. Upper (blue) symbols show the total response, bottom (red) symbols are the Bragg contribution, green symbols are the quasi elastic contribution. Figure taken from [143].

becomes extremely diffuse and stretches across the majority of the Brillioun zone. The Q-integrated data in the study by Zaliznyak, *et. al.* suggest that the overwhelming majority of the spectral weight lies in energy transfers below 30meV Fig. 4.1b). Thus, it is only over this energy interval [0meV, 30meV] that they integrated their data to obtain estimations of the total moment. However, due to the diffuse nature of the scattering, background subtraction above 30meV becomes extremely difficult and could lead to an unintentional subtraction of magnetic scattering which would artificially suggest that spectral weight suppresses quickly above 30meV, thereby leading to corresponding incorrect moment calculations. To check against this possibility we collected data with good statistics to very high energies over a range of temperatures from 2K to 300K. We plan to first perform moment integrations of background subtracted data up to 30meV so that we may directly check our result against theirs over an identical integration region. Next, to check the contribution of higher energy excitations to the moment, we will integrate to much higher energies. Although difficult, it is our hope that we will be able to properly correct for both background and detector bank gaps. However this may not be possible, in this event we will leave the background intact, which should be mostly temperature independent at energies above the phonon cutoff frequency of 30meV, and then account for the background contribution by taking ratios of moments at different temperatures.

$$R = \frac{\mu_{\text{eff}}^{E>30}(T_1) + \int BKG}{\mu_{\text{eff}}^{E>30}(T_2) + \int BKG} \tag{4.1}$$

The ratios (R) obtained from this procedure will restrict us from determining the absolute value of the moment at a particular temperature. However, we will be left with the capability to check for temperature dependence, which is the primary motivation for our study.

4.1.2 High Temperature Study of Magnetic Excitations in $BaFe_2As_2$

In our previous study of $BaFe_2As_2$ (see Section 2.1) we carried out measurements at three different temperatures: 7K where the spin lattice carries long range magnetic order and temperatures roughly 10% (T = 125K) below and 10% (T = 150) above the magnetic phase transition (T_N = 135K). Since these measurements were carried out using time of flight spectroscopy, we were able to map out the magnetic excitations all the way to the zone boundary (∼250meV). At 7K, the spin wave dispersion observed in our Ba(122) parent study differed significantly from the closely related Ca(122) parent. In Ca(122) the spin waves remain centered at the (1,0,0) wavevector all the way to the zone boundary and are well described by an anisotropic $J_{1a} - J_{1b} - J_2$ Heisenberg model [144]. However, in Ba(122) there is a wavevector transfer of scattering to the (1,1,0) position for energy transfers greater than 150meV and the data can only be fit with the same Heisenberg model if a strong Q-anisotropic damping is used. We found that the scattering in close to proximity to T_N was identical to the low temperature spin wave scattering for energy transfers above 100meV and that only energy transfers below this threshold carried any significant differences among the different temperatures. Given that the scattering is not strongly modified across the phase transition, we collected an entirely new set of data for E_i's at much higher temperatures (up to room temperature) to see how these excitations evolve. In our priliminary analysis of the data we have found that the striking similarity of the scattering profile at 10% above T_N to the 7K ordered spin wave data is not associated with the close proximity of the phase transition. Rather, at T = 300K we find that the scattering was modified only slightly by the large increase in temperature.

Altogether our data sets on $BaFe_2As_2$ provide us with enough coverage of $S(\mathbf{Q}, \omega)$ to also integrate out the effective moment at five different temperatures: 7K, 125K, 150K, 225K, 290K. This provided us with the opportunity to directly compare our results with the existing results for FeTe described above. We found that, unlike FeTe,

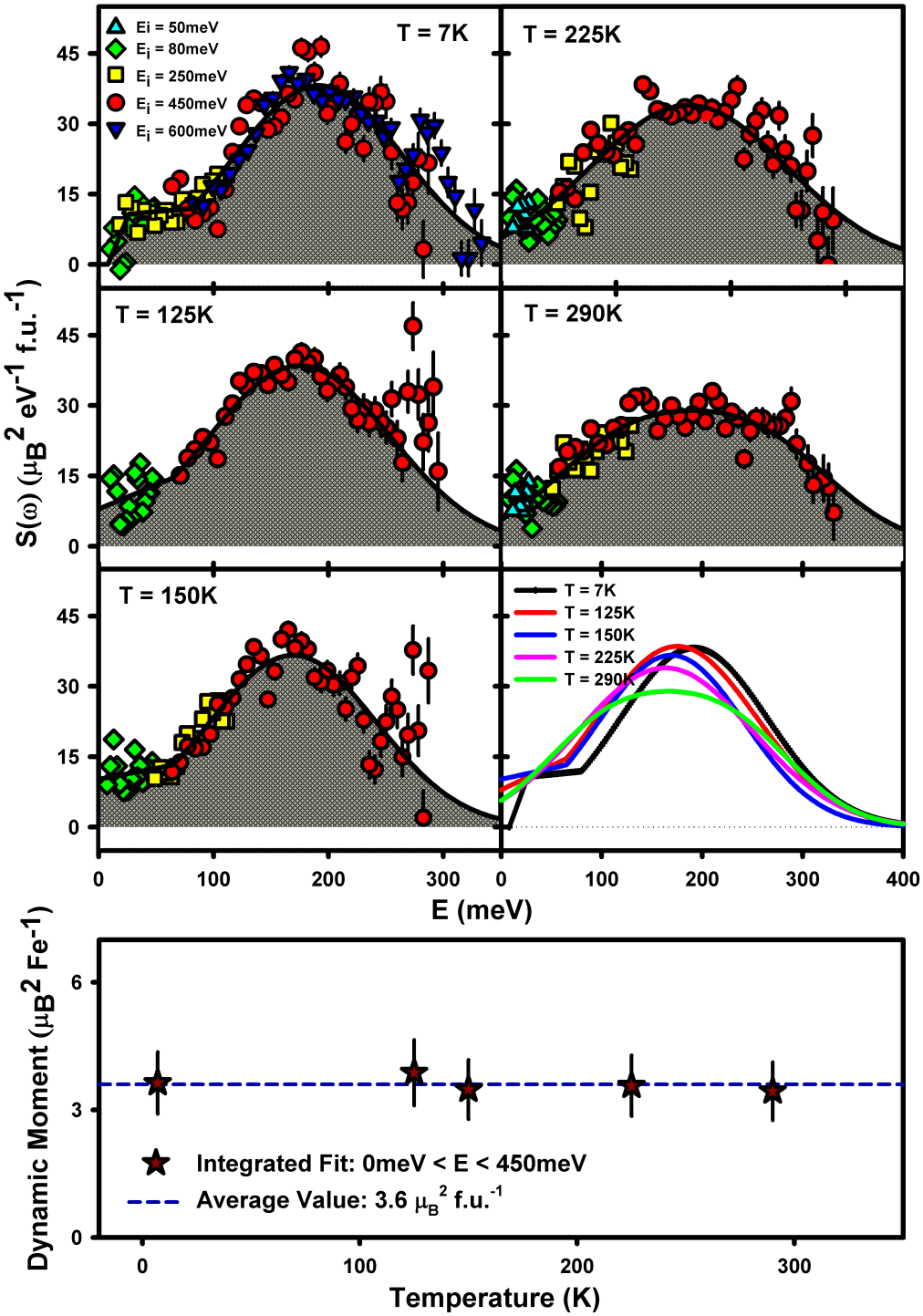

Figure 4.2: (a)-(e) Temperature dependence of S(E), excluding Bragg scattering. (f) Overplot at all temperatures of the empirical fits used to integrate out the moment. (g) Square of the effective magnetic moment as a function of temperature. Figure taken from unpublished work by our group.

the total moment sum rule is satisfied and the effective moment remains constant as a function of temperature Fig. 4.2. In $BaFe_2As_2$, the scattering is much less diffuse and so carrying out the integration was much more straightforward compared to FeTe. Thus, it is unclear if our result signals that the physics of these systems truly are different in this respect, or if the integration of FeTe needs to be re-evaluated for error.

Currently, our progress towards publication of our high temperature results on $BaFe_2As_2$ is fairly well advanced. Final figures are nearing completion and a rough draft is pending upon a more critical review and interpretation of the results.

4.2 Future Work

When deciding on the direction of my future work, it is important to balance projects that I am interested in against the spectroscopic techniques and samples that are most accessible. Upon leaving UT, I will immediately take a position at the National Institute of Standards and Technology as a local contact on the spin polarized inelastic neutron scattering (SPINS) spectrometer with 15% of the instument's beamtime reserved for my own studies. Since SPINS is a cold triple axis spectrometer, it will carry a low flux (high count times) and only allow for consecutive collection of 1D scans through $(\mathbf{Q}, \omega)$ (as opposed to TOF where all of $(\mathbf{Q}, \omega)$ is collected concurrently.) The benefit is that these 1D scans can reach exceptionally low energy transfers of $\sim$0.2meV with no spectrometer coupling of energy to a direction in $\mathbf{Q}$. As well, the supermirrors of spins should allow for the collection of polarization data without a drastic reduction in incident flux and within the year SPINS will be retooled so that it can be outfitted with a 14T magnetic. Thus, my studies would benefit the most by taking into account the above considerations.

Although specific future studies have not been finalized, there has been some thought given to doing a pressure study of Ru doped $BaFe_2As_2$. Another possibility would be to look at a possible disorder effect in the parent $BaFe_2As_2$ that is suggested

by a shift in T_N when the system is annealed. There has also been work by Wilson *et. al.* [129] demonstrating that the nuclear and magnetic phase transitions always follow an Ising order parameter in the pnictides with the dimensionality 2D if T_c and T_N are concomitant and 3D if they are separated. However, there is much work that can still be done to test the universality of this relationship. This is especially interesting given that the separation of the phase transition is controlled by the exchange coupling along the c-axis J_c [28]. In our work on underdoped $BaFe_2As_2$ (see Sec. 2.2) we find that J_c reduces very quickly with even a very modest amount of doping and that this, in turn, reduces the dimensionality of the system from 3D to 2D and drives the phase transitions away from one another. Yet oddly, in Wilson's work, separated phase transitions lead to 3D Ising behavior which is counterintuitive to what is expected. Apart from the pnictides, it would be interesting to return to studies of the electron doped cuprates which were still trending just before the Fe-based superconductors were discovered. Particularly, in PLCCO it was discovered that extremely small amounts of Ni doping could drastically reduce the T_c of the system, thus it would be very interesting to map out the low energy magnetic fluctuations of Ni doped compounds and compare them to their corresponding non-Ni doped counterparts.

Aside from experiments, my work on time of flight data has revealed several improvements that can be made to the existing data analysis software. The standard's right now for cutting and slicing the large 4D data sets for analysis is Mslice. Instrument convolution and model fitting of this processed data is achieved using a separate program Tobyfit. There is also some built-in capability to directly send data to mFit, a primarily triple axis software written at ILL, that allows for very quick unconvolved fitting of 1D cuts to several general forms. Separately, each piece of software works exceptionally well. However, a close integration of these softwares is lacking which leads to alot of undue front-end effort by users to move data and spectrometer parameters from one place to another. As well, to acquire a global view of the 4D data set requires a very cumbersome amount of cutting and slicing of the data. This is also a problem for certain tasks, such as building a dispersion,

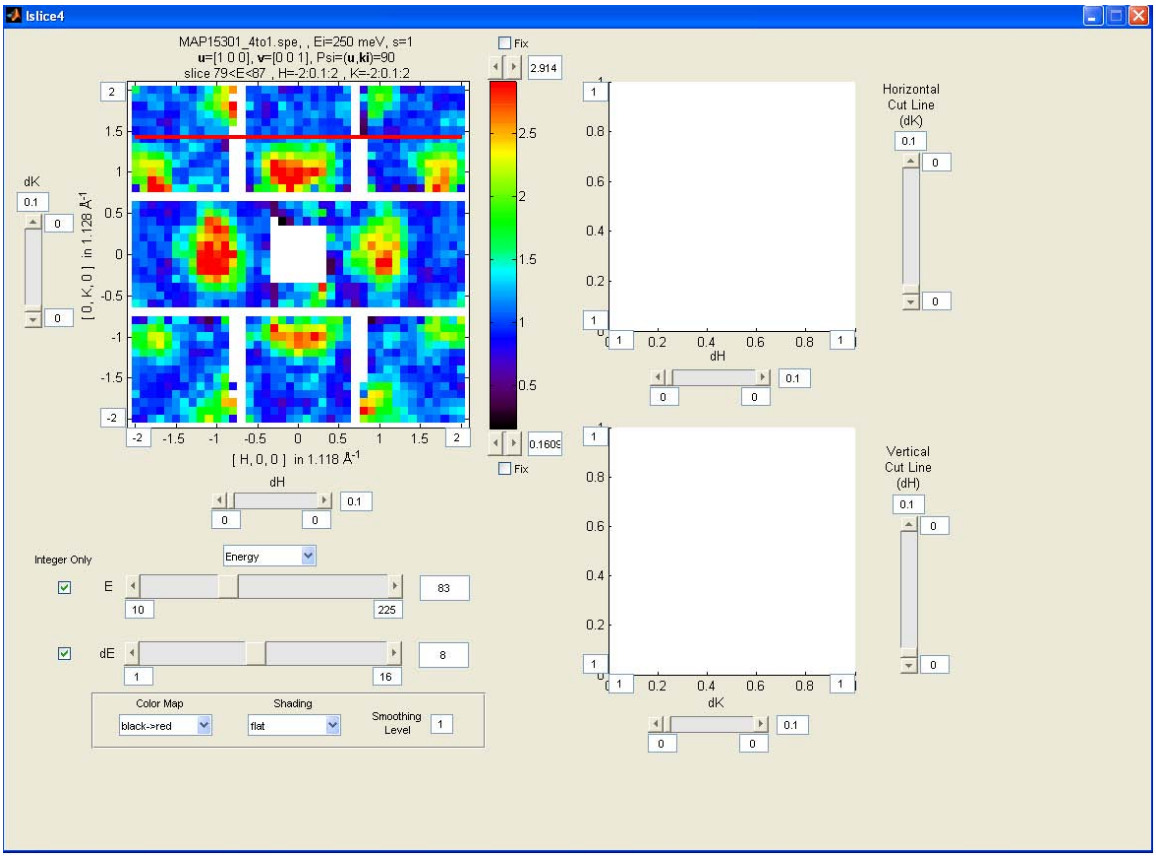

Figure 4.3: Screen shot of Lslice, a developmentary software for improving the functionality, user friendliness, and integration of existing time of flight software.

which require the user to systematically extract a host of mostly identical cuts that differ only by a step in **Q** or E and painstaking fit them individually and compile the fitted results. To address these problems, I have extracted out and modified the core subroutines in Mslice so that they may be called by an upper level of routines that automates many of the step-wise and repetitive procedures that currently slows down and unneccesarily burdens users. All of this will then be wrapped into a new GUI that provides a user friendly interface for the new functionality. To date, I have roughly a quarter of the upper level routines written and half of the first layer GUI. Ultimately, the hope is to fully integrate all three pre-existing softwares (as well as an internal data storage) and provide a tabbing between the multiple layers of a master GUI that allows you to quickly navigate between the different levels of functionality. Fig. 4.3 shows a screenshot of the program. To give a few of the more basic details, a 2D slice of real data is plotted in the upper left graphing window. The red horizontal line running through this window allows the user to cut the 2D slice into a 1D cut. This cut would show up in the top right graphing window (routine not finished). The line is interactive and can be moved up and down with the results changing in real time in the 1D plotting window. A similar vertical line will be included to plot data in the lower left plotting window. All quantities are set on sliders so that users can quickly step systematically through sliced data in the four different directions (H, K, L, E). A 'plot all' option will allow users to create and save an entire series of 1D or 2D plots that all change by a set step. These can be compiled into a collection of side by side plots, or overplotted for easy viewing. As well, systematic fitting can be performed where the fitted parameters from a plot are used as the starting parameters for the consecutive plot one step up.

4.3 Concluding Remarks

Before the discovery of the Fe-based superconductors, the cuprates were the only known source of high temperature superconductivity. Although comparison to the

heavy fermions provided a good measure of insight, the extremely low T_c, exotic physics, and very different magnetic origin of these systems meant that they were in many ways far removed from their Cu-based counterparts. Thus, the Fe-based systems provide an exciting opportunity to probe novel compounds with transition temperatures and a chemical structure that are similar to the cuprates, yet different enough in electronic and magnetic structure to be unique in their own right. It is my hope that the experiments detailed above will help further our understanding of the relationship between unconventional superconductivity and magnetism and add to the growing body of scientific work necessary to acquire a comprehensive picture of these systems.

Bibliography

[1] P. Anderson. *Science*, 235:1196, 1987. 60

[2] P. Anderson, P. Lee, M. Randeria, T. Rice, N. Trivedi, and F. Zhang. *J. Phys. Cond. Matter*, 16:R755, 2004. 15

[3] W. Bao, Y. Qiu, Q. Huang, M. Green, P. Zajdel, M. Fitzsimmons, M. Zhernenkov, M. Fang, B. Qian, E. Vehstedt, J. Yang, H. Pham, L. Spinu, and Z. Mao. *Phys. Rev. Lett.*, 102:247001, 2009. xiii, 7, 113

[4] J. Bardeen, L. N. Cooper, and J. R. Schrieffer. *Phys. Rev.*, 108:1175, 1957. 1

[5] J. G. Bednorz and K. A. Muller. *Z. Phys.*, B64:189, 1986. 3

[6] S. Blundell. *Magnetism in Condensed Matter*. Oxford University Press, Oxford, 2001. xiv, 17, 18

[7] S. L. Bud'ko, N. Ni, and P. C. Canfield. *Phys. Rev. B*, 79:220516, Jun 2009. xxi, 83, 84

[8] S. Chi, J. A. Rodriguez-Rivera, J. W. Lynn, C. Zhang, D. Phelan, D. K. Singh, R. Paul, and P. Dai. *Phys. Rev. B*, 84:214407, Dec 2011. xxv, 116, 117, 120, 134

[9] S. Chi, A. Schneidewind, J. Zhao, L. W. Harriger, L. Li, Y. Luo, G. Cao, Z. Xu, M. Loewenhaupt, J. Hu, and P. Dai. *Phys. Rev. Lett.*, 102:107006, 2009. 54, 82, 85, 100, 121, 124

[10] A. D. Christianson, E. A. Goremychkin, R. Osborn, S. Rosenkranz, M. D. Lumsden, C. D. Malliakas, I. S. Todorov, H. Claus, D. Y. Chung, M. G. Kanatzidis, R. I. Bewley, and T. Guidi. *Nature*, 456:930, 2008. xxii, 7, 54, 82, 94, 95, 100

[11] A. D. Christianson, M. D. Lumsden, S. E. Nagler, G. J. MacDougall, M. A. McGuire, A. S. Sefat, R. Jin, B. C. Sales, and D. Mandrus. *Phys. Rev. Lett.*, 103:087002, Aug 2009. 82

[12] J. H. Chu, J. G. Analytis, K. D. Greve, P. L. McMahon, J. Islam, Y. Yomatomo, and I. R. Fisher. *Science*, 329:824, 2010. xviii, 64, 76

[13] J.-H. Chu, J. G. Analytis, C. Kucharczyk, and I. R. Fisher. *Phys. Rev. B*, 79:014506, Jan 2009. 82

[14] T.-M. Chuang, M. P. Allan, J. Lee, Y. Xie, N. Ni, S. L. Budko, G. S. Boebinger, P. C. Canfield, and J. C. Davis. *Science*, 327(5962):181–184, 2010. 76

[15] C. Cohen-Tannoudji, B. Diu, and F. Laloe. *Quantum Mechanics, Volume One*. John Wiley and Sons, Singapore, 2005. 38

[16] R. Coldea, S. Hayden, G. Aappli, T. Perring, C. Frost, T. Mason, S.-W. Cheong, and Z. Fisk. *Phys. Rev. Lett.*, 86:5377, 2001. xiii, 13, 14, 54

[17] L. N. Cooper. *Phys. Rev.*, 104:1189, 1956. 1

[18] P. Dai, J. Hu, and E. Dagotto. *In review by Nat. Phys.*, 2012. xiv, xv, 21, 23

[19] P. Dai, H. A. Mook, G. Aeppli, S. M. Hayden, and F. Dogan. *Nature*, 406:965, 2000. 95, 100

[20] P. Dai, H. A. Mook, S. M. Hayden, G. Aeppli, T. G. Perring, R. D. Hunt, and F. Dogan. *Science*, 284:1344, 1999. 133

[21] C. de la Cruz, Q. Huang, J. W. Lynn, J. Li, W. R. II, J. L. Zarestky, H. A. Mook, G. F. Chen, J. L. Luo, N. L. Wang, and P. Dai. *Nature*, 453:899, 2008. 6, 20, 93

[22] E. Demler, W. Hanke, and S. C. Zhang. *Rev. Mod. Phys.*, 76:909, 2004. 138

[23] O. Diallo, D. K. Pratt, R. M. Fernandes, W. Tian, J. L. Zarestky, M. Lumsden, T. G. Perring, C. L. Broholm, N. Ni, S. L. Bud'ko, P. C. Canfield, H.-F. Li, D. Vaknin, A. Kreyssig, A. I. Goldman, and R. J. McQueeney. *Phys. Rev. B*, 81:214407, 2008. 71

[24] S. Diallo, V. Antropov, T. Perring, C. Broholm, J. Pulikkotil, N. Ni, S. Bud'ko, P. Canfield, A. Kreyssig, A. Goldman, and R. McQueeney. *Phys. Rev. Lett.*, 102:187206, 2009. 62

[25] M. Eschrig. *Adv. Phys.*, 55:47, 2006. 103

[26] R. Ewings, T. Perring, R. Bewley, T. Guidi, M. Pitcher, D. Parker, S. Clarke, and A. Boothroyd. *Phys. Rev. B*, 78:220501(R), 2008. 54, 55, 63, 66, 85, 90, 92

[27] R. A. Ewings, T. G. Perring, J. Gillett, S. D. Das, S. E. Sebastian, A. E. Taylor, T. Guidi, and A. T. Boothroyd. *Phys. Rev. B*, 83:214519, Jun 2011. xx, 78, 79, 82

[28] C. Fang, H. Yao, W.-F. Tsai, J. Hu, and S. A. Kivelson. *Phys. Rev. B*, 77:224509, Jun 2008. 82, 92, 146

[29] Y. feng Yang, Z. Fisk, H.-O. Lee, J. Thompson, and D. Pines. *Nature*, 454:611, 2007. xv, 27, 28

[30] Y. feng Yang and D. Pines. *Phys. Rev. Lett.*, 100:096404, 2008. 27

[31] Z. Fisk, J. Sarrao, J. Smith, and J. Thompson. *Proc. Natl. Acad. Sci.*, 92:6663, 1995. 27

[32] H. F. Fong, P. Bourges, Y. Sidis, L. P. Regnault, A. Ivanov, G. D. Gu, N. Koshizuka, and B. Keimer. *Nature*, 398:588, 1999. 5, 93

[33] H. F. Fong, B. Keimer, D. Reznik, D. L. Milius, and I. A. Aksay. *Phys. Rev. B*, 54:6708–6720, Sep 1996. xxv, 122, 123

[34] J. P. Franck. *Physical Properties of High Temperature Superconductors IV*. World Scientific, Singapore, 1994. 3

[35] V. L. Ginzburg and L. D. Landau. *Zh. Eksperim i. Teor. Fiz.*, 20:1064, 1950. 1

[36] S. Graser, A. Kemper, T. Maier, H.-P. Cheng, P. Hirschfeld, and D. Scalapino. *Phys. Rev. B*, 81:214503, 2010. 20, 112

[37] H. Gretarsson, A. Lupascu, J. Kim, D. Casa, T. Gog, W. Wu, S. Julian, Z. Xu, J. Wen, G. Gu, R. Yuan, Z. Chen, N.-L. Wang, S. Khim, K. Kim, M. Ishikado, I. Jarrige, S. Shamoto, J.-H. Chu, I. Fisher, and Y.-J. Kim. *Phys. Rev. B*, 84:100509(R), 2011. 22

[38] D. J. Griffiths. *Introduction to Quantum Mechanics*. Prentice Hall, Inc., Upper Saddle River, NJ, 1995. 12

[39] G. Gruner. *Density Waves in Solids*. Westview Press, 2000. xiv, 17, 18

[40] L. Harriger, H. Luo, M. Liu, C. Frost, J. Hu, M. Norman, and P. Dai. *Phys. Rev. B*, 84:054544, 2011. xvii, 56, 57, 82, 108

[41] L. W. Harriger, O. J. Lipscombe, C. Zhang, H. Luo, M. Wang, K. Marty, M. D. Lumsden, and P. Dai. *Phys. Rev. B*, 85:054511, Feb 2012. 124

[42] L. W. Harriger, H. Q. Luo, M. S. Liu, C. Frost, J. P. Hu, M. R. Norman, and P. Dai. *Phys. Rev. B*, 84:054544, Aug 2011. xxiv, 106, 109

[43] L. W. Harriger, A. Schneidewind, S. Li, J. Zhao, Z. Li, W. Lu, X. Dong, F. Zhou, Z. Zhao, J. Hu, and P. Dai. *Phys. Rev. Lett.*, 103:087005, Aug 2009. 85, 96

[44] N. Headings, S. Hayden, R. Coldea, and T. Perring. *Phys. Rev. Lett.*, 105:247001, 2010. xiii, 13, 14, 59

[45] A. Hewson. *The Kondo Problem to Heavy Fermions*. Cambridge University Press, Cambridge, 1993. 24

[46] T. Hsu. *Phys. Rev. B*, 41:11379, 1990. 60

[47] Q. Huang, Y. Qiu, W. Bao, M. A. Green, J. W. Lynn, Y. C. Gasparovic, T. Wu, G. Wu, and X. H. Chen. *Phys. Rev. Lett.*, 101:257003, Dec 2008. 82

[48] Q. Huang, J. Zhao, J. W. Lynn, G. F. Chen, J. L. Luo, N. L. Wang, and P. Dai. *Phys. Rev. B*, 78:054529, 2008. 7, 93

[49] D. S. Inosov, J. T. Park, P. Bourges, D. L. Sun, Y. Sidis, A. Schneidewind, K. Hradil, D. Haug, C. T. Lin, B. Keimer, and V. Hinkov. *Nat. Phys.*, 6:178, 2010. xxv, 121, 123, 124, 126, 130

[50] D. S. Inosov, J. T. Park, A. Charnukha, Y. Li, A. V. Boris, B. Keimer, and V. Hinkov. *Phys. Rev. B*, 83:214520, Jun 2011. 137

[51] Y. Kamihara, T. Watanabe, M. Hirano, and H. Hosono. *J. Am. Chem. Soc.*, 130:3296, 2008. 5, 19

[52] E. Kaneshita and T. Tohyama. *Phys. Rev. B*, 82:094441, 2010. xviii, 61, 71

[53] T. Kasuya. *Prog. Theor. Phys.*, 16:45, 1956. 26

[54] N. Katayama, S. Ji, D. L. S. Lee, M. Fujita, T. J. Sato, J. Wen, Z. Xu, G. Gu, G. Xu, Z. Lin, M. Enoki, S. Chang, K. Yamada, and J. M. Tranquada. *J. Phys. Soc. Jpn.*, 79:113702, 2010. 116

[55] C. Kim, P. White, Z.-X. Shen, T. Tohyama, Y. Shibata, S. maekawa, B. Wells, Y. Kim, R. Birgeneau, and M. Kastner. *Phys. Rev. Lett.*, 80:4245, 1998. 13

[56] S. A. Kimber, A. Kreyssig, Y.-Z. Zhang, H. O. Jeschke, R. Valenti, F. Yokaichiya, E. Colombier, J. Yan, T. C. Hansen, T. Chatterji, R. J. McQueeney, P. C. Canfield, A. I. Goldman, and D. N. Argyriou. *Nat. Mat.*, 8:471, 2009. 55

[57] J. Kondo. *Solid State Phys.*, 23:184, 1969. 25

[58] C. Lee, K. Kihou, H. Kawano-Furukawa, T. Saito, A. Iyo, H. Eisaki, H. Fukazawa, Y. Kohori, K. Suzuki, H. Usui, K. Kuroki, and K. Yamada. *Phys. Rev. Lett.*, 106:067003, 2011. 20

[59] C. Lester, J.-H. Chu, J. G. Analytis, T. G. Perring, I. R. Fisher, and S. M. Hayden. *Phys. Rev. B*, 81:064505, Feb 2010. 109

[60] L. J. Li, Y. K. Luo, Q. B. Wang, H. Chen, Z. Ren, Q. Tao, Y. K. Li, X. Lin, M. He, Z. W. Zhu, G. H. Cao, and Z. A. Xu. *New J. of Phys.*, 11:025008, 2009. 83

[61] S. Li, Y. Chen, S. Chang, J. W. Lynn, L. Li, Y. Luo, G. Cao, Z. Xu, and P. Dai. *Phys. Rev. B*, 79:174527, May 2009. 82, 85

[62] S. Li, C. de la Cruz, Q. Huang, G. F. Chen, T.-L. Xia, N. L. W. J. L. Lou, and P. Dai. *Phys. Rev. B*, 80:020504(R), 2009. xiii, 7, 20

[63] S. Li, C. Zhang, M. Wang, H.-q. Luo, X. Lu, E. Faulhaber, A. Schneidewind, P. Link, J. Hu, T. Xiang, and P. Dai. *Phys. Rev. Lett.*, 105:157002, Oct 2010. xxvi, 125, 127, 130, 133

[64] O. J. Lipscombe, G. F. Chen, C. Fang, T. G. Perring, D. L. Abernathy, A. D. Christianson, T. Egami, N. Wang, J. Hu, and P. Dai. *Phys. Rev. Lett.*, 106:057004, Feb 2011. xxv, 114, 115, 140

[65] O. J. Lipscombe, L. W. Harriger, P. G. Freeman, M. Enderle, C. Zhang, M. Wang, T. Egami, J. Hu, T. Xiang, M. R. Norman, and P. Dai. *Phys. Rev. B*, 82:064515, Aug 2010. 76

[66] C. Liu, T. Kondo, N. Ni, A. D. Palczewski, A. Bostwick, G. D. Samolyuk, R. Khasanov, M. Shi, E. Rotenberg, S. L. Bud'ko, P. C. Canfield, and A. Kaminski. *Phys. Rev. Lett.*, 102:167004, Apr 2009. 92

[67] M. Liu, L. W. Harriger, H. Luo, M. Wang, R. Ewings, T. Guidi, H. Park, K. Haule, G. Kotliar, S. Hayden, and P. Dai. *Nat. Phys.*, 8:376, 2012. xv, xxiv, 23, 24, 106

[68] T. J. Liu, J. Hu, B. Qian, D. Fobes, Z. Q. Mao, W. Bao, M. Reehuis, S. A. J. Kimber, K. Proke, S. Matas, D. N. Argyriou, A. Hiess, A. Rotaru, H. Pham, L. Spinu, Y. Qiu, V. Thampy, A. T. Savici, J. A. Rodriguez, and C. Broholm. *Nat. Mat.*, 9:718, 2010. 116, 120

[69] J. Lorenzana, G. Seibold, and R. Coldea. *Phys. Rev. B*, 72:224511, 2005. 13, 109

[70] M. D. Lumsden, A. D. Christianson, D. Parshall, M. B. Stone, S. E. Nagler, G. J. MacDougall, H. A. Mook, K. Lokshin, T. Egami, D. L. Abernathy, E. A. Goremychkin, R. Osborn, M. A. McGuire, A. S. Sefat, R. Jin, B. C. Sales, and D. Mandrus. *Phys. Rev. Lett.*, 102:107005, Mar 2009. 54, 82, 85, 90, 100

[71] M. D. Lumsden1, A. D. Christianson1, E. A. Goremychkin, S. E. Nagler, H. A. Mook, M. B. Stone, D. L. Abernathy, T. Guidi, G. J. MacDougall, C. de la Cruz, A. S. Sefat, M. A. McGuire, B. C. Sales, and D. Mandrus. *Nat. Phys.*, 6:182, 2010. 117

[72] Q. Luo, G. Martins, D.-X. Yao, M. Daghofer, R. Yu, A. Moreo, and E. Dagotto. *Phys. Rev. B*, 82:104508, 2010. 24

[73] W. Lv. personal communication with first author of [74], 2012. 80

[74] W. Lv, F. Krüger, and P. Phillips. *Phys. Rev. B*, 82:045125, Jul 2010. 80, 157

[75] J. W. Lynn and P. Dai. *Physica C*, 469:469, 2009. xiii, 7

[76] T. A. Maier, S. Graser, D. J. Scalapino, and P. Hirschfeld. *Phys. Rev. B*, 79:134520, Apr 2009. 138

[77] T. A. Maier and D. J. Scalapino. *Phys. Rev. B*, 78:020514, Jul 2008. 138

[78] A. Martinelli, A. Palenzona, M. Tropeano, C. Ferdeghini, M. Putti, M. R. Cimberle, T. D. Nguyen, M. Affronte, and C. Ritter. *Phys. Rev. B*, 81:094115, Mar 2010. 115

[79] K. Matan, R. Morinaga, K. Iida, and T. J. Sato. *Phys. Rev. B*, 79:054526, 2009. 54, 55, 85, 90, 92, 96

[80] A. Mathai, Y. Gim, R. C. Black, A. Amar, and F. C. Wellstood. *Phys. Rev. Lett.*, 74:4523, 1995. 3

[81] E. Maxwell. *Phys. Rev.*, 78:477, 1950. 2

[82] I. Mazin and J. Schmalian. *Physica C*, 469:614, 2009. 22, 82, 92

[83] M. Metting. Discussions during talks, 2012. 80

[84] H. Miao, P. Richard, Y. Tanaka, K. Nakayama, T. Qian, K. Umezawa, T. Sato, Y.-M. Xu, Y. B. Shi, N. Xu, X.-P. Wang, P. Zhang, H.-B. Yang, Z.-J. Xu, J. S. Wen, G.-D. Gu, X. Dai, J.-P. Hu, T. Takahashi, and H. Ding. *Phys. Rev. B*, 85:094506, Mar 2012. 137, 138

[85] H. A. Mook, M. D. Lumsden, A. D. Christianson, S. E. Nagler, B. C. Sales, R. Jin, M. A. McGuire, A. S. Sefat, D. Mandrus, T. Egami, and C. dela Cruz. *Phys. Rev. Lett.*, 104:187002, May 2010. 126, 130, 134

[86] T. Moriya and K. Ueda. *Rep. Prog. Phys.*, 66:1299, 2003. 3

[87] N. Ni, M. E. Tillman, J.-Q. Yan, A. Kracher, S. T. Hannahs, S. L. Bud'ko, and P. C. Canfield. *Phys. Rev. B*, 78:214515, Dec 2008. 82

[88] S. Onari and H. Kontani. *Phys. Rev. B*, 84:144518, Oct 2011. 138

[89] S. Pailhès, Y. Sidis, P. Bourges, V. Hinkov, A. Ivanov, C. Ulrich, L. P. Regnault, and B. Keimer. *Phys. Rev. Lett.*, 93:167001, Oct 2004. xxiv, 103, 104

[90] H. Park, K. Haule, and G. Kotliar. *Phys. Rev. Lett*, 107:137007, 2011. xx, 22, 24, 81, 112

[91] J. Park, D. Inosov, A. Yaresko, S. Graser, D. Sun, P. Bourges, Y. Sidis, Y. Li, J.-H. Kim, D. Haug, A. Ivanov, K. Hradil, A. Schneidewind, P. Link, E. Faulhaber, I. Glavatskyy, C. Lin, B. Keimer, and V. Hinkov. *Phys. Rev. B*, 82:134503, 2010. 20

[92] J. T. Park, G. Friemel, T. Loew, V. Hinkov, Y. Li, B. H. Min, D. L. Sun, A. Ivanov, A. Piovano, C. T. Lin, B. Keimer, Y. S. Kwon, and D. S. Inosov. *arXiv:1204.0875v1*, 2012. 90, 96

[93] W. K. Park, C. R. Hunt, H. Z. Arham, Z. J. Xu, J. S. Wen, Z. W. Lin, Q. Li, G. D. Gu, and L. H. Greene. *arXiv:1005.0190*, 2012. xxvii, 124, 128, 130

[94] R. Pathria. *Statistical Mechanics, 2nd Edition*. Elsevier, Oxford, 1996. 40

[95] T. Perring. *TOBYFIT v2.0 Least-Squares Fitting to Single Crystal Data on HET, MARI, MAPS*. Rutherford Appleton Laboratoris, Chilton, Didcot, Oxfordshire OX11 0QX, 2005. 52

[96] D. K. Pratt, A. Kreyssig, S. Nandi, N. Ni, A. Thaler, M. D. Lumsden, W. Tian, J. L. Zarestky, S. L. Bud'ko, P. C. Canfield, A. I. Goldman, and R. J. McQueeney. *Phys. Rev. B*, 81:140510, Apr 2010. xxiii, 101, 102, 124

[97] D. K. Pratt, W. Tian, A. Kreyssig, J. L. Zarestky, S. Nandi, N. Ni, S. L. Bud'ko, P. C. Canfield, A. I. Goldman, and R. J. McQueeney. *Phys. Rev. Lett.*, 103:087001, Aug 2009. 82

[98] Y. Qiu, W. Bao, Y. Zhao, C. Broholm, V. Stanev, Z. Tesanovic, Y. C. Gasparovic, S. Chang, J. Hu, B. Qian, M. Fang, and Z. Mao. *Phys. Rev. Lett.*, 103:067008, 2009. 121, 122, 124, 126, 130, 134

[99] K. M. S. H. M. D. S. B. J. T. R. C. R.I. Bewley, R.S. Eccleston. *Physica B*, 385-386:1029–1031, 2006. 108

[100] P. Richard, T. Sato, K. Nakayama, T. Takahashi, and H. Ding. *Rep. Prog. Phys.*, 74:124512, 2011. 19

[101] M. Roger and J. Delrieu. *Phys. Rev. B*, 39:2299, 1989. 13

[102] J. Rossat-Mignod, L. Regnault, C. Veiqqer, P. Bourges, P. Burlet, and J. Bossy. *Physica C*, 185:86, 1991. 5, 93

[103] M. Rotter, M. Tegel, and D. Johrendt. *Phys. Rev. Lett.*, 101:107006, 2008. 19

[104] M. Ruderman and C. Kittel. *Phys. Rev.*, 96:99, 1954. 26

[105] J. Sanchez. Esrf, 2002. xv, 25

[106] A. Sandvik and R. Singh. *Phys. Rev. Lett.*, 86:528, 2001. 60

[107] N. K. Sato, N. Aso, K. Miyake, R. Shiina, P. Thalmeier, G. Varelogiannis, C. Geibel, F. Steglich, P. Fulde, and T. Komatsubara. *Nature*, 410:340, 2001. 8, 93

[108] D. J. Scalapino. *Science*, 284:1282, 1999. 5

[109] A. Schilling, M. Cantoni, J. Guo, and H. Ott. *Nature*, 363:56, 1993. 3

[110] J. R. Schrieffer and J. S. Brook. *Handbook of High-Temperature Superconductivity*. Springer Science and Business Media, LLC, 2007. xiv, 15, 16

[111] H.-B. Schuttler and A. Fedro. *Phys. Rev. B*, 45:7588, 1992. 13

[112] G. Shirane, S. M. Shapiro, and J. M. Tranquada. *Neutron Scattering with a Triple-Axis Spectrometer*. Cambridge University Press, Cambridge, 2002. 45, 47

[113] G. Squires. *Introduction to the Theory of Thermal Neutron Scattering*. Dover, Mineola, 1996. 29

[114] F. Steglich, J. Aarts, C. Bredll, W. Lieke, D. Meschede, W. Franz, and J. Schafer. *Phys. Rev. Lett.*, 43:1892, 1979. 8

[115] C. Stock, C. Broholm, J. Hudis, H. J. Kang, and C. Petrovic. *Phys. Rev. Lett.*, 100:087001, 2008. 8, 93

[116] C. Stock, E. Roderiguez, and M. Green. *arXiv:1202.4152v1*, 2012. xxv, 114, 117, 119

[117] C. Stock, E. E. Rodriguez, M. A. Green, P. Zavalij, and J. A. Rodriguez-Rivera. *Phys. Rev. B*, 84:045124, Jul 2011. 114

[118] A. Subedi, L. Zhang, D. J. Singh, and M. H. Du. *Phys. Rev. B*, 78:134514, Oct 2008. 113

[119] V. Svetkovic and Z. Tesanovic. *Europhys. Lett.*, 85:37002, 2009. 110

[120] M. Takahashi. *J. Phys. C*, 10:1289, 1977. 13

[121] M. Tinkham. *Introduction to Superconductivity*. McGraw-Hill, Inc., New York, 1996. 2, 3

[122] C. C. Tsuei and J. R. Kirtley. *Phys. Rev. Lett.*, 85:182, 2000. 3

[123] S. Wakimoto, H. Zhang, K. Yamada, I. Swainson, H. Kim, and R. J. Birgeneau1. *Phys. Rev. Lett.*, 92:217004, 2004. xii, 5, 6

[124] F. Wang, H. Zhai, Y. Ran, A. Vishwanath, and D.-H. Lee. *Phys. Rev. Lett.*, 102:047005, Jan 2009. 82

[125] M. Wang, H. Luo, J. Zhao, C. Zhang, M. Wang, K. Marty, S. Chi, J. W. Lynn, A. Schneidewind, S. Li, and P. Dai. *Phys. Rev. B*, 81:174524, May 2010. xxiii, 100

[126] M. Wang, M. Wang, G. Li, Q. Huang, C. Li, G. Tan, C. Zhang, H. Cao, W. Tian, Y. Zhao, Y. Chen, X. Lu, B. Sheng, H. Luo, S. Li, M. Fang, J. Zarestky, W. Ratcliff, M. Lumsden, J. Lynn, and P. Dai. *Phys. Rev. B*, 84:094504, 2011. 6

[127] R. M. White. *Quantum Theory of Magnetism*. McGraw-Hill, New York, 1970. 38, 40

[128] S. D. Wilson, P. Dai, S. Li, S. Chi, H. J. Kang, and J. W. Lynn. *Nature*, 442:59, 2006. 5, 95, 137

[129] S. D. Wilson, C. R. Rotundu, Z. Yamani, P. N. Valdivia, B. Freelon, E. Bourret-Courchesne, and R. J. Birgeneau. *Phys. Rev. B*, 81:014501, Jan 2010. 146

[130] C. Windsor. *Pulsed Neutron Scattering*. Taylor and Francies, London, 1981. 50

[131] D. A. Wollman, D. J. V. Halingen, W. C. Lee, D. M. Ginsberg, and A. J. Leggett. *Phys. Rev.*, 71:2134, 1993. 3

[132] T. Wu, J. J. Ying, G. Wu, R. H. Liu, Y. He, H. Chen, X. F. Wang, Y. L. Xie, Y. J. Yan, and X. H. Chen. *Phys. Rev. B*, 79:115121, 2009. 22

[133] A. L. Wysocki, K. D. Belashchenko, and V. P. Antropov. *Nat. Phys.*, 7:485, 2011. 78

[134] F. Ye, S. Chi, W. Bao, X. Wang, J. Ying, X. chen, H. Wang, C. Dong, and M. Fang. *Phys. Rev. Lett.*, 107:137003, 2011. 6

[135] M. Yi, D. Lu, J.-H. Chu, J. G. Analytis, A. P. Sorini, A. F. Kemper, B. Moritz, S.-K. Mo, R. G. Moore, M. Hashimoto, W.-S. Lee, Z. Hussain, T. P. Devereaux, I. R. Fisher, and Z.-X. Shen. *Proceedings of the National Academy of Sciences*, 108(17):6878–6883, 2011. 76

[136] Z. Yin, K. Haule, and G. Kotliar. *Nat. Mat.*, 10:932, 2011. 24

[137] Z. Yin, K. Haule, and G. Kotliar. *Nat. Phys.*, 7:294, 2011. 112

[138] K. Yosida. *Phys. Rev.*, 106:893, 1957. 26

[139] G. Yu, Y. Li, E. M. Motoyama, and M. Greven. *Nature Physics*, 5:873, 2009. xii, 5, 6, 95, 137

[140] R. Yu, K. T. Trinh, A. Moreo, M. Daghofer, J. A. Riera, S. Hass, and E. Dagotto. *Phys. Rev. B*, 79:104510, 2009. 24, 121

[141] R. Yu, Z. Wang, P. Goswami, A. Nevidomskyy, Q. Si, and E. Abrahams. *arXiv:1112.4785*, 2011. xx, 77, 78

[142] V. Zabolotnyy, D. Evtushinsky, A. Kordyuk, D. Inosov, A. Koitzsch, A. Boris, G. Sun, C. Lin, M. Knupfer, B. Bchner, A. Varykhalov, R. Follath, and S. Borisenko. *Physica C (Amsterdam*, 469:448, 2009. 92

[143] I. A. Zaliznyak, Z. Xu, J. M. Tranquada, G. Gu, A. M. Tsvelik, and M. B. Stone. *Phys. Rev. Lett.*, 107:216403, Nov 2011. xxix, 114, 115, 120, 140, 141

[144] J. Zhao, D. Adroja, D.-X. Yao, R. Bewley, S. Li, X. Wang, G. Wu, X. chen, J. Hu, and P. Dai. *Nat. Phys.*, 5:555, 2009. xvii, 20, 55, 57, 58, 59, 70, 71, 82, 90, 109, 143

[145] J. Zhao, Q. Huang, C. de la Cruz, S. Li, J. W. Lynn, Y. Chen, M. A. Green, G. F. Chen, G. Li, Z. Li, J. L. Luo, N. L. Wang, and P. Dai. *Nature Materials*, 7:953, 2008. 7, 90

[146] J. Zhao, L.-P. Regnault, C. Zhang, M. Wang, Z. Li, F. Zhou, Z. Zhao, C. Fang, J. Hu, and P. Dai. *Phys. Rev. B*, 81:180505, May 2010. 122, 126, 133

Vita

Leland Harriger was born August 1st 1978 in Asheville, NC. He was raised in western North Carolina and attended Madison High School for the first half of his high school years. In his junior year he halted studies for a year to thru-hike the Appalachian Trail, setting the world record at the time as the youngest self-supported thru-hiker to complete the 2000 mile trek. He returned to school in his senior year where he graduated from Mount Pisgah Academy in 1996. He spent the next 2 years as a counselor and assistant teacher at an outdoor based academic program for at-risk youths.

In 1998 he enrolled at Asheville Buncombe Technical Community College where he earned an Associate in Science. During his time at AB-Tech he held two terms as the president of the honors society chapter of Phi Theta Kappa. He also won the Academic Excellence Award, given to two students each year for outstanding achievement in academics and/or exceptional extracurricular involvement. At the end of his last year he won the Math Award, given to one student each year for outstanding academic achievement in mathematics. After receiving his two year degree he enrolled as a transfer student at the University of North Carolina at Chapel Hill. During his three years at UNC-CH he worked under Richard McLaughlin in the Applied Math Department where he ran fluid dynamic experiments in their laboratory and wrote video data analysis software for the group used to constructed motion capture routines that could extract out the position and velocity of fluid elements of interest. After

graduating in 2005 with a double Bachelors of Science in Mathematics and Physics, he returned to AB-Tech as a math instructor where he worked for 2 years.

In August of 2007 he enrolled at the University of Tennessee and began studies towards a doctoral degree in Physics. He joined Pengcheng Dai's Neutron Scattering group on a Neutron Scattering Fellowship though the UT/ORNL collaboration, The Joint Institute of Neutron Science (JINS). During his time at UT his research focused on studies of the spin dynamics in the recently discovered class of Fe-based superconductors where he received the Paul H. Stelson Fellowship for Professional Promise. Upon graduation, he plans on continuing his work in the field as a local contact on the cold triple axis spectrometer SPINS at the National Institute of Standards and Technology (NIST).